UNIVERSITAT AUTÒNOMA DE BARCELONA
Departament de Química
Unitat de Química Analítica

Application of X-ray Synchrotron Based Techniques to the Study of the Speciation, Sorption and Bioavailability of Hg in Environmental and Biological Systems

Centre Grup de Tècniques de Separació en Química

Memòria presentada per **Anna Bernaus Darbra**

per aspirar al grau de Doctor en Química

Bellaterra, Octubre de 2006

UNIVERSITAT AUTÒNOMA DE BARCELONA
Departament de Química
Unitat de Química Analítica
Grup de Tècniques de Separació en Química (GTS)

Manuel Valiente Malmagro, Catedràtic de Química Analítica del Departament de Química de la Universitat Autònoma de Barcelona i

Xavier Gaona Martínez, Doctor en Química,

CERTIFIQUEN:

Que els estudis descrits en la present memòria sota el títol, **"**Application of X-ray Synchrotron Based Techniques to the Study of the Speciation, Sorption and Bioavailability of Hg in Environmental and Biological Systems**"** que presenta la Llicenciada en Química na Anna Bernaus Darbra per optar al Grau de Doctor en Química, han estat realitzats sota la nostra direcció.

I per a què així es faci constar, firmem la següent certificació a

Bellaterra, 20 d'Octubre de 2006

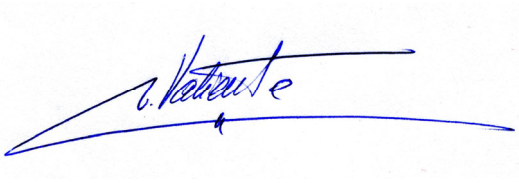

Manuel Valiente Malmagro Xavier Gaona Martínez

Edifici C – Campus de la UAB
08193 Bellaterra (Cerdanyola del Vallès)
Barcelona, Spain
Tel.: 34-935812903; Fax: 34-935812379
gts@uab.es – http://gts.uab.es/gts

Universitat Autònoma de Barcelona

Els estudis que es recullen en la present memòria formen part del projecte d'investigació europeu "Development of Improved Detection Systems for Monitoring of Toxic Heavy Metals in Contaminated Groundwaters and soils, EVK1-CT-1999-00002", i dels projectes del Pla Nacional en I+D+i del Miniterio de Educación y Ciencia, PPQ2002-04267-C03-01, CTQ2005-09430-C05-01 i CTM2006-13091-C02-02.

Igualment voldria agrair:

- Al Ministerio de Educación y Ciencia, per la concessió d'una Beca Predoctoral per a la Formació de Personal Universitari (2002-2006), així com també d'una bossa de viatge per tal de dur a terme una estada de tres mesos al grup del Professor Gordon Brown Jr. de la Universitat de Stanford (California, USA).
- Als projectes de la Comunitat Europea HPRI-CT-1999-00040 i RII3-CT-2004-506008 per finançar els experiments realitzats en la instal·lació sincrotró HASYLAB (Hamburg). S'agraeix també de manera especial el suport tècnic brindat per Gerald Falkenberg i Edmund Welter durant els experiments.
- A l'ERSF (Grenoble) pel proveïment de les instal·lacions de radiació sincrotró, i a Laurent Álvarez per l'ajuda prestada.
- Al SENSPOL Thematic Network (contracte nº EVK1-CT1999-20001) de la Comunitat Europea pel suport amb els experiments realitzats al NICPB (Institut Nacional de Química Física i Biofisica) de Tallinn, Estonia, i la participació al *Technical Meeting* sobre l'impacte de la indústria clor-àlcali a Holanda.
- A l'empresa "Mina de Almadén y Arrayanes S.A." (Ciudad Real) pel subministrament desinteressat de mostres i per l'assessorament rebut.
- Als grups col·laboradors: *Department of Environmental Sciences and Technology*, de la Universitat d'Hamburg (Prof. Wolfgang Calmano); *Department of Environmental Sciences*, de l'Institut Jozef Stefan de Ljubljana, Slovenia (Dr. Milena Horvat); *National Institute of Chemical Physics and Biophysics* de Tallinn, Estònia (Prof. Anne Kahru i Dr. Angela Ivask); *Department of Geological and Environmental Sciences* de la Universitat de Stanford, USA (Prof. Gordon E. Brown, Jr. i David Singer); *GeoDelft-National Institute for Geo-Engineering,* Delft, Holanda (Dr. Derk van Ree); *Departamento de Ingeniería Geológica y Minera*, Escola Universitària Politècnica d'Almadén, Ciudad Real (Prof. Pablo Higueras i Jose Mª Esbrí); l'empresa *ENVIROS S.L.*, Valldoreix, Barcelona; Facultat d'Odontologia de la Universitat de Barcelona (Prof. Isabel Martínez i Prof. Ángel Espías); *School of Dental Medicine* de la Universitat de Buffalo, USA (Prof. Carlos Muñoz); i el Departament d'Odontologia i Estomatologia de la Universitat Internacional de Catalunya (Dr. Lluís Giner).
- Als següents serveis d'anàlisi: el Servei d'Anàlisi Química, per la seva col·laboració en l'ús de l'ICP-OES i per l'atenció mostrada. Al Servei de Microscòpia de la UAB, per a l'obtenció d'imatges i espectres resultants del SEM-EDS. Al Laboratori de Física de les Radiacions del Departament de Física, per l'ús del microones analític de les seves instal·lacions.I al Laboratori de Làmines Primes del Departament de Geologia, per la preparació de làmines de material dental.

Index

Summary

Mercury may be found in the environment in different forms or chemical species of different toxicity. Sources of mercury are both natural (ores, volcanic activity, etc.) and anthropogenic (power plants, chlor-alkali industries, paints, batteries, etc.), although nowadays human activities represent the main contribution of mercury to our environment. Despite its well known toxicity, elemental mercury (together with other mercury compounds) is still used in a wide range of applications in the industry. Hence, mercury is used as extractant in gold and silver production, as mercury-cathode in chlor-alkali industries, in discharge lamps, thermometers, laboratory products and dentistry (dental amalgam), among others applications. Nevertheless, the increasing social awareness of mercury adverse impacts both on the human health and the environment, has lead to a significant reduction of its industrial applications in many of the developed countries.

Toxicity of mercury is determined by the likelihood of exposure, the geochemical and ecological factors influencing its evolution and migration within the environment (such as soil type, redox potential, pH, reaction kinetics, etc) and in particular by the chemical species in which it is found. Consequently, chemical speciation becomes of an utmost importance when assessing the risk associated to mercury impacted environments. Despite this, the number and reliability of analytical techniques able to recognise different mercury species is still very limited, even more when dealing with solid samples. Hence, conventional speciation methodologies normally deal with a first extraction step, followed by a second separation step (usually chromatography) and a final selective measurement. Two main drawbacks have been already pointed out regarding these methodologies: the risk of speciation modification during the extraction process and the limited amount of detectable species (which are basically stacked to organometallic forms of mercury). At this point, synchrotron-based X-rays absorption (XAS) techniques have risen as an interesting and readily available tool to overcome the mentioned speciation gap. Consequently, they had to become a key issue in a Thesis devoted to the study of heavy metal impacted environments.

XAS techniques provide information about the molecular environment of a given element in either aqueous or solid samples with almost no sample pre-treatment. They are based on the interaction between the sample and a high brilliant X-rays radiation generated in a synchrotron facility. The absorbance or fluorescence of the target element when the energy of the incident radiation is close to the energy of its electronic core excitation provides a spectrum with the correspondent absorption edge. Characteristic features are found in this region for each species of the target element, giving information about the oxidation state and

element coordination symmetry. Among others, the most common techniques dealing with these features are XANES (X-ray Absorption Near Edge Spectroscopy) and EXAFS (Extended X-ray Absorption Fine Structure). Further developments in this field focus on the coupling of X-ray absorption techniques to a spatial resolution at a micro-scale level. Along this Thesis, this option has been considered both with the application of μ-XRF (microscopic X-ray Fluorescence) and μ-XAS techniques.

This PhD Thesis has taken advantage of these techniques by studying the problematic of mercury at three different levels:

1. **Basic research**, by assessing the bonding character of methylmercury species adsorbed onto a number of key soil components.
2. **Basic research applied to environmental issues**, by studying two examples of anthropogenic activities that lead to the release of mercury to the environment: mining and chlor-alkali industries.
3. **Applied research**, by assessing the possible diffusion of mercury in teeth holding amalgam filling.

One of the issues raised from these investigations has been the sometimes ambiguous or biased information obtained by synchrotron-based techniques. Consequently, the latter have been complemented with lab-scale techniques and methodologies, such as MW (Microwave) system, ICP-OES (Inductively Coupled Plasma - Optical Spectroscopy), luminescent biosensors, SEM-EDS (Scanning Electron Microscopy - Energy X-ray Dispersive Spectrometer), XRD (X-Ray Diffraction) or SES (Sequential Extraction Schemes), among others.

The understanding of the environmental hazard posed by methylmercury adsorbed onto a number of key soil materials has been accomplished by the combination of XAS techniques and luminescent sensor bacteria (*Escherichia coli* MC1061, pmerBR$_{BS}$luc). Both clays (montmorillonite and kaolinite) and humic acid were spiked with CH_3HgCl and CH_3HgOH at different pH values. The amount of Hg adsorbed was observed to be pH-dependent, whereas the bond character determined by XAS was found to be pH-independent. When comparing interaction between methylmercury and clays or humic materials, the former resulted in a higher ionic character and consequently in a larger possibility of mercury mobilisation. In accordance with XAS results, analyses by luminescent bacteria showed higher bioavailability for methylmercury adsorbed onto montmorillonite. Additionally, this interaction was observed

to be more stable for CH_3HgOH than for CH_3HgCl, probably due to the higher reactivity of the hydroxyl group.

The Almadén district in Ciudad Real (Spain) is the largest known mercury mine in the world. Along the 2000 years of mining activity, more than 285 ktones of mercury have been produced at the different open pits distributed within the district. Such an important mining activity has lead to one of the most interesting, but still relatively unstudied, Hg-impacted environments found around the world. In this context, XAS techniques (complemented with SES, XRD and SEM-EDS analyses) have been utilised to study mercury behaviour in ore, soil, slag and calcine samples. Cinnabar (HgS_{red}) has been found to be the main species in ores and soils (41 to 77% of the total mercury content), whereas metacinnabar (a polymorph of cinnabar) was shown to be the main species in slag samples (42-88 %). In all samples, slightly soluble mercury salts ($HgCl_2$, $HgSO_4$ and schuetteite) have been also found with contents ranging from 5 to 49 % of the total mercury concentration. This fraction might become an important source for mercury mobilisation, and therefore should deserve further attention in risk assessment exercises. In addition, the use of microprobe techniques has revealed elemental correlations between Hg and Pb, Ni and S, indicating a possible geochemical linkage of these elements. Correlations were also identified between Hg and Fe/Mn, which have been attributed to sorption of mercury onto oxy-hydroxides of Fe and Mn. This finding was supported by results from SES.

Chlor-alkali industries with mercury cathode remain as one of the most important industrial applications of mercury in Western Europe. Despite the increasingly rigorous environmental legislations, these industries are commonly pointed as one of the most important point-sources for mercury contamination. The assessment of mercury behaviour in these mercury-impacted environments has been conducted by XAS techniques coupled to SES. Speciation information obtained by XANES showed that inorganic mercury compounds dominate in all soil samples considered, being cinnabar (HgS_{red}) and corderoite ($Hg_3S_2Cl_2$) the main species. The presence of Cl-bearing mercury compounds has been found consistent with this specific industrial context, as chlor-alkali plants utilise brines as raw material. Slightly soluble phases (HgO and $HgSO_4$) have been also identified in minor proportions (from 6 to 20 % of the total mercury concentration), extent which has been also confirmed by SES. The sequenced extractions revealed a larger fraction of weakly available Hg, with mercury bound to the exchangeable phase accounting for 17% of total mercury content. On the other hand, μ-

XRF analysis showed a geochemical correlation of Hg, Cu and Ni, which suggest the possible formation of solid solutions of these elements within the same crystalline structure.

Finally, synchrotron X-ray microprobe techniques have been proposed for the direct observation of mercury present in human teeth restored with dental amalgams. This study aimed at assessing the possible diffusion of mercury from tooth fillings and its possible uptake by the blood stream via the tooth pulp. Before experiments at the synchrotron facility, bulk analysis of major components within the different regions of teeth samples (enamel, dentine and root region) was performed by SEM-EDS. As expected, a main contribution of Ca, P and O has been found at the enamel region. Mercury, Ag, Sn and Cu were found to dominate at the amalgam region, whereas Ca, Zn, Na and O appeared to be the main components in the dentine region. Then, μ-XRF analyses have been undertaken to identify elemental profiles within the considered teeth samples, while also looking for qualitative trends on elemental associations at the different tooth regions. Variations of elemental distribution in both the surface and depth of sample revealed heterogeneous distribution within and among the observed regions. The microprobe analyses showed a minimum diffusion of Hg throughout the tooth, with the identification of a linear correlation between Hg and Cu. On the other hand, a significant diffusion of Cu and Zn from the amalgam to the dentine region was identified, which was correlated with a slight depletion on Ca concentration in this region. This fact suggests the possible exchange of Ca^{2+} by Cu^{2+}/Zn^{2+} in hydroxiapatite crystals ($Ca_{10}(PO_4)_6(OH)_2$), the dominating mineral compound in the dentine region. On the other hand, μ-EXAFS analyses were performed to assess the speciation and molecular environment of Hg in the considered teeth samples. Results show a similar Hg coordination environment at the amalgam itself and at the interface amalgam – tooth. Moreover, a first approach to the first coordination shells fitting in the amalgam region reveals the presence of Ag and Hg atoms around the target element (Hg), and the absence of oxygen. This result corroborates the poor (or null) interaction of mercury with the tooth environment as well as the lack of mercury transformation with time.

Chapter 1

General Introduction

1.1 GENERAL PROPERTIES OF MERCURY

Mercury is known by human beings since more than 4000 years. Ancient Chinese and Hindus already used the cinnabar (red HgS) to colour the skin[1], as paint, as well as in ointments. The Hindus also believed in mercury's aphrodisiac properties[2], and Phoenician used it within the recovery process of gold. Mercury has been also found in Egyptian graves (1600-1500 b.C.), whilst Romans and Grecians used it for medical purposes. In fact, mercury was believed to be the panacea of any illness, in spite of its toxicity[3].

Hence, during more than twenty centuries, mercury was known and used by several cultures worldwide. However, its consumption until the end of 15th century was scarce. In 1557, Bartolomé Medina developed the method named "Beneficio del Patio" for the cold amalgamation of silver minerals. This was the inflexion point concerning mercury consumption and applications. For instance, Parcelaso, at the 16th century, considered by first time its application in the treatment of syphilis[3]; Torricelli, in 1643, used mercury in his barometer; and Fahrenheit, in 1720, used it in his thermometer.

A variety of other applications have been completed since then, taking advantage of mercury tendency to alloy with most metals, its liquid character at room temperature, a rather poor conduction of heat but fair conduction of electricity[4].

The chemical symbol for mercury, Hg, comes from the Latin "hydrargyrum" (liquid silver), as at ordinary temperatures, mercury is a shiny liquid, silvery and odourless. Mercury is the heaviest known elemental liquid. Some Hg properties are presented in Table 1.1. The surface tension of mercury is about six times higher than that of water, being this the reason for its poor wettability by water. On the other hand, the dynamic viscosity of mercury is of the same order of magnitude as that of water. Some other metals, such as gold, silver and zinc, readily dissolve in mercury to form amalgams. Its unusual high volatility accounts for its presence in the atmosphere as elemental Hg vapour in appreciable amounts. A saturated atmosphere at 20 ºC has almost 15 mg m^{-3}, a value 300 times higher than the maximum punctual value

[1] Kirk-Othmer. *Kirk-Othmer Encyclopedia of Chemical Technology*, Second Edition, Wiley-Interscience, New York, 1964

[2] Kaiser, G.; Tolg, G. *Mercury. The handbook of Environmental Chemistry,* Hutzinger, O. (ed.), Vol. 3, Part A, Springer Verlag, Berlin, 1980, pp.1-58

[3] Berman, E. *Toxic Metals and their Analysis*, Heyden & Son, Ltd., London, 1980

[4] Adriano, D.C. Trace Elements in Terrestrial Environments: Biogeochemistry, Bioavailability, and Risks of Metals, Second Edition, Springer, New York, 2001

allowed (0.05 mg m^{-3}), or 1000 times higher than the continuo exposure level (0.015 mg m^{-3})[5].

Table 1.1 General properties of mercury (after Domy C. Adriano, 2001[4]).

	Atomic number	Atomic weight	Melting point	Boiling point	Specific gravity	Vapour pressure	Solubility in water
Hg	80	200.6 g mol^{-1}	-38.8 ºC	356.6 ºC	13.55 g cm^{-3}	1.22×10^{-3} mm at 20 ºC (2.8×10^{-3} mm at 30 ºC)	6×10^{-6} g/100 ml (25 ºC)

Mercury has seven stable isotopes with the following abundance: ^{195}Hg (0.15 %), ^{198}Hg (10.1 %), ^{199}Hg (17.0 %), ^{200}Hg (23.3 %), ^{201}Hg (13.2 %), ^{202}Hg (29.6 %), and ^{204}Hg (6.7 %)[4]. There exist three stable oxidation states of Hg: 0 (elemental), I (mercurous), and II (mercuric), which determine its properties and behaviour. Metallic mercury dissolves in nitric acid, aqua regia, warm concentrated hydrochloric acid and sulphuric acid. It is sparingly soluble in dilute HCl, HBr, and HI as well as in cold sulphuric acid. Mercury is rarely found in nature as the pure, liquid metal, but rather as inorganic salts and compounds. Mercuric and mercurous oxidation states form a significant number of organic and inorganic compounds, although the mercurous state is less stable under common environmental conditions[6].

1.2 MERCURY IN THE ENVIRONMENT

Mercury is a natural component of the Earth, with an average abundance *ca.* 0.05 mg kg^{-1} in the Earth's crust, showing significant local variations[7]. Three aspects of the chemistry of mercury influence its presence in the environment and distinguish it from the other heavy metals:

- the volatility of elemental mercury
- an accessible redox chemistry whereby elemental mercury can be quite easily produced in soils from mercury compounds

[5] World Health Organization (WHO), *Environmental Health Criteria 118: Inorganic Mercury*, International Programme on Chemical Safety, Geneva, 1991

[6] Fergusson, J.E. The Heavy Elements: Chemistry, Environmental Impact and Health Effects, Pergamon, Oxford, 1991

[7] United Nations Environment Programme (UNEP) Chemicals, Global Mercury Assessment, Geneva, December 2002, [on-line], <http://www.chem.unep.ch/mercury/Report/>, [29 May 2006]

- the biomethylation process, which produces very toxic, and often volatile compounds, e.g. $(CH_3)_2Hg$

The most common Hg compounds in the environment are inorganic species of Hg(II): HgS, $HgCl_2$, HgO and $Hg(OH)_2$. When mercury combines with organic carbon, the compounds formed are called "organic" mercury compounds or organomercurials. Nowadays, a large number of organic mercury compounds are known (such as dimethylmercury, phenylmercury, ehylmercury and methylmercury). However, methylmercury is by far the most commonly found in the environment (either as CH_3HgCl or CH_3HgOH).

1.2.1 Inorganic species of mercury

Mercuric mercury is a polarisable ion that, as a soft acid, strongly associates with soft bases, such as the S^{2-} ion. The reaction of mercury with sulphur leads to the highly insoluble HgS, analogously to the addition of H_2S to a Hg(II) solution. There exist two polymorphic forms of this compound, metacinnabar, cubic HgS (ZnS structure), which is stable at high temperatures and cinnabar, trigonal HgS with linear Hg-S linkages, stable at low temperatures. This compound shows an extremely low solubility (log K_{sp}= -53). Under reducing conditions, the chemistry of the system Hg – S is very reach, and a large number of aqueous complexes are known. In this sense, the formation of species such as $Hg(SH)_2(aq)$, $HgS(SH)^-$ and HgS_2^{2-} enhances the solubility of HgS(s) under increasing sulphide concentrations (see Figure 1.1).

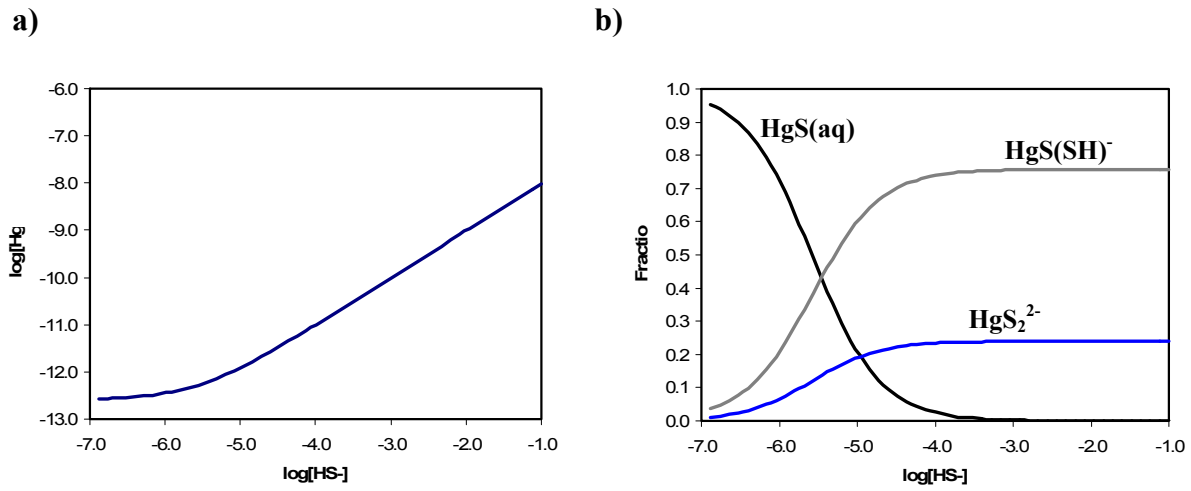

Figure 1.1 Solubility curves of HgS(s) **(a)** and underlying aqueous speciation **(b)** under increasing HS- concentration. Considered parameters: Eh = -0.3V; pH = 8.

Under aerobic conditions, HgS can be oxidised to mercury sulphite and sulphate. This occurs under the conditions of natural water (< 0.5 ‰ of dissolved salts, pH *ca.* 7 and redox potential 400-500 mV) presence of oxygen and bacteria. Several halides of Hg(II) are known, the stability of them increasing in the order Cl-<Br-<I-. Regarding chlorides, different chloro-species can be found in aqueous solutions (see Figure 1.2)[6].

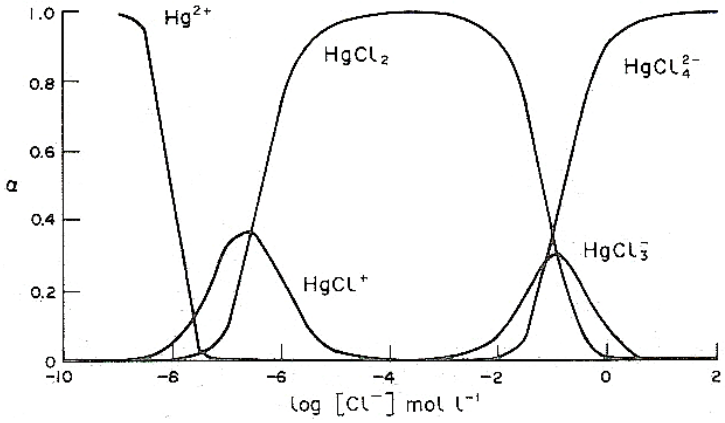

Figure 1.2 Distribution diagram for Hg(II) chloro-species (after Jack E. Fergusson, 1991[6]).

Consequently, both chloride and sulphide particularly influence the speciation of mercury in aqueous systems. Figure 1.3 (a,b) shows the stability regions for mercury sulphides, oxide and chlorides. Chloride complexes and compounds dominate in acidic and oxidising environments, whereas the oxides and hydroxide predominates under alkaline and oxidising conditions. Sulphide complexes and compounds dominate under reducing environment. A marked feature is the stability of metallic mercury over a wide range of conditions, being basically found under reducing environments. Its solubility in water is 2.8×10^{-7} M. [8]

Carbonate species may control mercury speciation ($HgCO_3$) under alkaline conditions and with medium to high carbonate concentration. In presence of carbonate, solid compounds can occur either by precipitation of Hg(II) or by oxidation of mercury sulphide compounds (e.g. HgS, HgS_2^{2-}) [6]. On the other hand, the soluble species $HgHCO_3^+$ (log K= 15.08 ± 0.1, I= 0.5 mol dm^{-3}) and $HgCO_3^0$ (log K= 11.01 ± 0.2, I= 0.5 mol dm^{-3}) predominate in solution[9].

[8] Spencer, J.N.; Voigt, A.F. Journal of Physical Chemistry, 1968, 72, 464-470

[9] Bilinski, H.; Markovic, M.; Gessner, M. Inorganic Chemistry, **1980**, *19(11)*, 3440-3443

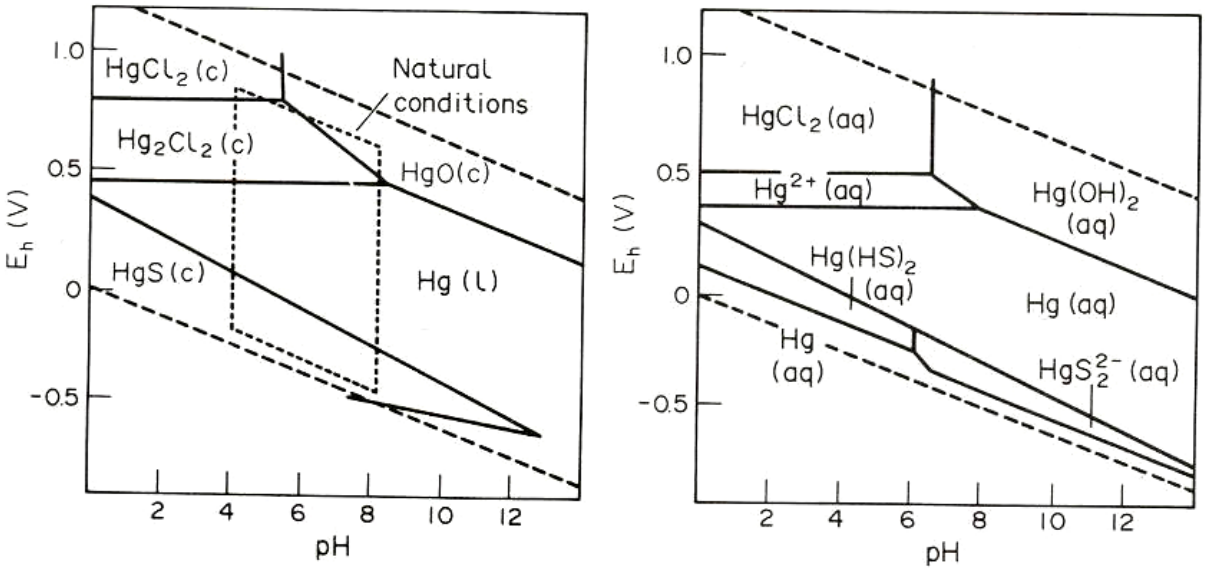

a) **b)**

Figure 1.3 Predominance diagram of solid mercury compounds **(a)** and aqueous mercury complexes **(b)** (after Leckie and James, 1976[10]).

Mercurous ion forms weaker complexes than mercuric ion, and this tendency is exhibited in hydrolysis behaviour. Mercury (I) is moderately stable towards disproportion in solution (Eq. 1.1), and any oxidising agent that oxidises mercury to give Hg(I) will also produce Hg(II).

$$Hg_2^{2+} \rightarrow Hg + Hg^{2+} \qquad \textbf{Eq. 1.1}$$

The four halides, Hg_2X_2, are known and have a linear structure. The chloride, bromide and iodide are insoluble and precipitate from solution by adding an alkali metal halide to mercurous nitrate. The chloride (calomel) is used in the saturated calomel secondary reference cell (Eq. 1.2),

$$Hg_2Cl_2 + 2e \rightarrow 2Hg(l) + 2Cl^- \qquad E = 0.2415 \pm 0.00076 \text{ V at } 25^\circ C \qquad \textbf{Eq. 1.2}$$

Mercurous sulphate is used in the standard Weston cell[6], whereas there exist poor evidences concerning the existence of Hg(I) oxides and hydroxides .

1.2.2 Organomercury species

Organomercury compounds are characterised by a Hg-C covalent, non-polar bond. This bond is thermodynamically quite weak (60-120 kJ mol^{-1}), which eases the use of these compounds for the preparation of more stable organometallic systems[11]. However, the Hg-C covalent

[10] Leckie, J.O.; James, R.O. Control mechanisms for trace metals in natural waters, in: Aqueous Environmental Chemistry of Metals, Ann Arbor Science Publishers, Michigan, 1976, pp.1-76

[11] Greenwood, N.N.; Earnshaw, A. *Chemistry of the Elements*, Pergamon Press, Oxford, 1984

bond is still stronger than such between Hg-O. This is the main reason for the observed stability of organomercury compounds in air and water.

Inorganic and organomercury species transform in the environment, either in presence or absence of bacteria. A general scheme of this cycle is given in Figure 1.4.

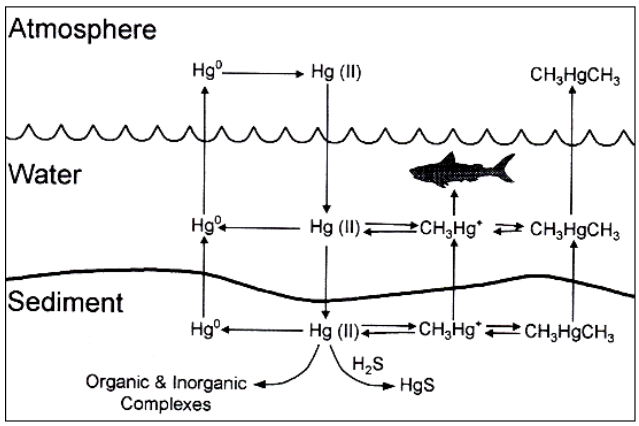

Figure 1.4 Cycling and interconversion of various mercury species in freshwater lakes (after Winfrey and Rudd, 1990[12]).

Methylmercury accounts for approximately 0.1-1.5% of the total mercury in sediments, and around 2% of the total mercury in seawater. Fish are known as bio-accumulators of methylmercury, reaching high values. In some species and under certain conditions, methylmercury might represent >80% of the total mercury[6].

The rate of production of CH_3Hg^+ is generally higher in saline water than in fresh water[13]. In acidic groundwaters, the cation CH_3Hg^+ is the main organomercury species. However, under near-neutral conditions, methylmercury hydrolyses and CH_3HgOH becomes the most stable species. Accounting for the high chloride concentrations found, the species $CH_3HgCl(aq)$[14] is the predominating methylmercury species under seawater conditions. The binuclear species $(CH_3Hg)_2OH$ appear to be of minor importance at low concentrations of organomercury

[12] Winfrey, M.R.; Rudd, J.W.M. Environmental Toxicology and Chemistry, **1990**, *9*, 853-861

[13] Craig, P.J. *Environmental aspects of organometallic chemistry,* in: *Comprehensive Organometallic Chemistry*, Wilkinson, G.; Stone, F. G. A. (eds.), Vol. 2, Pergamon, New York, 1982

[14] Dyrssen, D.; Wedborg, M. Major and minor elements, chemical speciatoin in estuarine waters, in: Chemistry and Biogeochemistry of Estuaries, Wiley-Interscience, New York, 1980, pp. 121-151

species, being the addition of the second methyl group around 6000 times slower than the production of CH_3Hg^{+}[15].

Most organic compounds show a limited solubility in water. Differing to this, CH_3HgOH rather dissolves in water due to the high capacity of its hydroxyl group to establish hydrogen bonds with the water molecules.

1.2.2.1 Methylation of inorganic mercury

Methylmercury found in the environment hardly comes from anthropogenic sources. In this sense, both biotic and abiotic methylation of inorganic mercury are known as the main sources of methylmercury, being biotic the more common process in the greater part of environments.

Biotic methylation is associated with the activity of sulphate reducing bacteria, which are mainly found in the bottom sediments of rivers, estuaries and lakes[16,17]. Although other bacteria have been described as participating in this process, around 95 % of mercury biomethylation is carried out by sulphate reducing microorganisms[18]. Several factors influence the formation of CH_3Hg^{+}, such as temperature, mercury and bacteria concentration, pH and type of soil or sediment, sulphide concentration, the redox conditions, among others[6].

Methylation of mercury occurs both under aerobic and anaerobic conditions, although higher methylation rates are given in reducing environments[13,19]. The exact methylation mechanism remains still unknown, although some studies suggest HgS as being the starting species in the methylation process[20-22]. Its neutral character and small size eases the HgS permeation through the cell barriers toward the bacteria core, where the methyl group is released by some donor groups, as acetate, pyruvate or serine, and the methylation reaction takes place.

Transmethylation of organometallic species is the main abiotic mechanism of mercury methylation. This process involves organometallic species of elements such as lead, arsenic or

[15] Craig, P.J. *Organomercury compounds in the environment*, Longmans, Harlow, UK, 1986, pp. 65-110

[16] Guimaraes, J.R.D.; Roulet, M.; Lucotte, M.; Mergler, D. The Science of the Total Environmental, **2000**, *261*, 91-98

[17] Zillioux, E.J.; Porcella, D.B.; Benoit, J.M. Environmental Toxicology and Chemistry, **1993**, *12*, 2245-2264

[18] Choi, S-C.; Chase Jr., T.; Bartha, R. Applied and Environmental Microbiology, **1994**, *60(11)*, 4072-4077

[19] Povari, P.; Verta, M. Water Air and Soil Pollution, **1995**, *80*, 765-773

[20] Benoit, J.M.; Gilmour, C.C.; Mason, R.P. Environmental Science and Technology, **2001**, *35(1)*, 127-132

[21] Jay, J.A.; Murray, K.J.; Gilmour, C.C.; Mason, R.P. Morel, F.M.M.; Roberts, A.L.; Hemond, H.F. Applied and Environmental Microbiology, **2002**, *68(11)*, 5741-5745

[22] Hammerschmidt, C.R.; Fitzgerald, W.F. Environmental Science and Technology, **2004**, *38(5)*, 1487-1495

tin. In this sense, this mechanism might be certainly important in heavily polluted fluvial environments, for instance the Elba river[23,24].

1.2.2.2 Demethylation of methylmercury

Unlike methylation of inorganic mercury, the mechanism for mercury demethylation is known and well understood. The reaction takes place in cell-core of organomercury-resistant bacteria and is driven by the presence of the gene organomercurial-lyase. The presence of this gene permits the breaking down of the Hg-C bond by the bacteria[25]. As described elsewhere, two main mechanisms exist depending on the involved bacteria[26]. On the one hand, demethylation carried out by methanogen bacteria leads to inorganic mercury accompanied by the release of methane, hydrogen and carbon dioxide:

$$4CH_3Hg^+ + 2H_2O + 4H^+ \rightarrow 3CH_4 + CO_2 + 4Hg^{2+} + 4H_2 \qquad \textbf{Eq. 1.3}$$

on the other hand, demethylation is also performed by sulphate reducing bacteria. In this case, inorganic mercury is released together with sulphidric acid, carbon dioxide and water:

$$SO_4^{2-} + CH_3Hg^+ + 3H^+ \rightarrow H_2S + CO_2 + Hg^{2+} + 2H_2O \qquad \textbf{Eq. 1.4}$$

1.3 PRODUCTION OF MERCURY

Mercury production by human activity throughout the history[27] has been estimated as close to one million tons of metallic Hg. Production was fairly constant at about 3.6×10^3 tonnes yr^{-1} from 1900 to 1939[28]. Since the 1960s, however, production has more than doubled but declined to 2.2×10^3 tonnes yr^{-1} average world mercury production from 1990 to 2000. In 2005, China (500 t), Kyrgyztan (300 t), and Spain (150 t) were the apparent leaders in world production of mercury[29]. Eventually, mercury production is declining, owing to the global environmental and human health concerns. Taking into account such declining consumption rates, world mercury resources (nearly 600000 tones) are sufficient for at least another century.

---

[23] Ebinghaus, R.; Wilken, R.D. Applied Organometallic Chemistry, **1993**, *7*, 127-135

[24] Ebinghaus, R.; Hintelmann, H.; Wilken, R.D. Journal of Analytical Chemistry, **1994**, *350*, 21-29

[25] Oremland, R.S.; Culbertson, C.W.; Winfrey, M.R. Applied and Environmental Microbiology, **1991**, *57(1)*, 130-137

[26] Marvin-DiPasquale, M.C.; Oremland, E.S. Environmental Science and Technology, **1998**, *32*, 2556-2563

[27] Hylander, L.D.; Meili, M. The Science of the Total Environment, **2003**, *304*, 13-27

[28] Gavis, J.; Ferguson, J.F. Water Research, **1972**, *6*, 989-1008

[29] Brooks, W.E. *U.S. Geological Survey, Mineral Commodity Summaries*, January 2006, [on-line], <http://www.usgs.gov>, [29 May 2006]

Hg production refers both to primary and secondary production. Primary production comprises the Hg extraction from mineral ores either as a main element or as a by-product. The latter accounts for several types of gold-silver and massive sulphide deposits, reporting values up to 5% of the world's production[30]. The secondary production includes the recycling, recovering and reuse of Hg from industrial processes. This option represented in 2000 around 25% of the total Hg production[31]. Three main areas contribute to the recover of liquid mercury:

- dismantling of chlor-alkali industries
- recovery from mercury counters in the natural gas piping
- recovery from rectifiers and Hg manometers

Thermal extraction is the main process applied to the recovery of Hg from waste. Waste is exposed to temperatures up to 538 ºC to vaporize Hg. Finally, mercury is recovered as a liquid by cooling down the vapour through water condensers.

1.3.1 Primary production: natural mercury deposits

The estimated primary production of Hg until the year 2000 was *ca.* 840000 t with the distribution shown in Figure 1.5. The principal deposits are located in Almadén (Spain, 30% of the total world's production), Idrija (Slovenia), Monte Amiata (Italy), Huancavelica (Peru), as well as smaller deposits located at the California Coast range (New Almadén and New Idria)[27,30].

Due to the growing environmental concern and the consequent drop of the mercury price, large scale mercury mining facilities were strongly affected from the 80's. Hence, all the abovementioned Hg mines are nowadays closed, whereas the (smaller) Khaydarkan mining complex in Kyrgyzstan has taken the leadership in primary mercury production.

[30] Rytuba, J.J. Environmental Geology, **2003**, *43*, 326-338

[31] Maxon, P. *Mercury flows in Europe and the world: the impact of decommissioned chlor-alkali plants*, February 2004, [on-line], <europa.eu.int/comm/environment/chemicals/mercury/pdf/report.pdf>, [22 May 2006]

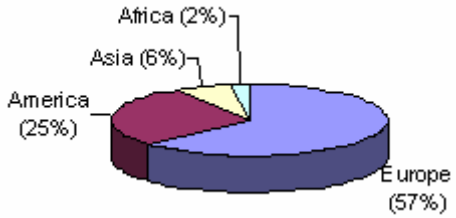

Figure 1.5 Distribution of global primary production of Hg until 2000. (after Hylander and Meili, 2003[27]).

Natural mercury deposits are globally distributed in three types of mineral belts: silica-carbonate, hot-spring and Almadén type, which are co-genetic and reflect similar tectonic and volcanic processes that contributed to the concentration of mercury.

Silica-carbonate type deposits, well developed in the California Coast Range, are associated with serpentinite, commonly emplaced along fault zones, to an assemblage of silicate and carbonate minerals. The mercury ores are hosted in silica-carbonate-altered serpentinite and adjacent sedimentary rocks.

Hot-spring-type mercury deposits, the most common of the world's mercury mineral belts, are closely associated with volcanic centres and form in the near surface environment. Mercury ores are hosted in hot-spring sinter (banded silica phases and beds of hydrothermal eruption breccia) and associated with sedimentary and volcanic rocks that have been silicified and altered to a clay alteration assemblage.

Finally, the **Almadén-type deposit** is the largest and highest-grade mercury deposit, and is essentially restricted to the Almadén district in Spain. These deposits are associated spatially with mafic submarine vent complexes that consist of mafic dikes and sills, and oval craters with typical dimensions of 300 m by 150 m, and submarine calderas[30]. Given the related studies undertaken in the present PhD thesis, further details on this Hg deposit and the site-mining activity are given in section 1.3.1.1.

Mercury content in mined ores usually ranges from 0.5 to 2%. However, the Almadén mine shows significantly higher concentrations, with contents up to 12-14% of mercury[7]. Cinnabar is the main mineral in all three mercury deposit types, with only a few exceptions. The primary processing method for the extraction of mercury consists of an inexpensive thermal process, where the ores are heated at temperatures above the upper stability temperature of cinnabar (583.5 ºC). At this point, cinnabar decomposes and mercury is released as volatile,

elemental mercury. The process ends up with a condensation recovering elemental liquid mercury[32]. The equation for this extraction is:

$$HgS + O_2 \rightarrow Hg + SO_2 \qquad \textbf{Eq. 1.5}$$

In addition to cinnabar, other minerals and mercury phases can be found in the abovementioned mercury belts. Therefore, elemental mercury is found in some Almadén-type and silica-carbonate-type deposits; mercury sulfates and chlorides are present in some silica-carbonate deposits, whilst corderoite ($Hg_3S_2Cl_2$), schwartzite [$(HgCuFe)_{12}Sb_4S_{13}$], and livingstonite ($HgSb_4S_7$) are the dominant mercury minerals in some hot-spring-type deposits[30].

Secondary phases, such as metacinnabar or several chloride compounds can be also found as a result of diverse processes taking place in the mine environment: cinnabar conversion during the roasting of the ore, weathering of the waste piles, etc.[33].

1.3.1.1 'Mina de Almadén y Arrayanes'

The Almadén area is located some 285 km south of Madrid (south-central Spain, see Figure 1.6) and is the largest and oldest (more than 2000 years) point source of mercury in the world. The mineral belt consists of 11 mercury deposits located within a small area of about 200 km^2.

Almadén geology is dominated by a faulted syncline in Palaeozoic siliciclastic shelf sediments intruded by mantle-derived mafic igneous sills, dykes and diatreme-like breccias containing ultramafic xenoliths[34]. A detailed geologic profile is shown in Figure 1.6. The ore bodies show extremely high mercury concentrations (up to several percent w/w), mostly as cinnabar. Elemental mercury is present in all the deposits, but it is significantly important in the deposit of Las Cuevas. This deposit is situated in a submarine caldera whereas some of the smaller deposits are localized in mafic dikes that are associated with mafic volcanic centers[30].

[32] Rytuba, J.J. Mercury Geoenvironmental Models, in Progress on geoenvironmental models for selected mineral deposit types, 2002, [on-line], <http:// pubs.usgs.gov/of/2002/of02-195/>, [23 May 2006]

[33] Kim, C.S; Brown Jr., G.E.; Rytuba, J.J. The Science of the Total Environment, **2000**, *261*, 157-168

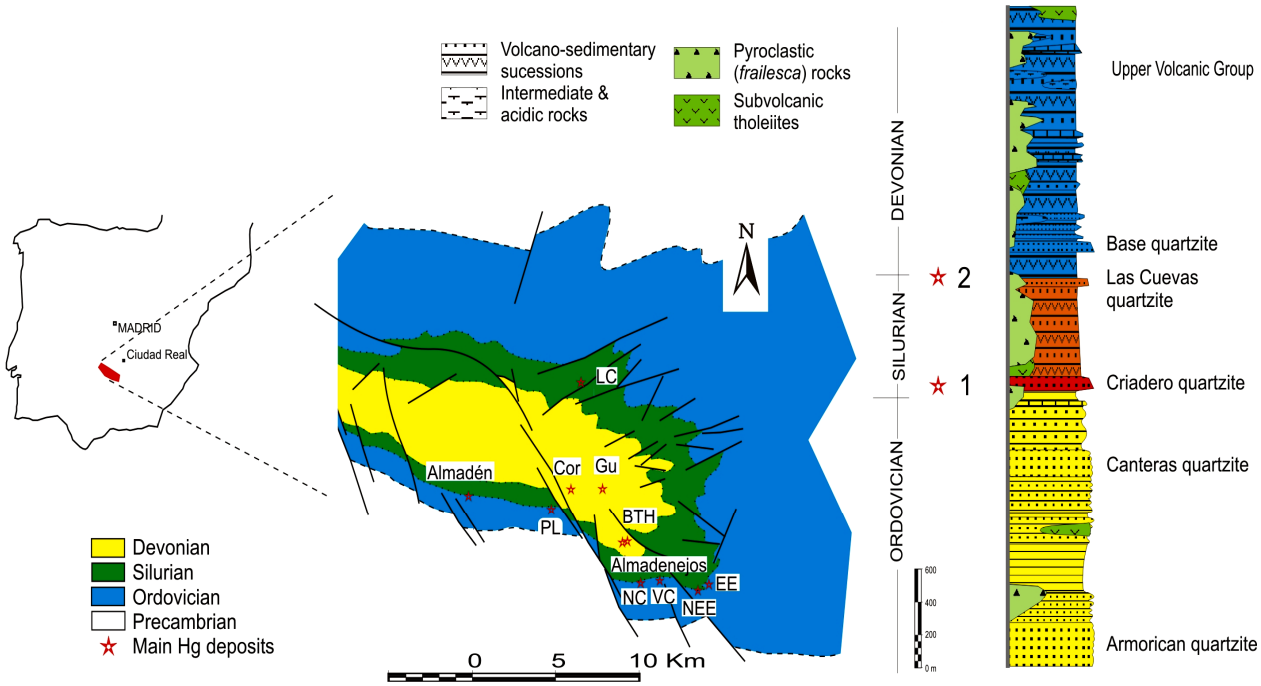

Figure 1.6 Location of Almadén in Spain, geologic profile of the area and main Hg deposits: Almadén, LC (Las Cuevas), COR (Corchuelo), GU (Guadalperal), PL (Pilar de la Legua), BTH (Burcio Tres Hermanas), Almadenejos, NC (Nueva Concepción), VC (Vieja Concepción), EE (Entredicho) and NEE (Nuevo Entredicho).

The mining operation dates from the Roman age, whereas the total Hg extracted from the mine amounts to about 285000 tons of Hg[34]. The production was more than 1000 t of Hg per year in 1995 and 1996, but was reduced to approximately 400 t y^{-1} during 1997-2000, mainly due to the declining demand for Hg[27]. Mining activity in Almadén ceased in 2002. Nevertheless, the extensive mining of the area has left an impressive legacy of contamination that poses a health treat to the current population and to the local ecosystem[35].

During the 17th-19th century, retorting furnaces were used in the extraction process, involving simple roasting of the HgS at high temperatures. The mercury was then recovered by condensing the vapour within enclosed pottery channels that were manually cooled with slave labour and cold water. At the end of the V-shaped pottery line was a chamber capped by a metal lid where gas expansion induced further mercury condensation. In more recent times, the processing was done at the Almadén mine itself using propane ovens with roasted the ore

[34] Hernández, A.; Jébrak, M.; Higueras, P.; Oyarzun, R.; Morata, D.; Munhá, J. Mineralium Deposita, **1999**, *34*, 539-548

[35] Higueras, P.; Oyarzun, R.; Lillo, J.; Sánchez-Hernández, J.C.; Molina, J.A.; Esbrí, J.M.; Lorenzo, S. The Science of the Total Environment, **2006**, *356*, 112-114

at 700ºC, with considerable mercury losses to the atmosphere[36,37]. Moreover, the roasted mine wastes (calcines) were typically transported short distances from the furnace and dumped in loose, unconsolidated piles, containing high Hg concentrations[38].

1.4 USES OF MERCURY

Hg is liquid at room temperature, is a good electrical conductor, has very high density and high surface tension and expands/contracts uniformly over its entire liquid range in response to changes in pressure and temperature. Because of its unique characteristics, mercury shows a wide range of applications in the industry. Additionally, and given its high toxicity, mercury has been also used in the past in agriculture as pesticide and herbicide.

Nevertheless, the increasing social awareness of the mercury adverse impacts on the human health and the environment has involved the drop in the number of industrial applications, where mercury-bearing products are being substituted for less toxic equivalent components[29]. Consequently, the amount of mercury used and produced in many of the industrialised countries has been significantly reduced.

Though declining, mercury is still widely used as extractant in gold and silver production, in mecury-cathode for chlor-alkali industries, in discharge lamps, power rectifiers, mercury batteries, thermometers, barometers and electrical switches, laboratory products and dentistry (dental amalgam)[4].

Though forbidden in several countries, Zn/Hg batteries are still widely used. The working mechanism of these batteries includes a cathode of HgO and an anode of Zn. The cell reaction is shown in Eq. 1.6, where KOH saturated with ZnO acts as electrolyte[2].

$$Zn + HgO \rightarrow ZnO + Hg \qquad \textbf{Eq. 1.6}$$

A number of mercury compounds have fungicidal activity. Hence, additionally to its agricultural applications, several mercury compounds have been used in paints and as seed dressings to prevent the growth of fungi and mildew. This use of mercury is now banned in many countries, especially those applications involving the use of methylmercury compounds. Similar compounds are used in the pulp and paper industry as slimicides[2].

---

[36] Ferrara, R.; Maserti, B.E.; Andersson, M.; Edner, H.; Ragnarson, P.; Svanberg, S.; Hernandez, A. Atmospheric Environment, **1998**, *32*, 3897-3904

[37] Moreno, T.; Higueras, P.; Jones, T.; McDoland, I.; Gibbons, W. Atmospheric Environment, **2005**, *3*9, 6409-6419

[38] Gray, J.E.; Hines, M.E.; Higueras, P.L.; Adatto, I.; Lasorsa, B.K. Environmental Science and Technology, **2004**, *38*, 4285-4292

Mercury salts are used as catalysts in the production of vinyl chloride (eq. 1.7), vinyl acetate and acetaldehyde (Eq. 1.8) from acetylene,

$$C_2H_2 + HCl \xrightarrow{HgCl_2} CH_2{=}CHCl \qquad \textbf{Eq. 1.7}$$

$$C_2H_2 + H_2O \xrightarrow{HgSO4} CH_3CHO \qquad \textbf{Eq. 1.8}$$

In the last reaction Hg(II) is reduced to Hg, which later on is regenerated by conversion to Hg(II) with iron (III). In this sense, one of the most important mercury poisoning incidents of the modern history resulted from the uncontrolled effluents of a factory in Minamata (Japan), which used the reaction described by Eq. 1.8 to produce acetaldehyde[39].

Substitution of products and modification of processes using mercury has been one of the most used preventive measures influencing the flow of mercury, both from an economical and environmental point of view. For instance, Zn/Hg batteries have been substituted by lithium, nickel-cadmium, and zinc-air batteries; diaphragm and membrane cells replace mercury cells in the chlor-alkali industry; ceramic composites are rapidly replacing mercury dental amalgams; organic compounds have replaced mercury fungicides in latex paint and digital instruments have replaced mercury thermometers in many applications[40].

Prevention has also reached mercury mining as well as activities consuming raw materials which lead to the release of mercury. Likewise, several protection measures are being applied to reduce (or delay) mercury release to the environment, including end-of-pipe techniques (e.g. exhaust gas filtering), monitoring of mercury releases and mercury waste management[41], among others.

Nevertheless, given the long technical lives of those industrial processes using mercury, it may take decades before most of the mercury in use would be collected and removed from the production chain.

[39] Löfroth, G. Methylmercury, a review hazards and side effects associated with the emission of mercury compounds into natural systems, Stockholm, 1970

[40] Reese Jr., R.G. U.S. Geological Survey, *Mineral Commodity Summaries*, February 2000, [on-line], <http:// pubs.usgs.gov/of/2002/of02-195/>, [23 May 2006]

[41] Paine, P.J. *Compliance with chlor-alkali mercury regulations*, 1986-1989 Status report, Minister of Supply and Services Canada, Ottawa, 1994

1.4.1 Chlor-alkali industry

Mercury cathodes for chlor-alkali industries are one of the biggest Hg users and emitters. These industries produce chlorine and sodium hydroxide by the electrolysis of a brine solution. This production process was introduced at the end of the 19th century by Castner-Kellner (1892), and was characterized by the Hg cathode, which allows the reduction of Na^+/Na, instead of the H^+/H_2 reduction. This fact is due to the over-potentials given for the H^+/H_2 reduction and the amalgamation of the metallic Na with the liquid Hg, the latter acting as the driving force of the overall reaction. The second step of the process is the reaction of the amalgam with water to obtain hydrogen and caustic soda, whilst mercury is recycled back to the first cell. The related reactions are shown in Eq. 1.9:

Anode:	$Cl^- \rightarrow 0.5Cl_2 + e^-$	
Cathode:	$xHg + Na^+ + e^- \rightarrow NaHg_x$	
Subsequent cathode reaction:	$NaHg_x + H_2O \rightarrow 0.5H_2 + NaOH + xHg$	
Global balance:	$NaCl + H_2O \rightarrow 0.5Cl_2 + 0.5H_2 + NaOH$	**Eq. 1.9**

This process produces high purity Cl_2 and NaOH solution (50%), although high-purity brines and high electricity consumption are required. The process has also strong environmental connotations given the use of huge mercury amounts.

An average-size plant accounts for a total of 100 Hg-cell, containing each about 3 t of Hg. Along the production process and in spite of the mercury recycling in-plant, mercury can be potentially released to the environment through the air, water and solid wastes, as well as impurity in the same product[41]. In this sense, and due to the increasing environmental concern, Hg-cathode plants are being replaced by other technologies which show a higher degree of agreement with environmental parameters and run at lower voltages: diaphragm (using asbestos), membrane and, in small quantities, by electrolysis of hydrochloric acid and fused salt (see Figure 1.7).

In 1990, a total phase-out of the Hg-cathode process for chlor-alkali production by the year 2010 was recommended by the Parties to the OSPAR Convention, the Convention for the protection of the marine environment of the north-east Atlantic of the North European region (PARCOM Decision 90/3 of 14 June 1990). However, in 2002, chlor-alkali facilities under the responsibility of OSPAR (most of them belonging to the European Union), still held more than a half of production with Hg-cathode-based industries.

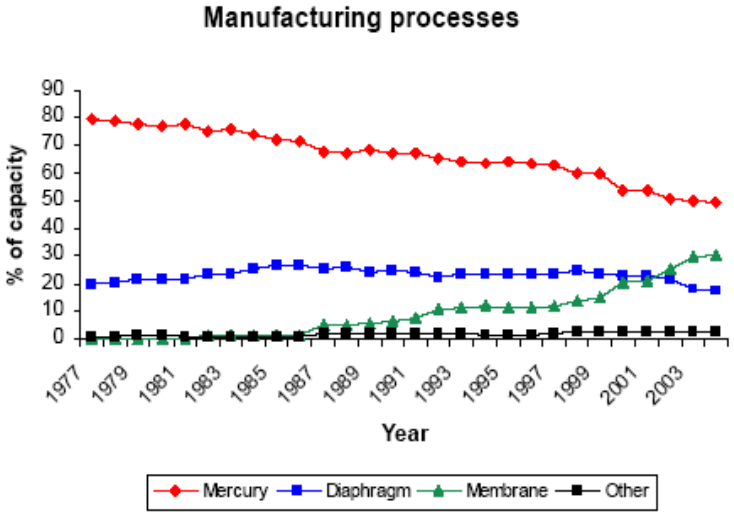

Figure 1.7 Use of manufacturing processes (as %) to produce chlorine and sodium hydroxide in Europe during the last decades (after Euro Chlor, 2005[42]).

The disposal of mercury after closure of Hg-cathode industries needs to be further assessed. Hence, the effect that re-marketing of available mercury from decommissioned chlor-alkali facilities would have on the global mercury market, has been widely discussed among OSPAR countries. According to the European Commission (in 2002), "the decommissioned mercury is not automatically governed by the Community waste legislation or by the requirements of the Basel Convention". This means that each member state of the EU will determine whether or not this mercury is a "waste". In this sense, Euro Chlor as a representative of the European chlor-alkali industry, has signed a contractual agreement with Minas de Almadén (Ciudad Real, Spain), which provides the permission to Minas de Almadén to buy the surplus mercury from the West-European chlor-alkali plants and reintroduce it into the market. This agreement substitutes the mercury that Almadén would otherwise have mined. Other countries, such as Sweden, have decided that the growing stockpile of metallic Hg and Hg-bearing wastes would be permanently stored in a deep rock repository, for instance, an abandoned mine with suitable geological and hydrological characteristics[7,27].

[42] Euro Chlor, *The European chlor-alkali industry. Steps towards sustainable development*, Progress Report, August 2005, [on-line], <http://www.eurochlor.org/>, [24 May 2006]

1.4.2 Dental amalgam alloys[43,44]

Dental amalgam is one of the oldest materials employed in oral health care, known since more than 150 years. About 200 million amalgams are inserted each year in the United States and Europe, with an estimated amount of mercury used of about 100 tons. In this sense, dental amalgam is a highly successful material from a clinical point of view, whilst being very cost effective. However, an increasing concern arises about the biocompatibility of this amalgam, and alternatives such as esthetical restorative materials are importantly growing.

1.4.2.1 Composition and morphology[43]

The chemical composition of the dental amalgam consists of a mixture of liquid mercury (40%-50 % w/w) with solid particles of an alloy of Ag/Sn/Cu. In some cases, small amounts of Zn, Pd, In or Se are also used. This combination of solid metals is known as the amalgam alloy. Such alloys are broadly classified as low-copper (< 5%) and high-copper alloys (13-30% Cu), as well as, as zinc-bearing (> 0.01%) or non-zinc-bearing (< 0.01%) alloys. Particles can be irregularly shaped, microspheres of various sizes or a combination of both. At the same time, alloys may contain all the spherical particles of the same composition (unicompositional) or a mixture of irregular and spherical particles with different or same composition (admixed). The approximate composition of commercial amalgam alloys, along with the shape of the particles, is shown in Table 1.2.

It is estimated that more than 90% of the dental amalgams placed during the last years are high-copper alloys, being the admixed shape the most common type. Nevertheless, an increasing interest has focussed in admixed amalgams containing 10-15 % indium. This addition decreased the amount of Hg needed and the Hg vapour released during and after setting, due to the formation of indium oxides at the surface of the amalgam. Moreover, the In addition increases the wetting properties of the material.

[43] Craig, R.G.; Powers, J.M. *Restorative dental materials*, Eleventh edition. Elsevier Health Sciences, St. Louis, 2002, pp. 288-327

[44] DAMS (Dental Amalgam Mercury Syndrome) Inc. *Mercury Free and Healthy. The Dental Amalgam Issue*, August 2005, [on-line], <http://www.amalgam.org/>, [26 May 2006]

Table 1.2 Approximate compositions and particle shape of low- and high- copper amalgam alloys. (after Craig and Powers, 2002[43]).

		Element (wt %)						
		approx. 50%	Amalgam alloy (approx. 50%)					
Alloy	**Particle shape**	**Hg**	**Ag**	**Sn**	**Cu**	**Zn**	**In**	**Pd**
Low copper	Irregular or spherical		63-70	26-28	2-5	0-2	0	0
High copper								
Admixed regular	Irregular		40-70	26-30	2-30	0-2	0	0
	Spherical		40-65	0-30	20-40	0-1	0	0-1
Admixed unicomposition	Irregular		52-53	17-18	29-30	0	0	0.3
	Spherical		52-53	17-18	29-30	0	0	0.3
Unicompositional	Spherical		40-60	22-30	13-30	0	0-5	0-1

1.4.2.2 Amalgamation processes. Properties of amalgam[43]

The two main components employed in the amalgamation process are liquid Hg and Ag_3Sn particles (with presence of Cu). During the preparation of these particles, the metal ingredients of the amalgam alloy are heated and protected from oxidation until melted and then poured into a mold to form an ingot. The ingot is cooled down slowly, leading to the formation of a main phase of Ag_3Sn and some minor phases of Cu_3Sn, Cu_6Sn_5 and Ag_4Sn. Thereafter, the ingot is heated up to 400 ºC to produce a more homogenous distribution of Ag_3Sn, which is then reduced to filings by being cut on a lathe and ball-milled. The particle size is defined in a last step, where the resulting particles are sieved and ball-milled again to form the proper particle size. The final shape is achieved within the last process, where all the elements are melted together under high pressure of an inert gas.

Before teeth-filling, the amalgam alloy is intimately mixed with liquid mercury, in a process called *trituration*. During this process, Hg diffuses into the Ag_3Sn phase (in excess) of the alloy particles and begins to react with the silver and tin portions of the particles forming various compounds, predominantly Ag_2Hg_3 and $Sn_{7-8}Hg$. The exact proportion of each phase depends on the initial composition of the alloy. The formed phases are not pure but contain some copper and occasionally small amounts of zinc. Additionally, Ag_2Hg_3 dissolves small amounts of tin and Cu_6Sn_5, and, similarly, Cu_6Sn_5 may dissolve some of the major phases. The freshly prepared amalgam shows certain plasticity that permits its packing and condensation into the tooth cavity. After condensing, the dental amalgam is carved to generate the required anatomical features.

Dental amalgam restorations are reasonably easy to insert, keep an anatomical form, have reasonably adequate resistance to fracture, prevent marginal leakage after a period of time in the mouth, can be used in stress bearing areas and show a relatively long service life. Metals such as Pd, Au and In (in small amounts) and copper (in larger proportions) are added to improve the corrosion resistance and certain mechanical properties of the finished amalgam mass. Moreover, small amounts of zinc in high-copper dental amalgams improve clinical performance, presumably by reducing brittleness.

One of the main (esthetical) disadvantages is the silvery colour of the amalgam, which does not match tooth aesthetics. Additionally, mercury amalgams are somewhat brittle, may experience corrosion and galvanic degradation, show a degree of marginal breakdown and do not help to retain on weakened tooth structure. Finally, there should be highlighted the increasing social awareness and regulatory concern regarding dental amalgams.

1.4.2.3 Mercury and biocompatibility issues

The safety of dental amalgams has been reviewed worldwide over the past fifteen years. In 1994, an international conference of health officials concluded that there was no scientific evidence about the health hazard posed by dental amalgams, despite the acknowledged existence of some rare cases of allergy. The World Health Organization (WHO) in its Consensus Statement on Dental Amalgam, the U.S. Public Health Service, the European Commission, the National Board of Health and welfare in Sweden, the New Zealand Ministry of Health, Health Canada and the province of Quebec reached a similar conclusion some years after[45].

Although this general agreement, several countries have restricted the use of dental amalgams or have recommended limitations in their use. For instance, the government of Canada recommended in 1996 the avoidance of mercury amalgam use in children and pregnant women. In 1997, a major manufacturer of dental amalgam, *Dentsply*, contraindicated the use of amalgams for children and pregnant women, as well as for those with mercury hypersensitivities, or with kidney problems[44]. The 1999 report on mercury by the *Agency for Toxic Substances & Disease Registry* stated that mercury passes through the placenta into the developing child's brain.

[45] U.S. Food and Drug Administration, *Consumer Update: Dental Amalgams*, December 2002, [on-line], <http://www.fda.gov/cdrh/consumer/amalgams.html>, [29 May 2006]

Mercury vapour is released in minor quantities during all steps involving amalgam preparation, including mixing, setting, polishing and removal. The human daily intake of mercury per amalgam has been estimated to be in the order of 10 micrograms (see Table 1.3), being the main source of human exposure to elemental mercury[46]. This mercury can be either accumulated in the body or excreted via urine and faeces into the wastewater systems. In the body, inhaled Hg^0 is oxidized by catalase to Hg^{2+}, which reacts with tissue functional groups and may cause neurotoxic and nephrotoxic effects. Nevertheless, Hg^{2+} does not readily pass cellular membranes, given its ionic character. On the other hand, Hg^0 do cross the placental and blood-brain barriers[47]. Clarkson and co-workers[46] observed that mercury concentration in urine was 2.54 $\mu g\ l^{-1}$ 4 days after placing amalgams, returning to zero after 7 days. When removing the amalgam, urine levels reach a maximum value of 4 $\mu g\ l^{-1}$ and return to zero after a week. Likewise, higher values of mercury vapour were recorded on removal on an amalgam than on insertion. According to the WHO, neurological changes are not detected until urine mercury levels exceed 500 $\mu g\ l^{-1}$, nearly 170 times the peak levels found after the insertion of an amalgam[43].

Aside from several studies reporting mercury accumulation, no other local or systematic effects of mercury present in dental amalgams have been demonstrated[48]. For the sake of dental concerns, this point must be highlighted given the acknowledged neurotoxic effect of mercury (see section 1.6), as well as the questions raising from its possible influence on kidney malfunctions, Alzheimer's disease and host of neurological disorders.

1.4.2.4 Environmental effect of mercury dental amalgams

Mercury dental amalgams represent an important source of environmental pollution. Cremation or burial of human bodies, release to the wastewater system and dental office disposals represent one of the most important diffuse sources of mercury contamination. Several dental offices do not handle mercury as a special waste and dispose it into municipal wastewater systems. Municipal treatment plants separate wastewater into water and sludge, although mercury is neither separated nor reprocessed during this process. Furthermore, mercury concentration in air at the dentistry offices must be considered and appropriately

[46] Clarkson, T.W.; Friberg, L.; Hursh, J.B.; Nylander, M. *Biological monitoring of toxic metals,* in: *The prediction of intake of mercury vapour from amalgams*, Plenum Press, New York, London, 1988, pp. 247-264

[47] Vater, M.; Akesson, A.; Lind, B.; Björs, U.; Schütz, A.; Berglund, M. Environmental Research Section A, **2000**, *84*, 186-194

[48] Bellinger, D.C.; Trachtenberg, F.; Barregard, L.; Tavares, M.; Cernichiari, E.; Daniel, D.; McKinlay, S. Journal of the American Medical Association, **2006**, *295*, 1775-1783

assessed. With a proper ventilation system, mercury levels return to background levels 10 or 20 minutes after the placement of the amalgam[43,44].

1.5 SOURCES AND CYCLE OF MERCURY

Mercury cycle in the environment is affected both by natural processes and anthropogenic activities. There exist four main types of emission sources:

- Natural Hg emissions, related to the mobilization or release of geologically bound Hg by natural processes, such as volcanic eruptions, weathering of rocks, emissions from the ocean, and degradation of minerals and forest fires
- Anthropogenic Hg emissions, corresponding to the mobilization or release of geologically bound Hg by human activities, such as fossil fuels, and treatment and recycling of minerals
- Anthropogenic Hg emissions, resulting from mercury used intentionally in products and processes, such as during manufacturing, leaks, or disposal or incineration of spent products
- Re-emission of Hg. Mass transfer by biological and geological processes of Hg already deposited on the earth's surface after initial mobilization (by either natural or anthropogenic activities)

The relative contribution of each source varies between countries and geographic areas, depending on a number of factors such as industrial activities (e.g. whether mining and metal extraction takes place in the country or not), environmental polices of the country, mineral resources of the area, volcanic activity of the region, etc.

Within its cycle, mercury undergoes a series of complex chemical and physical transformations. The flow of Hg from the atmosphere to land or water at a given place is affected by a series of contributions:

- natural global cycle
- global cycle perturbed by human activities
- regional sources
- local sources (such as chlor-alkali production, coal combustion and waste incineration facilities)

In this sense, the chemical and physical form of mercury affect the amount and mechanism by which mercury is transferred from pool to pool, influencing the direction and proportion of total depositional flows[7] (see Figure 1.8).

The comparison of contemporary and historical records indicates that the total global atmospheric Hg load has increased since the beginning of the industrialized period by a factor of 2 to 5 (Figure 1.8). Anthropogenic emissions (direct or re-emitted) have been estimated to contribute with about two-thirds of the worldwide mercury atmospheric emissions[4]. In this sense, the emissions from stationary combustion of fossil fuels (especially coal) and incineration of waste materials account for approximately 70 percent of the total atmospheric emissions[7].

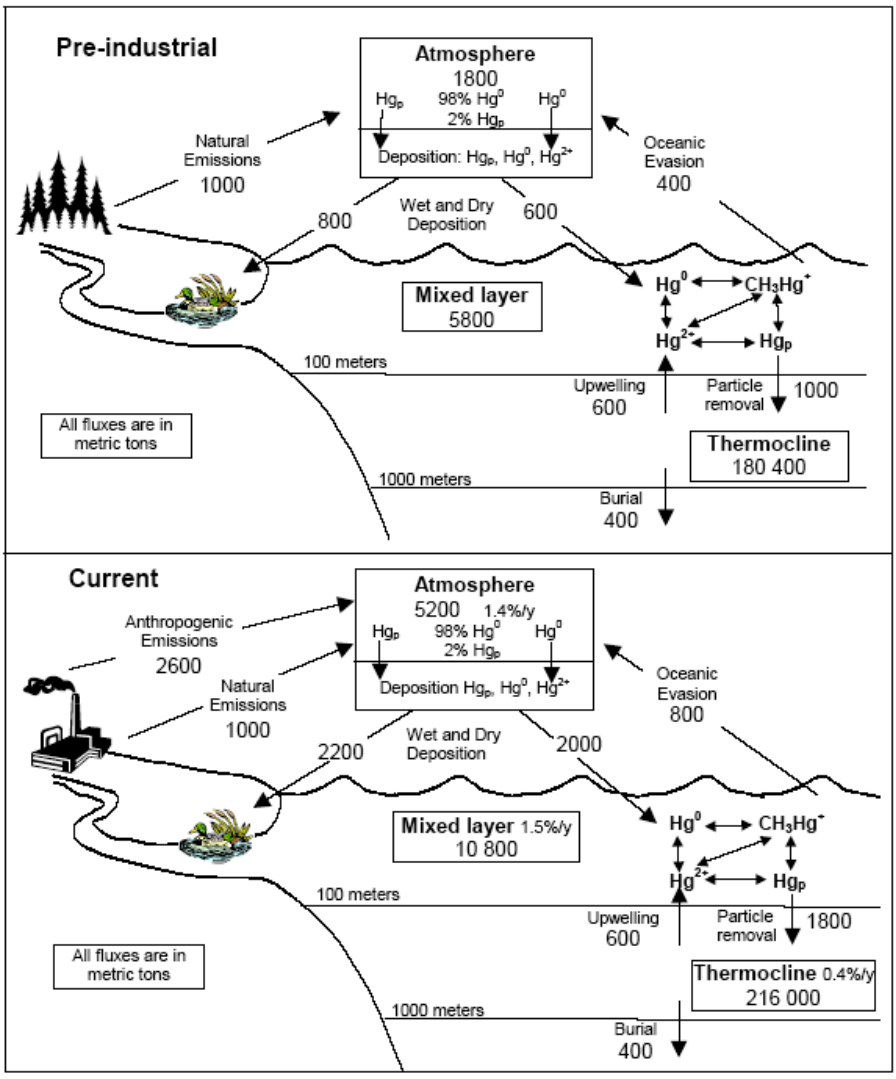

Figure 1.8 Comparison of estimated pre-industrial and current mercury fluxes (arrows) and pools (in frames) in metric tons (after UNEP, 2002[7]).

Recent estimates of total mercury emissions refer to about 4400 to 7500 metric tons emitted per year[49]. Even a gradual reduction of Hg anthropogenic release would only be noticeable after several decades. Nevertheless, faster local improvements may occur in specific locations heavily impacted by local or regional sources[7]. Hence, many industrialised countries have already defined stronger legal frames aiming at controlling the actual mercury impact. The following list reviews some of the measures already implemented[7]:

- Environment quality standards. The European Community Council Directive 98/83/EEC of 3 November 1998 on the quality of water intended for human consumption set a maximum concentration of 1µg l^{-1} of mercury in drinking water. Likewise, in the Commission Decision 93/351/EEC a maximum concentration of 0.5 mg kg^{-1} (wet weight) was set for mercury in fishery products, except for the following species for which a concentration of 1 mg kg^{-1} applies: anglerfish, atlantic catfish, bass, blue ling, tuna, eel, halibut, little tuna, marlin, pike, plain bonito, portuguese dogfish, rays, redfish, sail fish, scabbard fish, shark (all species), snake mackerel, sturgeon and swordfish.
- Environment source actions and regulations that control mercury releases into the environment, including emission limit on air and water point sources (e.g. Council Directive 96/61/EC, 24 September 1996) and promoting the use of best available technologies and waste treatment capabilities (Directive 2000/76/EC of the European Parliament and of the Council of 4 December 2000 on the incineration of waste) as well as disposal restrictions. In this sense, the article 16 of Directive 2000/60/EC phased-out the control of mercury release in the aquatic environment 20 years, with a final implementation foreseen for 22 December 2015.
- Product control actions and regulations for mercury-containing products, such as batteries, cosmetics, dental amalgams, pesticides, thermometers, etc.
- Other standards, actions and programmes, such as regulations on exposure to mercury in the working-place, requirements for information and reporting on use and release of mercury in industry, fish consumption advisories and consumer safety measures.

[49] United Nations Environment Programme Global Mercury Assessment, 2002, [on-line], <http://www.epa.gov/mercury/control_emissions/global.htm>, [30 May 2006]

1.5.1 Mercury in the atmosphere

Historically, mercury emitted to the atmosphere exceeds 10000 t[27]. The main sources of anthropogenic mercury emissions to the atmosphere are reviewed in the following list[7]:

- emissions from major point sources and diffuse sources such as housing (fossil fuel combustion)
- emissions from cremation, primarily due to dental fillings containing mercury
- diffuse release from uncollected waste products (fluorescent lamps, batteries, thermometers, etc.)
- evaporation of previous discharges to soil and water
- evaporation of mercury disposed of on landfills
- re-emission of mercury deposited from atmosphere

Mercury emitted to the atmosphere by anthropogenic means is mainly released as gaseous elemental mercury, whereas a smaller proportion is released as gaseous divalent compounds (such as $HgCl_2$) or bound to particles present in the emission gas[7]. Once in the atmosphere, Hg may be widely dispersed and transported far away from the source point. Several studies indicate that the residence time of Hg(0) in the atmosphere is ~ one year, therefore allowing its transport over long distances before being deposited back to earth surface[4].

During atmospheric transport, significant conversion reactions between mercury species may occur. These mechanisms play a very important role in the long-range transport of mercury, as well as in the deposition fate. Hence, the oxidized form of mercury, Hg(II) shows a residence time varying from a few hours to several months, as it can be easily deposited through dry (absorption of gaseous and particle-bound Hg) or wet (absorption of Hg over water surfaces) mechanism[50]. The relationship between mercury atmospheric processes and chemistry are summarised in Figure 1.9.

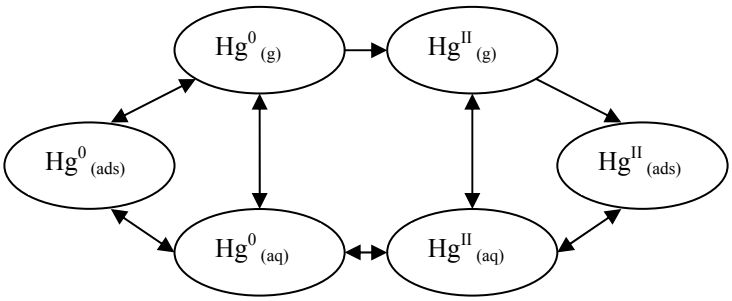

Figure 1.9 Interactions between mercury species in the atmosphere (after UNEP, 2002[7]).

[50] Lodenius, M. The Science of the Total Environment, **1998**, *213*, 53-56

1.5.2 Mercury in aquatic ecosystems

Rytuba[28] has reported that most river and lake waters worldwide show Hg concentrations in the range of <0.1 to 6 ppb. According to the WHO[51], the upper guideline limit of total mercury content in water for human consumption is 1 ppb.

The main source of mercury found in water corresponds to the direct discharge of mercury-containing wastewater (e.g. from chlor-alkali industries). Nowadays, such discharges take normally place in developing countries, where less strict legislations are given. Outlets from municipal sewage treatment plants do also face the problematic of mercury, as municipal wastewater may contain significant mercury concentrations originating from a number of sources: dentist's surgery, miscellaneous measurements and monitoring equipment, laboratories, among others. In some environments, anthropogenic actuations including farmlands, recent clear-cuttings and water reservoirs (hydroelectric, aquaculture, irrigation) may considerably enhance the release of mercury to aquatic systems and promote the bio-accumulation of mercury in organisms[7].

Levels of mercury in oceans lie around <0.01-0.03 ppm. In polluted areas, such as the Mediterranean Sea or the New York's harbour, levels can rise >1ppm. Significantly high mercury concentrations have been also found in the deep ocean. This fact is probably related to under-water volcanism phenomena, as mercury deposits are clustered around areas of hydrothermal activity[6]. Due to their high sorption capacity, sediments are also considered as an important mercury reservoir, from where mercury may recycle back into the aquatic ecosystem after several decades of inactivity[7].

Once in the aquatic ecosystems, mercury can be found either dissolved or in particulate forms, whilst potentially undergoing chemical/microbial transformation to methylmercury (see Figure 1.10). In this sense, almost all mercury bioaccumulating* in fish tissues corresponds to methylated mercury[52,53]. Some studies have observed a relationship between the methylmercury content in fish and the water pH of related lakes, with higher methyl Hg content in fish tissue typically found in more acidic lakes. Other factors influencing the bioaccumulation of Hg in aquatic biota are the length of the aquatic food chain, temperature,

[51] WHO, Guidelines for Drinking-Water Quality, Vol. 1: Recommendations, Geneva, 1984, pp. 55-56

[52] Bloom, N. Canadian Journal of Fisheries and Aquatic Sciences, **1992**, *49*, 1010-1017

[53] U.S.EPA, *Mercury: Study Report to Congreso,* Vol. 1: *Executive Summary*, The National Technical Information Service (NTIS), Springfield, 1996

DOC (dissolved organic carbon), among others. Elimination of methyl mercury takes place very slowly, resulting in tissue half-lives ranging from a few months to several years.

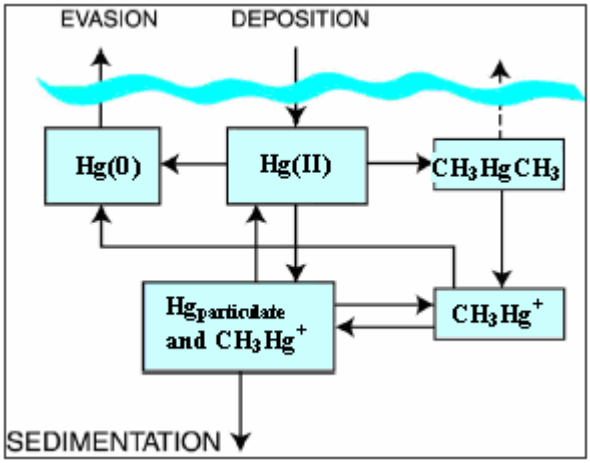

Figure 1.10 Interactions between mercury species in ocean waters (after Mason and Fitzgerald, 1996[54]).

*The term bioaccumulation refers to the net accumulation over time of metals within an organism from both biotic (other organisms) and abiotic (soil, air and water) sources[7].

1.5.3 Mercury in soils

Mercury naturally occurs in soils at concentrations ranging from a few ppb to a few hundred ppb. In this sense, concentrations falling within the <100 ppb level[4] are considered as normal in mercury non-impacted areas.

The main anthropogenic sources for mercury presence in soils are[7]:

- waste disposal on landfills
- diffuse release from uncollected waste products
- local releases from industry
- spreading of sewage sludge with trace contaminants on agricultural land (used as fertiliser)
- use of solid residues from waste incineration and coal combustion for construction purposes
- cementeries. Dental amalgam fillings from buried persons
- deposition of mercury previously emitted to the atmosphere

[54] Mason, R.P.; Fitzgerald, W.F. *Sources, sinks and biochemical cycling of mercury in the ocean*, Baeyens, W.; Ebinghaus, R.; Valiliev, O. (eds.), *Global and regional mercury cycles: Sources, fluxes and mass balances*, NATO ASI Series, Vol. 21, Kluwer Academic Publishers, Dordrecht (The Netherlands), 1996

The residence time of mercury in soils is very high, and therefore mercury-impacted soils may be considered as an important reservoir for the continuous release of mercury to ground and surface waters.

When mercury enters the soil bulk, the adsorption process is initially dominant in determining the fate of this element, although other phenomena such as volatilization, precipitation, leaching or uptake by organisms may also take place[4].

The Hg content and distribution of a soil horizon has been shown to be related to organic matter (OM), clay content as well as the presence of Fe and Mn oxi-hydroxides[4]. In acidic soils, the role of OM may predominate, whereas clay mineralogy and oxides of Fe may control the chemistry of mercury in alkaline and calcareous soils[55]. The presence of some inorganic ligands does also affect sorption processes and mercury mobility in soil phases. Hence, the presence of Cl^- reduces the adsorption of Hg(II) by clays, specially at low pH[56]. Similarly, the presence of SO_4^{2-} was observed to decrease Hg(II) retention by gibbsite [$Al(OH)_3$]. This fact was attributed to the formation of the $Hg(OH)_2SO_4^{2-}$ ion. However, the presence of PO_4^{2-} increased retention by gibbsite due to the formation of a phosphate bridge [$\equiv AlOPO_3Hg(OH)_2^{2-}$][57].

Adsorption of Hg by soils depends not only on soil properties but also on the chemical form of Hg (see section 1.7.3). In general terms, mercury is relatively unstable as it may be subject to chemical, biological, and photochemical reactions[2]. Many mercurial compounds decompose to yield elemental Hg, which may volatilize or be converted to HgS or complex with inorganic or organic ligands. As the transport of Hg within the plant is very limited, Hg tends to accumulate in roots[4].

1.6 TOXICITY OF MERCURY

Toxicity of mercury is known since the Antiques. To give an example, Romans were already aware of the toxic effects of mercury, and therefore used slaves and convicts for the mining of cinnabar[3]. The life expectancy of miners was lower than 6 months[2]. Nevertheless, one of the most popular representatives of mercury toxicity was the mad hat of the history of Lewis Carrol, “Alice in Wonderland”. Mercury (as mercury nitrate) was used in the felting of hats, being this use the origin of the term ‘mad as a hatter’. During the industrial and technological

[55] Andersson, A. *The Biogeochemistry of Mercury in the Environment*, Nriagu, J.O. (ed.), Elsevier, Amsterdam, 1979

[56] Newton, D.W.; Ellis Jr., R. ; Paulsen, G.M. Journal of Environmental Quality, **1976**, *5*, 251-254

[57] Sarkar, D.; Essington, M.E.; Misra, K.C. Soil Science Society of America Journal, **1999**, *63*, 1626-1636

revolution of the 19th and 20th centuries, a number of new applications where found to several mercury compounds. This had a strong effect both to the environmental and occupational exposure to mercury contamination.

One of the worst disasters related to mercury toxicity occurred in the Minamata bay (Japan) in the mid-fifties. During several years (1953-1960), an acetaldehyde plant released huge amounts of mercury to the wastewater stream. The result was a health disaster due to the consumption of poisoned fish (with methylmercury), with hundreds of people irreversibly affected and several dead[39]. A similar episode occurred in Niigata (Japan) in the mid 1960s[58]. Some years later, the Iraq episode in 1971-72 was the biggest single event where close to 6350 people were hospitalized, of whom 459 died. The source of mercury was a shipment of wheat and barley seed treated with methylmercury. These products were meant for sowing, although they were finally used for the preparation of flour[59].

All this poisoning incidents invoked the sensitivity of the international community, and the World Health Organization published in 1977 the first book of the *Environmental Health Criteria* series, exclusively dedicated to mercury[60]. Three more volumes followed to the first one, devoted to mercury in the environment[61], to methylmercury[59] and to the inorganic mercury[5].

All reported investigations agree that the risk associated to mercury is determined by the likelihood of exposure, as well as the chemical form in which mercury is found and the geochemical and ecological factors that influence how mercury moves and changes form in the environment[29]. In general, the order of decreasing toxicity is: alkyl Hg (e.g. CH_3Hg^+)>Hg metal vapour> Hg^{2+} salts[2]. Mercury has well characterized toxic effects on both the physiological and the neurological systems of the body, but the effects of methylmercury on the central nervous system are the most destructive.

1.6.1 Effects of mercury in aquatic ecosystems

Aquatic ecosystems are vulnerable ecosystems for the biotransformation of inorganic Hg species to methylated organic species, which are responsible for the main effect of mercury in

[58] Inskip, M.J.; Piotrowski, J.K. Journal of Applied Toxicology, **1985**, *5*, 113-133

[59] WHO, *Environmental Health Criteria 101: Methylmercury*, International Programme on Chemical Safety Geneva, 1990

[60] WHO, Critères d'hygiène de l'environnement 1: Mercure, Geneva, 1977

[61] WHO, *Environmental Health Criteria 86: Mercury-Environment Aspects*, International Programme on Chemical Safety, Geneva, 1989

aquatic ecosystems. This fact is due to the lipophilic nature of methylmercury, which enhances its ability to bioaccumulate. Additionally, methylmercury is taken up 10 to 100 times more rapidly than inorganic Hg and can be directly absorbed through the fish gills[62]. As a result, methylmercury is mainly absorbed from food compared to inorganic mercury: 70 to 90% and 5 to 15%, respectively. As accumulation of methylmercury is faster than its elimination, a biomagnification of methylmercury occurs through the food chain (*progressive build up of Hg by successive trophic levels*)[53]. In this sense, mercury in fish-eating animals and those that prey on other fish-eaters accumulates more efficiently than the mercury consumed in the terrestrial food chain. Exposure of this biota to Hg is enhanced in reservoirs and in low-alkalinity, low-pH ecosystems, and smaller organisms show a higher susceptibility to Hg poisoning than larger ones, due to a higher daily intake per unit of body weight[4].

The methylmercury toxicity in mammals that consume contaminated seafood is primarily manifested as central nervous system impairment, including sensory and motor deficits and behavioural disorders[63]. Animals initially become anorexic and lethargic. Muscle ataxia, motor control deficits, and visual impairment develop as toxicity progresses, with convulsions preceding death. In birds, symptoms of acute methyl Hg poisoning include reduced food intake leading to weight loss; progressive weakness in legs and wings; and an inability to coordinate muscle movements[4].

1.6.2 Effects of mercury in terrestrial ecosystems

As mentioned above, bioaccumulation of Hg in terrestrial organisms is relatively low compared to aquatic ones. Nevertheless, the release of mercury to the environment from different sources can impact human and biota through direct and indirect pathways. Direct pathways include, for instance, ingestion of soil contaminated with mercury and respiration of mercury vapour and enriched particles. Indirect pathways are more important but rare, and include consumption of fish and edible plants that have been contaminated with methylmercury[30], among others.

In general, the transfer of Hg from soil to roots is very low (transfer coefficients from 0.01 to 1 w/w[64]), and therefore does not constitute an important exposure pathway to animals. In this

[62] Glass, G.E.; Sorensen, J.A.; Schmidt, K.W.; Rapp, G.R. Environmental, Science and Technology, **1990**, *24* 1059-1069

[63] Wolfe, M.F.; Schwarzbach, S.; Sulaiman, R.A. Environmental Toxicology and Chemistry, **1998**, *17*, 146-160

[64] Wren, C.D.; Harris, S.; Harttrup, N. *Ecotoxicology of mercury and cadmium,* in: *Handbook of ecotoxicology*, Hoffman, D.J.; Rattner, B.A.; Burton, G.A.; Cairns, J. (eds.), Lewis Publishers, Boca Raton, Florida, USA, 1995, pp. 392-423

sense, vegetation collected in the vicinity of the Almadén mine shows only one- to three-fold Hg levels in their foliage, in spite of >100 times the threshold limit reached in the corresponding soil[65]. This pahtway pose little threat to the well-being of herbivorous.

Exposure to Hg can cause adverse effects in plants, birds, and mammals. Reproductive effects are the primarily concern for avian Hg poisoning and can occur at low Hg dietary concentrations. Sublethal effects of Hg on birds include liver and kidney damage, and neurobehavioral effects. Effects of Hg on plants include death and sublethal effects: decreased growth, leaf injury, root damage, and inhibited root growth and function[53].

1.6.3 Exposure and effects of mercury in humans

Exposure to inorganic mercury takes mainly place through inhalation, as well as through consumption of contaminated water and food. On the other hand, the most dangerous mercury compound concerning human health is methylmercury. Fish and aquatic wildlife being at the top of food chain are the most important exposure pathways for humans, with an international agreement concerning threshold limits between 0.30 and 1 mg kg^{-1} [66]. Some minor exposure pathways are related to consumption of contaminated water, food consumption other than fish as well as dermal uptake through soil and water.

Most highly exposed populations are those fish-eaters that live in polluted areas with high concentrations of methylmercury in freshwater. Among those, pregnant women, women of childbearing age and children, are especially sensitive to methylmercury toxicity[4]. In this sense, several publications have demonstrated the particular damaging capacity of methylmercury to developing embryos, which are five to ten times more sensitive to this species than adults[29].

A summary of the human exposure to the three major forms of mercury present in the environment is shown in Table 1.3.

[65] Lindberg, S.E.; Jackson, D.R.; Huckabee, J.W.; Janzen, S.A.; Levin, M.J.; Lund, J.R. Journal of Environmental Quality, **1979**, *8*, 572-578

[66] The Commission of the European Communities (CEC), 93/351/EEC: Commission Decision of 19 May 1993 determining analysis methods, sampling plans and maximum limits for mercury in fishery products, Official Journal L 144 , 1993, p. 0023 - 0024

Table 1.3 Estimate average daily intake and retention in the body of an adult (retention given in brackets) of different mercury forms in a scenario relevant for the general population not occupationally exposed to mercury; values in μg day^{-1} (after WHO/IPCS, 1991[5]).

Exposure	Elemental Hg vapour	Inorganic Hg compounds	Methylmercury
Air	0.03 (0.024)*	0.002 (0.001)	0.008 (0.0069)
Dental amalgams	3.8-21 (3-17)	0	0
Food			
- fish	0	0.60 (0.042)	2.4 (2.3)**
-non-fish	0	3.6 (0.25)	0
Drinking water	0	0.050 (0.0035)	0
Total	3.9-21 (3.1-17)	4.3 (0.3)	2.41 (2.31)

* If the concentration is assumed to be 15 ng m^{-3} in an urban area, it would be 0.3 (0.24) μg day^{-1}

** Assumes 100 g of fish per week with the mercury concentration of 0.2 mg kg^{-1}

The toxicokinetics (i.e., absorption, distribution, metabolism, and excretion) of Hg is highly dependent on the form of Hg to which a receptor has been exposed[53]. Elemental mercury is absorbed rapidly through the lungs, and is readily distributed throughout the body; it crosses both placental and blood-brain barriers. Distribution of elemental mercury is primarily limited by its oxidation to mercuric ion, which shows a much limited mobility. Moreover, elemental mercury can be eliminated via urine, faeces, exhaled air, sweat, and saliva.

The quantitative absorption of inorganic mercury strongly depends on the solubility of the mercury compound involved[53]; absorption of inorganic compounds can reach values as high as 20% of the total inorganic Hg intake. At the same time, mercuric compounds can be reduced to elemental mercury and excreted via exhaled air. Due to the relatively poor absorption of orally administered inorganic Hg, the main part of the ingested dose is excreted through the faeces[4].

On the other hand, methylmercury is rapidly and efficiently absorbed by humans through the gastrointestinal tract (90 to 95%). In blood, methylmercury distribution between red cells and plasma is 90 and 10%, respectively, whilst readily crossing the blood-brain and placental barriers. The transport of methyl Hg into the brain is mediated by its affinity for the anionic form of sulfhydryl groups. Methylmercury in the body is considered to be relatively stable, with a biological half-life between 44 and 80 days. Excretion occurs via the faeces, breast milk, and urine[4].

The chronic (long-term) exposure level for elemental and methylmercury affects the central nervous system. Effects such as paresthesia (a sensation of pricking on the skin), blurred vision, malaise, speech difficulties, and constriction of the visual field are associated from methylmercury exposure, whilst symptoms such as erythrism (increased excitability), irritability, excessive shyness, and tremor have been identified to elemental Hg exposure. The major effect from chronic exposure to inorganic Hg is kidney damage[4].

1.6.4 Treatment of mercury toxicity[6,7]

Two different approaches are usually used to deal with mercury intoxication:

- Formation of species which allows the metal to be excreted (e.g. a mercury complex) Two promising reagents are N-acetyl d,l-penicillamine CH_3-CO(NH)-CH($C(CH_3)_2$-SH)-CO_2H, and dimercaptosuccinic acid HO_2C-CH(SH)-CH(SH)-CO_2H. Other materials used for elimination include penicillamine, glutathione, and EDTA.
- Trapping and expulsion of the metal in the gastrointestinal tract. For instance, a thiol resin has been used for trapping the metal in the gut. In general terms, most of the reagents take advantage of the strong interaction between mercury and sulphur.

Selenium-rich diets show a protection effect against mercury toxicity. This fact is given by the release of methylmercury from sulphur, probably through the formation of CH_3Hg-Se species.

1.7 FACTORS AFFECTING MOBILITY AND BIOAVAILABILITY OF MERCURY

Mercury can be found in a number of chemical species and compounds, which show different physical and chemical properties. The knowledge of these species becomes of an utmost importance for the understanding of its chemical behaviour and biological availability[67]. In this sense, parameters influencing the mercury speciation in a given medium include the nature and concentration of the complexing agents, stability of the complexes formed, concentrations of competing cations, redox potential, temperature, pH, ionic strength, reaction kinetics, etc. The effect of both pH and redox potential on mercury mobility will be shortly described in section 1.7.1.

The most important mechanisms controlling mercury mobility in soils and sediments have been identified as sorption-desorption, precipitation-dissolution, acid-base, oxidation-reduction, and complexation reactions. As mentioned in previous sections, sorption and desorption processes play a very important role in the interaction of mercury with soil phases.

[67] Patterson, J.W.; Passino, R. *Metals Speciation. Separation and Recovery*, Proceedings of the International Symposium on Metals Speciation, Separation, and Recovery, Chicago, 1986, pp. 201-224

In this sense, the different soil materials (organic matter, clay minerals, etc.) show different trends concerning interaction with mercury species. Further details in this concern are given in section 1.7.2.

1.7.1 pH and redox potential

The pH has a significant influence on the speciation of mercury (see Figure 1.3). Hydrolysis of Hg^{2+}, formation of sulphide complexes, precipitation/dissolution of some mercury compounds, etc. show a strong dependence on the pH value of the media. Sorption of mercury onto different soil materials has been also shown to significantly depend on pH. Both surface charge characteristics of soil particles and metal speciation in solution are affected by pH. Figure 1.11 shows how organic matter is the main mercury adsorbent for a wide pH range (even under acidic conditions), whereas certain clay minerals may assume an increasing importance at pH values higher than 5.5.

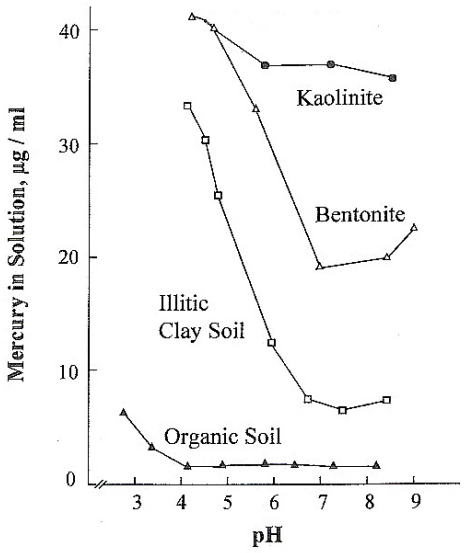

Figure 1.11 Retention of mercury by soils and soil components as influenced by pH (after Andersson, 1979[55]).

Likewise, the stability of Hg in soil is also influenced by pH. In some soil types, such as in limed loamy[68] or Montana[69] soils, an increase in volatile losses of Hg by reduction of Hg salts

[68] Frear, D.E.H.; Dills, L.E. Journal of economic entomology, **1967**, *60*, 970-974

[69] Landa, E.R. Journal of Environmental Quality, **1978**, 84-86

to Hg(0), was shown with increasing soil pH. On the contrary, in other soil types, such as humic acids, loss of Hg via reduction of mercuric ion decreased by increasing the pH[70].

The redox potential (E_h), together with the pH, is a very influential parameter. It defines the stability and distribution of Hg among its respective oxidation states[67]. In this sense, this parameter also determines the species susceptible of absorption and precipitation. The redox potential depends on several parameters, such as oxygen availability, presence of organic matter, biological activity, pH, etc. Thus, in anoxic soils, reducing and acidic conditions favour the solubility of metals adsorbed in oxidized compounds[71]. This is due to the lack of oxygen, which under anoxic condition is obtained through the attack of microorganisms to the present oxides, nitrates and sulphates. On the contrary, and under oxidant conditions, some compounds can dissolve, as is the case of pyrite at acidic pH.

1.7.2 Soil type and organic matter

Soil type and structure influences the stability of Hg in soils, since the different species of Hg depend on the soil environment. The soil reactions control the fate of Hg in soils, by affecting their degradation or decomposition, solubility, and precipitation by formation of complex compounds, and many others.

The physico-chemical properties of soils are attributed to soil constituents with highly reactive surfaces and large surface areas. In this sense, the main sorbing materials are both clays, Fe/Mn oxides and organic matter (see section 1.5.3), being the maximum Hg sorption when the clay, and/or the organic matter content of the soils is high[6]. Clay minerals represent the very fine (<0.002 mm) inorganic fraction (predominantly silicates and oxides) of soils, also named colloidal. This fraction has a high cation exchange capacity, since it carries negative charges and cations are attracted to maintain electroneutrality in soils. Moreover, its fine texture involves a diminution of the particle size and an increase of the reactive surfaces and the cation exchange capacity, due to the increase of the surface charge. Therefore, volatile losses of Hg can be expected to occur more in coarse-textured than in fine-textured soils.

Likewise, in a given soil profile, the total Hg and OM content are very highly correlated[72,73,74]. The humic and fulvic acids present in the OM have a big capacity to

[70] Alberts, J.J.; Schindler, J.E.; Miller, R.W.; Nutter Jr., D.E. Science, **1974**, *184*, 895-897

[71] Chuan, M.C.; Shu, G.Y.; Liu, J.C. Water, Air and Soil Pollution, **1996**, *90*, 543-556

[72] Lee, S.Z.; Chang, L.; Chen, C.M.; Tsai, Y.I.; Liu, M.C. Water Science and Technology, **2001**, *43(2)*, 187-196

[73] Skyllberg, U.; Xia, K.; Bloom, P.R.; Nater, E.A.; Bleam, W.F. Journal of Environmental Quality, **2000**, *29*, 855-865

complex Hg, mainly due to their tiol groups, and organo-complexes may occur in soluble and colloidal form that differs in mobility. For instance, humic substances containing S (e.g., in cysteine) are believed to keep Hg in soluble form[4]. Likewise, in aquatic systems, OM has a high affinity for methylmercury[75]. This interaction is of primary importance for the mobility, bioavailability, and toxicity of methylmercury in aquatic environments.

1.7.2.1 Clay minerals: kaolinite and montmorillonite[76]

Clays are of special importance in soil chemistry, since they show a surface chemistry significantly different from that of the larger mineral grains. Among clay compounds, kaolinite and montmorillonite are perhaps the most widely distributed in soils. Kaolinite minerals are hydrated aluminosilicates, with a general chemical composition Al_2O_3:SiO_2:H_2O=1:2:2, or $2SiO_2.Al_2O_3.2H_2O$ per unit cell. Structurally they are 1:1 type phyllosilicates (see figure 1.12). Due to the presence of exposed hydroxyl groups, kaolinite has pH-dependent negative charge. The cation exchange capacity of kaolinite is reatively small (in the range of 1-10 mEq/100 g) and varies with the pH. Moreover, its restricted surface area (7-30 m^2 g^{-1}) limits also the adsorption capacity for cations.

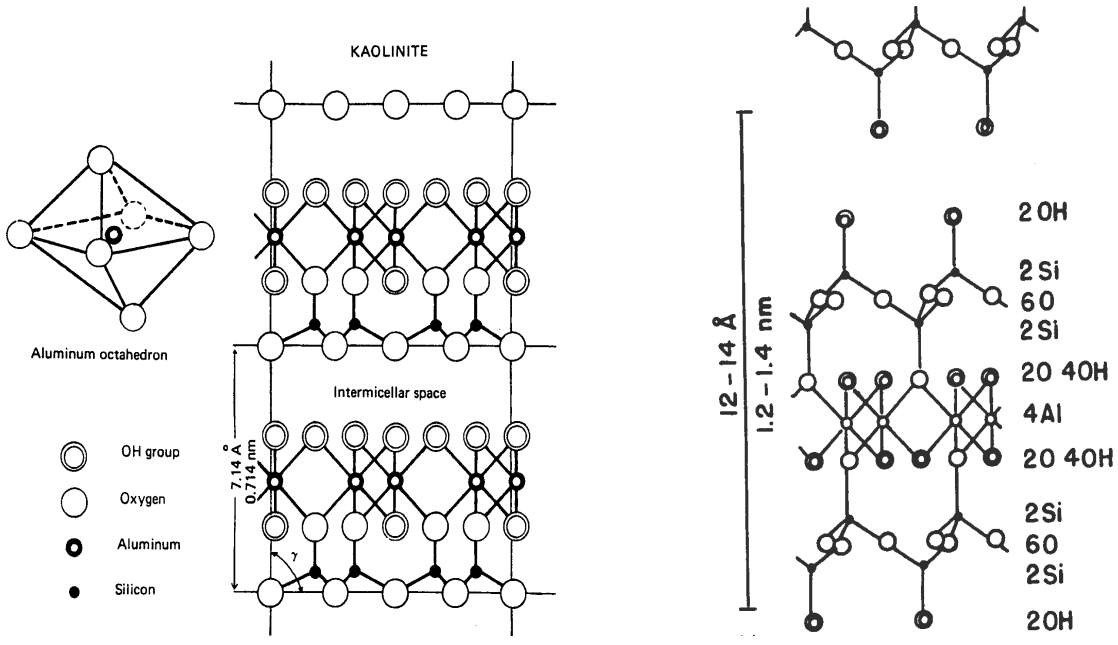

Figure 1.12 Structural model of kaolinite **(a)**, and montmorillonite **(b)** (after Kim H. Tan, 1998[76]).

[74] Yin, Y.; Allen, H.E.; Huang, C.P.; Sanders, P.F. Soil Sience, **1997**, *162(1)*, 35-45

[75] Choi, M.H.; Cech, J.H.; Laguras-Solar, M. Environmental Toxicology and Chemistry, **1998**, *17*, 695-701

[76] Tan, Kim H. *Principles of Soil Chemistry*, Third Edition, New York, 1998

Montmorillonite shows a variable composition, being its formula often expressed as $Al_2O_3 \cdot 4SiO_2 \cdot H_2O + xH_2O$, with Mg and ferric ions in octahedral positions. Differing from kaolinite, the unit structural cell of montmorillonite is considered symmetrical (see Figure 1.12), and its negative charge also arises mainly from its hydroxyl groups. The cation exchange capacity of a typical montmorillonite is ~ 70 mEq/100g, whilst the specific surface is approximately 700-800 $m^2 g^{-1}$.

1.7.2.2 Humic acid[76]

Like clays, humic substances are building constituents of soils. They are synthesized during the decomposition of plant and animal residues, either in presence or absence of microorganisms. Humic acids, which are the soil humic fraction soluble in bases, are defined as amorphous, colloidal polydispersed substances with variable colour. They have a significantly high molecular weight and show a hydrophilic and acidic character. Humic acids are usually rich in carbon (41-57%) and oxygen (33-46%), containing also minor amounts of nitrogen 2-5% (mainly NH_3 and N_2) and sulphur.

The total acidity or exchange capacity (5-6 mEq g^{-1}) of humic compounds is attributed to the presence of dissociable protons in aromatic and aliphatic carboxyl and phenolic hydroxyl groups, both showing pH dependence. The carboxyl groups starts to dissociate at pH 3. Below this pH, the charge is very small or even zero. Under alkaline conditions (pH > 9), the phenolic-OH groups start to dissociate and the molecule attains a high negative charge. Consequently, complex and chelation reactions between mercury and humic molecules have a significant importance in the soil chemistry.

1.7.3 Forms and chemical species of mercury

According to the International Union of Pure and Applied Chemistry (IUPAC), the term speciation is defined as "the distribution of an element amongst its defined chemical species in a system", considering the chemical species as "the specific form of an element defined as to isotopic composition, electronic or oxidation state, and/or complex or molecular structure"[77].

As stated in the preceding sections, the chemical speciation of mercury significantly determines mercury mobility, bioavailability and toxicity.

[77] IUPAC, Pure and Applied Chemistry, **2000**, *72*, 1453–1470

Speciation is strongly dependent on the type and concentrations of all potential coordinating ligands. Among those, hydroxyl, carbonate, phosphate and sulphide are the most important. Some of the principal mercury compounds in soils are $Hg(OH)_2$, at pH>7 $HgCO_3$, and mercury phosphate and sulphide species are predominant in reducing conditions, such as those found in flooded soils. Organomercury compounds (i.e. RHgOH) are likely to form in sediments, as well as some soluble hydroxyl and chloro-species depending on the pH and the chloride concentration[6].

The identification and determination of different species of a given element in an environmental sample use to present important difficulties. Such difficulties are given by the particularities of these samples:

- the concentration of heavy metals in the environment are generally low
- environmental matrices are normally very complex
- the possible similarities of the physical and chemical properties of two or more species of a given element.
- the stability of the species to be determined. Stability depends on the matrix and on physical parameters, such as temperature, humidity, organic matter, ultraviolet light, and so forth. The isolation and purification of the species, the study of the possible transformations through the procedure, and the study of their characteristics and interactions are also important[78].

A further description of some of the available speciation techniques and strategies are given in the following section.

1.7.3.1 Speciation methods

The majority of the methods developed so far for analytical speciation include spectroscopic, polarographic, chromatographic, and electrochemical methods[78]. A scheme of the available technologies used for metal ion speciation is shown in Figure 1.13. Among these techniques and regarding mercury speciation, chromatography are the most widely used once mercury species have been extracted from the soil/sediment matrix (e.g. through a selective liquid-liquid extraction[79]). Further information is given in section 1.7.3.1.1.

[78] Ali, I.; Aboul-Enein, H.Y. *Instrumental Methods in Metal Ion Speciation*, Chromatographic Science Series, Vol. 96, New York, 2006

[79] Rezende, M.C.R.; Campos, R.C.; Curtius, A.J. Journal of Analytical Atomic Spectrometry, **1993**, *8*, 247-251

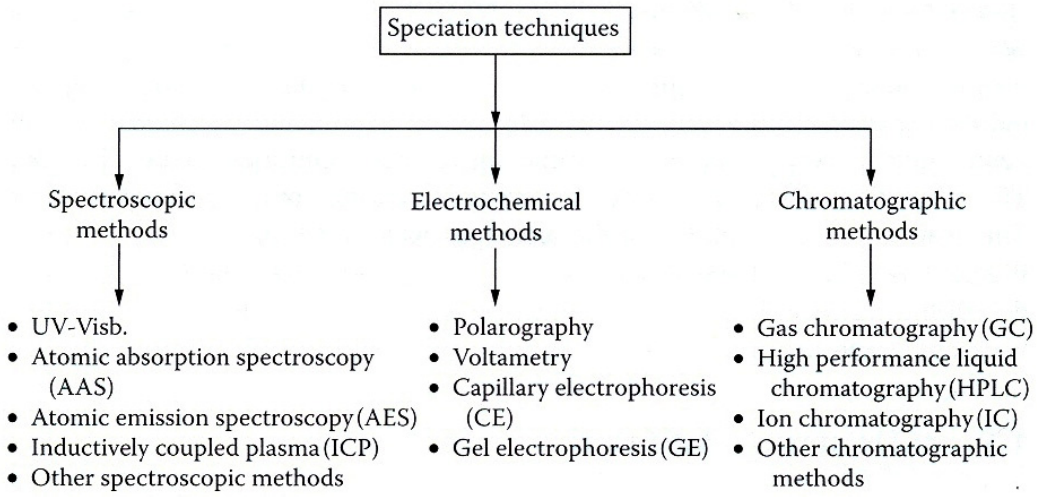

Figure 1.13 Different techniques for metal ion speciation (after Imran Ali and Hassan Y. Aboul-Enein, 2006[78]).

These speciation methods usually involve a number of steps, such as extraction, preconcentration, cleaning, derivatization, chromatographic separation and element specific detection. Nevertheless, other approaches are also used when dealing with Hg speciation in soils and sediments[80]:

- Computational approach. This is the more theoretical approach, which considers the use of thermodynamic constants to estimate the speciation of a given element under certain environmental conditions. Due to the associated uncertainties, this approach should be restricted to very well-known systems, where all parameters affecting metal speciation (pH, E_h, type and concentration of ligands, etc.) have been properly characterised.

- Direct speciation approach. This approach intends to determine 'in-situ' the species of a given element in the original matrix, without accounting for any pre-treatment step. Therefore, any disturbance of the species equilibrium is theoretically avoided. Nevertheless, only a few direct speciation techniques exist for solids samples where species are found in complexes matrices, as soils or sediments. Some physical methods have been applied relying on the interaction between the sample and an incident beam of either X-rays or electrons (see Table 1.4). However, these techniques show important drawbacks, as their high detection limits or the impossibility to

[80] Sanz-Medel, A. Spectrochimica Acta B, **1998**, *53*, 197-211

identify polymorphic forms (e.g. cinnabar and metacinnabar). Moreover, diffraction techniques need also to deal with species showing a crystalline structure.

Table 1.4 Direct techniques to soil speciation[33,81-84].

Radiation	Technique	Analysis objective
X-Radiation	**XRD**: X-Rays Diffraction	Identification of crystalline structures in the sample. Determination by comparison with reference compounds
	SEM-EDS: Scanning Electron Microscopy / Energy Dispersive Spectroscopy	Presence of elements capable of X-rays excitation in the sample superficies. Species identification by elemental associations
	SEM-WDS: Scanning Electron Microscopy / Wavelength-Dispersive Spectrometry	Presence of elements capable of X-rays excitation in the sample superficies. Species identification by elemental associations
e^- beam	**SEM**: Scanning Electron Microscopy	Observation of the crystal shape. Species identification by comparison with known crystals
	TEM-SAED: Transmission Electron Microscopy/ Selected Area Electron Diffraction	Identification of crystalline structures in the sample. Determination by comparison with reference compounds

In recent times, the use of synchrotron sources instead of the classical X-rays tubes has permitted a significant improvement of the direct speciation approach applied to environmental samples. These techniques take advantage of the highly brilliant X-rays radiation generated in a synchrotron facility, which allows the improvement of already existing techniques (fluorescence, diffraction, etc.), as well as the development of new techniques, such as XANES (X-ray Absorption Near Edge Structure) and EXAFS (Extended X-ray Fine Structure) (see section 1.8).

- Miscellaneous. This approach would include several techniques used for the mercury speciation and not included in previous approaches. Among these, thermal desorption is used to determine different mercury species according to their temperatures of decomposition[85]. Other techniques might include the determination of mercury

[81] Barnett, M.O.; Harris, L.A.; Turner, R.R.; Stevenson, R.J.; Henson, T.J.; Melon, R.C.; Hoffman, D.P. Environmental Science and Technology, **1997**, *31(11)*, 3037-3043

[82] Barnett, M.O.; Harris, L.A.; Turner, R.R.; Henson, T.J.; Melton, R.E.; Stevenson, R.J. Water, Air, and Soil Pollution, **1995**, *80*, 1105-1108

[83] Chen, X.; Wright, J.V.; Conca, J.L.; Peurrung, L.M. Environmental Science and Technology, **1997**, *31(3)*, 624-634

[84] Morin, G.; Ostergren, J.D.; Juillot, F.; Ildefonse, P.; Calas, G.; Brown Jr., G.E. American Mineralogist, **1999**, *84*, 420-434

[85] Windmöller, C.C.; Wilken, R.D.; Jardim, W.F. Water, Air, and Soil Pollution, **1996**, *89*, 399-416

toxicity by bioassay according to the survival of the bacterial population[86], or the determination of mercury compounds by luminescent biosensors[87] (see section 1.7.3.1.2).

1.7.3.1.1 Extraction, separation and determination of Hg species

As mentioned above, most of the analytical speciation methods involve an extraction of the analytes, a separation of the corresponding species and their final quantification. In the case of mercury, these techniques normally deal with the identification and quantification of methylmercury and inorganic mercury, whilst hardly allowing the recognition of different species of the latter. Therefore, such techniques show an important drawback taking into account the strict speciation concept. Moreover, they do not provide information of the molecular-level environment and have to deal with the potential risk of species modification during the extraction process.

Extraction procedures for mercury speciation are roughly classified in three groups: solvent extraction, distillation and extraction with supercritical fluids. The first is the most widely used since the late sixties, when Westöö developed his method for the extraction of methylmercury from different matrices[88]. The extraction method consisted of a first step with concentrated HCl, NaCl and an excess of $HgCl_2$ to liberate the methylmercury from the matrix. Then, methylmercury was extracted to an organic phase (benzene), and re-extracted again to an aqueous cysteine solution. A final extraction with benzene allowed the mercury determination by gas chromatography. Although still popular[89-91], the Westöo method is being rapidly substitute by the use of microwave, which has been shown as a fast and efficient extraction method[89]. Likewise, analytical techniques tend to avoid the use of toxic solvents (i.e. benzene). For instance, the U.S. Environmental Protection Agency has developed a

[86] Hempel, M.; Chau, Y.K.; Dutka, B.J.; McInnis, R.; Kwan, K.K.; Liu, D. Analyst, **1995**, *120*, 721-724

[87] Ivask, A.; Hakkila, K.; Virta, M. Analytical Chemistry, **2001**, *73*, 5168-5171

[88] Westöö, G. Acta Chemica Scandinavica, **1968**, *22*, 2277-2280

[89] Lorenzo, R.A.; Vázquez, M.J.; Carro, A.M.; Cela, R. Trends in Analytical Chemistry, **1999**, *18(6)*, 410-416

[90] Hintelmann, H.; Falter, R.; Ilgen, G.; Evans, R.D. Fresenius Journal of Analytical Chemistry, **1997**, *58*, 363-370

[91] Lambertsson, L.; Lundberg, E.; Nilsson, M.; Frech, W. Journal of Analytical Atomic Spectrometry, **2001**, *16*, 1296-1301

methodology where several mercurial species are extracted by an ethanolic mixture in acidic media[92].

Distillation appears as a good alternative to conventional extraction techniques[90,93,94]. Most of the publications conduct the distillation process in an -KCl or -NaCl aqueous media, to which an antiemulsifier is commonly added. Temperature is kept between 140-180ºC, whilst easing the distillation by flowing nitrogen through the aqueous solution. In spite of being one of the most used extraction techniques, some authors have highlighted the possible methylation of inorganic mercury during the distillation process[90,94]. Finally, supercritical extraction is gaining importance due to several factors, including the use of cheap and harmless reagents (mainly CO_2), as well as the short times this extraction requires. Nevertheless, the extraction efficiency is significantly lower for supercritical than for other methods[89,95].

Among mercury separation techniques, gas chromatography has been the most widely used since the development of the Westöö extraction method. Eventually, different kinds of capillary columns have been developed for the simultaneous determination of methylmercury, inorganic mercury and total mercury, using both polar and non polar stationary phases[78]. Columns with higher thickness of stationary phase and low polarity have been shown the most suitable, due to their higher separation efficiency and resolution, despite the very small injection volumes needed (around 1 μl). On the other hand, the detection system has been also improved with time. For a long time, the coupling of gas chromatography and electronic capture detection (GC-ECD) has been the most used[96,97], but its low selectivity requests the use of previous cleaning stages. One of the most popular specific detector was the atomic emission spectroscopy with microwave induced plasma (MIP-AES), but the most used in current times is the coupling of gas chromatography and inductively coupled plasma mass spectroscopy (GC-ICP-MS), due to its high sensitivity (detection limits between 100 and 200

[92] EPA, Method 3200: Mercury species fractionation and quantification by microwave assisted extraction, selective solvent extraction and/or solid phase extraction, July 2005, [on-line], <http://www.epa.gov/sw-846/pdfs/3200.pdf>, [13 June 2006]

[93] Hammerschmidt, C.R.; Fitzgerald, W.F. Analytical Chemistry, **2000**, *367*, 567-473

[94] Bloom, N.S.; Colman, J.A.; Barber, L. Fresenius Journal of Analytical Chemistry, **1997**, *358*, 371-377

[95] Emteborg, H.; Björklund E.; Ödman F.; Karlsson F.; Mathiasson L.; Frech W.; Baxter D.C. Analyst, **1996**, *121*, 19-29

[96] Carro A.M.; Rubí, E.; Bollain, M.H.; Lorenzo, R.A.; Cela, R. Applied Organometallic Chemistry, **1994**, *8*, 665-676

[97] Vázquez, M.J.; Carro, A.M.; Lorenzo, R.A.; Cela, R. Analytical Chemistry, **1997**, *69*, 221-225

fg as absolute mass for methylmercury, and between 500 and 600 fg for inorganic mercury using a 1 μl injection) and selectivity[98].

After GC, high performance liquid chromatography (HPLC) is gaining importance for mercury species separation. In general terms, HPLC is less sensitive than GC although being more suitable for the analysis of polar analytes. Therefore, HPLC has been shown as more appropriate for the joint determination of organic and inorganic species of mercury. Usually, separations take place in reverse phase, where the stationary phase is fixed on a silica base[99]. Different mobile phase has been applied for this purpose, such as cysteine-acetic acid[100], acetonitrile-water[101], pentasulfonate-acetonitrile[102], etc. A number of detection methods have been also used, standing out UV/visible spectrophotometry, electrochemical detector, graphite furnace-AAS, microwave-induced plasma-AES, IC-MS, and cold vapour-AAS detectors[78].

Recently, capillary electrophoresis (CE) has been also considered for the separation and detection of mercury species. The technique is characterized by thin capillaries with internal diameters between 20 and 200 μm, which show very high separation capacity (high efficiency) but a limited sensitivity[103]. This drawback can be overcome either by applying an on-line preconcentration method[104] or by using a more sensitive detector. In this sense, the coupling system HPCE-ICP-MS[105,106] allows a multielemental detection whilst significantly reducing the detection limits, as well as the multielemental detection.

1.7.3.1.2 Luminiscent biosensors

A biosensor is a device for the detection of a given analyte that combines a biological component with a physicochemical detector component. It consists of three parts:

[98] Garcia Fernandez, R.; Montes Bayon, M.; Garcia Alonso, J.I.; Sanz-Medel, A. Journal of Mass Spectrometry, **2000**, *35*, 639-646

[99] Harrington, C.F. Trends in Analytical Chemistry, **2000**, *19*, 167-179

[100] Munaf, E.; Haraguchi, H.; Ishii, D.; Takeuchi, T.; Goto, M. Analytica Chimica Acta, **1990**, *235 (2)*, 399-404

[101] Al-Rashdan, A.; Vela, N.P.; Caruso, J.A.; Heitkemper, D.T. Journal of Analytical Atomic Spectrometry, **1992**, *7(3)*, 551-555

[102] Shum, S.C.K.; Pang, H.; Houk, R.S.; Journal of Analytical Chemistry, **1992**, *64*, 2444-2450

[103] Dabek-Zlotorzynska, E.; Lai, E.P.C.; Timerbaev, A.R. Analytica Chimica Acta, **1998**, *359*, 1-26

[104] Carro-Díaz, A.M.; Lorenzo-Ferreira, R.A.; Cela-Torrijos, R. Journal of Chromatography A, **1996**, *730*, 345-351

[105] Lee, T.H.; Jiang, S.J. Analytica Chimica Acta, **2000**, *413*, 197-205

[106] Silva, M.; Soldado, A.B.; Blanco-González, E.; Sanz-Medel, A. Journal of Analytical Atomic Spectrometry, **2000**, *15*, 513-518

- the sensitive biological element, where the sensitive elements can be created by biological engineering. It includes biological materials (e.g. tissue, microorganisms, organelles, cell receptors, enzymes, antibodies, nucleic acids, etc), biologically derived materials or biomimics
- a transducer which associates both components
- the (physicochemical) detector element: optical, electrochemical, thermometric, piezoelectric or magnetic

During the last decade, very sophisticated analytical equipments dealing with different kind of transducers have been developed in the bioanalysis field. Nevertheless, the last technological trend is being the use of metal-specific whole-cell sensors to analyse the bioavailable fraction of certain toxic elements[107]. These sensors react to the presence of the toxicants by increasing their luminescence (due to the induction of the synthesis of luciferase), which is controlled by a toxicant-specific protein[108]. In the case of soils and sediments contaminated with heavy metals, analogous sensors have been used for the assessment of bioavailable metals (such as mercury[109-111]) in aqueous extracts. Recently, this test has been also applied to soil-water suspensions[109,112-114].

Whole-cell bacterial biosensors typically combine a specific promoter-operator in the recombinant strain (acting as the sensing element) with reporter gene(s) coding for the synthesis of reporter proteins (see Figure 1.14). Once the analyte binds to the sensor protein, a transcription of the reporter gene is activated, resulting in a higher production of the reporter protein (luciferase). This fact leads to the increase of the luminescence of the cell. This activation would be related to the synthesis of proteins that would combat the sensed hazard

[107] Ivask, A.; Francois, M.; Kahru, A.; Dubourguier, H. C.; Virta, M.; Douay, F. Chemosphere, **2004**, *55*, 147-156

[108] Köhler, S.; Belkin, S.; Schmid, R.D. Fresenius Journal of Analytical Chemistry, **2000**, *366*, 769–779

[109] Lappalainen, J.O.; Karp, M.T.; Nurmi, J.; Juvonen, R.; Virta, M.P. Environmental Toxicology, **2000**, *15*, 443-448

[110] Rasmussen, L.D.; Sorensen, S.J.; Turner, R.R.; Barkay, T. Soil Biology and Biochemistry, **2000**, *32*, 639–646

[111] Petänen, T.; Romantschuk, M. Analytica Chimica Acta, **2002**, *456 (1)*, 55–61

[112] Corbisier, P.; Thiry, E.; Diels, L. Environmental Toxicology and Water Quality, **1996**, *11*, 171–177

[113] Ivask, A.; Virta, M.; Kahru, A. Soil Biology and Biochemistry, **2002**, *34*, 1439–1447

[114] Petänen, T.; Romantschuk, M. Chemosphere, **2003**, *50 (3)*, 409–413

or adapt to it. At higher analyte concentrations, the luminescence decreases due to the toxic effect of the analyte[115] (see Figure 1.14).

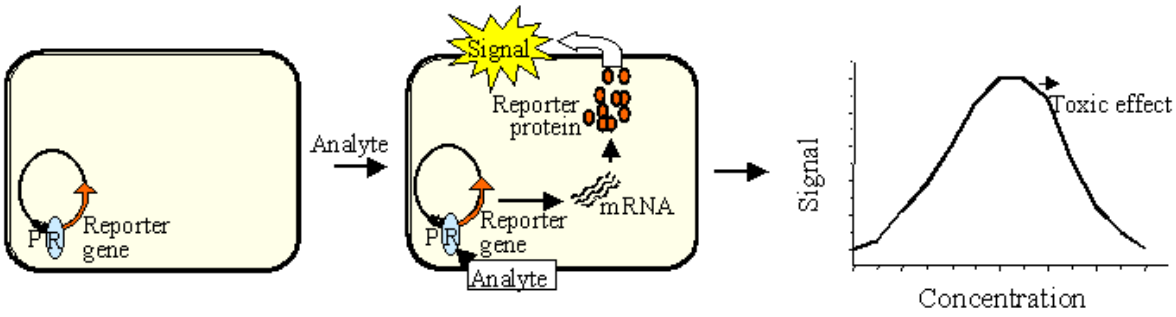

Figure 1.14 Schematic representations of the functional mechanisms of a luminescent biosensor (after NICPB, 2006[115]).

Analogously to direct speciation approaches, almost no sample pre-treatment is needed for biosensors analyses. Whole-cell biosensors provide data on the bioavailability of a pollutant without expensive equipment and providing extremely low detection limits (0.02 ppb for CH_3Hg^+ and 2 ppb for Hg^{2+}). Nevertheless, these biosensors are only able to quantify methylmercury and inorganic mercury, therefore having a limited speciation capacity.

1.7.3.2 Sequential extraction schemes

Sequential extraction schemes (SES) have been also widespread used as a complementary technique, to identify and understand trends within Hg association to specific matrix phases[116-118]. These procedures are defined as fractionation methodologies rather than as speciation techniques. According to the IUPAC, the term fractionation is defined as: "Process of classification of an analyte or a group of analytes from a certain sample according to physical (e.g., size, solubility) or chemical (e.g., bonding, reactivity) properties"[77]. Thus, the evaluation of the different fractions, through an empirical strategy that use sequentially leaching reagents of increasing strength, give rise to the named sequential extraction schemes (SES).

[115] National Institute of Chemical Physics and Biophysics (NICPB), *Molecular genetics: Biosensors*, Tallinn, 2006, [on-line], <http://www.kbfi.ee/>, [17 June 2006]

[116] Quevauviller, P. Trends in Analytical Chemistry, **1998**, *17*, 89-298

[117] Davidson, C.M.M.; Duncan, A.L.; Littlejohn, D.; Ure, A.M.; Garden, L.M. Analytica Chimica Acta, **1998**, *363*, 45–55

[118] Fedotov, P.S.; Zavarzina, A.G.; Spivakov, B.Ya; Wennrich, R.; Mattusch, J.; de Cunhal-Titze, K.P.; Demin, V.V. Journal of Environmental Monitoring, **2002**, *4*, 318–324

Many research groups have worked on the design and study of extraction schemes, aiming at the characterisation of the heavy metal distribution among the different soil phases. The determination of these metal fractions allows certain predictions regarding the possible release of a given analyte (metal) from a soil or sediment phase under certain conditions of gradual lixiviation power. Therefore, SES constitute a valuable tool in the determination of Hg mobility and bioavailability.

The strategy followed consists of the use of reagents able to selectively dissolve metal fraction bonded to certain soil materials of forming certain compounds, i.e. water soluble compounds, exchangeable cations, carbonates, easily reducible, oxidizable phase and residual. These fractions may vary among different extraction schemes. Most common reagents used include: no hydrolysable salts, weak acids, reducing agents, oxidant agents and strong acids[119].

Several SES schemes have been developed to evaluate metal fractionation in soils and sediments[120], including metal-specific methods, such as Hg[121-123]. These protocols are characterised by a number of extraction steps, normally varying between 3 and 8. The most widely used SES schemes are Tessier[124] and BCR-SES[125,126] (see Table 1.5). Comparatively, both methods provide a similar fractionation, although the exchangeable fraction of BCR resumes 'exchangeable' and 'carbonate' fractions from Tessier.

[119] Rauret, G. Talanta, **1998**, *46(3)*, 449-455

[120] Kersten, M.; Förstner, U. Speciation of Trace Elements in Sediments, Batley, G.E. (ed.), in: Trace Element Speciation: Analytical Methods and Problems, CRC Press, Boca Raton, Florida, USA, 1989

[121] Inácio, M.M.; Pereira, V.; Pinto, M.S. Geoderma, **1998**, *85*, 325-339

[122] Bloom, N.S.; Preus E.; Katon J.; Hiltner M. Analytica Chimica Acta, **2003**, *479(2)*, 233-248

[123] Neculita, C.M.; Zagury, G.J.; Deschênes, L. Journal of Environmental Quality, **2005**, *34*, 255-262

[124] Tessier, A.; Campbell, P.G.C.; Bisson, M. Analytical Chemistry, **1979**, *51*, 844-851

[125] Quevauviller, P.; Rauret G. ; Lopez-Sanchez J.-F. ; Rubio R., Ure. ; Muntau H. The Science of the Total Environment, **1997**, *205*, 223-234

[126] Quevauviller, P. ; Rauret, G. ; Lopez-Sanchez, J.F. ; Rubio, R. ; Ure, A.M.; Muntau, H. Report EUR 17554 EN, European Comission, Brussels, 1997

Table 1.5 Sequential extraction procedures defined by Tessier[124] and BCR-SES[125] applied to 1 g of sample.

	Fraction	Extraction conditions
Tessier	**T1**: Fraction 'exchangeable'	8ml 1M $MgCl_2$, pH 7, 25ºC, 1h
	T2: Fraction 'link to carbonates'	8ml 1M CH_3COONa + CH_3COOH, pH 5, 25ºC, 5h
	T3: Fraction 'link to iron and manganese oxides'	20ml 0.04M NH_2OH•HCl (25% v/v CH_3COOH), 96ºC, 6h
	T4: Fraction 'link to organic matter'	3ml 0.02M HNO_3 + 2ml 30% H_2O_2 (pH 2), 85ºC, 2h; 3ml 30% H_2O_2 (pH 2), 85ºC, 2h; 5ml 3.2M CH_3COONH_4 in 20% HNO_3 + 7ml H_2O, 25ºC, 30 min
	T5: Fraction 'residual'	7.5ml 37% HCl + 2.5ml 65% HNO_3, 25ºC during 1 night, reflux 2h
BCR-SES	**B1**: Fraction 'water soluble, exchangeable and link to carbonates'	20 ml 0.1M CH_3COOH, 25ºC, 16h
	B2: Fraction 'link to iron and manganese oxides'	20ml 0.1M NH_2OH•HCl, pH 2, 25ºC, 16h
	B3: Fraction 'link to organic matter and sulphides'	5ml 30% H_2O_2, 25ºC, 1h + 5ml 30% H_2O2, 85ºC, 1h. + 25ml 1M CH_3COONH_4, pH 2, 25ºC, 16h

One of the main drawbacks of SES is related to the large variety of existent schemes, and therefore to the difficulties in data comparison. In this sense, the program 'Standards, Measurements and Testing' of the European Commission has done an important effort to the compilation of the bibliography, homogenisation and optimisation of the procedures[126], to generate a consensus procedure for the comparison of results and their proper interpretation. Also, with the same finality and focused to the study of mercury in polluted soils and sediments, U.S.EPA have prepared the Method 3200 to the classification of Hg in extractable and no extractable[92]. In this procedures, the extractant used is a dissolution of ethanol (10%), with HCl (2%) and HNO_3 2M.

Other drawbacks posed by SES are the different extraction results according to the treated matrix, the excessive time required, the possible species modification during extraction procedure, or the autoabsorption effects, among others[127]. Moreover, the entire procedure request of the exhaustive control in the extracting agent's concentration, as well as in the number of extractions needed to complete each phase.

[127] Gómez-Ariza, J.L.; Giráldez, I.; Sánchez-Rodas, D.; Morales, E. Analytica Chimica Acta, **2000**, *414*, 151-164

1.8 DIRECT SPECIATION: SYNCHROTRON-BASED TECHNIQUES

X-rays Absorption Spectroscopy (XAS) techniques using synchrotron facilities as X-rays radiation source can contribute to very valuable information regarding speciation both in environmental and biological samples. Among those, XANES and EXAFS are considered as very powerful techniques for the recognition of different species of the same element, given their specificity signal at both atomic level and atom surrounding. In the following sections, a brief introduction to synchrotron radiation (SR) generation, XAS techniques and their applications will be presented.

1.8.1 Historic remarks of synchrotron radiation

The first accelerators (cyclotrons) were built during the 30s by particle physicists, who intended to look at the splitting of the atom's nucleus forced by the collision of high energy particles. In those facilities, synchrotron radiation remained unknown until the late 40s, when American scientists discovered its relationship with the lost of energy observed in the accelerated particles. During the 60s, synchrotron light was recognised as to holding very exceptional properties and, since then, became a premier research tool for the study of matter. From this starting point, facilities around the world constantly worked to provide a more brilliant, intense and stable synchrotron light. Some highlights of this SR development as well as its X-rays background are shown in Table 1.6.

Table 1.6 History of the X-rays background and the synchrotron radiation development[128,129].

Period	Highlight
Early history	1895: discovery of X-rays by Röntgen 1897: Larmor derived an expression for the light emission of non relativistic accelerated electrons 1912: von Laue Friedrich, and Knipping observe X-rays diffraction 1913: Bragg, father and son, build and X-rays spectrometer 1930s: construction of the first accelerators 1953: the structure of DNA was solved by J.Watson and F.Crick, thanks to the use of X-rays
Discovery of synchrotron radiation	1947: first observation of SR at the General Electric Research Laboratory in Schenectady, New York
The first generation: 60s-70s	Use of SR in investigation (DESY in Hamburg, Daresbury in United Kington and NBS in Maryland). Small synchrotrons are constructed at the end of 60s, and at the beginning of 70s, the first storage ring multi-GeV class to provide X-rays to a large community of synchrotron users developed at the Stanford Linear Accelerator Center (SLAC)
The second generation: late 70s- early 90s	Worldwide uses of SR. VUV installations and X-rays rings are exclusively constructed for the SR. Synchrotron light is generated by bending magnets. The users community spread to a big number of disciplines
The third generation: early 90s- nowadays	Insertion devices (wigglers and undulators) are employed to create periodic fields of alternating polarity. The ESRF (6 GeV) in Grenoble was the first of the hard X-rays sources to operate with such devices. This was followed by the APS (7 GeV) in Chicago, and Spring-8 (8 GeV) in Japan. Among the long-wavelength X-rays, some sources using insertion devices are the ALS at Berkeley (1.9 GeV), Synchrotrone Trieste (2 GeV) in Italy, SRRC in Taiwan (1.3 GeV) and the PLS (2 GeV) in Korea. Moreover, a number of new 3rd-generation SR sources will come on line over the next few years (SPEAR3 at Stanford, Diamond in the U.K., ALBA in Barcelona and NSLS-II in New York)
The forth generation: in development	Special applications: free-electron laser (FEL) in the hard X-rays region (e.g. TESLA in Hamburg; SPPS and LCLS in U.S), lineal accelerators of energy recuperation, among others. These light sources will produce highly coherent, very short pulses (< 100 femtoseconds) containing on the order of 10^{13} photons. Such pulses will allow studies of the mechanisms of chemical reactions at an unprecedented level of detail

Advances in SR within generations are mainly related to the improvement of brightness (photons per second per unit of source area and per unit of solid angle) of the source. Figure 1.15 reviews the brightness of different X-rays sources, from X-rays tubes to FEL facilities.

[128] Thompson, A. et al. *X-Ray Data Booklet*, University of California, Berkeley, 2001

[129] European Synchrotron Radiation Facility (ESRF), [on-line], <http://www.esrf.fr/>, [6 July 2006]

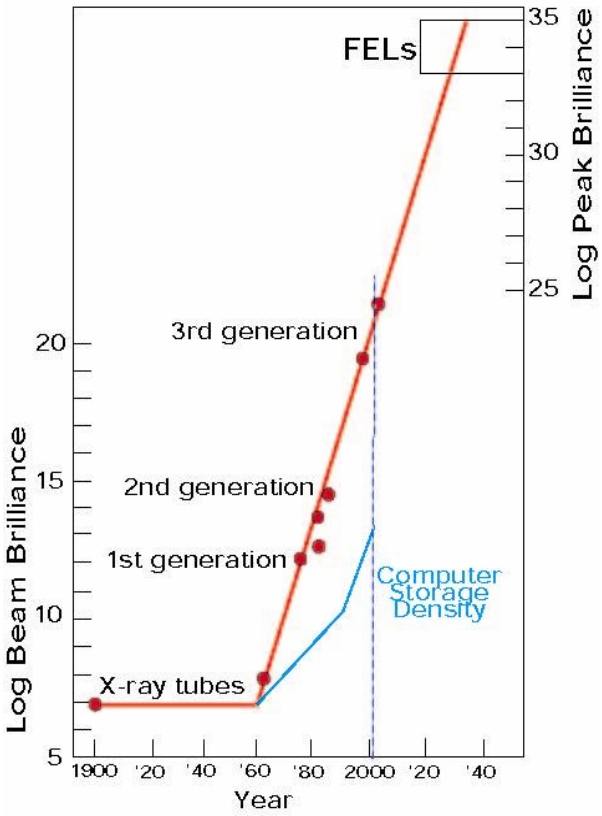

Figure 1.15 Eventually brightness improvement of different light sources.

1.8.2 Introduction to synchrotron radiation and the physics of storage rings

Synchrotron radiation (also named synchrotron light) is emitted when elementary charged particles (such as electrons or positrons) travel with a velocity close to the velocity of light along a curved trajectory. For non-relativistic energies, the radiation is emitted in a dipole pattern with the intensity varying as the sinus of the angle between the observation direction and the acceleration vector, perpendicularly to the direction of movement. However, for relativistic velocities the dipole pattern is compressed along the direction of movement, therefore leading to the generation of synchrotron radiation (see Figure 1.16). The transformation of angles is given by,

$$\tan\theta' = \frac{\sin\theta}{\gamma(\beta + \cos\theta)} \qquad \textbf{Eq. 1.10}$$

where θ and θ' stand for the angle between the observation direction and the acceleration vector for non-relativistic and relativistic energies respectively; β is the ratio between velocity of the particle and velocity of light; γ is the relation between the mass (m) of a relativistic electron and its mass in repose (m_0), expressed as,

$$\gamma = \frac{E}{m_0 c^2} = \frac{1}{\sqrt{1-\beta^2}} = 1957E(GeV) \qquad \textbf{Eq. 1.11}$$

where E is the electron energy expressed in GeV; $E=\gamma mc^2$. For non-relativistic electrons, $\beta \sim 0$, $\gamma=1$, whereas for relativistic electrons, $\beta \sim 1$. The angular distribution is narrowed down to an aperture angle of $1/\gamma$ width (the half part of the divergent synchrotron light above and below the orbital plane) (see Figure 1.16). Thus, the higher the electron energy is, the lesser aperture angle of the generated synchrotron radiation, the lesser divergence and the higher brightness. An observer looking at the electron along its velocity vector would see light during the time the electron travels an arc length ρ/γ where ρ is the radius of curvature, $\rho = m\gamma c/eB$, being B the magnetic field. During this time, light travels a distance $\rho/\gamma\beta$. Actually, this means that the length of the observed pulse is,

$$\frac{1}{c}\left(\frac{\rho}{\gamma\beta} - \frac{\rho}{\gamma}\right) \approx \frac{\rho}{c\gamma^3} \qquad \textbf{Eq. 1.12}$$

In order to have this length, a pulse must contain frequency components up to,

$$\omega \approx \frac{1}{\Delta t} \approx \frac{c\gamma^3}{\rho} = \omega_0 \gamma^3 \qquad \textbf{Eq. 1.13}$$

where ω_0 is the angular frequency of rotation for the electrons. This explains the origin of the broad white beam emitted by synchrotron radiation; for example, a 500 MeV machine has γ = 1000, which means the radiation spectrum extend to frequencies of order $10^9\ \omega_0$.

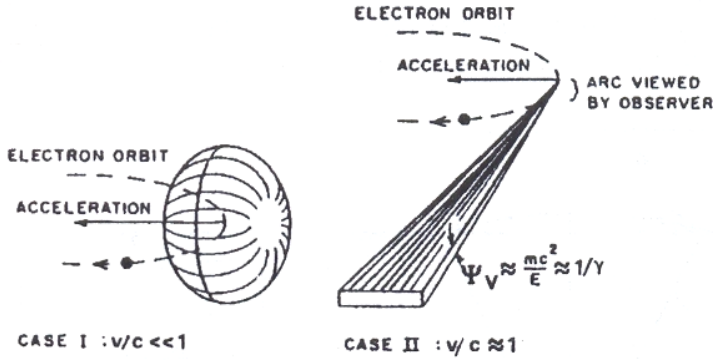

Figure 1.16 Radiation emission patterns of electrons in circular motion: case I, non-relativistic electrons, case II, relativistic electrons (after Raoux, 2003[130]).

[130] *Neutron and Synchrotron Radiation for Condensed Matter. Volume 1: Theory, Instruments and Methods*, Baruchel, J.; Hodeau, J.L.; Lehmann, M.S.; Regnard, J.R.; Schlenker, C. (eds.), Les Editions de Physique, Les Ulis, France, 1993

The energy irradiated by relativistic electrons when these are deviated by a magnetic field with a curvature radius ρ (see Figure 1.17), is given by the expression,

$$P = \frac{2}{3}\frac{e^2\gamma^2}{m_0^2 c^3}\left|\frac{dp}{dt}\right|^2 \qquad \textbf{Eq. 1.14}$$

where *e* is the charge of the electron and p the momentum ($p=m_0 v$). Considering the electron circular motion in an orbit for an angular differential dα (Figure 1.17), dp/dt can be expressed as,

$$\frac{dp}{dt} = p\frac{d\alpha}{dt} = p\frac{v}{\rho} \qquad \textbf{Eq. 1.15}$$

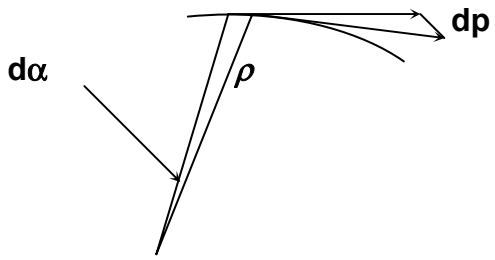

Figure 1.17 Electron orbit, indicating the momentum differential dp, corresponding to the angle variation dα.

Hence, using Eq. 1.11, Eq. 1.15 and substituting pc by E, the irradiated energy can be expressed as:

$$P = \frac{2}{3}\frac{e^2 c}{(m_0 c^2)^4}\frac{E^4}{\rho^2} \qquad \textbf{Eq. 1.16}$$

If radius is the same through the whole orbit, the energy loss (ΔE) as synchrotron radiation per electron and bend can be calculated as,

$$\Delta E = \oint_{orbit} P\,dt = P\frac{2\pi\rho}{c} \qquad \textbf{Eq. 1.17}$$

Taking into account Eq. 1.16 and 1.17 and using the appropriate units, Eq. 1.18 is obtained,

$$\Delta E[keV] = 88.5\frac{E^4[GeV]}{\rho[m]} \qquad \textbf{Eq. 1.18}$$

Equation 1.18 shows that the loss of energy is a forth potency of the electron energy. Hence, generation of synchrotron radiation is significant for electrons with energies of a few tenths of

MeV and becomes very important for energies in the range of GeV. Consequently, a higher energetic synchrotron radiation is produced in high energy rings.

Synchrotron radiation is produced in storage rings under high vacuum conditions (typically 10^{-9}-10^{-10} torr). In these facilities, high energy electrons (or positrons) are maintained in a planar orbit[131] by using bending magnets. A distinction is usually made between rings producing "hard" X-rays (2000-50000 eV) and those producing "soft" X-rays and vacuum ultraviolet (VUV) radiation (1-2000 eV). In both cases, it is extremely important to reach a high vacuum in order to obtain longer life-times for the stored current.

The charged particles are usually pre-accelerated by electric fields in a linear accelerator (Linac) to energies between a few hundreds MeV to several GeV. Then, these particles are further accelerated in a booster circular accelerator with the aid of powerful magnetic and electric fields, until they reach velocities very close to velocity of light. This step allows the reduction of the emittance of the beam delivered by the Linac, therefore increasing the efficiency of the injection into the storage ring. Once in the storage ring, electrons are maintained in a circular orbit by strong magnetic fields, whereas velocity is kept constant by compensating for the energy lost (as light emission) with electric fields from radio-frequency sources. It is important to highlight that electrons do not circulate as single particles around the ring, but they are bunched in packets containing about 150 billion particles.

Synchrotron radiation is obtained either in curved sections of small diameter (5-10 cm) by bending magnets or in straight sections by insertion devices such as wiggler and undulator magnets. Insertion devices are due to improve the intensity and collimation of synchrotron radiation. These devices are built by two rows of alternating magnets that create periodic fields of alternating polarity perpendicular to the electron beam, which cause the electrons to have a sinusoidal trajectory[132] (see Figure 1.18a). The difference between wigglers and undulators is given by the size of the oscillations produced by magnetic fields. In undulators, a smaller angular deflection of the electron beam results in constructive and destructive interferences between certain wavelengths, causing a non-uniform brightness over the broad spectral range[131] (see Figure 1.18b). Nevertheless, narrow bandwidth radiation of high intensity at well defined energies is obtained. In the case of a multi-pole wiggler magnet,

[131] Brown Jr., G.E.; Calas, G.; Waychunas, G.A.; Petiau, J. X-ray Absorption Spectroscopy and its Applications in Mineralogy and Geochemistry, in: Reviews in Mineralogy. Spectroscopic methods in mineralogy and geology, Hawthorne, F.C. (ed.), Vol. 18, Chap. 11, Mineral Society of America, Washington, 1988, pp. 431-512

[132] Spencer, J.E.; Winick, H.; Doniach, S.; Rosenbaum G.; Holmes, K.C.; Brown, G.S.; Sayers, D.E.; Bunker, B.A. *Synchrotron Radiation Research*, Winick, H.; Doniach, S. (eds.), Plenum, New York, 1980

additional bends of the electron beam produce additional flux over a large angular spread. This additional flux increases the brightness of the emitted radiation by a factor roughly equal to the number of magnetic poles, if compared to a bending magnet of the same field strength. Summarizing, undulators do not radiate at higher flux than wigglers do, but concentrates radiation in a narrower angular range for certain wavelengths.

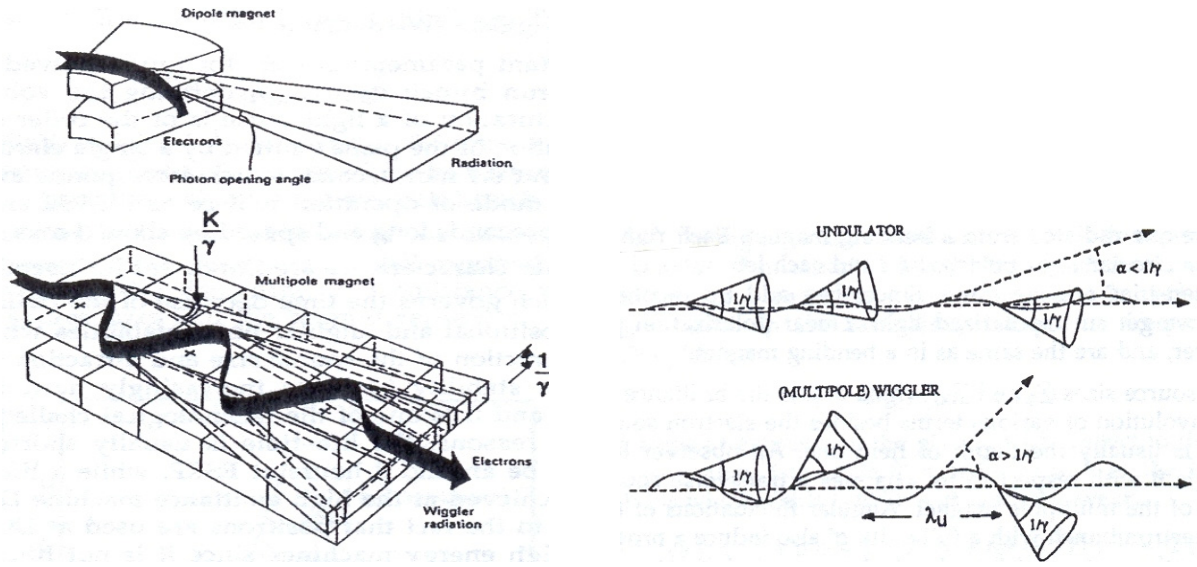

a) **b)**

Figure 1.18 (**a)** Radiation beams from a bending magnet and from the individual poles of an insertion device, and (**b)** Schematic pictures of the undulator and multipole wiggler regimes (after Raoux, 2003[130]).

Synchrotron light presents very special characteristics, the most important being reviewed as follows:

- high intensity or flux (photons per second) over a continuous wavelength spectrum from microwaves to hard X-rays and gamma radiation. In contrast to laser light, synchrotron radiation is non-monochromatic
- high brightness, thousands of million-fold higher than conventional X-rays sources
- linearly polarized light, the light oscillates only within certain planes. The light is emitted in very short (picoseconds) pulses with a periodic structure (microseconds), therefore showing a high potential for studies of transient phenomena
- light source remaining stable along the time. Depending on the facility, each bunch refill shows a lifetime between 4 and 24 hours

Once generated at the magnet, synchrotron light is propagated by stainless steel pipes through the experimental station, which is placed tangentially to the ring. The experimental station (also called beamline) contains the equipment needed to make synchrotron radiation available to the experimentalist. The X-rays beamline consists of three major sections[133]:

- the machine interface or front end, where synchrotron radiation is coupled to the experiment through a beam port (tangent to the ring) and a fast valve
- the beamline optics, which have two basic goals: to collect as much radiation as possible, and, in most of the experiments, to monochromize the collected "white beam" of X-rays. Due to the high thermal and radiation loads, rugged monochromator crystals are needed (commonly silicon or germanium).
- the experimental apparatus with personnel safety interlocks. A beamline must contain diverse safety devices to protect the storage ring from vacuum contamination produced by the user, as well as to protect the user from radiation hazard. The experiment is usually built in an interlocked enclosure or hutch with lead walls. The hutch can only be opened when appropriate beamline shutters are closed, whilst having additional interlocks to avoid the presence of any person inside the hutch when synchrotron radiation is running

Despite the strong potential shown by synchrotron-based techniques and the spectacular increase of their possible uses, these techniques present as well some drawbacks:

- poor detection limits. Despite the continuous improvement, actual detection limits are still too high when dealing with real environmental concentrations
- limited number of synchrotron facilities worldwide: difficult access to these techniques and high analysis cost
- in some cases, complex data treatment

1.8.3 Interaction of X-rays with matter

Synchrotron light allows the view of structures hardly visible by other means. Recording the image of a given structure requires the use of a wavelength equal to or smaller than the size of this structure. X-rays hold wavelengths similar to interatomic distances in condensed matter, and about ten thousands times shorter than wavelength of light detectable by human eye (see

[133] Stern, E.A.; Heald, S.M. *X-Ray Absorption. Principles, applications, techniques of EXAFS, SEXAFS and XANES*, in: *Chemical Analysis*, Koningsberger, D.C.; Prins, R. (eds.), John Wiley & Sons, New York, 1988

Figure 1.19). Therefore, X-rays seem a rather appropriate tool for the study of matter at atomic level.

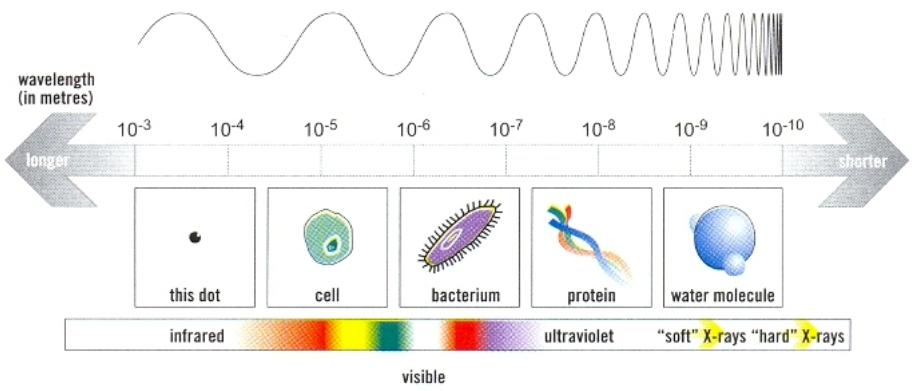

Figure 1.19 The electromagnetic spectrum.

The interaction between X-rays and matter leads to several types of processes:

- X-rays absorption, which produces photoelectrons (see section 1.8.4)
- X-rays scattering (elastic (without energy loss) and inelastic (with energy loss)). In both cases, light dispersion can occur either randomly (incoherent dispersion, when interacting with irregular objects) or coherently (diffraction, when objects are well-arranged). Elastic dispersion provides a good tool for crystallographic studies of small crystals, proteins crystallography, powder diffraction and small angle scattering. Inelastic dispersion is mainly used for the study of dynamic physical processes, such as Compton dispersion, magnetic dispersion or inelastic nuclear resonant scattering
- production of electron-positron pairs by the incident photons ($h\nu > 1$ MeV)
- production of optical photons
- production of phonons (i.e. lattice vibrations)

However, in the X-rays energy range (0.5 keV to 100 keV), photoelectric absorption is the dominant process[130,131]. In this context, XAS techniques become a valuable tool for the study of the local structure of individual elements by simply tuning the incident radiation energy to such corresponding to the target element[134,135].

[134] Fay, M.J.; Proctor, A.; Hoffman, D.P.; Hercules, D.M. *Unraveling EXAFS Spectroscopy*, in: *Instrumentation in Analytical Chemistry 1988-1991*, Voress, L. (ed.), American Chemical Society, Washington, 1992

[135] de Groot, F.; Vogel, J.; Lengeler, B. et al. *Neutron and X-ray Spectroscopy*, Hippert, F.; Geissler, E.; Hodeau, J.L.; Lelièvre-Berna, E.; Regnard, J.R. (eds.), Springer, Dordrecht, The Netherlands, 2006

1.8.4 Basics of X-rays Absorption Spectroscopy (XAS)

The absorption of electromagnetic radiation by matter is a relatively old concept which has been used to study the discrete (quantized) energy levels of electrons in atoms, molecules, and condensed matter[136]. From the 70s, the techniques applying this concept have tended to a versatile, element-specific structural probe that has been successfully applied to problems in a number of disciplines. Among other reasons, this change was mainly stimulated by advances in theory[137-139] and by the availability of synchrotron radiation[132].

X-rays absorption process is characterised by an absorption edge (a sharp increase in absorption of X-rays by matter over a narrow energy range), which is caused by the excitation of an electron from a deep core state of an atom to either an empty or a continuum state. The absorption edge only occurs when the energy of incident X-rays photons equals the energy required for excitation[131,140] (see Figure 1.20).

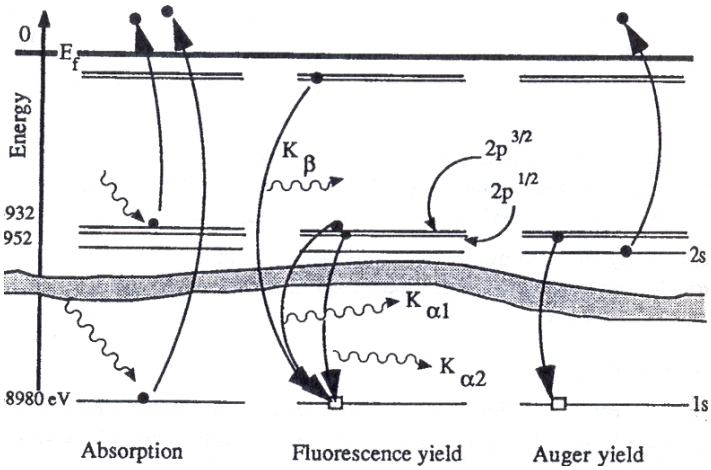

Figure 1.20 Schematic diagram of the absorption process and decay channels for copper (after Fontaine, 2003[130]).

In order to fix the terminology, we recall that the K edge corresponds to transitions from a 1s inner shell to empty levels. Similarly, L_I, M_I and N_I edges are respectively transitions from 2s, 3s or 4s inner shell levels. Nevertheless, further edges than K and L are not currently used. L_{II}-

[136] Glenn, G.L.; Dodd, C.G. Journal of Applied Physics, **1968**, *39*, 5372-5377

[137] Sayers, D.E.; Stern, E.A.; Lytle, F.W. Physical Review Letters, **1971**, *27*, 1204-1207

[138] Stern, E.A. Physical Review B, **1974**, *10*, 3027-3037

[139] Ashley, C.A.; Doniach, S. Physical Review B, **1975**, *11*, 1279-1288

[140] Kossel, W. Zeitschrift für Physik, **1920**, *1*, 119-134

$_{III}$ are transitions from the 2p level, whilst similar quotations stand for M_{II-III} (3p inner shell) and N_{II-III} (4p inner shell). Labels II and III refer to transitions where the orbital momentum (*l*) and the spin momentum (*s*) are coupled to give *j=l-s* for "II" and *j=l+s* for "III". The selection rules of X-rays absorption determine that, in dipole transitions the orbital quantum number of the final state must differ by 1 from the initial state ($\Delta l = \pm 1$, i.e. s→p, p→s or d, etc.), whilst in quadrupole transitions, final state must differ by 2 from the initial state ($\Delta l = \pm 2$, i.e. s→d, p→f)[135]. In both cases the spin must be conserved ($\Delta s = 0$).

Once the absorption of the photon occurs, the excited atom is left with an electronic vacancy (a core hole), which will be filled by an electron from an upper shell. This process is accompanied either by the emission of a fluorescence photon or by the emission of Auger electrons (Figure 1.20). In light elements (core levels below 1 keV), Auger emission is more probable, whereas for heavy elements fluorescence become more likely. Since the Auger electrons originate at about 3 nm of the surface, X-rays absorption spectroscopy in Auger mode is significantly surface sensitive. Therefore this technique is commonly used for surface EXAFS studies (SEXAFS)[135].

The incident X-rays beam holds an intensity I_0 and energy E. The intensity of the transmitted beam, I, is described by Lambert-Beer's law, following the equation:

$$I = I_0 \exp(-\mu x) \qquad \textbf{Eq. 1.19}$$

where x (cm) is the sample thickness and μ (cm^{-1}) is the linear absorption coefficient. On the other side, μ is defined as:

$$\mu = \mu_m(cm^2\ g^{-1})\ \rho(g\ cm^{-3}) \qquad \textbf{Eq. 1.20}$$

where μ_m is the mass absorption coefficient and ρ the density. The linear absorption (μ) depends on the physical and chemical state of the absorber, as well as on the energy of the incident X-radiation[131].

Several detection setups have been developed for XAS studies, depending on the nature of the absorber and the matrix type[131]. In this sense, the most commonly used involve the measurement of either transmission or fluorescence.

Transmission method measures sample absorption and is typically used for high concentrations absorbers (> 2 % w/w) with Z> 16-20. The absorption by a sample of thickness x and absorption coefficient μ is related to the ratio of I_0 and I as:

$$\mu x = \ln(I_0/I) \qquad \textbf{Eq. 1.21}$$

Consequently, sample absorption can be adjusted by modifying sample thickness, with optimum sample thickness decreasing as the absorption edge energy decreases. This effect is related to the higher matrix self-absorption rates given at low energies, which requires the use of extremely thin samples for soft X-rays analysis[135].

The control of sample homogeneity is especially important when dealing with transmission EXAFS measurements. Either the presence of inhomogeneities or pinholes in the sample will strongly affect transmission phenomena, leading to a reduction of the ratio I_0/I and the EXAFS amplitude.

Fluorescence detection follows the fluorescent X-rays yield from the front-face of the sample. Fluorescence detection is used for samples with lower absorber concentrations (< 2% w/w), with high matrix absorption or for very small samples. The fluorescence, I_f, is directly proportional to the number of absorption events for dilute samples, and therefore I_f/I_0 is proportional to μ. Hence, due to a higher signal-to-noise ratio, the fluorescence yield is 10 to 100 times more sensitive than absorption coefficients measured in transmittance mode. On the other hand, fluorescence is not significantly affected by sample thickness, as μx value is small and loss through the sample has hardly any effect on the fluorescence signal[131].

1.8.4.1 Setup for measuring X-rays absorption

XAS requires a continuous and intense X-rays source covering a broad range of energies. After being generated at the magnet, synchrotron radiation reaches the beamline through a beryllium window, which is commonly used to isolate the beam line from the storage ring. However, when dealing with soft X-rays XAS studies (<2 keV), high vacuum conditions ($>10^{-8}$) and avoidance of beryllium windows are required because of additional absorption phenomena[131].

Once at the beamline, synchrotron radiation goes through an optical system that consists of up to three elements:

- **slits or apertures**, which are used to limit the size of the beam, avoiding scattered radiation and improving the energy resolution of the monochromator
- **set of mirrors**, which are widely applied as high energy cut-off filters and as focusing devices[130]. Several types of optical elements are available for measurements performed at high X-rays energies. The most common and useful for XAS are Bragg reflecting crystals and grazing incident mirrors. Materials chosen for X-rays mirrors

must be resistant to radiation, have good thermal properties, be highly polishable, and be available in large sizes.

- **tuneable monochromator**, which permits the selection of the incident photon energy. Monochromation of polychromatic incident X-rays is essential for XAS measurements. The basic monochromator system for synchrotron XAS studies uses two parallel crystals. The first crystal is used to monochromize the incident beam (with typical bandwidth ($\Delta E/E$) in the order of 10^{-4}), whilst the second crystal is used to keep the outgoing beam parallel to the incident one, with a slight offset given by $h=2d\cos\theta$, where d is the crystal separation. The energy scale is therefore determined by the crystal rotation. For X-rays from 2 to 10 keV a Si(111) double crystal monochromator is recommended. The range between 10 and 20 keV is usually covered by Si(311) crystals, whereas Si(511) are recommended for X-radiation above 20 keV[135]. Harmonics present in the synchrotron beam can be eliminated either by slightly "detuning" the second crystal or by inserting a mirror before the monochromator. In the last case the mirror has to be adjusted so that only the higher wavelengths are reflected and used in the XAS experiment. Otherwise, beam harmonics can strongly affect the measurement of absorption spectra, as the higher energy photons will be transmitted without significant absorption by the sample, resulting in an effective decrease in the amplitude of EXAFS oscillation[131].

The beam reaches the sample at the sample-holder, which is usually able to handle different sample environments, such as cryostats, ovens, goniometers, etc.

As mentioned above, **detection** can be followed either by transmittance or fluorescence. There exists a large variety of detectors, such as ionisation chambers, photodiodes, photomultipliers, wavelengths dispersion detectors, etc. Concerning **transmission measurements**, the most commonly used detectors are gas-filled ion chambers[141]. The selection of the gas or gas mixture is determined by the energy of the beam and the amount of absorption of the incident beam desired. Hence, N_2, Ne, Ar (in increasing order of absorbance), and mixtures of these gases with He are commonly used. The detector is placed in front of the sample to detect the incident (or reference) intensity (I_0), which absorbs about 20% of the incident beam. A second ion chamber detector stands after the sample to monitor transmitted intensity (I). The energy scale is calibrated using the absorption edge of a

[141] Rossi, B.B.; Staub, H.H. Ionization Chambers and Counters: Experimental Techniques, McGraw-Hill, New York, 1949

reference sample (e.g. a metal foil), and this calibration is repeated on a regular basis during data collection (e.g. recorder along with the sample through a third ionisation chamber). This procedure aims at detecting and correcting any energy shift caused by changes in experimental conditions.

Two different techniques are commonly used for the measurement of the absorption signal. The most popular uses the monochromator to select a small wavelength range, whereas ion gas detectors monitor I and I_0. The full spectrum is acquired by sequentially stepping the monochromator through the required energies. A second technique allows the full energy range to impact upon the sample and uses a crystal to spatially disperse the different energies[142,143]. Examples of the possible geometries are shown in Figure 1.20.

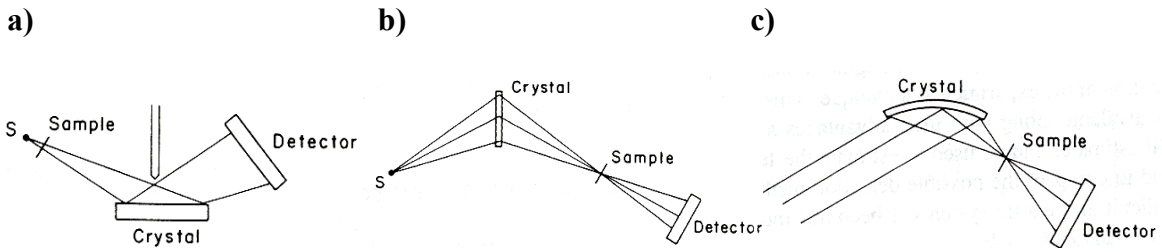

Figure 1.21 Three possible geometries for a dispersive EXAFS measurement: arrangements **(a)** and **(b)** are most appropriate for laboratory sources for which the X-rays are not collimated while **(c)** is appropriate for the more collimated output of a synchrotron (after Heald, 1988[133]).

Fluorescence X-rays yield is measured at the same side of the sample that the incident X-rays beam strikes. The setup is usually mounted with the beam showing the same incident and exit angle (beam – sample – beam). Such orthogonal position is important to reduce the scattering signal, as the major contributors to background are Compton scattering (partial absorption and scattering) and elastic scattering. These contributions are often much more intense than the signal from fluorescence emission. Nevertheless, these phenomena can be discriminated by using appropriate filters (usually made by an element with a Z slightly below the target element), by monochromators, or by direct energy discrimination using a solid state detector. The latter, normally of silicon or germanium, are based on self-scanning photodiode

[142] Mallozzi, P.J.; Schwerzel, R.E.; Epstein, H.M.; Campbell, B.E. Physical Review A, **1981**, *23*, 824

[143] Matsushita, T. *Laboratory EXAFS Facilities*, Stern, E.A. (ed.), American Institute of Physics, New York, 1980, p. 109

arrays[132,144]. The X-rays photons can be detected directly or converted first to light that is coupled to the diode array through an optic-fibre face plate. A further charge amplification lead to the generation of pulses whose intensity is directly proportional to the number of electrons removed.

Counting of electrons released from the sample is also considered under certain conditions as an indirect detection technique[133]. During the sample irradiation, each absorbing atom releases electrons that can result from several contributions: direct Auger and photoelectrons, scattered and secondary electrons induced by electrons ejected into the sample as well as small contributions from electrons induced by fluorescent X-rays. The counting rate of such electrons is directly proportional to the absorption; although poor signal levels are normally achieved.

Figure 1.22 reviews the scheme of a typical XAS beamline.

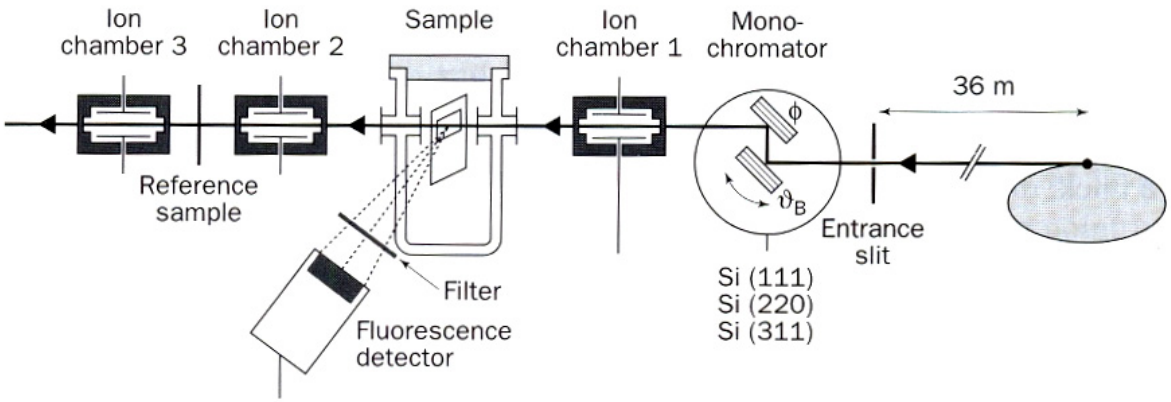

Figure 1.22 Typical beamline setup for a XAS experiment (after de Groot et al. 2006[135]).

1.8.4.2 Available information by XAS

The absorption spectrum of an element in the vicinity of an absorption edge can be divided in four main regions[131] (see Figure 1.23). This classification is based on the values of incident photon energy, E, and binding energy of a core-level electron, E_b, in the absorber. In this sense, XANES and EXAFS techniques take advantage of different 'windows' of the same absorption spectrum, as shown in Figure 1.23.

[144] Borso, C.S.; Danyluk, S.S. Review of Scientific Instruments, **1980**, *51*, 1669-1675

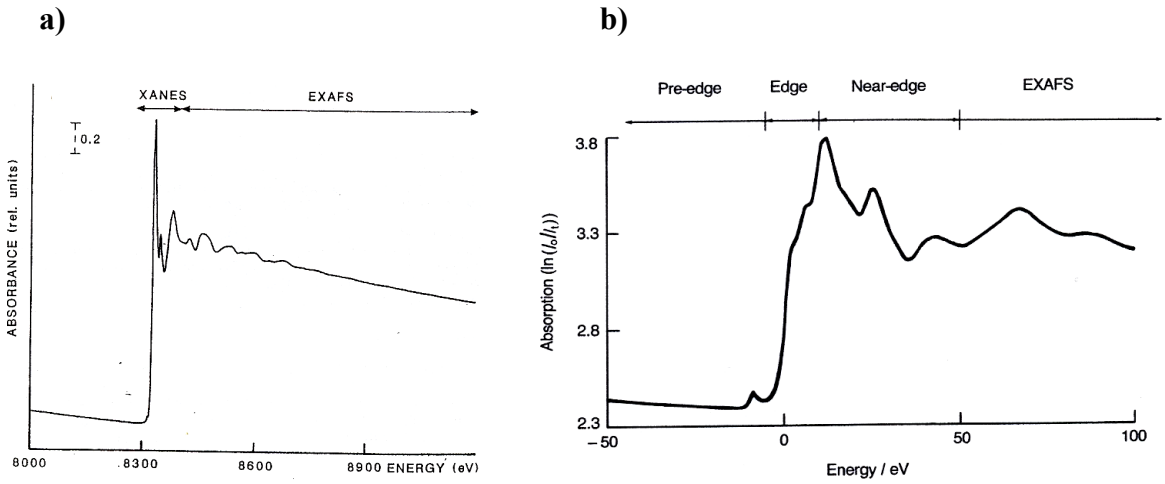

Figure 1.23 (a) K-edge X-rays absorption spectrum of Ni-kerolite, and (**b)** expanded X-rays absorption spectrum of $CoAl_2O_4$ indicating the pre-edge, edge, near-edge, and EXAFS region (after Fay et al., 1988[134]).

- $E < E_b$ (E_b: energy at the edge jump), which is referred as the pre-edge region when E is ~ 2-50 eV below the main absorption edge. No significant absorption phenomena occur in this region, except for those caused by localized electronic transitions to unfilled (or partially-filled) atomic levels. Processes other than photoelectron production are also feasible in this region.

  The transition probabilities and intensity of pre-edge features are partly determined by the symmetry of the ligands surrounding the absorber. Additionally, these features may provide information of the absorber's oxidation state, the site geometry of the absorber, and absorber-ligand bonding.

- $E \approx E_b$, referred as edge region (from ~ 2 eV below to ~ 2 eV above the absorption edge). Electronic transitions occur with high probability from the core level to unoccupied bound states or continuum states.

- $E \geq E_b$, defined as the near edge region (~ 2 to 50 eV above the edge). Low-energy photoelectrons are strongly scattered and multiple scattering is thought to dominate[145]. The resulting features are intense, and arise from strong multiple scattering of photoelectrons with moderate kinetic energy from atoms surrounding the absorber. These features give rise to information about interatomic distances and angles.

[145] Bianconi, A. *In EXAFS and Near Edge Structure*, Bianconi, A.; Inococcia, L.; Stipcich, S. (eds.), Springer-Verlag, Berlin, 1983, pp. 118-129

- $E > E_b$, sometimes referred as EXAFS region (from ~ 50 eV to ~ 1000 eV above the edge). Electronic transitions occur with low probability and the excited photoelectrons remain in the sample for a short time with an excess of kinetic energy $E_k = E - E_b$. EXAFS region can be analysed to obtain information about the distance between the absorber and the neighbouring atoms, extending out to several shells of ligands. The number and type of backscatterers can be also assessed through the analysis of this region. The frequency of EXAFS oscillations is inversely related to average absorber-backscatterer distance, and the amplitude of the oscillations is directly related to the number of backscattering ligands. This chemical selectivity makes XAS-derived distances unique against other direct structural methods based on scattering, which typically yield distances from all atom pairs.

1.8.5 X-ray Absorption Near Edge Structure (XANES)

XANES spectrum embraces the energy region defined from the pre-edge to ~ 50 eV above the absorption edge. Therefore, both features caused by electronic transitions to empty bound states and multiple-scattering resonances of the photoelectrons ejected at low kinetic energy are considered by this technique. The former can be used as spectroscopic probes of the local crystal chemistry of the absorber (oxidation state, site symmetry), whereas multiple-scattering features (due to scattering of continuum electrons) provide information about the first coordination shells around the absorber. At low kinetic energy, elastic multiple-scattering processes are dominant, whilst with the increase of photoelectron energy, the single-scattering regime of the EXAFS oscillations gain importance.

The main edge and pre-edge absorption features are essentially unaffected by the matrix in which the transition element complex occurs, but only depends on the geometry and bonding of the nearest neighbour environment and the oxidation state of the element. In ionic bonds, a shift of the position of edge features to higher energies is observed as metal becomes more oxidized. Hence, in general terms, a difference of one unit in the oxidation state is related to a shift of ~ 5 eV in the main edge and about 1-3 eV in the pre-edge features. This fact is due to the electronic charge removed from the cell of the metallic ion, which is related to the increase of its formal valence and the electronegativity of the ligands. Likewise, the variation of coordination and covalence of metal-ligand bonding also affects the intensity of the pre-edge; for instance, tetrahedral-coordinated metal ions have more intense pre-edge features than the octahedral -coordinated metal ions.

The analysis of the XANES region requires high energy resolution due to the small energy differences existing between pre-edge and main-edge features (even lower than 1 eV). Several factors affect this resolution, including source size, beam collimation, choice of monochromator crystal reflecting plane (high index diffraction planes imply high resolution), width of the rocking curve of the monochromator crystal, and finite core-hole lifetime of the absorbing element. All these factors but the finite core-hole lifetime can be controlled experimentally. The core-hole lifetime increases regularly and rapidly with increasing atomic number Z for a given electronic level[146].

The resulting resolution level of the experiment is an addition of these factors. A good approach to achievable energy resolution with a monochromator crystal of spacing d is given by:

$$\Delta E / E = 2.12 r_0 \frac{2d^2}{2\pi(1+n)^2} \qquad \textbf{Eq. 1.22}$$

where r_0 is the electron radius and n is the order of the harmonic present in the beam.

1.8.5.1 Analysis of the XANES spectrum

Data treatment is one of the most critical points of the process for both XANES and EXAFS techniques. In this concern, a few commercial programs are available, although in all cases the expertise of the analyst is of the utmost importance. As stated in section 1.8.4.2, the study of the intensity, shape, and position of pre-edge features provides indirect information about the symmetry of the absorber environment and its oxidation state, as well as direct information about the bonding between absorber and first-neighbour ligands.

The features of a XANES spectrum can be interpreted in terms of multiple scattering from atoms in the first several coordination shells around the absorber, yielding information about interatomic distances and angles. In these terms, XANES has been widely utilized as a speciation technique.

Given the complexity of the theoretical approach to phenomena occurring in the XANES region, speciation concept in XANES is usually based on the comparison of an unknown spectrum with a database of reference spectra. The fitting process looks for the best linear combination of the latter able to appropriately reproduce the unknown spectrum.

[146] Kostroun, V.O.; Cehn, M.H.; Crasemann, B. Physical Review A, **1971**, *3*, 533-545

The main steps required for the appropriate data treatment are briefly described below. It should be highlighted that the order of the steps is not always critical, whereas not all steps described are strictly necessary for the correct analysis of the data.

1. Critical review of spectra and average of raw data. A first visual review of the raw data is recommended, in order to identify deficiencies on the quality of data and to correct possible experimental problems. If the spectra have been taken in fluorescence mode, the signal of each pixel should be also averaged.

2. Calibration of the energy scale. XANES analysis is based on the comparison between different spectra. Therefore, slight deviations of energy occurring during the experiment may lead to significant errors in the data evaluation. On the other hand, XANES is insensitive to the absolute calibration of the monochromator[133]. For instance, slight misalignments of the monochromator zero point, will be offset to a good approximation by a simple change in edge energy.

Energy calibration is normally achieved by following the first derivative of the spectrum from a reference sample. The first maximum in the derivative spectrum is usually chosen as the edge position, which is compared with tabulated values. If a difference exists, a shift in the energy scale of the reference and unknown spectra is applied. It is also possible to calibrate the edge position simultaneously with the measurement of the XANES spectra by introducing a reference compound before a third ion chamber (see Figure 1.22).

3. Deglitching. This step involves removing "glitches" or sharp features from the raw spectrum, usually resulting from spurious reflections of the X-rays beam by the monochromator crystal at certain energies. Normally, deglitching is achieved by fitting a polynomial function between both sides of the glitch. For this technique to work, glitches must be narrow compared with any feature of interest in the data.

4. Deadtime corrections. Deadtime refers to the time required by the amplifier to recover after the count of an incident photon. If another photon arrives during this period, the deadtime is extended again and the photon is not counted. Therefore, this effect becomes important when high incoming fluxes reach the detector and lead to a significant number of missed events. Under these circumstances, fluorescence measurements should be avoided. Deadtime effects can be an important source of amplitude loss in XAS spectra collected with solid state detectors. Nevertheless, these effects can be generally compensated by collecting the response curve for detector deadtime. This curve corresponds to the relationship between

the windowed counts for the flourescence line being monitored (SCA) and the total incoming count rate (ICR) for each of the elements in the detector array.

5. Pre-edge and post-edge absorption background correction (see Figure 1.25b). This step aims at obtaining an independent signal from the monitored element. This goal is achieved by removing from the experimental spectrum the effects of other atoms in the sample, as well as the effect of other electron shells of the absorbing atom. The main correction corresponds to the subtraction of the signal from the isolate atom ($\mu_0(E)$) to the sample signal ($\mu(E)$):

$$\chi(E) = \frac{\mu(E) - \mu_0(E)}{\mu_0(E)} \qquad \textbf{Eq. 1.23}$$

Nevertheless, the value of $\mu_0(E)$ is hardly determined experimentally. Therefore, the usual correction process relies on the fitting of polynomial functions, which are later on subtracted to the original spectra. Normally, the fitting of the pre-edge region is achieved by a smooth polynomial function, whereas the fitting of the post-edge region is carried out with a cubic polynomial spline function. A cubic spline is a curve build up by several linked cubic polynomials; the function value and first derivative match at the "knots" where the polynomials meet. The number of knots is variable and depends on the particular data, although typical values range from 2 to 6. A reduced number of knots might not completely remove the background, whilst a too large number may lead to overadjustments of the spectra and the consequent reduction of spectra original features. The definition of the different regions, order of polynomials and choice of weights is a complex procedure which usually takes place interactively.

6. Edge normalization. This step basically removes the effects of sample thickness and concentration of the target element, in order to allow the direct comparison of different samples. Usually, the X-rays absorption coefficient is normalized by the following equation:

$$\chi(E) = \frac{\mu(E) - \mu_b(E)}{\mu(E_i)} \qquad \textbf{Eq. 1.24}$$

where $\mu_b(E)$ is the background absorption coefficient and $\mu(E_i)$ the absorption coefficient at an energy close the edge so that Eq. 1.24 represents data normalized to the edge step. In this way, original spectral data are transformed to normalized $\chi(E)$ data to overcome the mentioned sample differences.

7. Principal component analysis (PCA). This option can be used to mathematically decompose a set of data files into the minimum number of components needed to describe the

variance in the data. These principal components are mathematically sufficient to reconstruct each of the experimental spectra by any linear combination. Consequently, the remaining components considered in the reference compounds database refer to the noise. The main outcome of this procedure is the determination of the number and type of reference compounds needed to describe the set of data files within the experimental error. Due to the complexity and importance of this step, a detailed discussion will be undertaken in the section 1.8.5.1.1 described below.

8. Least-squares fitting. This is the final step regarding speciation analysis, which consists of the fitting of standard reference compounds to the already corrected experimental data. The fingerprint adjustments are normally achieved by the minimisation of the least squares fitting between the sample spectra and a combination of reference spectra. The error of this adjustment can be calculated as a standard deviation for each fitting coefficient.

Additionally, an algorithm for the correction of fluorescence self-absorption can be applied. This phenomenon is caused by significant attenuation of the incident beam by the absorption of the photon generated in the same sample when high incoming fluxes are being measured. Nevertheless, in a number of data treatment software (i.e. IFEFFIT, WinXAS), this correction is performed in previous steps.

1.8.5.1.1 Principal component analysis[147-150]

When the evaluation of XAS spectra is performed by linear combination of standards spectra, the number and type of such standards can be determined by principal component analysis (PCA). This tool becomes especially useful in environmental analysis, where the use of a large number of standard spectra in the fitting procedure may easily lead to overadjustments without any realistic analytical meaning.

The PCA procedure is based on the singular value decomposition (SVD) algorithm in linear algebra, which states that any $m \times n$ matrix **A** can be expressed (decomposed) as the product of an $m \times n$ column-orthogonal matrix **E**, an $n \times n$ diagonal matrix **V** with positive or zero elements, and the transpose of an $n \times n$ orthogonal matrix **w** (Eq. 1.25). In practice, each

[147] Ressler, T.; Wong, J.; Roos, J.; Smith, I. L. Environmental Science and Technology, **2000**, *34*, 950-958

[148] Beauchemin, S.; Hesterberg, D.; Beauchemin, M. Soil Science Society of America Journal**, 2002**, *66*, 83-91

[149] Rudolf, P.; Struis, W. J.; Ludwig, C.; Lutz, H.; Scheidegger, A.M. Environmental Science and Technology, **2004**, *38*, 3760-3767

[150] Sarret, G.; Balesdent J.; Bouziri L.; Garnier J.M.; Marcus M.A.; Geoffroy N.; Panfili F.; Manceau A. Environmental Science and Technology, **2004**, *38*, 2792-2801

column vector in matrix **A** represents an experimental XAS spectrum, whilst there are *n* unknown spectra in the data set to be analyzed, each containing *m* data points. The columns of the output matrix, **E**, are the eigenvectors, and the diagonal elements of the **V** matrix are the corresponding eigenvalues. Each eigenvector represents an independent abstract component or source of variation affecting the experimental spectra of the data matrix, whereas the associated eigenvalues determine how many of such components are sufficient to reproduce the experimental XAS spectra: the number of principal components. Therefore, the number of compounds present in unknown sample has to be equal or smaller than the number of analyzed spectra.

$$\begin{bmatrix} x_{11} & x_{12} & \cdot & x_{1n} \\ a_{21} & a_{22} & \cdot & a_{2n} \\ n_{31} & n_{32} & \cdot & n_{3n} \\ e_{41} & e_{42} & \cdot & e_{4n} \\ \cdot & \cdot & \cdot & \cdot \\ \cdot & \cdot & \cdot & \cdot \\ \cdot & \cdot & \cdot & \cdot \\ s_{m1} & s_{m2} & \cdot & s_{mn} \end{bmatrix} = \begin{bmatrix} E_{11} & E_{12} & \cdot & E_{1n} \\ i_{21} & i_{22} & \cdot & i_{2n} \\ g_{31} & g_{32} & \cdot & g_{3n} \\ e_{41} & e_{42} & \cdot & e_{4n} \\ \cdot & \cdot & \cdot & \cdot \\ \cdot & \cdot & \cdot & \cdot \\ \cdot & \cdot & \cdot & \cdot \\ n_{m1} & n_{m2} & \cdot & n_{mn} \end{bmatrix} \bullet \begin{bmatrix} v_{11} & 0 & \cdot & 0 \\ 0 & v_{22} & \cdot & 0 \\ \cdot & \cdot & v_{n} & \cdot \\ 0 & 0 & \cdot & v_{mn} \end{bmatrix} \bullet \begin{bmatrix} w_{11} & w_{12} & \cdot & w_{1n} \\ w_{21} & w_{22} & \cdot & w_{2n} \\ \cdot & \cdot & \cdot & \cdot \\ w_{n1} & w_{n2} & \cdot & w_{nn} \end{bmatrix}$$

$$[A] = [E] \bullet [V] \bullet [w]^{t}$$

Eq. 1.25

The output of SVD algorithm can now be utilized to determine whether a particular vector **T**, representing the compounds used as standards, lies within the vector subspace spanned by the eigenvectors or principal components. This procedure is known as target transformation, which results from the multiplication of a column matrix **E** containing the eigenvectors, the transpose of this matrix, and the vector **T** (Eq. 1.26). If **T*** and **T** are identical within experimental errors, the vector **T** is included in the vector subspace and is a principal component of the input vector set that is given in the column vectors of matrix **A**. Hence, this particular reference compound is a probable species in the unknown mixture.

$$\begin{pmatrix} T_1^* \\ e_2^* \\ s_3^* \\ t_4^* \\ \cdot \\ \cdot \\ \cdot \\ v_m^* \end{pmatrix} = \begin{bmatrix} E_{11} & E_{12} \\ i_{21} & i_{22} \\ g_{31} & g_{32} \\ e_{41} & e_{42} \\ \cdot & \cdot \\ \cdot & \cdot \\ \cdot & \cdot \\ n_{m1} & n_{m2} \end{bmatrix} \bullet \begin{bmatrix} E_{11} & i_{21} & g_{31} & e_{41} & \cdot & \cdot & \cdot & n_{m1} \\ E_{12} & i_{22} & g_{32} & e_{42} & \cdot & \cdot & \cdot & n_{m2} \end{bmatrix} \bullet \begin{pmatrix} T_1 \\ e_2 \\ s_3 \\ t_4 \\ \cdot \\ \cdot \\ \cdot \\ v_m \end{pmatrix}$$

$$(T^*) = [E] \bullet [E]^{t} \bullet (T)$$

Eq. 1.26

1.8.6 Extended X-ray Absorption Fine Structure (EXAFS)

EXAFS refers to the absorption coefficient (μx) modulation found along a few hundred eV beyond the absorption edge. Although the fine structure had been discovered long time ago, the EXAFS theory remained relatively unknown until beginning of the 70s[151], when Sayers and co-workers[137] introduced the Fourier transform as a quantitative tool for structure determination. As a consequence, the demand for performing EXAFS measurements grew very rapidly from 1975 to 1980 and still keeps growing nowadays.

The general aspects of EXAFS spectroscopy have been presented in a number of review papers and books[132,152-154], as well as its applications to mineralogical and geochemical problems[155-157], among others. Therefore, only some basics on this spectroscopy will be presented here. The reader is referred to the abovementioned reviews for more detailed information.

The absorption of the X-rays is given quantum mechanically by a matrix element between the initial and final states[133]. In the EXAFS case, the initial state corresponds to the electron in the atomic core, whereas the final state is the electron excited to the escaping photoelectron. Quantum mechanically, photoelectron must be considered as a wave, whose wavelength is given by the de Broglie equation:

$$\lambda = \frac{h}{p} \qquad \textbf{Eq. 1.27}$$

where p is the momentum of the photoelectron and h is Planck's constant. In the EXAFS regime p can be determined by the free electron relation:

$$\frac{p^2}{2m} = h\nu - E_0 \qquad \textbf{Eq. 1.28}$$

---

[151] Azaroff, L.V.; Pease, D.M. *X-Ray Spectroscopy*, Chap. 6, McGraw-Hill, New York, 1974

[152] Lee, P.A.; Citrin, P.H.; Eisenberger, B.M. Reviews of Modern Physics, **1981**, *53*, 769-806

[153] Stern, E.A.; Heald, S.M. *Basic principles and applications of EXAFS*, in: *Handbook on Synchrotron Radiation*, Koch, E.E. (ed.), Vol. 1b, New York, 1983, pp. 995-1014

[154] Teo, B.K. EXAFS: basic principles and data analysis, in: Inorganic Chemistry Concepts 9, Springer-Verlag, New York, 1986, pp.1-349

[155] Waychunas, G.A.; Brown Jr., G.E. Application of EXAFS and XANES spectroscopy to problems in mineralogy and geochemistry, in: EXAFS and Near-Edge Structure III, Hodgson, K.O.; Hedman, B.; Penner-Hahn, J.E. (eds.), Springer Proceedings in Physics, Vol. 2, Springer-Verlag, New York, 336-342

[156] Brown Jr., G.E.; Waychunas, G.A.; Ponader, C.W.; Jackson, W.E.; McKeown, D.A. Journal de Physique, **1986**, *47*, 661-668

[157] Calas, G.; Brown Jr., G.E.; Waychunas, G.A.; Petiau, J. Physics and Chemistry of Minerals, **1987**, *15*, 19-29

where the photon of frequency ν has an energy hν and E_0 is the binding energy of the photoelectron, being m the electron mass.

For an isolated atom, the photoelectron can be represented as an outgoing wave (solid lines in Figure 1.24). The neighbouring atoms will scatter this wave (dashed lines in Figure 1.24) and the constructive and destructive interferences between both the outgoing and backscattered photoelectrons will produce the so-called fine structure.

As the energy of the photoelectron varies, its wavelength varies as indicated in Eqs. 1.27 and 1.28, consequently modifying the relative phase between outgoing and backscattered waves. How the phases vary depends also on the type of backscatterer, as well as on the distance between the centre and backscattering atoms. Therefore, the variation of the fine structure is a direct consequence of the wave nature of the photoelectron.

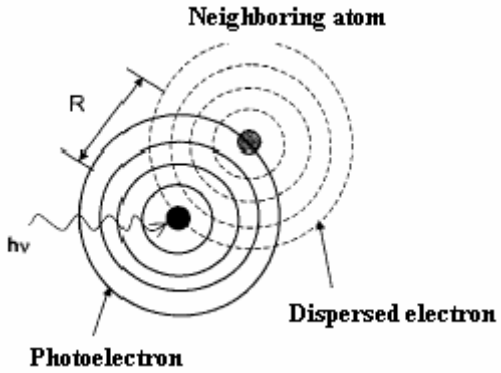

Figure 1.24 Schematic illustration of the single-scattering process in the EXAFS energy region.

In the following lines, the theoretical formulation of the EXAFS modulation will be developed. For this purpose, several simplifications are to be considered:

- the outgoing photoelectron has a kinetic energy large enough to be assumed as a free electron in the interatomic potential
- the process producing the oscillations is assumed to be a single-electron process
- only single scattering is considered. The photoelectron is ejected by the central atom, which is modelled using a simplified plane wave approximation, and backscattered only once at 180º by a neighbouring atom (single scattering). Multiple scattering is of low probability in this energy domain and is predominant only in the low-energy domain corresponding to the XANES region

As stated, EXAFS oscillations are due to interferences between the outgoing and the backscattered photoelectron. These interferences modulate the absorption coefficient because of the increase (constructive interference) or decrease (destructive interference) in the photoelectron's wave function along the energy region of the absorbing atomic orbital (initial state). EXAFS can be therefore defined as the function $\chi(E)$:

$$\chi(E) = \frac{\mu(E) - \mu_0(E)}{\mu_0(E)} \qquad \textbf{Eq. 1.29}$$

where $\mu(E)$ is the experimental absorption coefficient and $\mu_0(E)$ is the atomic contribution to the absorption coefficient, if no EXAFS structure was present. $\mu_0(E)$ cannot be measured experimentally because of the physical impossibility of isolating the atoms of the sample. Consequently, $\mu_0(E)$ has to be determined numerically[134]. This expression looks similar to Eq. 1.24, the one used in XANES to normalized data at the edge region, but the meaning of this transformation is different. In this case, it corresponds to the EXAFS function.

The first step when converting $\chi(E)$ to structural-related information consists of the conversion of the energy E into the modulus of the wave vector k ($Å^{-1}$) of the photoelectron. This conversion is achieved by means of Eq. 1.30:

$$k = \sqrt{\frac{2m(E - E_0)}{\hbar^2}} = \{0.262\,(E - E_0)\}^{1/2} \qquad \textbf{Eq. 1.30}$$

where m is the mass of the electron, h is the Planck's constant, E is the kinetic energy of the photoelectron and E_0 is the energy of the photoelectron at k=0. E_0 is generally a function of distance and should therefore vary from shell to shell[158].

Once in the space k, the general formulation of the EXAFS modulations (Eq. 1.31) consists of a theoretical expression that describes $\chi(k)$ in terms of structural parameters.

$$\chi(k) = -1/k \sum_j A_j(k) \sin\left[2kR_j + \phi_j(k)\right] \qquad \textbf{Eq. 1.31}$$

Strictly speaking, this EXAFS equation is valid only for K edges; however, it adequately describes L_{III} edges within experimental error[159].

The EXAFS function is a superposition of the individual sinusoidal photoelectron scattering contributions by atoms in a number of coordination shells, where j refers to the jth shell. R_j is

[158] Rehr, J.J.; Stern, E.A. Physical Review B, **1976**, *11*, 4413-4419

[159] Teo, B.K.; Lee, P.A. Journal of the American Chemical Society, **1979**, *101*, 2815-2832

the average distance from the absorbing atom to the backscattering atom(s) in the jth coordination shell. ϕ_j (k) is the phase shift, defined as the sum of the photoelectron phase shifts contributions from the absorbing and backscattering atoms. The phase shift is created by the central atom and backscattering atoms potential and depends on the nature of the atom (e.g. the magnitude of phase shifts increases with increasing Z) as well as the value of k (e.g. the phases of the absorber always decrease monotonically with increasing k[135]). Finally, A_j is the amplitude function for the jth shell, which primarily depends on the type of backscattering atoms, and is defined as:

$$A_j(k)= (N_j/R_j^2)\, f_j(\pi,k)\, S_0^2(k)\, \exp(-2R_j/\lambda)\, \exp(-2\sigma_j^2k^2) \qquad \textbf{Eq. 1.32}$$

where N_j is the average number of backscattering atoms in the jth shell, $f_j(\pi,k)$ is the backscattering amplitude characteristic of a particular type of coordination atom and dependent on k. Hence, for low-Z atoms, $f_j(\pi,k)$ is large at low k, whilst decreasing rapidly with increasing k. As Z increases, a maximum appears at intermediate k values, being the position of the amplitude maximum at higher k values as Z of the backscatterer increases[133]. $S_0^2(k)$ is an amplitude reduction factor due to many-body relaxation effects of the absorbing atom and multielectron excitations such as shake-up and shake-off processes of the passive electrons (electrons not directly excited by the X-rays) at the *L*-edges. Typically, it ranges between 0.7 and 0.8[160,161]. There exist both theoretical[161] and experimental evidences[162,163] that the variation of S_0^2 with chemical environment is not important; thus, the tabulated atomic values of S_0^2 can be used as a reasonable approximation.

The term $\exp(-2R_j/\lambda)$ accounts for inelastic losses in the scattering process. The parameter λ is the photoelectron mean free path, which is due to the finite core hole lifetime and the interactions with the valence electrons[133]. This term shows a decreasing probability of excitation with increasing photoelectron energy in the high energy regime[160]. For the first shell, the S_0^2 and the backscattering energy loss include most of the energy losses.

The last term includes the Debye-Waller factor σ_j, which accounts for the effect of disorder. This factor measures the mean square deviation of the absorber-scatter interatomic distance

[160] Carlson, T.A. *Photoelectron and Auger Spectroscopy*, Chap. 3, Plenum Press, New York, 1975

[161] Rehr, J.J.; Stern, E.A.; Martin, R.L.; Davidson, E.R. Physical Review B, **1978**, *17*, 560-565

[162] Stern, E.A.; Bunker, B.; Heald, S.M. Physical Review B, **1980**, *21*, 5521-5531

[163] Stern, E.A.; Heald, S.M.; Bunker, B. Physical Review Letters, **1979**, *42*, 1372-1375

from its average length, whilst having two main contributions: a static (typical in glasses or melts with highly coordinated, weakly bounded elements) and a thermal (or vibrational) term:

$$\sigma^2 = \sigma^2_{static} + \sigma^2_{vibrational} \qquad \textbf{Eq. 1.33}$$

The term $\exp(-2\sigma_j^2 k^2)$ assumes that vibrational motion is harmonic and that static disorder is Gaussian[164,165]. Thus, for systems with large disorder ($\sigma \geq 0.1$ Å) either due to an asymmetric pair distribution function or to an anharmonic vibrational potential, the term is not valid[166], and an asymmetric pair distribution function must be used to approximate structural disorder.

When carrying out EXAFS studies of atoms with weak bonds (i.e., large ν), it is recommended to also analyse at low temperatures in order to reduce $\sigma_{vibrational}$. Large disorder effects can lead to a reduction of EXAFS amplitude and the derived coordination numbers[167], as well as to an apparent contraction in the nearest-neighbour distances[166,168,169] (as large as 0.15 Å).

Despite the already mentioned exceptions, it can be concluded that equation 1.29 provides an adequate model for EXAFS in most cases. The use of this equation permits to derive structural parameters from an unknown substance, once certain parameters are known. Among these parameters, the total phase shift (ϕ_j (k)) and amplitude (A_j(k)) functions can be extracted either from known reference (or model compounds) or calculated for free atoms using some approximations. During the last decade, very efficient computer codes, as EXCURVE[170], FEFF[171,172] and GNXAS[173], have substantially improved the XAFS data analysis eliminating the need for tabulated phase shifts.

1.8.6.1 Analysis of the EXAFS spectrum

Analysis of EXAFS data can be classified in the basis of the final aim of the study[133]:

[164] Greegor, R.B.; Lytle, F.W. Physical Review B, **1979**, *20*, 4902-4907

[165] Bohmer, W.; Rabe, P. Journal of Physics C, **1979**, *12*, 2465-2474

[166] Eisenberger, P.; Brown, G.S. Solid State Communications, **1979**, *29*, 481-484

[167] Eisenberger, P.; Lengeler, B. Physical Review B, **1980**, *22*, 3551-3562

[168] Crozier, E.D.; Seary, A.J. Canadian Journal of Physics, **1980**, *58*, 1388-1399

[169] de Crescenzi, M.; Antonangeli, F.; BVellini, C.; Rosei, R. Solid State Communications, **1983**, *46*, 875-880

[170] Binsten, N.; Campbell, J.W.; Gurman, S.J.; Stephenson, P.C. *EXCURVE*, SERC Daresbury Laboratory, Worringten, UK, 1991

[171] Rehr, J.J.; Mustre de Leon, J. ; Zabinski, S.I. ; Albers, R.C. Journal of the American Chemical Society, **1991**, *113*, 5136-5140

[172] Rehr, J.J.; Albers, R.C. Reviews of Modern Physics, **2000**, *72*, 621-654

[173] Filipponi, A.; Di Cicco, A.; Natoli, C.R. Physical Review B, **1995**, *22*, 15122-15134

- Fingerprint adjustments, where the spectrum of an unknown sample is compared with the spectra of the selected reference compounds (normally a linear combination of these spectra). Chemical speciation can be therefore assessed, if proper reference compounds have been selected.
- Identification of the bonding configuration or valence state of the absorbing atom, achieved through the frequency of the oscillations. Usually, these experiments are performed on biological or disordered systems that have an isolated first shell.
- Assessment of structural information: coordination numbers, bonding distances, definition of neighbouring atoms. This information is obtained through the use of several shells of the EXAFS data.

A similar procedure is applied to undertake fingerprint adjustments both in the XANES and EXAFS regions (see section 1.8.5.1). On the other hand, and despite sharing several steps with fingerprint adjustments, the assessment of structural information requires further data treatment.

Hence, first steps basically consist of pre and post-edge removal and background normalisation, as previously described in section 1.8.5.1 (steps 1-6). Further steps needed are shallowly reviewed in the following lines:

7. Definition of E_0. As mentioned above, E_0 is normally experimentally defined by considering the first maximum in the first derivative spectrum of the absorption edge. However, E_0 is often incorrectly defined due to experimental deviations, resulting in important errors in the phase shift function, especially at low k values. This problem is generally handled by analysing well-characterized, crystalline model compounds, where E_0 is an adjustable parameter. Additionally, E_0 can be also adjusted to an optimum value by following the method suggested by Lee and Beni[174], which involves shifting E_0 until the maxima of the imaginary and real (modulus or absolute value) parts of the Fourier transform coincide. This procedure assures that the absolute phase is correctly given.

8. Conversion of the energy to the k-space, according to equation 1.30 (see Figure 1.25d). In this point, data is commonly multiplied by the weighting function k^n (n typically chosen between 1-3), which aims at compensating for amplitude reduction. In order to separate the

[174] Lee, P.A.; Beni, G. Physical Review B, **1977**, *15*, 2862-2883

different shells in the next step, it is advisable to have a signal of almost equal amplitude in the whole k range.

9. Fourier transformation of χ(k), which produces a radial distribution function (rdf) (Figure 1.25e). This is the most accurate method for deriving structural parameters from EXAFS oscillations. The Fourier transformation of the experimental spectrum is given by the following function:

$$F.T.\left[k^n \cdot \chi(k)\right] = (2\pi)^{-1/2} \int_{k_{min}}^{k_{max}} k^n \chi(k) W(k) e^{2ikR}\, dk \qquad \textbf{Eq. 1.34}$$

where W(k) is the window function of the Fourier transform. By selecting a k range, this function minimizes parasitic oscillations of the Fourier transform without eliminating the distance information at low and high k (the larger the k-range considered is, the narrower the peaks in the rdf are). The Hanning function is a commonly used window function, which is defined as:

$$W(k) = 1/2\{1 - \cos 2\pi[(k - k_{min})/(k_{max} - k_{min})]\} \qquad \textbf{Eq. 1.35}$$

In the Hanning function, W(k) is equal to 0 at $k=k_{min}$ and $k=k_{max}$, whilst the lower k-space limit is generally taken as 3 $Å^{-1}$. This selection is related to the use of the single-scattering approximation, as this approximation is not valid at lower wave vector values where multiple scattering dominates.

Equation 1.34 transforms the EXAFS function from k-space (or frequency space) to real space (or distance), producing a pair correlation function where peaks correspond to average absorber-backscatterer distances. Nevertheless, each peak is shifted a distance α, which is relatively constant for a given absorber-backscatterer pair and normally ranges between 0.2 and 0.5 Å[131]. The width of a peak indicates the range of radial distances and the static or thermal disorder, being both higher with wider peaks.

10. Inverse Fourier transformation. Data extracted from each single-shell are transformed individually back to the k-space (see Figure 1.25f). The isolation of the EXAFS contribution from a selected region in distance space (R range) permits to obtain the structure-dependent parameters relative to this distance. Hence, a peak in the Fourier transform is isolated by an appropriate window, and the inverse Fourier transform of this peak gives the contribution of this isolated shell to the EXAFS. This procedure is commonly termed “Fourier filtering”. The inverse transform uses both the real and imaginary parts of the rdf and produces a complex

function from which the total phase and amplitude can be obtained. The inverse transform is very sensitive to the choice of the window size and position. If too small, the amplitude and phase will be artificially constrained: the phase will appear more linear than it is and the amplitude will smooth, leading to incorrect determination of Debye-Waller factors and coordination numbers. Additionally, it is important to highlight that two or more peaks appearing very close in the R-space might be preferably transformed together to the k-space, in order to perform the fitting approach of the entire region[132].

The experimental, filtered spectrum is handled with specific computer codes or compared with a model compound, if the latter is close in structure and chemical state to the system to be analysed. Values of the various parameters are adjusted in the simulated EXAFS spectrum (by least-square fitting) until the acceptance threshold is reached. If more than one atom type is contributing to a given shell, either real or imaginary part of the transform (Eq. 1.34) may use to achieve conclusive information. This can be understood if considering that the phases of different atoms are linearly combined in the real and imaginary part but not in the magnitude of the Fourier transform[132].

11. Least-squares fitting of the analytical EXAFS expression. The EXAFS function produced is fitted, yielding average distance, coordination number, E_0, and Debye-Waller factor for the absorber-backscatterer shell. The number of free parameters, N_{free}, that might be properly determined by the fit is given by the ratio of the window width, Δr_W, and the resolution in Fourier space $(k_{max}-k_{min})^{-1}$:

$$N_{free} \leq 2/\pi \, \Delta r_W (k_{max}-k_{min})^{-1} \qquad \textbf{Eq. 1.36}$$

The fitting process through least-squares is driven until the acceptance threshold limit is reached. Usually, this threshold is fixed at S^2 improvements lower than 1%, where S^2 is the sum of the squares of the residuals:

$$S^2 = \sum_i^n (\chi_i^T - \chi_i^E)^2 \qquad \textbf{Eq. 1.37}$$

where χ_i^T and χ_i^E are the theoretically calculated and experimental EXAFS functions, respectively.

Summarising section 1.8.6.1, Figure 1.25 reviews the usual data treatment sequence in the analysis of EXAFS spectrum.

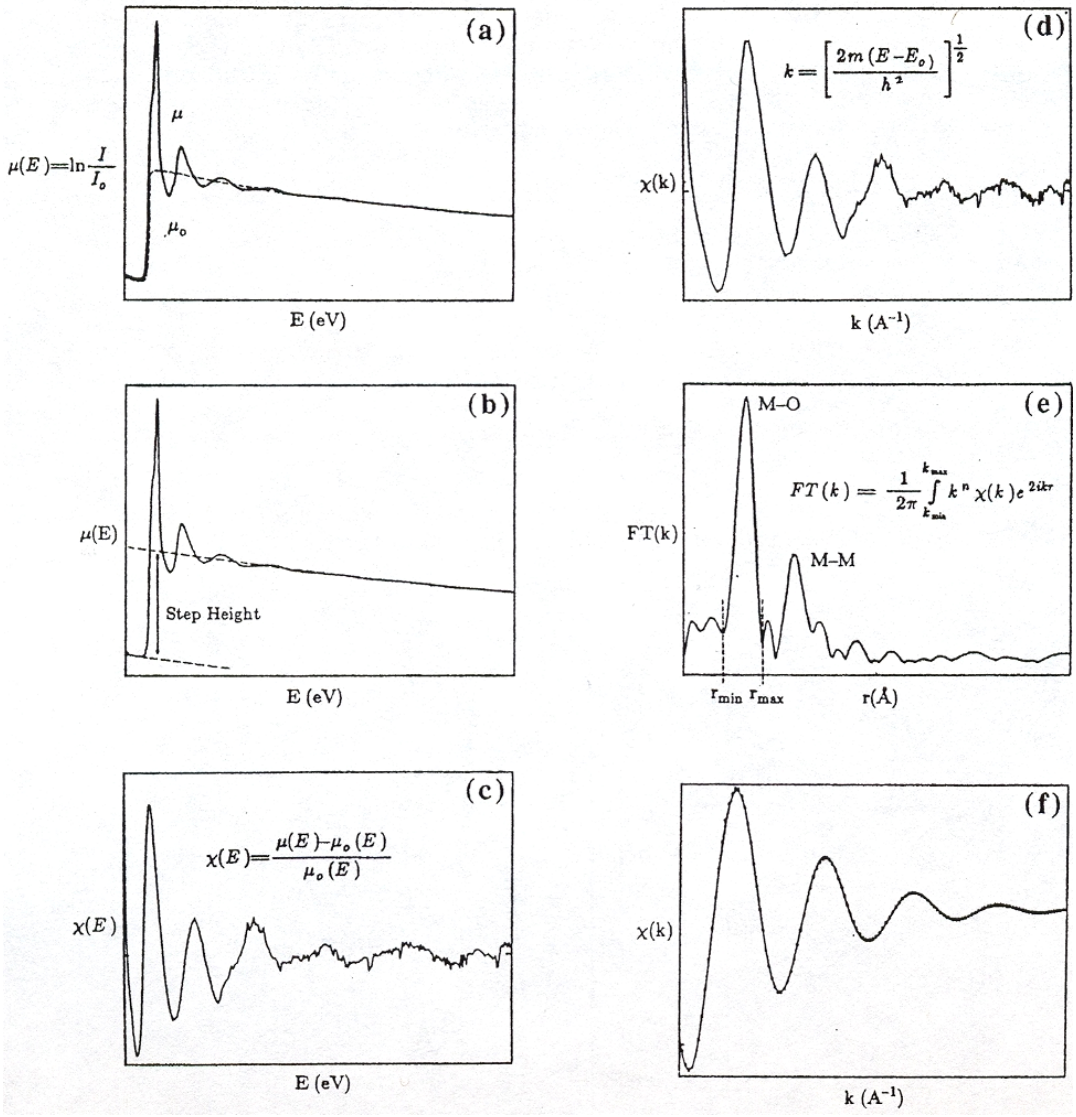

Figure 1.25 Steps in the analysis of an EXAFS spectrum: (a) raw spectrum showing the smooth background absorption; (b) fit of backgrounds to pre-edge and EXAFS regions and definition of step height or edge step; (c) the background-substracted EXAFS plotted as function of energy; (d) the background-substracted EXAFS plotted as function of wave vector k; (e) Fourier transform of (d) resulting in a radial distribution function. A Fourier filter window is defined by r_{min} and r_{max}; (f) back Fourier transform of the windowed peak in (e) over the filter range (after Brown et al., 1988[131]).

1.8.7 Microprobe techniques

Microprobe techniques are defined as those techniques able to deal with microscopic samples. In this sense, the concept of microprobe applied to X-rays absorption techniques is gaining importance in the study of microscopic environments.

Whilst usual beamspot size in bending magnets is about 2×2 mm^2, the size achieved at microprobe beamlines may reach values as low as 1×1 μm^2. The focussing of the beam can be performed by different means, depending on the source type, spot-size requirements and

budget limitations, among others. Up to now, curved mirrors and multilayers, single and multiple capillaries, as well as diffracting lenses have been the standard tools to achieve a small focal spot size[175]. Some of them have been shown to work as imaging devices, with considerable applications in X-rays microscopy and microanalysis. A shallow review of available focussing options together with the poly-capillary system used in this thesis work, is described as follows:

- **Poly-capillary system.** This focussing system is usually utilised in 2nd generation facilities, where the beam is passed through a confocal poly-capillary system. The poly-capillary approach permits to collimate beam cross sections down to 15×15 μm^2. Throughout the analysis, the sample is supervised with a long distance zoom microscope with a magnification of 40 to 1200x and CCD-camera with a resolution of 3 μm. The overall scheme of a beamline equipped with a poly-capillary system is shown in Figure 1.26.

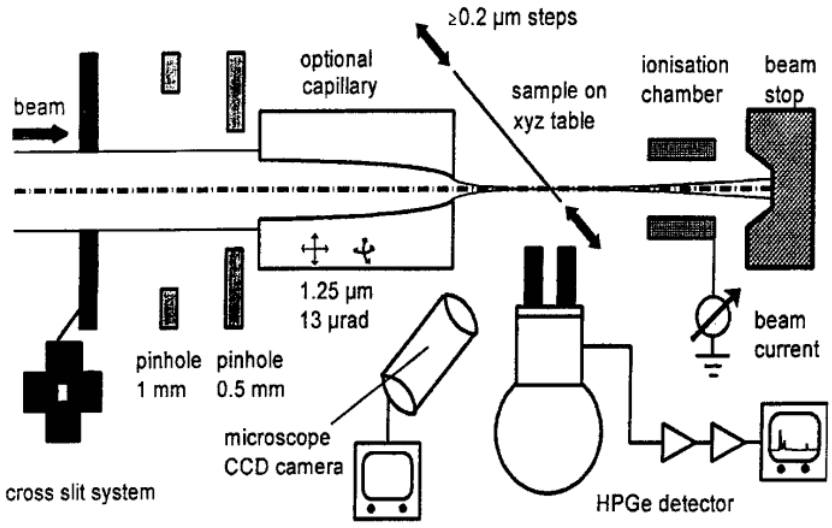

Figure 1.26 Synchrotron X-rays fluorescence microprobe setup (poly-capillary) at beamline L, HASYLAB[176].

- **K-B mirrors.** K-B mirrors have proven ability to focus beams to sub-micron dimensions, permitting a much higher scanning resolution to the existing scanning setup. Two orthogonal mirrors focus the beam successively in the horizontal and in the vertical planes (see Figure 1.27), based on specular reflection. The system can be

[175] Lengeler, B.; Schroer, C.G.; Richwin, M.; Tümmler, J.; Drakopoulos, M.; Snigirev, A.; Snigireva, I. Applied Physics Letters, **1999**, *74(26)*, 3924–3926

[176] Hamburger Synchrotronstrahlungslaborin (HASYLAB), [on-line], <http://www-hasylab.desy.de/>, [11 July 2006]

either static (optimised for a given incidence angle and focus) or dynamic. The latter holds bending flat mirrors into the elliptic shapes required by the experiment, which permit higher flexibility when dealing with an asymmetric source (as synchrotron sources). Figure 1.27 shown the overall scheme of a beamline equipped with K-B mirrors.

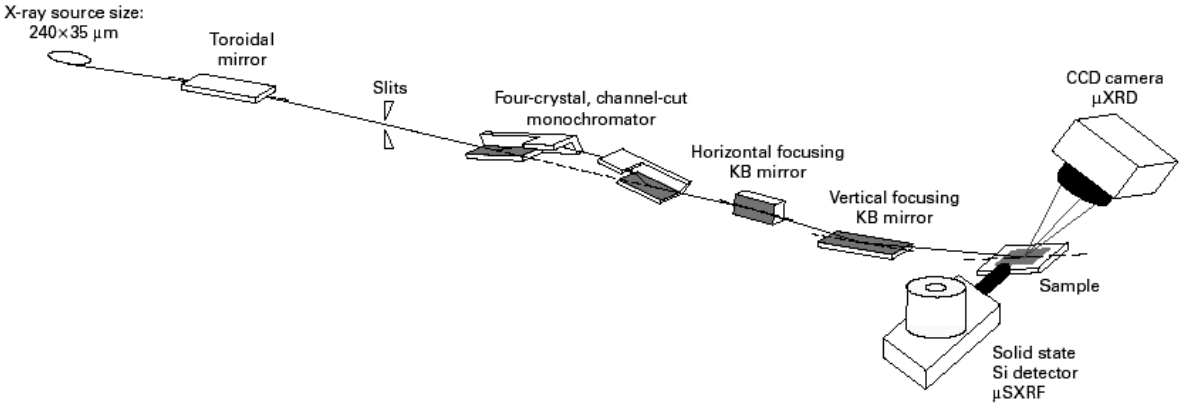

Figure 1.27 Schematic layout for X-rays microdiffraction experiments at beamline 7.3.3, Advanced Light Source (Berkeley)[177].

- **Refractive lenses.** X-rays lenses based on beam deviation by refraction, can be manufactured giving a focal length in the meter range and focal spot size in the micrometer range, determined by the de-magnification of the X-rays source. This system can withstand the full radiation (''white beam'') of a third generation source and might, therefore, be suited to be used together with future free-electron laser sources (see Figure 1.28). The lenses are mechanically robust and easy to align, since they work as inline devices and do not change the direction of the optical axis. Due to their parabolic shape, they are virtually free of spherical aberration. Same possibilities as glass lenses for visible light do also apply to lenses for the hard X-rays radiation.

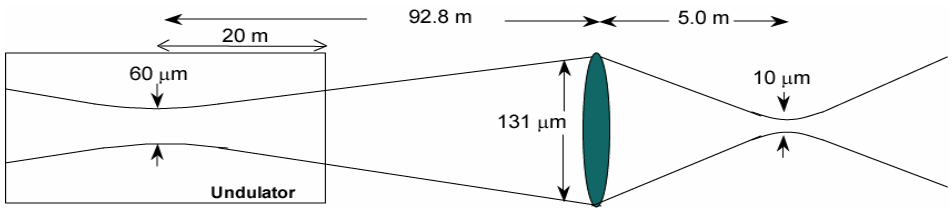

Figure 1.28 Refractive lens focusing to a spot of 10 μm needed for plasma experiments (after J. Arthur and W.W. Craig, 2002[178]).

[177] The Advanced Light Source (ALS), [on-line], < http://www-als.lbl.gov/>, [11 August 2006]

- **Fresnel optics.** X-rays Fresnel zone plate microfocusing optics with high spatial resolution and high focusing efficiency, have made possible the creation of a new tool for materials characterization on micron and submicron length scales[129,179]. In this system, the beam coherently illuminates the zone plate in the horizontal direction so that a horizontal spot size limited by the outermost zone width of the zone plate is obtained.

During the last decade, synchrotron-based microprobe techniques have become increasingly utilized to map elemental distributions by step-scan mode and simultaneous multi element trace analysis of microsamples. At the same time, both XANES and EXAFS techniques can be performed at each spot of the incident microbeam, therefore bridging their powerful speciation capacity to the spatial resolution at micro-scale.

1.8.8 Novel techniques and approaches for XAFS[180]

Recently, a range of novel techniques has emerged thanks to the use of High Energy Resolution Fluorescence Detection (HERFD). These techniques enhance the potential of XAFS experiments, as they are able to provide detailed electronic, magnetic and geometric information, even under extreme conditions.

One of the main advances concerning the use of HERFD detection methods is related to the more precise determination of the XANES spectrum, particularly of its pre-edge features. Hence, HERFD-XANES represents a very useful tool to study the empty electronic states with very high energy resolution (~0.3 eV). Even more interesting is the application of these tools for the study of environments under extreme conditions, i.e. the in-situ evaluation of nanoparticle-adsorbate interactions.

Additional tools include:

- **Valence selective XAFS.** Independent spectra for different valences in the same system can be obtained.

---

[178] John Arthur, SLAC & William W. Craig, LLNL, LCLS DOE Review, 2002, [on-line], <www-ssrl.slac.stanford.edu/lcls/doe_reviews/2002-04/april_2002_talk_finals/arthur_optics_22-apr-2002.ppt>, [11 August 2006]

[179] Lai, B.; Yun, W.; Xiao, Y.; Yang, L.; Legnini, D.; Cai, Z.; Krasnoperova, A.; Cerrina, F.; DiFabrizio, E.; Grella, L.; Gentili, M. Review of Scientific Instruments, **1995**, *66(2)*, 2287–2289

[180] Proceedings of the *13th International Conference on X-ray Absorption Fine Structure*, July 9-14, 2006, Stanford, California, USA

- **Site selective XAFS.** Independent spectra for only those metal atoms that bind to a specific ligand atom can be obtained (i.e. this can be used to discriminate nitrogen from oxygen ligands).
- **Energy range extension in XAFS measurements.** EXAFS experiments may be performed over a large k-range whilst avoiding edge-jumps rising at higher energies.
- **Local-spin-selective XAFS** to determine the 'spin-polarised' XANES.
- **Measurements of soft X-rays spectra** with hard X-rays to allow 3d metal L edge experiments under extreme conditions. This is particularly of interest to determine the detailed electronic structure under the conditions of a chemical reactor, fuel cell of battery system.

Time resolved X-rays absorption spectroscopy is becoming increasingly useful for the investigation of kinetic processes in chemical systems. Advances in synchrotron radiation sources and detector technology are lowering significantly the time resolution, currently reaching milliseconds to microseconds. Meanwhile, they have also gained in data acquisition quality, which makes feasible the identification of structural and electronic motifs characteristics of intermediate states in chemical processes.

1.9 OBJECTIVES

Taking into account the already described insights on mercury toxicity and bioavailability, as well as the proven capacity of XAS techniques for the analysis of samples at molecular scale, this PhD thesis aims at studying mercury speciation in different environmental and biological samples while assessing their influence on the specific behavior of mercury.

This main objective has been carried out by accomplishing the following more specific goals:

- Study of the interaction between mercury and two soils components: clays (kaolinite and montmorillonite) and humic acid. This objective embraced the assessment of the influence of pH on sorption capacity, whilst aiming at the coupling of conventional laboratory techniques with XAS speciation capacity and bioavailability studies through luminescent bacteria. Due to its very high toxicity, special attention was paid to methylmercury compounds (chloride and hydroxide).
- Application of the gained know-how to the study of highly Hg-impacted environments:
    - Assessment of mercury mobility and bioavailability in mine environments. Study of mercury distribution and speciation throughout mineral samples, mine soils and slag from the Almadén mine in Ciudad Real (Spain)
    - Characterisation of soils surroundings of a chlor-alkali plant. Assessment of mercury mobility and bioavailability
- Study of Hg behaviour in human teeth restored with dental amalgames. Application of microprobe technique to the assessment of diffusion processes and the study of molecular environment of Hg

Chapter 2

Experimental Methods

This chapter addresses a description of the most relevant methodologies and techniques used throughout this thesis, taking into account both XAS and conventional analytical procedures.

2.1. SAMPLING

2.1.1 Environmental samples

Two representative Hg-impacted environments have been considered within this PhD thesis, basically affected by anthropogenic activities:

Mining of Hg. A number of samples from the mining area of Almadén (Ciudad Real, Spain) were used for the study of Hg-impacted areas in mine environments. Both samples from Almadén and Almadenejos mines were considered (see Figure 1.6).

- Samples from the Almadén mine were collected at 10-20 cm depth using an Eijelkamp 04.15.SA undisturbed soil sampler device. Ore samples were randomly collected at the entrance of the oven, before their roasting. Soil samples were collected within the mine surroundings, whereas slag samples were taken at the exit of the oven, after 1h45' of ore treatment through the conveyor belt.
- Two calcine samples (AJ-701, AJ-702) were taken from the top of two old furnaces at the Almadenejos decommissioned plant (see Supporting Information, Annex 5).

Each sample was dried, milled with a pestle in an automatic agate mortar, and then homogenized and sieved under 100 μm. This process was considered to maintain unaltered Hg speciation. Although a few references have reported the influence of the grain size on the speciation, this parameter has not been considered within this study. Nevertheless, the proposed methodology aims to achieve representative data of the samples analyzed spite of grain heterogeneity.

Chlor-alkali plants with Hg-cathode. Five surface soil samples (M1-M5) were collected in the nearby of a chlor-alkali plant in the Netherlands. Thus, M1, M2, M3 and M4 were collected in the vicinity of the mercury cell and the mercury recycling unit (distillation) in the northern part of the site, whereas M5 was collected in the settling basins located at the southern end of the site. An overview of the physico-chemical characterisation of samples and site conditions is shown in Table 1, Annex 4. Shallow depth sampling of the soil materials was done by means of a hand-auger, and samples were kept in glass jars sealed by a rubber ring, protected against light. These samples were later split into several aliquots and sent in a polystyrene box in dry ice pellets to the analysis laboratory.

2.1.2 Biological samples

The study of Hg behaviour in human teeth restored with dental amalgam was accomplished by selecting sixteen human molar teeth from clinical offices. All samples contained the same type of metallic amalgam (high-copper, zinc-bearing alloys of admixed shape). Each sample was accompanied by a short description of the donor (see Table 2.1). After extraction, each tooth was rinsed and disinfected.

This study has taken advantage of the interdisciplinary collaboration with two dentistry research groups: the School of Dental Medicine of Buffalo University (Prof. Carlos Muñoz), and the Faculty of Odontology of University of Barcelona (Prof. Isabel Martínez). This collaboration is seeking for a better understanding of the dental materials as well as to improve the clinical assessment based on the appropriate knowledge of their behaviour.

Table 2.1 Characteristics of the teeth's donors for this study.

Tooth sample nº	1	2	3	4	5	6	7	8	9	10	11	12	13	14	15	16
Sex (M: male; F: female)	F	M	F	M	M	M	F	M	M	F	F	M	F	F	M	F
Age (years old)	22	62	58	55	53	58	56	68	47	n.a.	62	59	59	26	69	65
Time in mouth (years)	12	20	12	12	20	23	10	n.a.	n.a.	10	9	3	10	20	8	8

n.a.: non available

2.2 TOTAL METAL CONTENT DETERMINATION

Prior to synchrotron experiments, total metal content of environmental samples was determined. First step consisted of sample digestion, followed by the ICP-OES analysis of the related sample solution. A short description of both techniques as well as experimental conditions used is given in the following sections.

2.2.1 Analytical microwave system

Microwave-assisted extraction is a process consisting of heating the mixture of a solid sample and a solvent with microwave energy. The process achieves the correspondent partitioning of the elements of interest between the sample and the solvent. The technique uses a reduced amount of low-cost chemicals, shows a good efficiency and reproducibility, whilst being almost non-time consuming[78]. Therefore, it was considered as a suitable method for the

analysis of environmental samples. Further details on fundamentals of the technique can be found elsewhere[181].

Digestions were performed in perfluoroalcoxy (PFA) vessels with an Analytical Microwave system (MARS-5 model from CEM Corporation, USA). Two different methodologies were applied:

- Modified EPA method 3051[182]. Digestion of 0.5 g of sample with 9 ml of aqua regia (6 ml HCl, 2 ml HNO_3, 1 ml H_2O). This method is proposed for the microwave assisted acid digestion of sludges, sediments, soils and oils, whilst permitting the detection of up to 26 elements
- The second methodology aimed at developing a stronger digestion environment than EPA method 3051. This goal was achieved by the addition of hydrofluoric acid (HF) to the aqueous mixture[183]. Hydrofluoric acid is a non-oxidizing acid whose reactivity is based on its strong complexing nature. Therefore, it is commonly used in inorganic analysis because it can dissolve silicates. In this case, digestion proceeded by contacting 0.25 g of solid sample with a mixture of 10 ml aqua regia, 10 ml water and 4 ml hydrofluoric acid. As this methodology is not standardized, the certified material SRM 2710[184] was also analysed in order to assess the reliability of the digestion process.

The electrical power steps used in the digestion process of both methods are shown in Table 2.2.

[181] De la Guardia, M.; Salvador, A.; Burguera, J.L.; Burguera, M. Journal of Flow Injection Analysis, **1988**, *5*, 121-132

[182] EPA Method 3051 [on-line], <http://www.epa.gov/epaoswer/hazwaste/test/pdfs/3051.pdf>, [24 July 2006]

[183] Fernández-Martínez, R.; Rucandio, M.I. Analytical and Bioanalytical Chemistry, **2003**, *375*, 1089-1096

[184] Certificate of analysis standard reference material 2710 Montana soil (highly elevated trace element concentrations), National Institute of Standards & Technology, Gaithersburg, MD, 28 October 1997

Table 2.2 Microwave program for samples digestions with aqua regia and HF.

	Aqua regia digestion			HF digestion		
Step	1	2	3	1	2	3
Power (W)	100	100	100	50	100	100
Pressure (psi)	30	70	120	50	120	120
Time (min)	4	4	10	30	60	60
Time at pressure (min)	0	0	15	10	30	30

After digestion, vessels were cooled down to room temperature and the remaining solution filtered through 0.22 μm cellulose paper. Then, a few ml of $AuCl_3$ solution (1000 mg l^{-1}) were added in order to stabilize the Hg in solution. When dealing with HF digestion, the acid remaining in solution was neutralized with H_3BO_3.

Finally, the mixture was diluted with ultrapure water (Milli-Q) to a volume of 50 ml, and the final solution was then analysed by means of ICP-OES.

In order to avoid any memory effect, a cleaning step of the vessel was performed after each digestion. This step was carried out with an aqueous mixture of HNO_3 1:1 and the power program defined in Table 2.2.

2.2.2 Inductively Coupled Plasma-Optical Spectroscopy (ICP-OES)

After digestion, the concentration of Hg in the resulting aqueous solution was determined by means of ICP-OES. This technique is based on the atomization, ionisation and excitation of the sample through a plasma source[185], which forms when energy is transferred to a gas by means of an induction coil (Figure 2.1a). The metal ions enter into the plasma as an aerosol through a nebulization system, a spray chamber, and a desolvation system (Figure 2.1b). Argon is used as a carrier gas for the samples introduction. The emission of the elements in the sample occurs when sufficient thermal or electrical energy is available to excite a free atom or ion to an unstable energy state. This radiation is captured by a detector in a sequential or simultaneous way (depending on the instrument), and is able to control the different element emission through the wavelength selection[186].

[185] Moore, G.L. *Introduction to inductively coupled plasma atomic emission spectroscopy*, Elsevier Science Publishers, New York, 1989

[186] Thomas, P. Chemical Análisis of Contaminated Land, Thompson, K.C.; Nathanail, C.P. (eds.), Blackwell Publishing, U.S.A./Canada, 2003, pp. 64-95

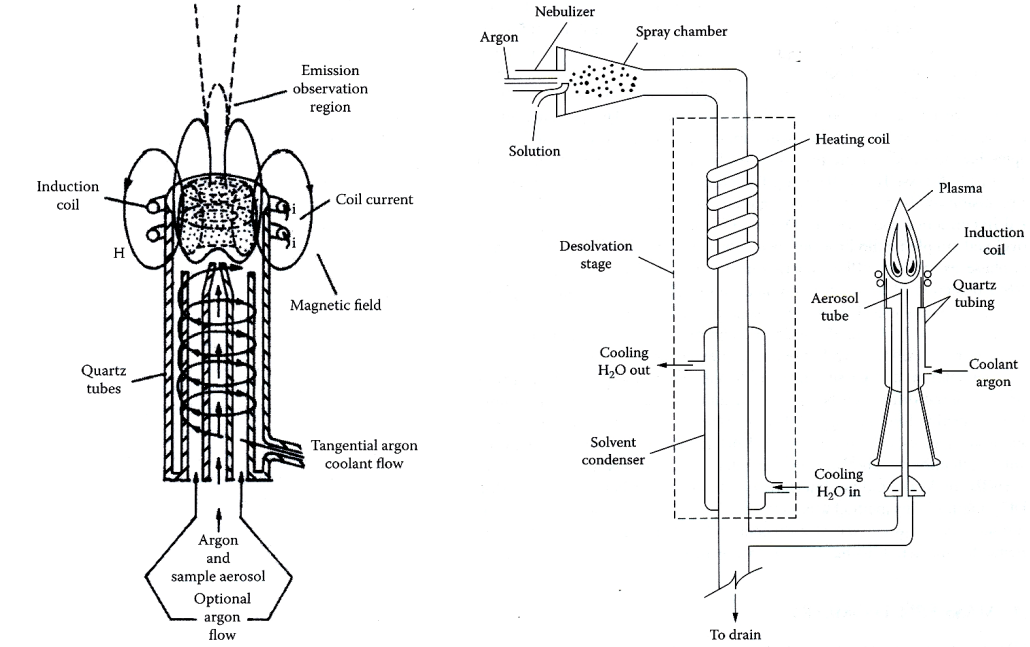

Figure 2.1 (a) Inductively coupled plasma spectrometer; and **(b)** nebulizer, spray chamber, and desolvation parts of an inductively coupled plasma spectrometer.

Two different equipments were used along this thesis: an ARL, model 3410 with minitorch, USA[187] and a Thermo Elemental, model Iris Intrepid II XSP, USA[188]. Some technical details of both equipments are given in Table 2.3.

Table 2.3 Instrumental parameters of the ICP-OES equipments: ARL3410 and Intrepid II XLS.

Parameter	ARL3410	Intrepid II XLS
Generator power (W)	600-700	1350
Generator frequency (MHz)	27.12	27.12/40.68
Integration time (s)	20	30
Ar flow plasma (l min^{-1})	7.5	15
Ar flow auxiliary (l min^{-1})	0.8	0.5
Ar flow nebulizer (l min^{-1})	0.8	0.6-1
Flow peristaltic pump (ml min^{-1})	1.5	1.9

[187] Manual ARL3410 Minitorch®, Plasma Vision V 1.0., ARL, Valencia/USA, 1989

[188] Manual Intrepid II XLS, TEVA™ ICP Software User's Manual, ThermoElemental, Franklyn, USA, 2001

In addition to Hg, elemental analysis of the aqueous phase included As, Cu, Fe, Ni, Pb, Mn, and Zn. Table 2.4 indicates the emission lines selected for the analysis of these elements, as well as their detection limits and most important interferences. Special attention was paid to the analysis of As, Zn and Pb, as these elements might importantly contribute to spectral interferences for Hg analysis by XAS in fluorescence mode. On the other hand, the analysis of major elements as Fe was also considered as a must. Hence, the presence of high concentrations of iron leads to important non-spectral interferences in XAS analysis, where the excess of photons released by highly concentrated elements easily leads to the saturation of the fluorescence detector.

Table 2.4 Spectroscopic specifications for the studied elements. Values of detection limits are evaluated according to the 3σ criteria for ideal samples[189].

	Hg	As	Zn	Cu	Fe	Mn	Ni	Pb
Emission line (nm)	194.227	197.2	213.86	224.7	238.204	293.93	227.02	220.35
Theoretic detection limit (μg l^{-1})	0.5	17	0.5	0.8	1.1	0.15	2	11
Interferences	Al, V	Al,Fe,V	Fe, Mg	Fe,V,Ti	Cr,V	Al, Mg	Cu,Fe,V	Al,Cr,Fe

Quantitative analysis of the target elements was carried out by signal interpolation in a calibration curve. When possible, standards of the selected elements were prepared in aqueous solutions matching aqueous matrices of unknown samples.

The most relevant advantages[190] of the technique are related to its capacity of multielemental analysis, a wide lineal range (from 4 to 6 orders of magnitude), as well as the low detection limits which permit the analyses of both main components and traces with a good exactitude and precision. The main drawback refers to its high costs of acquisition, daily work and maintenance.

2.3 SORPTION OF METHYLMERCURY ON DIFFERENT SOIL COMPONENTS

In order to assess the availability of methylmercury present in soils and sediments, the sorption of this specie onto different soil materials was evaluated. Both clays (kaolinite,

[189] Rubinson, K.A.; Rubinson, J.F. *Análisis Instrumental*, Prentice Hall, Madrid, 2001

[190] Boumans, P.W.J.M. *Inductively Coupled Plasma Emission Spectroscopy – Part 1*, Boumans, P.W.J.M. (ed.), John Wiley & Sons, New York, 1987, p.69

montmorillonite) and humic acid were considered as typical representatives of soil materials. All three components were purchased from Aldrich (Germany) and used as received.

Adsorption of either methylmercury chloride or hydroxide was performed by mixing 0.25 g of each soil material with 25 ml of an aqueous solution of the correspondent methylmercury species (25 μg ml^{-1}). The pH of each sample was adjusted with diluted HNO_3 (0.05 M) or NaOH (0.05 M), in order to cover a pH range between 3 and 9. After 24 hours of equilibration (with pH control and adjustment), samples were centrifuged at 4700 rpm (Pacisa, Digicen, Spain) and the correspondent solid and liquid phases separated. The solid phase was air-dried in a fume hood until constant weight and kept under dry conditions. Finally, dry solid samples were prepared for synchrotron analysis according to the procedure described in section 2.7.1. Figure 2.2a shows the experimental setup utilised for the adsorption experiments.

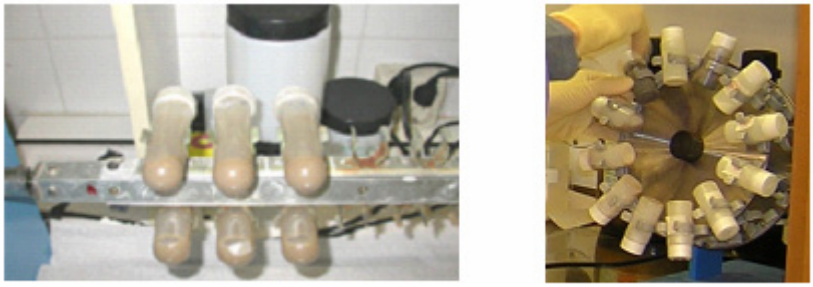

Figure 2.2 Experimental setup for methylmercury sorption studies in a test tube shaker, performed in **(a)** UAB laboratories, and **(b)** NICPB laboratories.

The remaining solution was filtered through 0.22 μm cellulose paper, acidified with HNO_3 (0.5% v/v), stabilized with a few ml of $AuCl_3$ solution (1000 mg l^{-1}) and diluted up to 50 ml with ultrapure water (Milli-Q). The resulting solution was analysed by ICP-OES, taking into consideration the calibration curve build up either with CH_3HgCl or CH_3HgOH standard solutions. Methylmercury adsorbed in each soil material was determined as the difference between the initial and final Hg concentration of the aqueous solution.

2.3.1 Analysis by luminescent biosensors

Bioavailability of organic mercury sorbed on the different soil components essayed was determined by luminescent biosensors at the NICPB, in Estonia. For this analysis, the same methodology as such described above was applied (see Figure 2.2b), although more diluted samples were prepared. In this case 25 ml of 0.8 μg l^{-1} aqueous solution of methyl mercury

chloride were contacted with 2 g of soil material, resulting in approximately 10 µg of $HgCH_3Cl$ per kg dry weight of soil material.

After preparation of the Hg-doped soil materials, samples were mixed with water (1:9 w/v solid to water ratio). Resulting suspensions were rotated for 24 hours at room temperature, and incubated at 37ºC for 2 h together with the bacterial organomercury sensor [*Escherichia coli* strain MC1061(pmerBR$_{BS}$luc)][87] at pH 7. Then, soil-water suspensions were centrifuged at 10000 g and the particle-free extracts as well as the suspensions were analysed with the sensors. Within this time, bioavailable fraction of methyl mercury enters the sensor bacteria and induces the synthesis of the reporter protein, luciferase (see section 1.7.3.1.2). After 2 h of exposure the luminescence is measured (see Figure 2, Annex 2), by a luminometer (model 1253, Thermo Labsystems, Helsinki, Finland).

The analysis of particle-free water extracts with the bacterial sensors provides information on water-extracted bioavailable metals, whereas the analysis of suspensions refers to the bioavailability of particle-bound fraction of metals. In order to account for the interferences of the bacterial luminescence from the sample aqueous matrix (quenching of the luminescence by solid particles, colour or toxicity from any unknown components in the sample on bacteria), a luminescent control bacteria, *E.coli* MC1061(pTOO02) was used[107].

Calibration of the methodology was achieved by incorporating a standard of methyl mercury chloride. Measurements of either sorption samples or standards were performed by triplicate.

The quantification of bioavailable methylmercury was determined using the normalized luminescence of the sample (NL_S):

$$NL_S = \frac{CSL_S}{SL_B} \qquad \textbf{Eq. 2.1}$$

where SL_B is the luminescence value of the blank water in the sensor bacteria measurement, and CSL_S is the corrected luminescence value of the sample measured with the sensor bacteria, expressed as,

$$CSL_S = CF \times SL_S \qquad \textbf{Eq. 2.2}$$

being SL_S the luminescence value of the sample in the sensor and CF the correction factor calculated using equation 2.3.,

$$CF = \frac{L_B}{L_S} \qquad \textbf{Eq. 2.3}$$

In this equation, L_B refers to the luminescence value of the blank water and L_S to the luminescence value of the sample when measured with the control strain.

Bioavailable $HgCH_3Cl$ in suspensions as well as in water-extracts was calculated according to the NL of the sensor bacteria in the sample and the standard calibration curve[191] (see Figure 1, Annex 1). On the other hand, the bioavailable fraction of $HgCH_3Cl$ adsorbed to the sample (contact exposure) was determined by subtracting the value obtained for particle-free extracts from that obtained for the suspension.

2.3.2 Safety aspects

Due to the high toxicity of the mercury compounds used in this work (particularly concerning methylmercury), special safety precautions were taken into consideration.

Non-encapsulated samples were only handled under fume hood and adequate clothing. This included protective gloves, goggles and mask. Nitrile gloves were absolutely necessary when manipulating Hg solutions of organic solvents.

In addition to these precautions, Vermiculita Exfoliada, a universal absorbent of laminated hydrated minerals (mainly aluminium, iron and magnesium silicates, purchased from CARL ROTH, Spain) was always available in order to face any accidental pour off. Uncontrolled Hg release to the environment was avoided by the use of specific mercury-waste containers, which were managed and disposed by the certificated waste-management company ECOCAT.

2.4 X-RAY DIFFRACTION (XRD)

X-ray diffraction was used to study the bulk mineralogy and primary matrix components of samples from the mining area of Almadén. The XRD analyses were carried out at the I.R.I.C.A. (University of Castilla-La Mancha), using a Philips diffractometer, (Model 1700, with CuKα radiation, automatic divergence aperture and curved graphite monochromator). The reception and dispersion aperture were 0.1 mm and 1º respectively. A Xe-filled gas was used, and the scan range was 3º - 75º 2Θ with a scan speed of 0.1º 2Θ s^{-1}.

This technique follows the diffraction of X-rays through the closely spaced lattice of atoms in a crystal. The signal is recorded and analyzed in order to reveal the nature of the original lattice. This generally leads to an understanding of the material and molecular structure of a substance. The spacing in the crystal lattice can be determined using the Bragg's law,

[191] Hakkila, K.; Green, T.; Leskinen, P.; Ivask, A.; Marks, R.S.; Virta, M. Journal of Applied Toxicology, **2004**, *24*, 333-342

$$n\lambda = 2d \sin\theta \qquad \textbf{Eq. 2.4}$$

where, d is the distance between atomic layers in a crystal, λ is the wavelength of the incident X-ray beam, and n is an integer.

2.5 SEQUENTIAL EXTRACTION SCHEMES (SES)

As already introduced in section 1.7.3.2, SES have been widely used as a complementary technique for the understanding of heavy metal distribution and behaviour among different types of soil phases. Given the different nature of soil samples studied in this thesis, two different SES procedures have been applied and are briefly described below.

Polluted soils surrounding a chlor-alkali plant in the Netherlands were characterised by a SES procedure developed by Neculita et al.[123]. This procedure was considered to be the most appropriate, as it had already been tested in samples from the neighbouring soils of chlor-alkali plants. Additionally, the method had been validated using a certified reference material (CRM) and pure Hg compounds. The procedure consists of four steps, which permit the identification of the correspondent fractions defined as:

- **F1**, water-soluble
- **F2**, exchangeable under alkaline conditions
- **F3**, bound to organic matter
- **F4**, residual Hg, quantified in this study by subtracting the sum of metals extracted in previous steps from the total amount obtained by digestion with HF.

Table 2.5 summarizes the analytical procedure followed.

Table 2.5 Sequence of operationally defined fractions and extracting agents in the sequential extraction procedure developed by Neculita et al.[123].

Step	Fraction	Reagents	Contact time (hours)
1	Water soluble	2 g sample + 20 ml H_2O milli-Q	2
2	Exchangeable cations	Residue + 20 ml 0.5 M CH_3COONH_4-EDTA (pH=8.4)	2
3	Bound to organic matter	Residue + 20 ml 0.2 M NaOH + 20 ml CH_3COOH 4% (v/v)	2

In all extraction steps, the mixture was stirred at room temperature in a test tube shaker. The extract from the solid residue was separated by centrifugation at 4700 rpm for 25 minutes, followed by a filtration step with a 0.22 μm filter. The extract was immediately analysed by

ICP-OES, whereas the residue was washed with 10 ml of milli-Q water, stirred for 15 minutes and again centrifuged for 15 minutes at 4700 rpm. The supernatant was decanted and discarded, whereas the solid residue was used in the next extraction step.

On the other hand, a specific SES procedure developed by the CIEMAT Research Centre[192,193], was applied to study the distribution of Hg, As, Cu, Fe, Ni, Pb and Mn in calcine samples from the Almadenejos site. This scheme includes six different extraction steps:

- **F1**, water soluble compounds
- **F2**, exchangeable cations
- **F3**, carbonates
- **F4**, easily reducible elements
- **F5**, compounds soluble in 6M HCl
- **F6**, oxidizable compounds.

The residual metal concentration was also estimated by the difference between total concentration (from HF digestion) and the sum of metal concentration within the complete extraction procedure. Detailed information on SES experimental procedure is given as Supporting Information in Annex 5.

2.6 SCANNING ELECTRON MICROSCOPY (SEM) ANALYSIS

The use of SEM coupled to an energy X-ray dispersive spectrometer (EDS) provides a rapid and non-invasive way to describe the bulk characteristics of each sample. Additionally, it permits the acquisition of qualitative information about the chemical composition of the sample with a relatively high spatial resolution (~ 2-4 nm[194]). Moreover, with suitable standards, it is possible to perform quantitative analysis of the elemental composition at 1-2 μm depth[195].

[192] Pérez del Villar, L.; Quejido, A.J.; Crespo, M.T.; Sánchez, M.; Cózar, J.S.; Galán, M.P.; Fernández-Díaz, M. Trends in Geochemistry, **2002**, *2*, 19-42

[193] Sánchez, D.M.; Quejido, A.J.; Fernández, M.; Hernández, C.; Schmid, T.; Millán, R.; González, M.; Aldea, M.; Martín, R.; Morante, R. Analytical and Bioanalytical Chemistry, **2005**, *381*, 1507-1513

[194] Webb, J.; Holgate, J.H. *Scanning Electron Microscopy*, Encyclopedia of Food Sciences and Nutrition, 2003, pp. 3922-3928

[195] Goldstein, J.I.; Newbury, D.E.; Joy, D.C.; Lyman, C.E.; Echlin, P.; Lifshin, E.; Sawyer, L.C.; Michael, J.R. *Scanning Electron Microscopy and X-Ray Microanalysis*, 2nd Edition, Plenum Press, New York, 1992

The technique is based on the interaction between a beam of electrons and the surface of a solid sample. This interaction leads to different phenomena, including the emission of secondary or backscattered primary electrons and X-rays. The collection and amplification of the latter can be used to create an image corresponding to the surface topography of the sample. Emission of X-rays through interaction of the electron beam is caused by shell transitions of the atoms in the sample. As each element has a unique X-ray spectrum, the elemental composition can be determined on the basis of detected X-rays.

In this study, the apparatus utilised was an electron microscope JEOL JSM 6300 (Jeol LTD, Tokio, Japan), equipped with an EDS Link ISIS-200 (Oxford Instruments, England), with an energy resolution of ~140 eV. In order to get proper images, samples were coated with a carbon spray (Figure 2.3b). This coating treatment is needed to avoid the accumulation of charges in the surface of the sample when bombarded with the electronic beam. Surface metal coats (~10 nm) were prepared by resistive evaporation in a high-vacuum coating unit.

In the study of Almadén samples, SEM-EDS analysis was also used for the qualitative evaluation of the chemical speciation of Hg-rich particles in ore samples, by following the Hg (L_α: 9.98 KeV; M_α: 2.28 KeV) and S (K_α: 2.31 KeV) fluorescent lines. Due to the overlapping of S-K_α and Hg-M_α lines, Hg-L_α line was used to perform a line intensity ratio (LIR)[81]. This ratio is defined as:

$$\mathrm{LIR} = \frac{\text{intensity of S - } K_\alpha \text{ and Hg - } M_\alpha \text{ lines}}{\text{intensity of Hg - } L_\alpha \text{ line}} \qquad \textbf{Eq. 2.5}$$

LIR of HgS standards (cinnabar and metacinnabar), as well as LIR ratio for non-bearing S mercury standards (HgO and $HgCl_2$) were measured for comparison. A detailed description of the followed methodology is given in Annex 3.

Given the costless of SEM-EDS technique compared to synchrotron measurements, the former was used to localize Hg-rich particles in unknown samples before XAS analysis. After the identification of each Hg-rich particle, its position was referred against the position of two Pt filaments that had been disposed on the sample surface (see Figure 2.3c). In this sense, a significant gain on precision and time during XAS analysis was achieved.

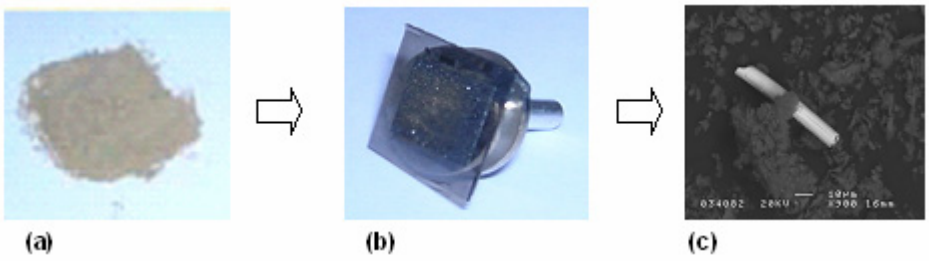

Figure 2.3 (a) Soil sample (milled, sieved and homogenized); **(b)** soil sample with two platinum filaments longitudinally inserted in both sides of the sampler, coated with a carbon spray for SEM-EDS analysis, and; **(c)** SEM image of the platinum filament inserted to the sample.

2.7 XAS MEASUREMENTS

XAS experiments were performed both at HASYLAB (beamlines A1 and L) in Hamburg (Germany) and ESRF (beamline ID26) in Grenoble (France), synchrotron facilities. Details about beamline setup are given in Table 2.6, whereas Figure 2.4 shows some details of beamline A1 at HAYLAB.

XANES data from Almadén minerals and some methylmercury adsorbed compounds were collected at beamline ID26, while the remaining methylmercury adsorbed compounds as well as XANES data from polluted soils samples and slags, were collected at beamline A1. On the other hand, all microprobe analyses were performed at the bending magnet L (see section 1.8.7 and 2.7.3 for detailed information).

Table 2.6 Setup for the different beamlines used in this study.

Element	ESRF, beamline ID26	HASYLAB, beamline A1	HASYLAB, beamline L
(Insertion) device	Undulator	Bending magnet	Bending magnet
Source energy	6 GeV	4.5 GeV	4.5 GeV
Maximum Current	200 mA	150 mA	150 mA
Monochromator crystals	Si(111) (Si(220) also available)	Si(111) (Si(311) also available)	Si(111)
Resolution (ΔE/E)	~10^{-4}	~10^{-4}	~10^{-4}
Photon flow at the sample	> 10^{13} phot s^{-1}	about 10^{9} phot s^{-1}	about 10^{9} phot s^{-1}
Spot size at the sample	200 μm*80 μm	2 mm*3 mm	15 μm*15 μm
Detectors	-Three ionisation chambers	-Three ionisation chambers	-Two ionisation chambers
	-Photo-diodes for flux monitoring	-Si(Li) (7 pixel)	-Si(Li) and silicon drift detector
	-Si (13 elements)		
Angle bunch-sample	45º	45º	45º
Temperature	room	room, liquid Nitrogen/He	room

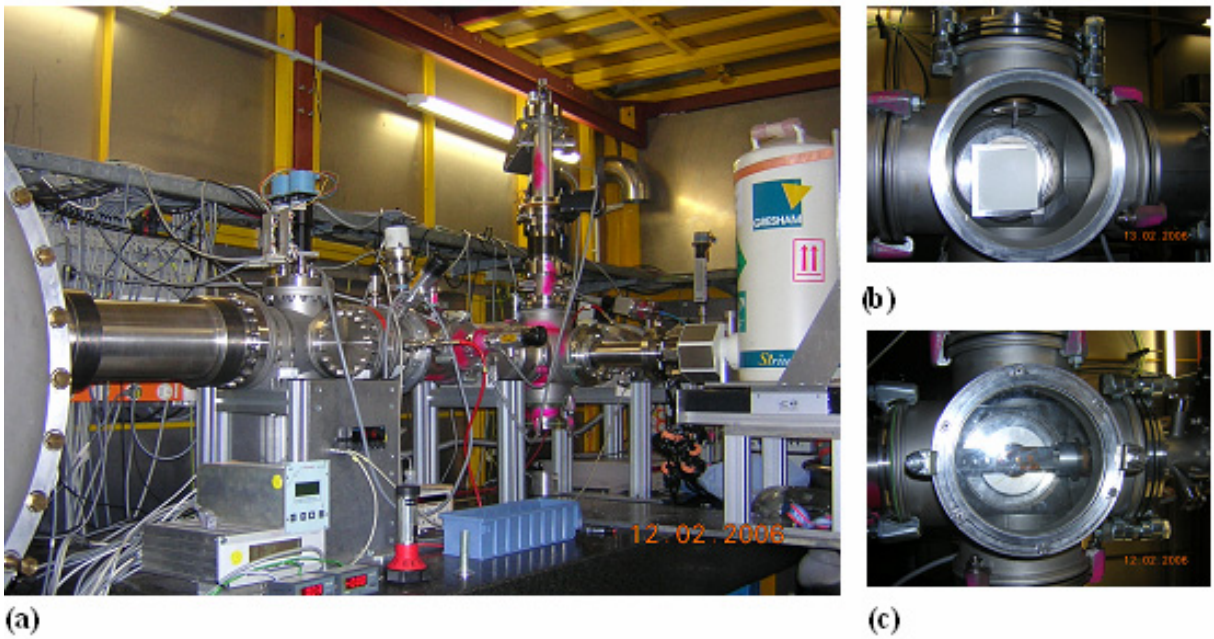

o**Figure 2.4 (a)** Setup of beamline A1, HASYLAB; **(b)** open high vacuum chamber where the sampler is placed in beamline A1, whit an Al filter inside, and; **(c)** sampler inside the high vacuum chamber before experiments.

2.7.1 Sample preparation

Sample preparation for synchrotron experiments differed significantly depending on the type of sample. When dealing with **environmental samples**, sample preparation for XAS analysis (either at beamline ID26 or A1) consisted of the pressing of pellets, both for unknown samples and reference compounds. Polyethylene (Merck UVASOL, Germany) was added in both cases, acting as diluting agent whilst giving consistency to the pellets. Homogenisation of the mixture was performed in a magnetic shaker (A-05, SBS, Spain), and the resultant powder was pressed (25-ton ring press, RIIC, London) as a pellet under 5 tons cm^{-2} for 5 minutes (see Figure 2.5). The total amount of sample and polyethylene in each pellet varied between 50 – 100 and 100 – 150 mg respectively.

Unknown samples studied with microprobe techniques (μ-XRF and μ-XAS) at beamline L (HASYLAB) were directly analysed in powder form. As described for XAS analysis, reference compounds were analysed as pellets.

Due to the high toxicity of mercury compounds used in this study, both unknown environmental samples and reference compounds were encapsulated in Kapton foils, avoiding the direct contact of the mercury pellets or soil samples with the atmosphere.

Mercury species considered as reference compound along the different studies were: $HgCl_2$, Hg_2Cl_2, $HgSO_4$, HgO_{red}, $Hg(CH_3COO)_2$, CH_3HgCl, HgS_{red} (cinnabar) and HgS_{black} (metacinnabar), C_6H_5HgCl, $Hg_2NCl_{0.5}(SO_4)_{0.3}(MoO_4)_{0.1}(CO_3)_{0.1}\cdot(H_2O)$ (mosesite), $Hg_3S_2Cl_2$ (corderoite), Hg_2ClO (terlinguaite) and $Hg_3(SO_4)O_2$ (schuetteite).

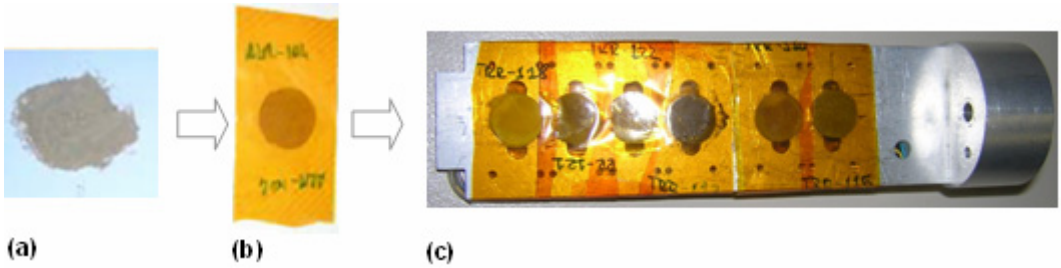

Figure 2.5 (a) Soil sample (milled, sieved and homogenized) ready to be encapsulated in Kapton foils just as it is (beamline L) or as a pellet for synchrotron analysis; **(b)** sample pellet placed between two Kapton foils, and; **(c)** six pellets mounted in the sampler for synchrotron analysis at beamline A1.

For **biological samples** (Figure 2.6a), thin longitudinal slices from tooth specimens were prepared for microprobe analysis. For this purpose, teeth were transferred to a cylindrical plastic mould, positioned in the center, and a mixture of 15 part epoxy resin (Epofix Resin, Struers, Spain) and 2 part hardener (Epofix Hardener, Struers, Spain) was poured over the teeth and allowed to set in a vacuum chamber. Once teeth were secured in the hardened resin block, they were removed from the plastic mould and longitudinally sectioned with a diamond blade (Petro-Thin, Buehler, USA) (Figure 2.6b). Teeth surface was polished with silicon carbide grit (320-1200 μm) (SiC) abrasive polishing power, whilst ultra pure water was used as lubricant and to minimize contamination of the tooth surface. The sectioned teeth were dried and embedded in epoxy resin (epoxy mounting media resin, Microtec section Lok, USA) and several slices between 50 and 600 μm thickness were obtained with the diamond blade from each specimen. Finally, slices were protected with a cover-slip and polyester-Grieβharz casting-resin (GTS, Vosschemie, Spain) (Figure 2.6c).

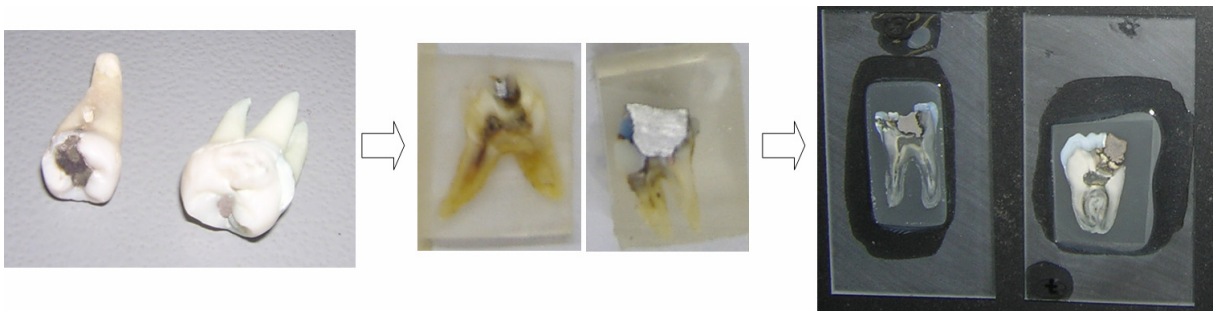

(a) **(b)** **(c)**

Figure 2.6 (a) Original teeth samples; **(b)** longitudinal section of teeth samples inserted in a hard resin block, and; **(c)** teeth slices mounted for synchrotron analysis.

2.7.2 XANES and EXAFS analyses

Mercury absorption was recorded at the edge energy for its L_{III} line at 12284 eV, while the monitored fluorescent lines were the $L_{\alpha 1}$ (9988.8 eV) and $L_{\alpha 2}$ (9897.6 eV). This is the common energy configuration for mercury XAS analyses, as Hg K-lines (68 – 70 keV) fall at energies far above maximum energies available at conventional beamlines. In all studies, pure reference compounds as well as ore samples were analysed in transmittance mode, whereas fluorescence detection mode was used for the analysis of the remaining unknown samples. As mentioned in section 1.8.4, fluorescence-yield measurements are more sensitive and therefore enable the detection of lower concentrations of target elements.

Arsenic and aluminium filters were used to attenuate elastic scattering and fluorescence from iron respectively (see Figure 2.4b). A thin pellet of $HgCl_2$ was periodically measured during analysis both at beamline ID26 (ESRF) and A1 (HASYLAB), aiming at correcting any energy displacement produced during the experiment.

In all beamlines, a Si(111) monochromator was chosen taking into account the energy range and scan step width detailed in Table 2.7.

Table 2.7 Energy and scan step width of the Si(1,1,1) monochromator.

ESRF, beamline ID26		HASYLAB, beamline A1		HASYLAB, beamline L	
Energy (eV) (XANES region)	Measurement intervals (eV)	Energy (eV) (XANES region)	Measurement intervals (eV)	Energy (eV) (EXAFS region)	Measurement intervals (eV)
12000-12250	5	12150-12240	2	12125-12215	2
12250-12270	1	12240-12270	1	12215-12245	1
12270-12295	0.5	12270-12350	0.5	12245-12325	0.5
12295-12600	5	12350-12450	1	12325-12425	1
		12450-12550	5	12425-13000	5

2.7.3 Microprobe analyses

As mentioned above, microprobe analyses were performed at beamline L. Figure 2.7 displays the experimental setup of beamline L together with its main components.

μ-XRF mappings were performed to provide an overview of elemental distribution within samples as well as to identify Hg-rich particles. In certain studies, this mapping also aimed at determining spatial correlations among mercury and other elements.

Mapping by μ-XRF was performed in step-scan mode, each map embracing 11×11 points with a 10 μm step-width (both vertically and horizontally). Consequently, each mapping figure was composed by 121 different pixels. During the whole mapping analysis, the energy of the incident radiation was monochromized with the Si(111) crystal at 13 keV for soil samples and at 17 keV for teeth samples, since the focal spot size of the polycapillary depends on the energy of the primary radiation. The spot size is 13 micron for 17 keV and 17 micron for 13 keV. In each case, the fluorescence signal was detected either with a GRESHAM Si (Li) detector or a RADIANT VORTEX silicon drift detector (50 mm^2 active area), respectively. In both cases, fluorescence detector was placed 90º with respect to the direction

of the incident beam in order to reduce the fraction of scattered radiation reaching the detector. The time of signal accumulation was selected as a function of total count-rate, varying between 1 and 10 seconds per step. Elements included within the μ-XRF analysis were: Hg, Fe, Mn, Ca, Cu, Ni, Pb, Ti, Zn, As, Sn, Br and S. Table 2.8 indicates the energy of some of their X-rays emission lines.

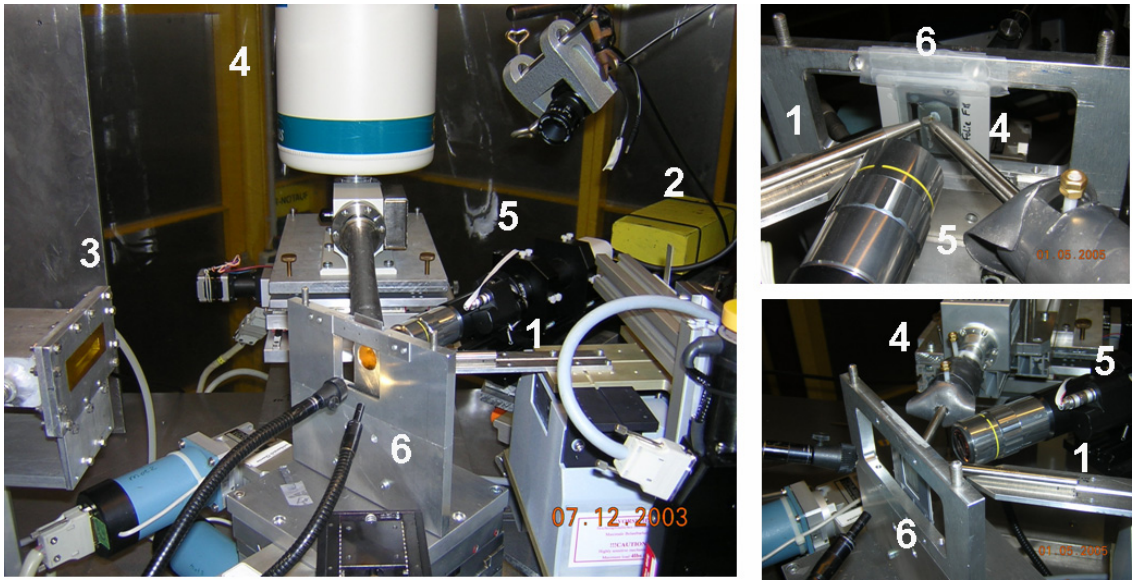

Figure 2.7 Setup of beamline L, HASYLAB: **1.** Polycapillary halflens; **2.** Ionisation chamber 1; **3.** Ionisation chamber 2; **4.** Fluorescence detector; **5.** CCD-camera; **6.** Sampler.

Table 2.8 Energies of X-ray emission lines of selected elements.

Element	Line	Energy (eV)
^{80}Hg	$L\alpha_1$	9988.8
^{33}As	$K\alpha_1$	10543.7
^{30}Zn	$K\beta_1$	9572.0
^{29}Cu	$K\alpha_2$	8027.8
^{28}Ni	$K\alpha_1$	7478.2
^{82}Pb	$L\alpha_2$	10449.5
^{27}Co	$K\beta_1$	7649.4
^{26}Fe	$K\beta_1$	7058.0
^{25}Mn	$K\beta_1$	6490.4
^{20}Ca	$K\beta_1$	4012.7
^{22}Ti	$K\beta_1$	4931.81
^{35}Br	$K\alpha_1$	11924.2
^{16}S	$K\alpha_1$	2307.84

Uptake of μ-XANES and μ-EXAFS spectra significantly differed depending on sample type:

- In **environmental samples**, μ-XANES and μ-EXAFS analysis were undertaken over Hg-rich particles previously identified by μ-XRF.
- In **biological (teeth) samples**, μ-EXAFS was performed at selected points in the nearby of amalgam filling region.

Data were analogously collected as conventional XAS analyses, by using the scan step width showed in Table 2.7.

2.7.4 Data treatment

XANES data from samples of Almadén area (Annex 3) and methylmercury sorption studies (Annex 1 and 2), were handled with WinXAS, a commercial program developed by Thorsten Ressler (Version 2.χ)[196]. The steps followed have been already described in section 1.8.5.1. A linear least-square fitting procedure was employed to fit the model spectra from the compound database to sample spectra within the energy range shown in Table 2.7, in order to obtain the chemical speciation. A residual value (R) was assigned to each fit, representing the proportion of the spectrum that remains unfitted by the linear combination procedure. R is calculated by the equation listed below where N is the number of data points, and y_{exp} and y_{theo} experimental and theoretical data points, respectively.

$$R = \frac{\sum_{i=1}^{N} \left| y_{\exp}(i) - y_{theo}(i) \right|}{\sum_{i=1}^{N} \left| y_{\exp}(i) \right|} \qquad \textbf{Eq. 2.6}$$

A significant residual value may result from noisy data, low total Hg concentrations, as well as the presence of additional unknown components not included in the model compound database[197].

Considering data from methylmercury sorption experiments, a qualitative study was performed in order to obtain information regarding bonding characteristics. Hence, the first derivative of the corrected spectra was done and the energy difference between both edge steps was measured. As reported elsewhere[198], the shorter the energy difference is, the higher

[196] Ressler, T. Journal of Synchrotron Radiation, **1998**, *5(2)*, 118-122

[197] Kim C.S.; Rytuba, J.J.; Brown Jr., G.R. Science of the Total Environment, **2000**, *261*, 157-168

[198] Riddle, S.G.; Tran, H.H.; Dewitt, J.G.; Andrews, J.C. Environmental Science & Technology, **2002**, *36*, 1965-1970

the covalent character of the bond is. A graphic representation of the data treatment is given in Figure 1, Annex 2.

XANES data from the chlor-alkali plant, as well as μ-XANES and μ-EXAFS data were evaluated by using SixPACK software package[199]. Steps followed for the spectra processing are described in chapter 1 (section 1.8.5.1 for XANES and 1.8.6.1 for EXAFS). Energy range considered for the fitting process is detailed in Table 2.7. In this case, the quality of the analyses was evaluated through the reduced chi square value (χ^2), which represents the goodness of the model fit to the spectra data using the linear combination procedure[200].

$$\text{reduced}\,\chi^2 = \frac{1}{N-P}\sum_{i=1}^{N}(\chi_i^{obs} - \chi_i^{fit})^2 \qquad \textbf{Eq. 2.7}$$

where χ_i^{obs} is the ordinate of the XAS spectrum measured from the sample at the i^{th} energy point, χ_i^{fit} is the ordinate of the fitted XAS spectrum, N the number of data points in the fitted XAS energy range (scaled by the wavenumber k), and P is the number of fitted components.

Taking into account Hg μ-EXAFS spectra of dental samples, known crystallographic data for Hg-containing compounds (γ-Ag_2Hg_3, $Hg_{0.1}Sn_{0.9}$ and HgO) and reasonable values for the Debye-Waller factor (σ^2= 0.001) with amplitude reduction function (S_0^2= 0.9), were simulated by FEFF7.0 calculations[201]. These simulated EXAFS spectra were compared to the unknown data, over a k-range of 3 to 9.5 $Å^{-1}$.

Elemental correlations carried out by μ-XRF (see Annex 4, 5 and 6) were performed by following fluorescence line intensities (counts s^{-1}) of all elements considered. Hence, intensity from each pixel and each element (both at Hg-rich particles or Hg-depleted regions) was taken, and pair correlations were obtained (Hg-Pb, Hg-S, Hg-Cd, Zn-Cd, etc.) by representing intensity of each pair at each pixel.

[199] Newville, M. *SIXPack (Sam's Interface for XAS analysis Package)*, Powered by IFEFFIT 1.2.6, University of Chicago, 2004

[200] Slowey, A.J.; Johnson S.B.; Rytuba J.J.; Brown, G.E.,Jr. Environmental Science & Technology, **2005**, *39(20)*, 7869-7874

[201] Rehr, J.J.; Albers, R.C.; Zabinsky, S.I. Physical Review Letters, **1992**, 69, 3397-3400

Chapter 3

Results and Discussion

This chapter is devoted to present and discuss the most relevant results of this Thesis. Nevertheless, taking into consideration the already published papers attached in the Annex section, only a general overview of these will be reported.

3.1 CHARACTERISATION AND BIOAVAILABILITY STUDIES OF METHYLMERCURY ADSORBED ON MODEL SOIL COMPONENTS

XAS techniques and biosensors have been coupled to achieve a better understanding of methylmercury sorption on soil materials as well as to assess its bioavailability.

3.1.1 Methylmercury sorption capacity and pH effect

The adsorption of methylmercury chloride and hydroxide on three different soil materials (montmorillonite, kaolinite and humic acid) has been studied within the pH range 3-9. Results are shown in Figure 3, Annex 2.

A similar trend was observed for both methylmercury compounds and all soil components. Nevertheless, the adsorption was higher for CH_3HgOH, probably due to its hydroxide group, which is more reactive with soil components than the corresponding chloride.

Montmorillonite and kaolinite have shown a higher adsorption capacity than humic acid, which has been attributed to the higher cation exchange capacity of clays (see sections 1.7.2.1 and 1.7.2.2). On the other hand, the larger adsorption of methylmercury on montmorillonite, compared to kaolinite can be explained by the limited surface area of the latter (surf. $area_{mont}$= 700-800 m^2g^{-1} ; surf. $area_{kaol}$= 7-30 m^2g^{-1}). This fact is consistent with the tendency described elsewhere for mercury adsorption capacity: montmorillonite> vermiculite> kaolinite[202].

Adsorption of methylmercury onto humic acid is almost constant with pH (see Figure 3, Annex 2). At pH > 9, adsorption decreases due to the competition of OH^- anions with the surface functional groups for CH_3Hg^+ complexation (see Figure 4, Annex 2). On the other hand, below the studied pH, the extent of adsorption decreases due to the competition of CH_3Hg^+ with H^+ for the active sites of the functional groups[203]. Furthermore, the carboxyl group of humic acids is unprotonated at pH 6.0-7.0, whereas the alcohol, amino and thiol groups are protonated[76], being probably the reason for the CH_3HgOH adsorption fall at this pH.

[202] Obukhovskaya, T. D. Pochvovedenie, **1982**, *6*, 53-58

[203] Zvonarev, B.A.; Zyrin, N.G. Pochvovedenie, **1982**, *4*, 43-48

3.1.2 Hg-soil compound bond characterization by XAS techniques

Bond type (or bond character) in single-bond Hg compounds has been studied by XAS techniques. Covalence has been qualitative assessed by measuring the energy between the two electronic jumps observed in the Hg L_{III} edge (see Figure 3.1a). This energy difference (ΔE) has been determined by the first derivative of the original fluorescence spectra (see Figure 3.1b).

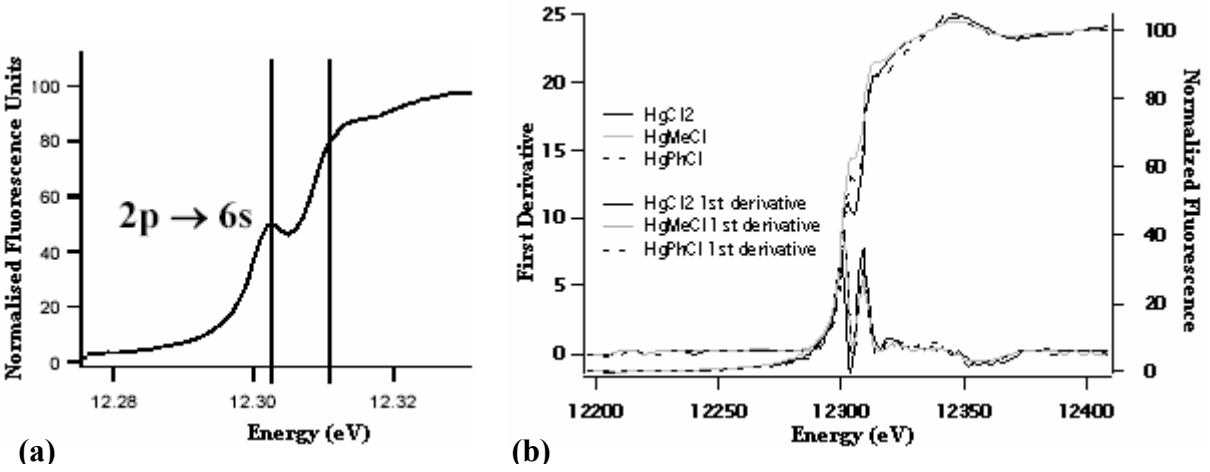

Figure 3.1 (a) Normalised fluorescence spectrum. It can be noticed two different absorption maxima corresponding to the two different electronic jumps. **(b)** Normalised and first derivative spectra of $HgCl_2$, $HgCH_3Cl$ and HgC_6H_5Cl.

The first inflexion point gives insight into the electronic environment of the absorbing atom. For the studied mercury species, it corresponds to the transition to the 6s orbital of Hg, and its position varies within the interval 12284.1±1 eV[198]. The energy of the first inflexion point corroborates the predominance of Hg(II) species. The presence of Hg(0) would increase the electron density around the absorbing mercury atom, consequently would had reduced the energy required to excite a core electron.

As shown for reference compounds (see Riddle et al.[198] and Table 3 in Annex 2), the higher the ΔE is, the lesser the covalent character of the bond is.

Figure 3.2 shows ΔE values corresponding to montmorillonite and humic acid samples spiked with methylmercury chloride and hydroxide. Kaolinite samples could not be analysed due to the excess of photons released by the high iron content of the samples, which lead to the detector saturation in fluorescence mode.

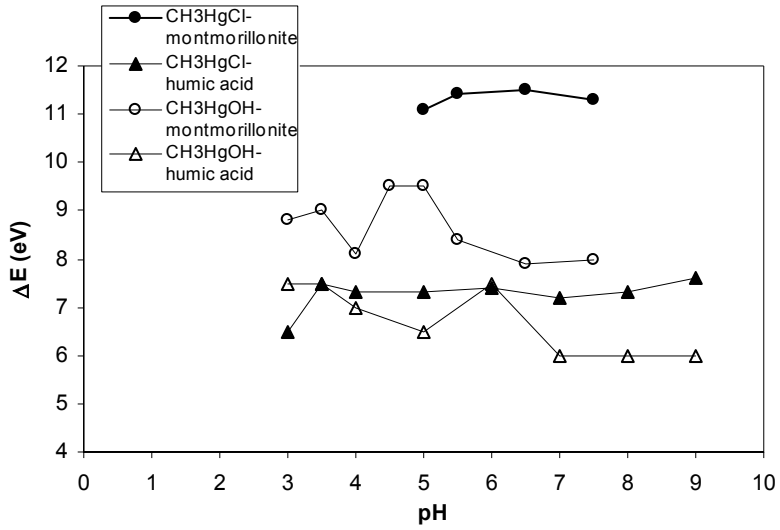

Figure 3.2 ΔE (energy difference between the two peaks of the first derivative of the XANES spectra) for montmorillonite and humic acid spiked with CH_3HgCl and CH_3HgOH.

Similar ΔE values have been obtained for each soil material at different pHs, supporting the hypothesis of a similar bonding character between surface species forming at different pH conditions. Comparison of spectra for montmorillonite and humic acid has lead to higher ΔE of the former, which refers to a more covalent bond between methylmercury and humic acids than with the clay mineral. This behaviour might be attributed to the presence of thiol groups in humic acids and the additional stabilisation achieved by their complexation to mercury.

The overall comparison of $HgCH_3Cl$ and $HgCH_3OH$ leads to a higher covalence degree for the latter, which may lead to the formation of hydrogen bonds with functional surface groups or even form condensed chemical bonds with surface OH^- groups by elimination of water.

3.1.3 Assessment of methylmercury bioavailability by luminescent bacteria

The analysis of both soil-water suspensions and particle-free extracts has permitted to determine the bioavailability of $HgCH_3Cl$ adsorbed on different soil materials. Hence, biosensors have demonstrated a higher bioavailability of methylmercury adsorbed in montmorillonite (~55 % of added $HgCH_3Cl$) compared to kaolinite (~9 % of added $HgCH_3Cl$) and humic acid samples (~13 % of added $HgCH_3Cl$). This extent could be also explained by the analysis of XANES data, which revealed the highest ionic character for mercury molecular environment in this clay soil component.

Summarizing, XANES analysis has been proven to provide valuable information on the type of interaction taking place between methylmercury compounds and some key soil

components, which is to be considered as a powerful tool to assess the environmental hazard of methylmercury related to the environment where it is found (soil components). Synchrotron analysis has been complemented and improved by the use of bacterial sensors, thanks to the capacity of the latter to assess methylmercury bioavailability even at very low concentrations.

3.2 CHARACTERISATION OF ALMADÉN MERCURY MINE ENVIRONMENT

Synchrotron-based XAS techniques have been coupled to laboratory-scale techniques (XRD, SEM-EDS and SES) to assess mercury speciation and potential mobilisation in samples from the Almadén mine environment.

3.2.1 Analysis of total metal content by MW digestion and ICP-OES

Aqua regia digestion (EPA method 3051) was found unable to successfully digest ore samples, whereas a complete digestion was achieved by HF-based MW digestion (see Table 2, Annex 3). Consequently, aqua regia was skipped and HF-digestion reliability was checked with the certified reference material SRM 2710. Digestion results fell within the certified values (see Table 3.1) and therefore the methodology was systematically used with the whole set of samples.

Table 3.1 Range of the certified value (first row) and average of three replicates (second row), in mg kg^{-1}, of selected metals present in the certified reference material SRM 2710.

	Hg	As	Zn	Cu	Mn	Pb
SRM 2710	27-37	490-600	5200-6900	2400-3400	6200-9000	4300-7000
HF digestion	35±1	640±80	5720±50	2520±30	8110±90	4567±40

Total metal content in ore, soil, slag and calcine samples (AJ-701, AJ-702) from the Almadenejos decommissioned plant is shown in Table 3.2. As observed in the table, mercury concentration is very high in all samples but slag and soil sample nº6. Significantly high mercury concentration was found in calcine samples. As calcines correspond to the residue of the mineral roasting process, these unexpectedly high mercury concentrations might indicate an incomplete Hg roasting process in this plant.

Table 3.2 Total metal content (mg kg^{-1}) determined by HF digestion + ICP-OES analysis, as average of three replicates. Standard deviation within the 95% confidence interval.

	Hg	As	Zn	Cu	Ni	Pb	Fe ($g \cdot kg^{-1}$)	Mn
ore 1	39000±1000	430±40	185±6	< 1	1700±300	260±40	52.4±0.4	600±10
ore 2	33000±3000	470±9	< 1	< 1	1400±100	290±20	50±2	540±10
ore 3	41000±3000	490±10	< 1	< 1	1580±50	278±5	53±4	639±7
ore 4	28900±800	500±8	280±10	< 1	1580±80	295±2	51.6±0.8	553±2
ore 5	38600±300	450±70	< 1	< 1	1500±100	260±40	49.9±0.2	632±3
soil 1	630±30	290±50	< 1	< 1	670±10	< 1	43±1	< 1
soil 2	1080±30	320±30	< 1	< 1	950±90	260±20	51.0±0.5	460±10
soil 3	1090±30	340±10	< 1	< 1	960±60	229±7	44±3	510±10
soil 4	1200±100	340±20	< 1	< 1	1000±200	208±6	51±2	420±20
soil 5	1450±30	310±6	< 1	< 1	860±30	< 1	44±1	< 1
soil 6	400±10	320±20	< 1	< 1	1008±6	< 1	37.1±0.2	330±10
soil 7	840±20	310±30	< 1	< 1	1160±20	220±30	40.9±0.2	632±6
soil 8	1820±10	340±40	< 1	< 1	1100±200	210±20	41.9±0.7	301±6
soil 9	1360±50	310±20	< 1	< 1	1100±100	< 1	40.2±0.4	640±10
soil 10	1720±10	320±5	310±30	< 1	1260±90	287±8	47.5±0.3	390±10
slag 1	460±30	320±20	< 1	< 1	1410±40	< 1	61.7±0.5	< 1
slag 2	380±6	300±10	390±10	65±1	1290±80	< 1	78.96±0.04	< 1
slag 3	240±3	340±40	< 1	73±1	1400±200	206±7	86.4±0.8	< 1
AJ-701	35000±6000	< 1	2200±400	33±7	36±6	91±13	70±16	280±60
AJ-702	6700±500	< 1	2500±200	33±2	41±2	276±190	65±2	798±8

Quantification of elements likely to produce spectral interferences in XAS measurements (As, Pb and Zn) revealed relatively low metal concentrations but for As in slag samples and soil nº 6. On the other hand, an important Ni background was found in most of the samples, but was considered no problematic for XAS analysis taking into account Ni fluorescence lines (K_α= 7478 eV, K_β= 8264 eV) are far from Hg lines. Very high Fe concentrations (from 37 to 86 $g \cdot kg^{-1}$) were found in all samples. These unexpectedly high Fe concentrations lead to severe analysis problems during the available beamtime at the ESRF synchrotron source. The extremely brilliant source of this third generation facility produced an overall excitation of the iron and the correspondent saturation of the fluorescence detector. Consequently, all samples but ores (analysed in transmittance mode at the ESRF) were analysed at the HASYLAB second generation synchrotron.

3.2.2 Bulk characterisation and analysis of Hg-rich particles

Ore, soil and slag samples were analysed by SEM-EDS to obtain some compositional information of the bulk, as well as to achieve a qualitative overview of Hg speciation. Hence, Figure 1, Annex 3, shows a full-field area of ore sample nº1, where the spectrum is dominated by a clayey composition (aluminium, silicon, potassium and iron). Likewise, the study of soils and slag showed a similar bulk composition.

Several Hg-rich particles were identified within the studied samples. The analysis of these particles by EDS suggested the presence of cinnabar, or, at least, particles where mercury and sulphide were spatially related (see Figure 2, Annex 3).

The presence of cinnabar was semi-quantitatively assessed by a LIR approach (see section 2.6). Table 4 in Annex 3 shows LIR results of Hg rich particles from five ore samples compared to the LIR ratio of four mercury reference compounds: the two polymorphs forms of HgS (cinnabar and metacinnabar), HgO and $HgCl_2$.

As observed in the table, LIR values of HgS standards (especially of red HgS) show important similarities with LIR obtained from ore samples, suggesting the predominance of this compound in the samples. Dissimilarities found within LIR values might be attributed to both the uncertainties of the technique and the possible presence of other mercury compounds.

3.2.3 Mineralogical characterisation of calcine samples by XRD

Mineralogy of major crystalline components present in calcines samples AJ-701 and AJ-702 was determined by XRD and is shown in Table 3.3. In both samples, phyllosilicates (mica and kaolinite, with a unit cell SiO_4^{4-} partially substituted by Al^{3+} or Fe^{3+}) are predominant. This observation is consistent with the geological origin of the Almadén mercury belt, as these deposits are primarily localized in Silurian quartzite adjacent to mafic craters[30,34]. Plagioclase ($Na_{0.5}Ca_{0.5}Si_3AlO_8$) and calcite ($CaCO_3$) were found as typical igneous and hydrothermal minerals from the surroundings. In addition, gypsum ($CaSO_4 \cdot 2H_2O$) was detected in one of the samples (AJ-701), presumably as a product of weathering processes or as a building material, since samples were from furnace ruins (see Figure 3.3). Nevertheless, no Hg crystalline phases were detected by XRD, indicating their presence in relatively low proportions (below 2%).

Table 3.3 Identifiable crystalline components in samples AJ-701 and AJ-702 (powder) determined by XRD analysis, as total fraction (%).

Sample	Quartz	Feldspar/ Albite	Plagioclase	Calcite	Dolomite	Gypsum	Phyllosilicates
AJ-701	19		7	5		7	62
AJ-702	11		5	22			62

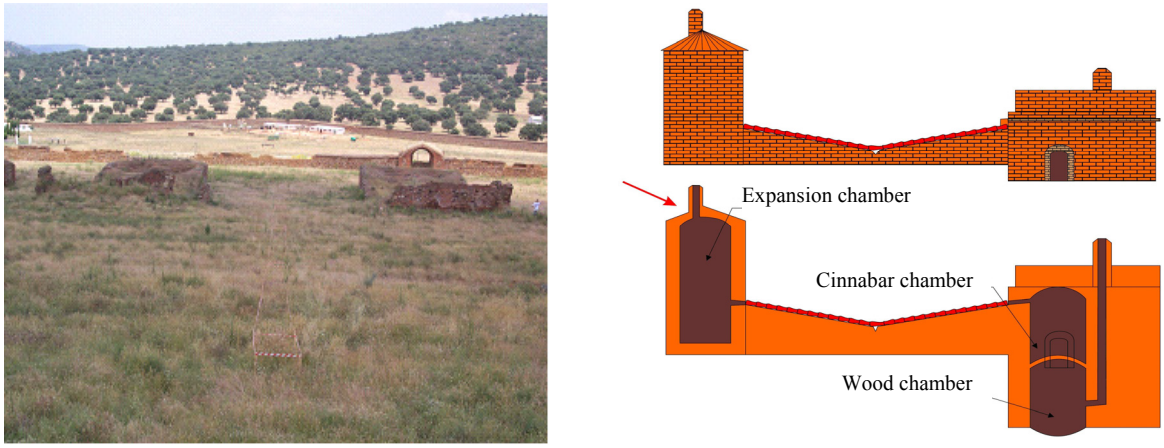

Figure 3.3 Picture and scheme of the Almadenejos decommissioned metallurgical plant, which was located some 10 km southeast of Almadén. The plant was active during the period of the 17th to 19th century, until its closure in 1860.

3.2.4 Chemical and geochemical characterisation of calcine samples by µ-XRF and SES

The assessment of elemental correlations at µ-scale level was considered as a specific data for the geochemical characterisation of calcine samples from the Almadenejos mine-facility. This information was then combined with results from the proposed SES scheme, leading to valuable knowledge concerning the mobilisation risk of mercury and other heavy metals from calcine wastes.

Line intensities of selected elements were extracted from each µ-XRF mapping scan. Figure 3.4 show a direct comparison of line intensities for a number of elemental couples (i.e. Hg–S, Hg–Ni, Hg–Pb). This comparison has lead to the identification of three different elemental behaviours:

- No correlation was found between Hg and Ca, Ti, Zn or Cu.
- Linear Pb-Hg, Ni-Hg and possible S-Hg correlations were identified within mercury-rich areas.
- Lineal correlation between Hg and the background of Fe and Mn.

These results suggest the association of Hg – Pb – Ni phases, which might be explained by the well-known tendency of these three elements to form very stable compounds with sulphide. In this sense, the pair correlation diagrams of Figure 3.4 may also indicate the affinity of Hg to S. However, the ascertainment of Hg-S correlation by μ-XRF must be considered with care, given the low count rate shown by S at the irradiated energy.

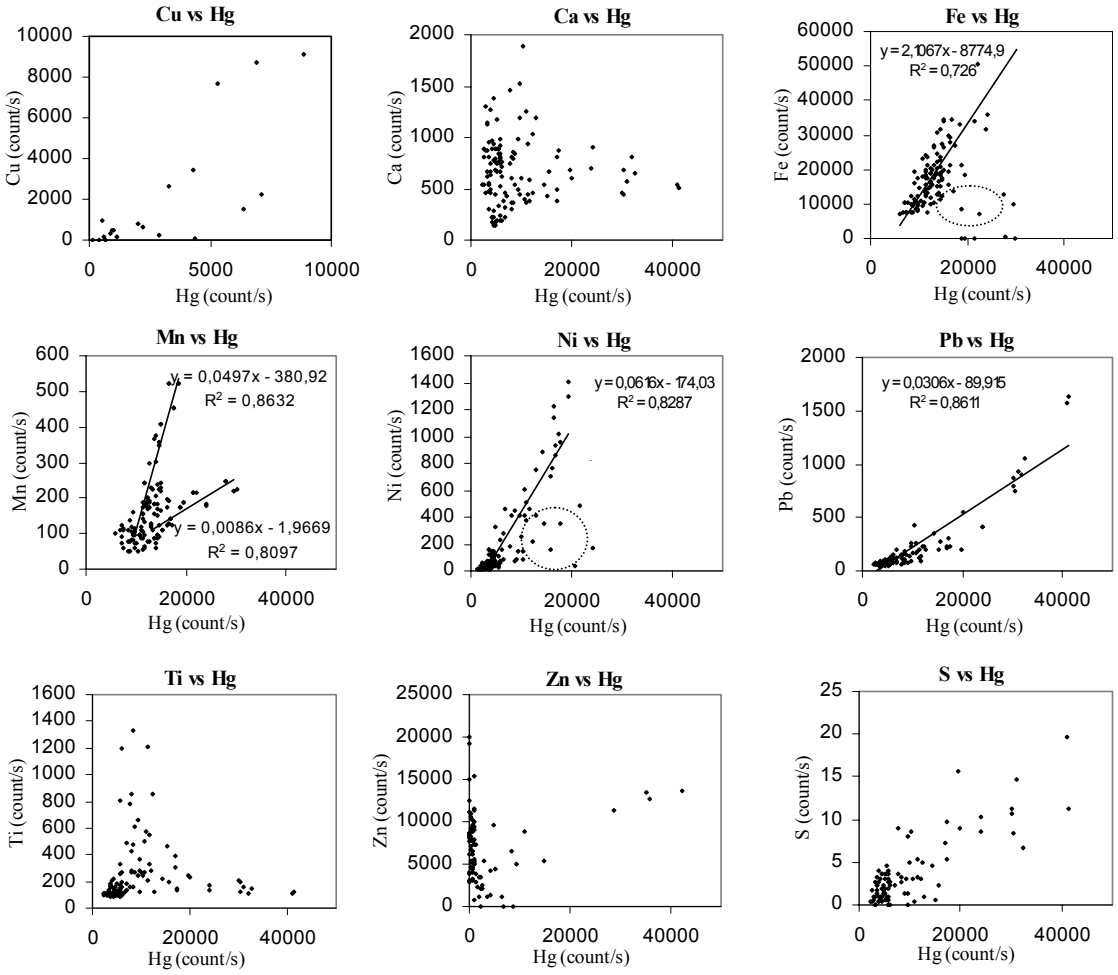

Figure 3.4 Pair correlation diagrams obtained from the μ-XRF maps of samples AJ-701 and AJ-702 (average of six regions belonging to the mercury rich particles). Fluorescence intensity represented in counts s^{-1}. Outlayers of Fe and Ni (dashed circles) are not considered for linear regressions.

On the other hand, the correlation Fe – Hg might be explained in the basis of two hypotheses:

- Phase association between cinnabar and pyrite. Nevertheless, this option was discarded given the low presence of pyrite in the area. In that case, drainage waters would have had a significantly high acidity, whereas the pH values of the groundwater of Almadén mining district fall within the neutral to alkaline conditions (7-8.5, see

additional details in Table 3.4). These pH values are consistent to streams related to deposits hosted in mafic volcanic rocks.

- Mercury is known to strongly adsorb onto iron oxyhydroxides. According to Kim et al.[204] Hg(II) sorbs to fine-grained powders of goethite (α-FeOOH) with a sorption density of 0.39-0.42 μmol m^{-2}. Moreover, Fe-oxyhydroxides are particularly abundant in natural aquatic systems and are effective substrates for Hg sorption, with a direct chemical bond between Hg(II) and the substrate surface (bidentate inner-sphere sorption complexes)[204,205].

Hg is also known to form inner sphere complexes with manganese oxides[30]. Although Mn is found in lower concentration than Fe in the Almadén mine waste, this fact may explain the correlation found between Hg and Mn. Nevertheless, results show two different Hg-Mn correlation trends that may indicate the occurrence of two different sorption processes.

Table 3.4 Chemical composition of water in the Almadén region. Data from the Guadiana Hydrographic Confederation, and Eh and pH values from this study. Results expressed in μg l^{-1} (ppm) and mol l^{-1} (M).

Sample	Average 2004 (ppm)	Average 2004 (M)
Chloride (Cl^-)	15.0	$4.2 \cdot 10^{-4}$
Sulphates (SO_4^{2-})	38.3	$4.0 \cdot 10^{-4}$
Nitrates (NO_3^-)	2.5	$3.4 \cdot 10^{-5}$
Bicarbonates (HCO_3^-)	72.3	$7.7 \cdot 10^{-4}$
Phosphates (PO_4^{3-})	0.22	
Calcium (Ca)	19.2	$4.8 \cdot 10^{-4}$
Eh* (mV)	194.5	
pH	7.83	

* Eh value is characteristic and its annual average belongs to Mars-December 2004

A SES scheme developed at CIEMAT research centre[192,193] was applied to samples AJ-701 and AJ-702 to assess mercury distribution among different soil phases and to evaluate its potential mobility under the conditions encountered in the Almadén environment. Additionally, such data obtained from SES studies were coupled with the information from μ-XRF elemental mappings and μ-EXAFS speciation studies.

[204] Kim, C.S.; Rytuba, J.J.; Brown, G.E.Jr. Journal of Colloid Interface Science, **2004**, *271(1)*, 1-15.

[205] Collins, C.R.; Sherman, D.M.; Ragnarsdottir, K.V. Journal of Colloid and Interface Science, **1999**, *219*, 345-350

Sequential extraction (see Table 3.5 in this section and Figure 1 in Annex 5) indicates that distribution of mercury among the different fractions in both samples is similar. Mercury extracted with HCl (51% AJ-701, 44% AJ-702) is exceptionally high with respect the mercury removed in the other steps, which corroborate the binding capacity of crystalline Fe-Mn oxyhydroxides or suphides to Hg. However, the previous fraction (easily reducible) releases little mercury (4% in both samples), suggesting a limited fraction of Hg bound to amorphous Fe-Mn oxyhydroxides. On the other hand, mercury concentrations remaining in the final residue (16% AJ-701, 42% AJ-702) indicates that an important fraction of mercury is associated with the residual refractory phase, probably as red cinnabar. The still significant concentration of mercury in the water-soluble, exchangeable, and carbonate fractions (23% in sample AJ-701 and 10% in sample AJ-702) suggests a possible risk of Hg mobilisation, and therefore deserves further attention.

Concerning other metal components, Ni has been mainly found in fraction 5, suggesting its association to crystalline oxyhydroxides of Fe and Mn. Similarly to mercury, Pb basically remains in the final residue, thus being expected as sulphide compound. This point is further supported by elemental correlations observed by μ-XRF elemental mappings. Arsenic content is negligible in both samples, whereas the risk of mobilization concerning other heavy metals such as Cu or Pb can be considered low.

Table 3.5 Amount removed (mg kg^{-1}) in samples AJ-701 and AJ-702, by the specific six-step CIEMAT sequential extraction procedure, and final residue (total amount extracted by digestion - total amount extracted by the six-step SES).

Sample	Fraction	Hg	As	Cu	Fe	Ni	Pb	Mn
AJ701	Water soluble	850±21	0	0	0	0	0	0.82±0.08
AJ-701	Exchangeable	4030±64	0	0	0	0	0	2.7±0.3
AJ-701	Carbonates	3500±156	0	0	23.2±0.4	0.52±0.04	0.35±0.05	106±3
AJ-701	Easily reducible	680±65	0.73±0.02	2.5±0.3	2640±84	2.9±0.2	2.3±0.2	150±5
AJ-701	Soluble in 6M HCl	18000±1393	0	13±2	30000±707	27±2	16±2	270±10
AJ-701	Oxidizable	2500±144	0	1.6±0.3	3710±14	3.8±0.6	1.3±0.6	27±7
AJ-701	Final residue	~ 5700	~ 0	~ 16	~ 33600	~ 2	~ 71	~ 0
AJ-702	Water soluble	12.9±0.8	0	0	9.1±0.1	0	0.23±0.05	0.18±0.01
AJ-702	Exchangeable	200±4	0	0	0	0	0	1.2±0.1
AJ-702	Carbonates	430±32	0	1.20±0.01	27.6±0.8	0.91±0.08	1.45±0.05	180±12
AJ-702	Easily reducible	120±18	1.6±0.2	2.9±0.1	3890±23	3.9±0.4	2.7±.0.2	274±4
AJ-702	Soluble in 6M HCl	2980±61	2.9±0.4	11±1	28900±704	32±2	20.8±0.8	310±42
AJ-702	Oxidizable	180±12	0	2.11±0.09	4200±163	4.85±0.05	1.31±0.08	37±4
AJ-702	Final residue	~ 2800	~ 0	~ 16	~ 27900	~ 0	~ 250	~ 0

3.2.5 Speciation results by XANES, µ-XANES and µ-EXAFS techniques

Treatment of raw XAS data has lead to spectra shown in Figure 3.5. Once corrected and normalized, samples and reference compounds spectra were available for the fitting procedure. As stated in section 2.7.4, WinXAS was utilised to determine the linear combination of reference compounds better explaining sample spectra in ore, soil and slag samples. On the other hand, µ-EXAFS data from calcine samples were evaluated by using SixPACK software package. Figure 4 in Annex 3 shows the XANES adjustments obtained for ore_1, soil_1 and slag_1, whilst Figure 4 in Annex 5 shows de linear combination fits of different particles of calcine samples analysed by µ-EXAFS.

Speciation results obtained for both set of samples, as well as additional technical details regarding synchrotron analysis are shown in Table 3.6.

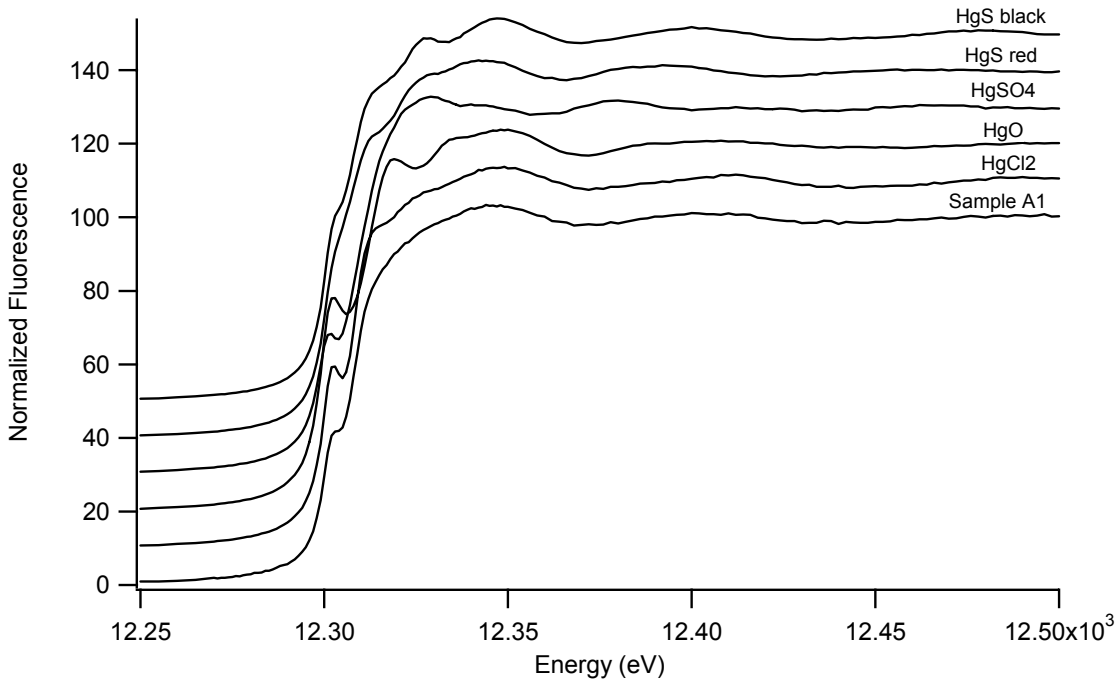

Figure 3.5 Comparison of XANES spectra (corrected and normalized) of different Hg standards and ore nº1 from Almadén. Deliberated offset added to each spectrum to facilitate the visual comparison of related data.

Table 3.6 shows how cinnabar appears to be the main mercury species in almost all ore and soil samples analysed, as expected. The analysis by μ-XANES of a single Hg-rich particle from soil sample number 6 indicates the predominance of $HgCl_2$, suggesting the presence of additional Hg species besides cinnabar and supporting the idea of a significant sample heterogeneity.

As shown in Figure 3.6, cinnabar is the thermodynamically stable form at ambient temperature and reducing to slightly oxidant conditions (depending on the pH values). However, taking into account pH and Eh conditions given in the Almadén environment (see Table 3.4), other mercury compounds (basically elemental mercury) might be also expected. Nevertheless, the absence of elemental mercury within the studied samples could be explained by the kinetic resistance of cinnabar to oxidation (even under relatively high oxidizing conditions), as had been reported elsewhere[81]. Moreover, Hg(l) in superficial and sunny samples (i.e. the Almadén area), can be easily volatilised[206,207].

[206] Higueras, P.; Oyarzun, R.; Biester, H.; Lillo, H.; Lorenzo, S. Journal of Geochemical Exploration, **2003**, *80*, 95–104

[207] Gustin, M.S.; Biester, H.; Kim, C.S. Atmospheric Environment, **2002**, *36*, 3241–3254

Table 3.6 Chemical speciation of ore, soil, slag samples from the Almadén mine and Hg-rich particles identified in calcine samples from the Almadenejos mine facility. Concentration values expressed in % over total mercury content in each sample.

Sample	Beamline	Detection mode[a]	XAS technique	HgS_{red}	HgS_{black}	$HgSO_4$	$HgCl_2$	HgO	Schuetteite	Residual
ore 1	ID26 – ESRF	T	XANES	77	12	6	6	<3		0.025
ore 2	ID26 – ESRF	T	XANES	54	19	14	6	5		0.059
ore 3	ID26 – ESRF	T	XANES	51	9	6	29	4		0.047
ore 4	ID26 – ESRF	T	XANES	63	10	8	14	4		0.054
ore 5	ID26 – ESRF	T	XANES	68	7	6	14	5		0.035
soil 1	A1 – HASY	F	XANES	66	<3	14	<3	17		0.218
soil 2	A1 – HASY	F	XANES	56	<3	22	22	<3		0.186
soil 3	A1 – HASY	F	XANES	41	<3	24	19	16		0.282
soil 4	A1 – HASY	F	XANES	74	<3	14	<3	10		0.178
soil 5	A1 – HASY	F	XANES	66	<3	17	18	<3		0.149
soil 6	L – HASY	F	μ-XANES	34	<3	5	47	14		0.111
soil 7	A1 – HASY	F	XANES	64	<3	18	18	<3		0.191
soil 8	A1 – HASY	F	XANES	62	<3	20	19	<3		0.155
soil 9	A1 – HASY	F	XANES	54	<3	21	25	<3		0.160
soil 10	A1 – HASY	F	XANES	76	<3	24	<3	<3		0.195
slag 1	L – HASY	F	μ-XANES	<3	88	12	<3	<3		0.126
slag 2	L – HASY	F	μ-XANES	10	65	18	<3	7		0.172
slag 3	L – HASY	F	μ-XANES	29	42	16	12	<3		0.122
AJ-701; part. 1	L – HASY	F	μ-EXAFS	<5				47	49	0.17[b]
AJ-701; part. 2	L – HASY	F	μ-EXAFS	34				41	24	0.74[b]
AJ-701; part. 3	L – HASY	F	μ-EXAFS	9				55	36	0.26[b]
AJ-702; part. 1	L – HASY	F	μ-EXAFS	89				5	6	0.23[b]
AJ-702; part. 2	L – HASY	F	μ-EXAFS	26				47	27	1.68[b]
AJ-702; part. 3	L – HASY	F	μ-EXAFS	14				38	47	1.32[b]

a. T: transmittance mode; F: fluorescence mode

b. Evaluated by the reduced chi square value (χ^2)

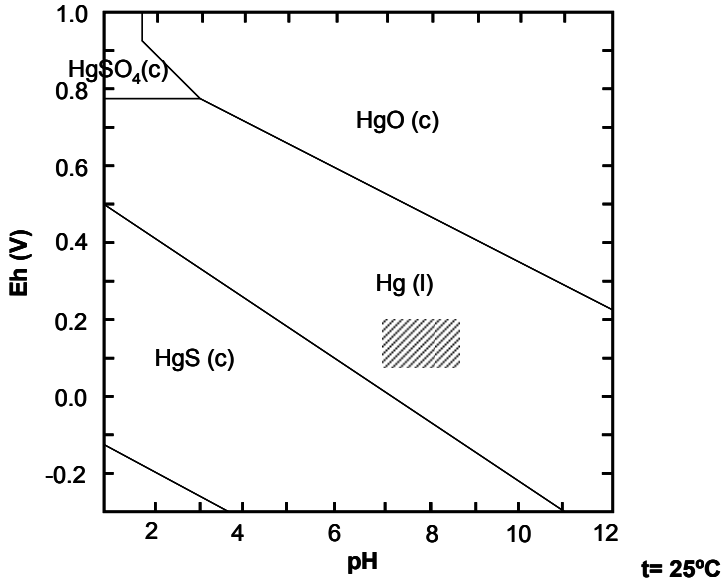

Figure 3.6 Eh – pH predominance diagram for the system Hg – S – Cl. Calculations performed with MEDUSA – HYDRA thermodynamic package[208]. Ruled square representing pH and Eh conditions found in the Almadén environment.

Metacinnabar (black HgS), a polymorph of HgS less common and stable than cinnabar has been identified in some samples, basically from slag. This species does form when the ore is processed under high temperatures (over 345ºC) during the extraction process at the roasting furnaces. The presence of small proportions of metacinnabar in the raw mineral samples (ore 1 – 5) can be geologically justified due to the volcanic origin of the Almadén mercury belt. The current presence of this compound might be explained by the additional stabilisation given by the presence of certain impurities (especially zinc, iron and selenium), which hinders the conversion of metacinnabar to cinnabar by decreasing the inversion temperature and by retarding the kinetics of conversion[209].

Nevertheless, a lower (or null, taking into consideration detection limits) conversion of cinnabar to metacinnabar was identified in calcine samples from the Almadenejos site. The historical investigation of the site, concerning Almadenejos mine and its furnace facilities, brought to the light the high Hg losses through the oven ashtrays, piping, and chimneys, as

[208] I. Puigdomenech, Chemical Equilibrium Software MEDUSA and Data Base HYDRA, 2002, http://www.kemi.kth.se/utbildning/gk/kemiskjmv/, Updated 18 February 2004

[209] Dickson, F.W.; Tunell, G. American Mineralogist, **1959**, *44*, 471-487

well as the very low efficiency of the roasting procedure applied in this facility[210]. Therefore, lower temperatures have been historically achieved, resulting in lower mercury recovery.

Small proportions of soluble mercury salts, such as $HgCl_2$ and $HgSO_4$ (see Figure 5, Annex 3) were also identified within the analysed samples. In this sense, both Almadén and a hot-spring Hg deposits (see section 1.3.1) have been found to contain soluble Hg-chloride and sulphate phases, which were largely absent in samples from silica-carbonate Hg deposits. Such phases could become available during roasting processes, due to the decomposition of the abundant hydrothermal alteration products, particularly clays, which are bathed in saline fluids, or even by the vaporization of remnant water[209,211]. Moreover, mercury ores and slag are exposed to repeated wetting–drying cycles and weathering processes that can induce dissolution and re-precipitation of soluble Hg species with time[212]. The presence of these species poses a risk of Hg mobilization, and therefore would require further attention.

The presence of HgO in some samples can be attributed to the slow conversion of HgS under aerobic conditions. On the other hand, the mineral schuetteite is related to supergene alteration of cinnabar, as shown by the common presence of schuetteite in many mine dumps, especially on sunlight-exposed rocks[206].

The identification of inorganic species in calcine samples form the Almadenejos site becomes of a significant importance for the overall understanding of the mercury cycle. Previous studies undertaken in the same area by Gray and co-workers[38] showed the extremely high methylmercury concentrations present within the analysed calcine samples, compared to similar samples from other mine and metallurgic facilities worldwide. Therefore, this study shall be considered as a first approach to understand the insights of the biomethylation process.

Hence, the proposed coupling of techniques has demonstrated to be a good alternative to the traditional solid-phase speciation based on chemical information. Concluding remarks have raised from XANES, μ-EXAFS and μ-XRF studies regarding the potential mobility of mercury in the frame of Almadén mining area. Additionally, these studies shall be considered as a first approach for the better understanding of the mercury cycle concerning methylation and bio-methylation mechanisms.

---

[210] Sumozas, R. Arquitectura Industrial en Almade´n: Antecedentes, Ge´nesis y Extensio´n de un Modelo, Ph.D. Thesis, University of Castilla-La Mancha, 2005; pp 171-202

[211] White, D.E.; Roberson, C.E. *Sulphur Bank, California: a major hot-spring quicksilver deposit*, Engel, A.E.J.; James, H.L.; Leonard, B.F. (eds.), New York, 1962, pp. 397-428

[212] Kim, C.S.; Rytuba, J.J.; Brown Jr., G.E. Applied Geochemistry, **2004**, *19(3)*, 379-393

3.3 CHARACTERISATION OF POLLUTED SOILS SURROUNDING A CHLOR-ALKALI PLANT

Chlor-alkali plants with mercury cathode represent one of the most important point sources for mercury environmental pollution. Consequently, this work aims at assessing the environmental impact of mercury in the neighbouring area of a chlor-alkali industry by studying mercury speciation and considering geochemical factors that might contribute to mercury mobility and contamination of the affected area.

For this purpose, XANES have been chosen for the determination of mercury species in the samples, whereas μ-XRF microprobe techniques have been used to identify possible elemental correlations (either related to natural or anthropogenic effects). Additional characterisation techniques, such as elemental analysis by ICP-OES or SES, have been considered to evaluate the overall chemical composition of the samples and the possible behaviour of Hg in the soil environment.

3.3.1 Total metal and methylmercury content analyses

Total metal content determined by MW digestions and ICP-OES analysis is summarized in Table 3, Annex 4. Hg concentrations were highly variable, ranging from more than 1 g kg^{-1} in sample M2 to about 4 mg kg^{-1} in sample M1.

These results suggest a significant spatial variability in Hg content. Additionally, it has been demonstrated that the Hg-impacted area is not restricted to the close neighbourhood of the plant, but the distribution of mercury is also strongly influenced by the transport mechanism, type of substrate and particle size[213], and redistribution by human activities on site (building, resurfacing, redistribution of materials from basins, etc.).

Methylmercury content was analysed by the combination of an extraction process (following the modified Westöo process) with the separation and quantification of the species by an HPCE-UV system[214]. Results did not show the methylmercury presence above the detection limit of 5 mg kg^{-1}. Nevertheless, it must be pointed out the high detection limits of the utilised HPCE-UV technique.

Quantification of other heavy metals revealed a strong variation in their distribution. In general terms, low concentrations of As were found, whereas a significant presence of Cu, Ni,

[213] Marvin, C.; Painter, S.; Rossmann, R. Environmental Research, **2004**, *95*, 351-362

[214] Gaona, X.; Valiente, M. Analytica Chimica Acta, **2003**, *480*, 219-230

Pb and Zn was identified within the studied samples. Finally, high contents of Fe and Mn have been found, which shall be considered as potential sorbents of Hg(II).

3.3.2 Application of SES schemes to soil samples

Similar fractional distribution of mercury has been found for all samples studied but for M4, as shown in Figure 3.7 (see also Table 4 in Annex 4).

Mercury in samples M1, M2, M3 and M5 is basically found in the residual fraction (F4) (74.4% M1, 87.4% M2, 70.0% M3, 90.7% M5), as a non-volatile weakly available Hg, most likely HgS. After the residual fraction, significant concentrations of mercury have been found in the exchangeable (16.3% M1, 9.3% M2, 17.2% M3, 5.8% M5), probably adsorbed onto Mn and/or Fe oxihydroxides. Finally, the fraction of mercury bound to organic complexes ranges from 3 to 12%.

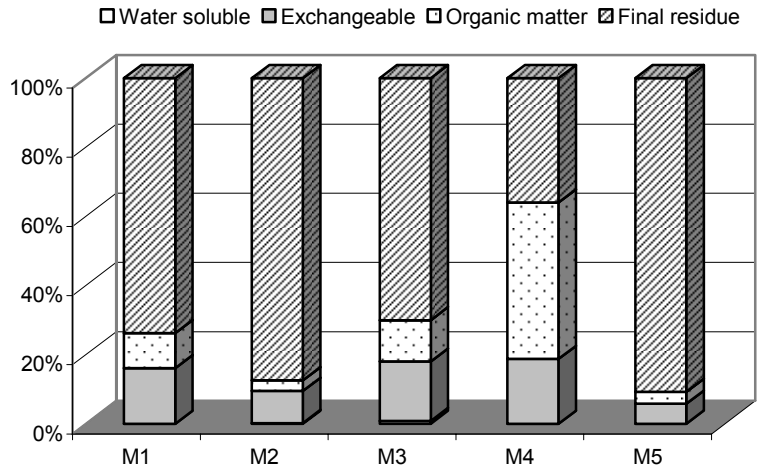

Figure 3.7 Results from the SES procedure applied to samples M1-M5.

On the other hand, mercury in sample M4 was basically found in the organic fraction (F3). This observation, together with the lower residual fraction and the higher fractions of mobile mercury (F1 + F2), might pose a higher risk of Hg mobilisation[215].

This result also corroborates the anthropogenic source of the mercury, as no correlation between the content of Hg and organic matter in sediments has been observed in natural soils[216,217,218].

[215] Biester, H.; Müller, G.; Schöler, H.F. The Science of the Total Environment, **2002**, *284*, 191-203

[216] Aston, S.R.; Rae, J.E. Environment International, **1982**, *7*, 331-336

3.3.3 Chemical characterisation by μ-XRF

μ-XRF elemental maps for Hg, As, Cl, Ca, Fe, Cu, Ni, Pb, Ti, Zn, Mn and S were carried out on mercury-rich particles identified within the studied soil samples. Figure 3.8 shows the example of a mapping obtained from a Hg-rich particle found in sample M5. In spite of the poor uniformity of Hg distribution in soils, similar qualitative information was obtained for every particle analysed by μ-XRF. Nevertheless, it must be pointed out that the obtained information might not be representative for the bulk of the samples.

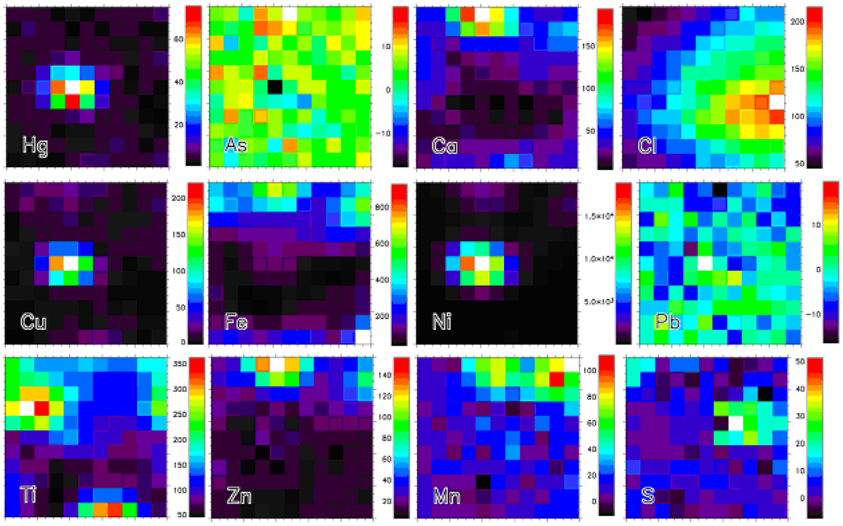

Figure 3.8

μ-XRF elemental maps for Hg, As, Cl, Ca, Fe, Cu, Ni, Pb, Ti, Zn, Mn and S on a 100 μm^2 area in a Hg-rich particle found in M5. White colour shows highest count-rate for each element, without normalising.

Figure 2 in Annex 4 shows pair correlation diagrams of different elements related to Hg, taking into account fluorescence signal from each mapping analysis. Different trends have been identified within this evaluation:

- No correlation between Hg and As, Cl and Pb. No further conclusions can be driven from this observation given the low content of As and Pb, as well as the low ionisation achieved for Cl at the working conditions (13 KeV, whilst K_α (Cl) = 2622 eV).
- The presence of Fe and Mn is related to the absence of Hg and vice versa. This point indicates that, for the studied Hg-rich particles, mercury is not associated (adsorbed) with Fe- or Mn-oxyhydroxides.
- Linear correlation between mercury and either Cu or Ni. These results suggest the possible formation of solid solutions of these elements within the same crystalline

[217] Loring, D.H.; Rantala, R.T.T.; Smith, J.N. Environmental Biogeochemistry, **1983**, *35*, 59-72

[218] Pelletier, E.; Canuel, G. Marine Pollution Bulletin, **1988**, *19*, 336-338

structure. Moreover, the absence of correlation between these elements and S would indicate that the correlation of these elements is not related with their known affinity toward sulphide.

- Linear correlation between Zn and Fe. This correlation has been attributed to the possible sorption of Zn onto Fe oxy-hydroxides.

3.3.4 Mercury speciation by XANES and µ-XANES

XANES spectra from samples M1 to M5 are shown in Figure 3.9. Due to the very low Hg concentration, a very noisy XANES spectrum was obtained from sample M1. Consequently, µ-XANES analyses were carried out over two Hg-rich particles identified by µ-XRF studies. Spectra shown in Figure 3.9 correspond to the average of five replicates for each XANES and µ-XANES spectrum.

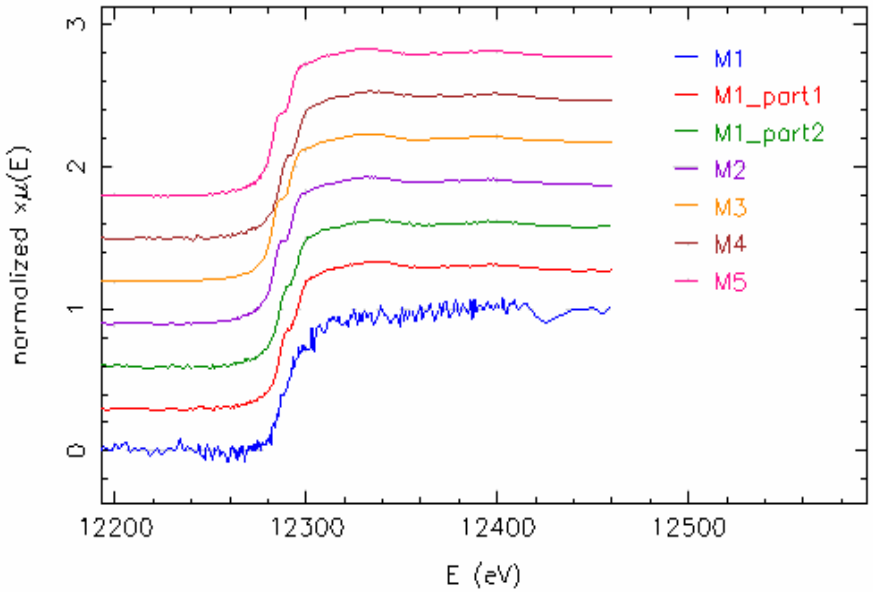

Figure 3.9 Comparison of normalised XANES spectra of M1,M2,M3,M4 and M5, and µ-XANES spectra of particle 1 and 2 of M1 (note deliberate offset of spectra to better observe the differences).

Results of principal component analysis (PCA) of samples M1 (Hg-rich particles) to M5 indicate a major contribution of inorganic species: cinnabar (HgS_{red}), HgO, $HgSO_4$ and corderoite.

Figure 1 in Annex 4 shows the corrected XANES spectra for samples M2 to M5 as well as the adjusted spectra from the linear combination of reference compounds obtained according to the PCA analysis. The relative proportions of each reference compound identified in each sample as well as the reduced chi-square value (χ^2) are reported in Table 3.7.

Table 3.7 Chemical speciation of Hg rich particles in M1, and sample bulk in M2, M3, M4 and M5. Concentration values expressed in % over total mercury content in each sample.

Sample	Beamline	Detection Mode	HgS_{red}	HgO	$HgSO_4$	Corderoite	Reduced χ^2
M1 part. 1	L	Fluorescence		86.4	16.85		0.028
M1 part. 2	L	Fluorescence	26.28		79.95		0.030
M2	A1	Fluorescence	32.85	10.31	19.82	33.47	0.00028
M3	A1	Fluorescence	32.96	10.19	19.79	33.58	0.00030
M4	A1	Fluorescence	33.18	9.91	19.85	33.82	0.00045
M5	A1	Fluorescence	36.78	6.12	18.05	37.28	0.00020

Analysis of sample bulk by XANES has shown the predominance of cinnabar and corderoite, representing together more than two thirds of total mercury concentration. Nevertheless, more soluble inorganic mercury compounds ($HgCl_2$ and HgO) have been also identified in significant proportion (from 6 to 20 %), posing a potential source of mercury mobilisation.

Analyses of Hg-rich particles by μ-XANES (sample M1) have shown the predominance of HgO and $HgSO_4$ compounds. This observation supports the hypothesis of a highly heterogeneous anthropogenically modified environment.

Taking into account the specific environmental conditions found in the site (see Table 1 in Annex 4), the presence of sulphide and polysulphide species in soils may lead to the formation of stable complexes with trace metals, with high stability constant for mercury sulphide complexes (i.e. log K_{HgS} = 42.0)[219]. On the other hand, the expected high chloride concentrations in the point source (brines are used as raw material in chlor-alkali plants) may induce the formation of Cl-bearing mercury compounds, such as corderoite.

Despite the well-known stability of cinnabar, mercury can be remobilized by oxidation in surface, highly-oxygenated soil or wastes. For instance, the transport of dissolved oxygen by burrowing organisms can cause the local oxidation of reduced inorganic compounds[220], with the consequent formation of HgO. Moreover, the partial or full oxidation of oxygen-reactive metastable sulphides (e.g., iron sulphides) to $S_xO_y^{-z}$, can lead to the formation of soluble mercury complexes, such as $HgSO_4$[221].

[219] Gagnon, C.; Pelletier, E.; Mucci, A. Marine Chemistry, **1997**, *59*, 159-176

[220] Oenema, O.; Steneker, R.; Reynders, J. Hydrobiological Bulletin, **1988**, *22*, 21-30

[221] Morse, J.W. Marine Chemistry, **1994**, *46*, 1-6

3.4 EVALUATION OF HUMAN TEETH RESTORED WITH DENTAL AMALGAM

Synchrotron X-ray microprobe techniques have been applied to assess the diffusion and molecular environment of Hg (as well as other elements) present in human teeth restored with dental amalgams.

3.4.1 Samples characterisation by SEM-EDS

The analysis by SEM-EDS of sixteen human molar teeth restored with mercury amalgam lead to a qualitative overview of the presence of major components within the different tooth regions considered (enamel, dentine, and root regions). A representative elemental mapping as well as a contrast microscope image at the interface enamel-amalgam-dentine, is shown in Figure 3.10.

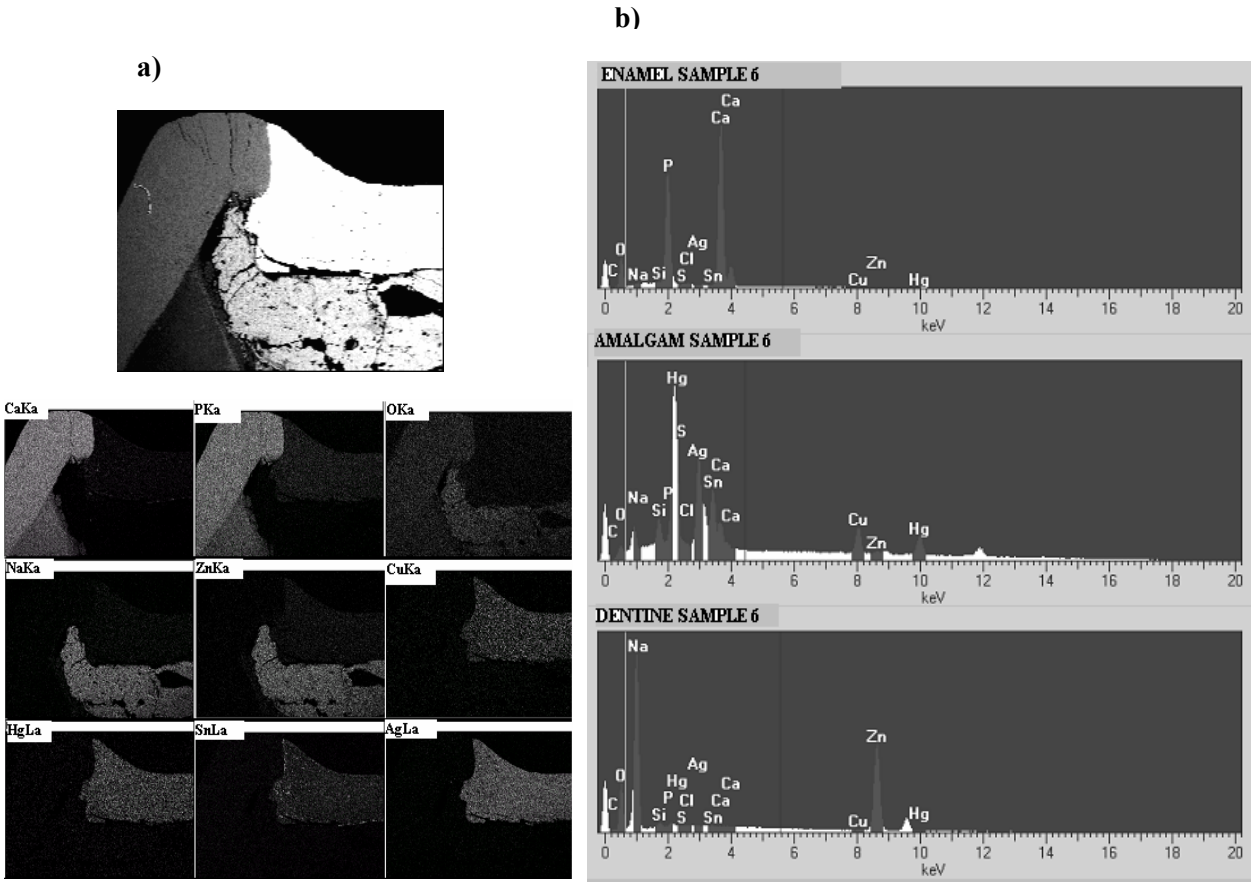

Figure 3.10 (a) Contrasted microscope image of the interface enamel-amalgam-dentine from a representative tooth sample, and mapping of some elements (Ca, P, O, Na, Zn, Cu, Hg, Sn and Ag) in this region. (**b)** EDS spectra from a full-field area of the enamel, amalgam and dentine regions from the same sample.

According to Figure 3.10, a main contribution of Ca, P and O is observed at the enamel region, whereas Hg, Ag, Sn and Cu were basically found at the amalgam region. Zn, Na, Ca and O were found to be the main elements in the dentine.

3.4.2 Microprobe analyses

The first step consisted of putting into gear the technical setup by determining the optimum sample thickness and depth for signal acquisition. μ-XRF mapping analyses were performed in selected points (amalgam, enamel and dentine regions) for a representative sample and at different depths (from 10 to 210 μm), in order to study the maximum fluorescence signal as function of depth for the studied elements (see Figure 2, Annexe 6). According to this figure, a heterogeneous elemental distribution was found throughout the considered depth range, although a maximum signal was obtained at ~100 μm depth. Therefore, and taking into account that thinner samples would be expected to yield better spatial resolution in the X-ray fluorescence images[222], 100μm-thickness samples were selected for microprobe analyses

Figure 3.11 shows μ-XRF elemental maps for several elements in the interface amalgam-dentine, and distribution profiles for Hg, Cu, Zn, Ca, Mn, Fe, Pb and Br along the sixteen restored teeth from μ-XRF elemental maps are shown in Figure 3, Annex 6. As expected, Hg is mainly located in the amalgam region of the tooth, suggesting a minimum diffusion of this element throughout the dentine, above the detection limit of the technique (~0.1 ppm).

Likewise, Cu, as a constituent of the amalgam, was found in higher proportions within this region, although showing a higher tendency to diffusion toward the dentine region. This observation has been attributed to a partial exchange with Ca ions present in this adjacent region. A similar pattern was found for Zn, a minor component of the amalgam. In both cases, a similar isovalent replacement of their divalent ions [Cu^{2+} and Zn^{2+}] has been found for Ca^{2+} in hydroxyapatite of hard tissues[223-227]. This point would indicate a relative ionic character of these elements within the studied teeth, the amalgam being a potential source for these ions.

---

[222] Martin, R.R.; Naftel, S.J.; Nelson, A.J.; Feilen, A.B.; Narvaez, A. Journal of Environmental Monitoring., **2004**, *6*, 783-786

[223] Lochner, F.; Appleton, J.; Keenan, F.; Cooke, M. Analytica Chimica Acta, **1999**, *401*, 299-306

[224] Carvalho, M.L.; Marques, J.P.; Brito, J.; Casaca, C.; Cunha, A.S. Nuclear Instruments and Methods in Physics Research B, **2002**, *196*, 148-154

[225] Barrea, R.A.; Pérez, C.A.; Ramos, A.Y.; Sánchez, H.J.; Grenón, M. X-Ray Spectrometry, **2003**, *32*, 387-395

[226] Tsutomu, T.; Junko, H.; Hitoshi, M.; Tetsuo, H. European Journal of Oral Sciences, **2005**, *113(2)*, 180-183

[227] Wakamura,M.; Kandori, K.; Ishikawa, T. Colloids and Surfaces A, **1998**, *142(1)*, 107-116

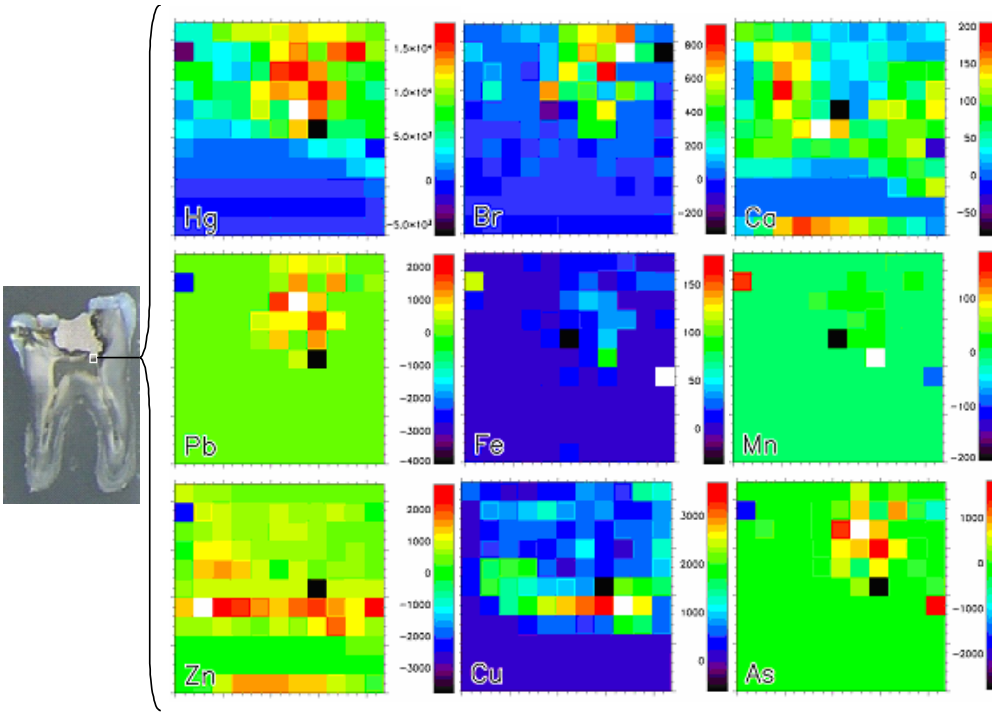

Figure 3.11 μ-XRF elemental maps for Hg, Br, Ca, Pb, Fe, Mn, Zn, Cu and As, on a thin section (100 μm^2 area) in the amalgam-dentine region, of a teeth slice mounted for synchrotron analysis. White colour shows the higher count-rate for each element (arbitrary units).

As for Cu and Zn, Pb would be expected to diffuse into the dentine region, taking into account the known tendency of Ca^{2+} substitution by Pb^{2+} in hydroxyapatite[227-229]. This extent has not been observed in the studied samples, therefore suggesting a lower ionic character of Pb than Cu or Zn within the dental amalgam.

Concerning Mn, Fe and Br, these elements show a similar behaviour: a higher concentration in the amalgam region, decreasing sharply to the root region.

Calcium concentration in the enamel is very high, as the region is basically formed by of calcium hydroxyapatite ($Ca_{10}(PO_4)_6(OH)_2$) crystals. On the other hand, dentine consists of ~ 75% inorganic calcium hydroxyapatite and ~ 25% organic material, mainly collagen. This point is consistent with observations made in Figure 3, Annex 6, where the amount of Ca decreases when approaching to the pulp region.

No heavy metals have been found in the pulp cavity and root regions (below the detection limits of the technique, ~ 0.1 ppm). Both regions consist of a soft connective tissue, richly

[228] Carvalho, M.L.; Casaca, C.; Pinheiro, T.; Marques, J.P.; Chevallier, P.; Cunha, A.S. Nuclear Instruments and Methods in Physics Research B, **2000**, *168*, 559-565

[229] Wiechula, D.; Fischer, A.; Kwapulinski, J.; Loska, K.; Fischer, T.; Kurpas, P. Archives of Environmental Contamination and Toxicology, **2006**, *51*, 314-320

supplied with blood vessels and nerve endings. Consequently, our observations suggest that a minimum diffusion of metals to the blood occurs.

Elemental correlation plots (see Figure 4, Annex 6) show a linear relationship between Hg and Cu, probably due to the formation of mixed Hg-Cu compounds during the amalgamation process. Moreover, Figure 4, Annex 6, supports the hypothesis of a substitution reaction between Cu/Zn and Ca, as for a given region, the increase of Cu and Zn is linearly related with the depletion on Ca signal. On the other hand, no Ca-Pb correlation has been found, suggesting the presence of this element in a rather immobile form.

3.4.3 Study of the local environment of mercury by μ-EXAFS analysis

The averaged data from the (Hg L_{III}-line) μ-EXAFS spectra of the amalgam, amalgam/dentine interface and amalgam/enamel interface, have lead to nearly identical EXAFS features (Figure 3.12). The similar Hg coordination environment could be due to either (1) no diffusion of Hg from the amalgam resulting in new Hg-bearing phases, or (2) to diffusion occurring by small molecular-scale clusters that are similar to the amalgam with respect to the local Hg coordination environment. However, the μ-XRF studies detected no Hg beyond the amalgam interface, indicating that no diffusion of Hg is taking place (above the detection limit of the technique) .

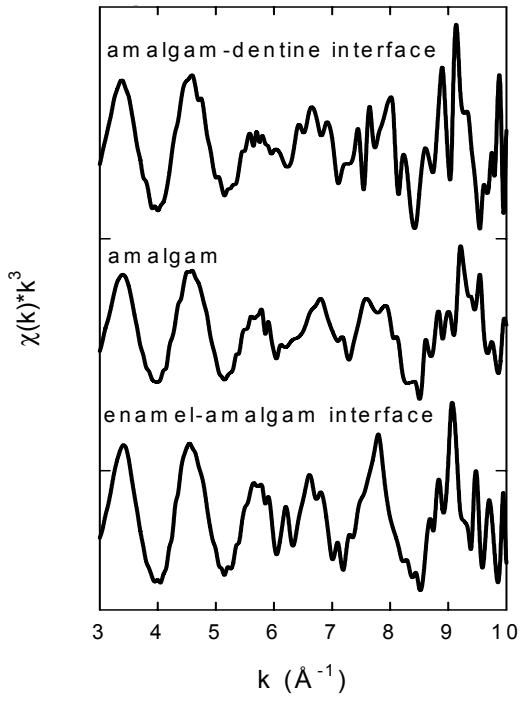

Figure 3.12

k^3-weighted Hg L_{III}-edge μ-EXAFS at three locations; **a.** the amalgam/dentine interface; **b.** the middle of the amalgam; and **c.** the amalgam/enamel interface.

The molecular environment of Hg in the amalgam region was determined by comparing the Hg L_{III}-edge μ-EXAFS spectrum of this region with the simulated EXAFS spectra of γ-

Ag_2Hg_3, $Hg_{0.1}Sn_{0.9}$ and HgO. Figure 3.13 shows the EXAFS data (left) and the Fourier transform (right) of the related spectra. The most striking difference between the simulated model compound spectra and that of the amalgam region is the lack of strong backscattering at higher k values in the amalgam spectra, which would be expected from Hg-Hg neighbours.

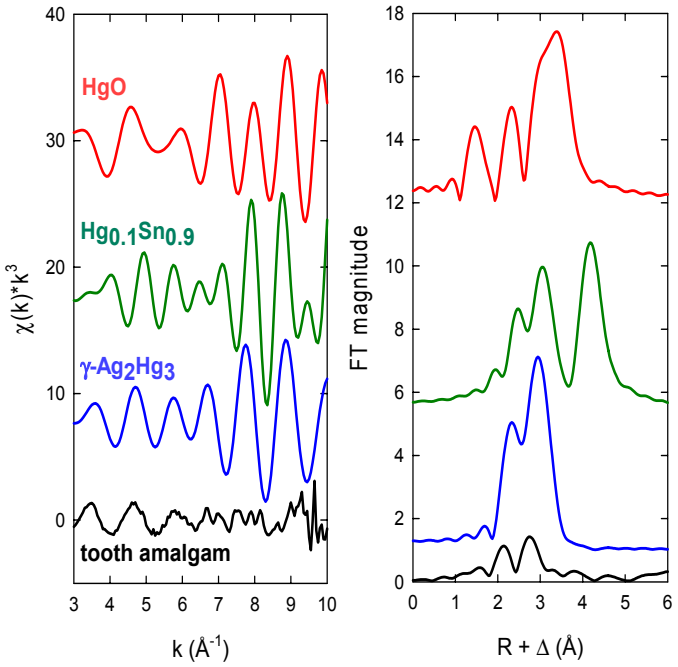

Figure 3.13

k^3-weighted Hg L_{III}-edge µ-EXAFS (left) at the tooth amalgam and the simulated compounds: γ-Ag_2Hg_3, $Hg_{0.1}Sn_{0.9}$, and HgO. And related Fourier transform (right).

Due to the low signal-to-noise ratio above k=6 $Å^{-1}$, only the initial coordination environment of Hg has been constrained. The µ-EXAFS spectrum of the amalgam region was fitted with three models: (1) one shell of Hg atoms, (2) one shell of Ag atoms and a second shell of Hg atoms, and (3) one shell of Sn atoms and a second shell of Hg atoms. Figure 3.14 displays the considered fits, and numerical results are shown in Table 3.8. Using the phase shifts and backscattering amplitudes from the Ag-Hg model, we obtain a good fit of the Hg amalgam data with respect to coordination numbers and bond distances, by reporting the smallest reduced χ^2. Therefore, this result suggests the formation of the γ-Ag_2Hg_3 phase at the first coordination environment of Hg during the amalgamation process. However, fit values for the Debye-Waller factors are unreasonably large, taking into account that reported values for σ^2 in the literature for Hg EXAFS are on the order of 0.001-0.006 $Å^2$ [230]. This fact may be related to poor data quality at intermediate to higher k values. Therefore, further analyses are strongly

[230] Allen, P.G.; Gash, A.E.; Dorhout, P.K.; Strauss, S.H. Chemistry of Materials, **2001**, *13(7)*, 2257 - 2265

recommended, taking into consideration optimal data collection protocols (i.e. data acquisition at much lower temperatures).

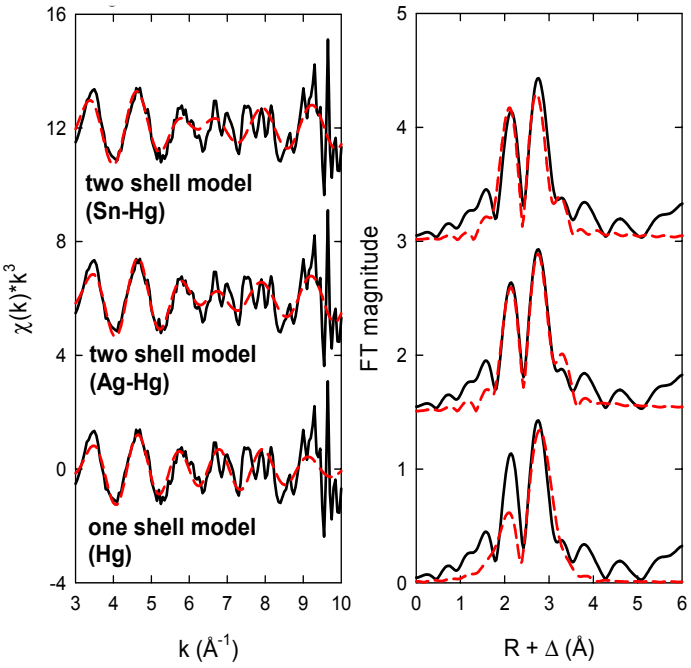

Figure 3.14

k^3-weighted Hg L_{III}-edge μ-EXAFS (left) and Fourier transform (right) in the amalgam region. Data are represented by the solid black line, and fits of the three considered models are shown as dashed red lines.

Table 3.8 Fit results of the Fourier transform of the three considered models, in the amalgam region.

Z	CN	R (Å)	σ^2 (Å^2)	ΔE°	Red χ^2	S_0^2
Sn	2	2.82	0.011	-3	3.5	0.9
Hg	9	2.91	0.03			
Ag	3	2.89	0.02	-1	2.6	0.9
Hg	4	2.97	0.02			
Hg	8	2.89	0.024	-2	4.3	0.9

A fourth fit with a first shell of oxygen atoms was also attempted, although it did not yield as credible a fit as the other three structures. In addition, this fit resulted in an Hg-O pair correlation at 1.7 Å, a distance too short to be considered realistic. As a matter of fact, the shortest predicted Hg-O distance derived from summing the Shannon radius values of $^{II}Hg^{2+}$ (0.69 Å) and $^{III}O^{2-}$ (1.36 Å) is 2.05 Å[231]. Therefore, the absence of oxygen is an indication of

[231] Shannon, R.D. Acta Crystallographica A, **1976**, *32*, 751-767

the poor (or null) interaction of mercury with the environment and the improbable transformation of this element with time.

Chapter 4

Conclusions

Results of the present thesis, described in Chapter 3 and Annex section, have demonstrated the qualitative and quantitative applicability of XAS techniques to the analysis of both environmental and biological samples. Although synchrotron-based techniques cannot be considered as a routine analytical tool for sample characterization due to both the high analysis costs and the limited synchrotron sources availability, they can importantly contribute to throw light to very required key issues that are not affordable with conventional techniques. Hence, XANES and EXAFS spectroscopies have been shown to be powerful speciation techniques, with high capacity for species recognition and practically no sample pre-treatment. On the other hand, microprobe techniques have been confirmed as a future trend toward the study of chemical speciation in microscopic environments. This future trend is confirmed by the construction of new beamlines or the upgrading of already existing conventional beamlines where the microprobe option has been considered. In this Thesis, the usefulness of available micro-scale techniques have been demonstrated both for environmental and biological samples.

Taking into consideration the studies carried out within this Thesis, the main conclusions driven from the obtained results can be summarized as:

<u>For the sorption and bioavailability of methylmercury on model soil components:</u>

- Adsorption trend of CH_3HgCl and CH_3HgOH onto selected soil components (montmorillonite, kaolinite and humic acid) is very similar along the whole pH range considered (3 to 9), although degree of adsorption is higher for CH_3HgOH due to the higher reactivity of its hydroxide group.
- For both methylmercury compounds considered, the adsorption capacity follows the series: montmorillonite > kaolinite > humic acid. This trend has been explained by the higher adsorption capacity of clay minerals, which is related to their higher cation exchange capacity. On the other hand, the limited surface area of kaolinite restricts the extent of adsorption of cations onto this clay material.
- XANES technique provides valuable information regarding the type of interaction taking place between CH_3HgCl or CH_3HgOH and some key soil components. Results show that a similar interaction occurs along the whole pH range considered, although significant differences have been identified within the different soil components considered. Hence, methylmercury – surface interaction was found to be more ionic for clays than humic acid, which is attributed to the thiol groups of the latter. On the

other hand, this interaction is more covalent for CH_3HgOH than CH_3HgCl, probably due to the formation of hydrogen bonds between CH_3HgOH and functional surface groups or condensed chemical bonds with surface OH- groups by elimination of water.

- Luminescent bacterial organomercury sensors have been successfully applied to the assessment of methylmercury bioavailability, even at very low concentration ranges. Experimental results reveal that the fraction of bioavailable methylmercury is about five-fold higher for spiked montmorillonite than for humic acids. These results are consistent with XANES observations, which determined a higher ionic character for methylmercury adsorbed onto montmorillonite.

For the mercury speciation in samples from the Almadén district:

- Aqua regia is found to incompletely digest ore and soil samples by microwave-assisted digestions. On the contrary, a complete digestion is successfully achieved by using HF.
- Speciation results reveal the predominant presence of cinnabar in ores and soils, metacinnabar in slag, and HgO in calcines. In all samples, slightly soluble mercury compounds ($HgCl_2$, $HgSO_4$ and schuetteite) are also identified with contents ranging from 5 to 49 % of the total mercury concentration. This fact favors the mobilization of mercury in the environment of Almadén, and poses an evident risk both to biota and human beings in the area. In terms of speciation, important similarities between Almadén and hot-spring type mercury deposits are found, despite its different geological origin.
- A lower (or null) conversion of cinnabar to metacinnabar is identified in calcine samples from the Almadenejos site. This finding has been related to the low efficiency of the roasting process developed in this facility.
- The combination of microprobe techniques and SES schemes is proven to be a powerful and reliable tool when assessing heavy metal behavior in a given site. In the study case, μ-XRF maps of selected mercury-rich particles reveal a correlation among Hg, Pb, Ni and S, indicating a possible (geo-)chemical linkage of these elements. Correlations are also identified between Hg and Fe/Mn, which are attributed to sorption of mercury onto oxy-hydroxides of Fe and Mn. This finding is supported by

results from SES. Correlation between Hg and Ni has been explained by the tendency of both elements to adsorb onto crystalline Fe-Mn oxyhydroxides.

Although further analysis of additional samples would be advisable to improve the robustness of the presented results, it is important to highlight that this is the first time that Almadén-type mercury samples have been characterized by a synchrotron-based spectroscopic technique. This contribution is to be used not only to improve the knowledge of the geo-chemistry of the area, but also to become a key issue within the forthcoming risk assessment exercises.

For the study and characterization of the surroundings of a chlor-alkali plant:

- Mercury concentration in surface soils around a chlor-alkali plant increases by a factor of ~10^4-fold when compared to the pre-industrial level. Significant spatial heterogeneities have been identified within the impacted area, supporting the need of a proper identification of the main anthropogenic and geochemical factors affecting mobility and distribution of mercury.
- SES analyses reveal large proportions of weakly available Hg in the residual fraction, although a significant fraction of Hg is still bound to exchangeable phases. A limited amount of Hg remains bounded to the water-soluble fraction, suggesting a poor Hg mobilisation due to weathering processes.
- Chemical speciation achieved by XANES indicates a main contribution of inorganic species (cinnabar and corderoite) with a limited presence (up to 20% of total Hg content) of more soluble inorganic compounds (HgO and $HgSO_4$). Evidences of a mobile mercury fraction have been obtained both by XANES and SES, therefore supporting the hypothesis of a possible mercury mobilisation.
- μ-XRF analysis shows a geochemical correlation of Hg, Cu and Ni, which suggests the possible formation of solid solutions of these elements within the same crystalline structure. No correlation has been found between Hg and Fe/Mn, indicating that sorption of Hg onto Fe- or Mn- oxyhydroxides is negligible.

For the Hg behavior in human teeth restored with dental amalgam:

- Experiments have proven the ability of μ-XRF and μ-EXAFS techniques to provide unique information of teeth specimens at micro-scale level. This extent opens interesting possibilities for research in dentistry.
- Assessment of elemental distribution by μ-XRF reveals a significant heterogeneity within and among the studied tooth regions (enamel, amalgam, dentine and root). Microprobe analyses shows no diffusion of Hg throughout the tooth above the detection limits of the technique, whereas elemental correlations have been identified between Hg and Cu.
- Diffusion of Cu and Zn from the amalgam to the dentine region has been identified by μ-XRF analyses. This fact correlates with the slight depletion on Ca concentration observed in the dentine region, suggesting the possible exchange of Ca^{2+} by Cu^{2+}/Zn^{2+} in hydroxiapatite crystals ($Ca_{10}(PO_4)_6(OH)_2$). On the other hand, Pb has been found not to diffuse into the dentine region, therefore indicating its presence in a less mobile form.
- μ-EXAFS analyses have been applied to assess the molecular environment of mercury in the studied regions and the possible impact on Hg release to saliva. Results support the existence of the same Hg coordination environment in both the amalgam bulk and the interface amalgam – tooth. This observation reinforces the hypothesis that no diffusion of mercury is taking place out of the amalgam, which would probably lead to the formation of new Hg-bearing phases.
- According with μ-EXAFS analyses, the molecular environment of Hg in the amalgam region seems to be related to the γ-Ag_2Hg_3 phase formed during the amalgamation process. Nevertheless, the high Debye-Waller factor found suggests the need of further μ-EXAFS analyses, in order to gain confidence on the proposed mercury environment.

Reported results should be only considered as indicative due to the limited number of specimens analyzed, the relatively poor data quality and the limitations of the technique. In this concern, further studies will be undertaken improving data acquisition and taking into consideration the medical history of each dental specimen.

The present results open a new research topic on the characterization of dental amalgams that will improve both the knowledge of dental materials and the assessment for clinical applications.

Chapter 5

Annexes

Annex 2

Anal Bioanal Chem (2005) 382: 1541–1548
DOI 10.1007/s00216-005-3338-6

ORIGINAL PAPER

**Anna Bernaus · Xavier Gaona · Angela Ivask
Anne Kahru · Manuel Valiente**

Analysis of sorption and bioavailability of different species of mercury on model soil components using XAS techniques and sensor bacteria

Received: 24 February 2005 / Revised: 8 May 2005 / Accepted: 13 May 2005 / Published online: 22 June 2005

Abstract The present work studies the adsorption behaviour of mercury species on different soil components (montmorillonite, kaolinite and humic acid) spiked with CH_3HgCl and CH_3HgOH at different pH values, by using XAS techniques and bacterial mercury sensors in order to evaluate the availability of methyl mercury on soil components. The study details and discusses different aspects of the adsorption process, including sample preparation (with analysis of adsorbed methyl mercury by ICP-OES), the various adsorption conditions, and the characterization of spiked samples by XAS techniques performed at two synchrotron facilities (ESRF in Grenoble, France and HASYLAB in Hamburg, Germany), as well as bioavailability studies using mercury-specific sensor bacteria. Results show that XAS is a valuable qualitative technique that can be used to identify the bonding character of the Hg in mercury environment. The amount of methyl in mercury adsorbed to montmorillonite was pH-dependent while for all soil components studied, the bond character was not affected by pH. On the other hand, clays exhibited more ionic bonding character than humic acids did with methyl mercury. This interaction has a higher covalent character and so it is more stable for CH_3HgOH than for CH_3HgCl, due to the higher reactivity of the hydroxyl group arising from the possible formation of hydrogen bonds.

The bioavailability of methyl mercury adsorbed to montmorillonite, kaolinite and humic acids was measured using recombinant luminescent sensor bacterium *Escherichia coli* MC1061 (pmerBR$_{BS}$luc). In case of contact exposure (suspension assays), the results showed that the bioavailability was higher than it was for exposure to particle-free extracts prepared from these suspensions. The highest bioavailability of methyl mercury was found in suspensions of montmorillonite (about 50% of the total amount), while the bioavailabilities of kaolinite and humic acids were five times lower (about 10%). The behaviour of methyl mercury in the presence of montmorillonite could be explained by the more ionic bonding character of this system, in contrast to the more covalent bonding character observed for humic acids. Thus, XAS techniques seem to provide promising tools for investigating the mechanisms behind the observed bioavailabilities of metals in various environmental matrices, an important topic in environmental toxicology.

Keywords Methyl mercury adsorption · Bonding type · Synchrotron · XANES · Recombinant luminescent mercury sensor bacteria

A. Bernaus · X. Gaona · M. Valiente (✉)
Departament de Química, Unitat Analítica,
Centre GTS, Facultat de Ciències,
Universitat Autònoma de Barcelona, Edifici Cn,
08193 Bellaterra, Barcelona, Spain
E-mail: manuel.valiente@uab.es

A. Ivask · A. Kahru
National Institute of Chemical Physics and Biophysics (NICPB),
Akadeemia tee 23, 12618 Tallinn, Estonia

Introduction

Hg is found in the environment mainly as inorganic mercuric compounds, although organomercuric compounds can be also important under certain conditions. Although CH_3HgCl is only found in small amounts (1–3% of the total mercury), its presence in the environment becomes a potential risk to human health given its high toxicity and capacity for bioaccumulation [1]. On the other hand, methyl mercury has a strong affinity to organic matter, which reduces its mobility in the environment [2]. It is known that organomercuric compounds, such as CH_3HgCl, are sparingly soluble in water and do not react with acids and bases. However, CH_3HgOH is very soluble due to the high ability of the hydroxide group to establish hydrogen bonds.

When Hg(II) species are present in the soil, they are exposed to several chemical reactions. Soil conditions (pH, pE, temperature, type of soil, and so on) normally favour the formation of inorganic Hg compounds

($HgCl_2$ and $Hg(OH)_2$), and Hg(II) complexes with organic anions. However, the chemical interaction of methyl mercury in soils and sediments when complexed with organic and inorganic substances has still not been clarified [3, 4]. This adsorption in soils also depends upon the physico-chemical properties of the latter, which are related to its composition. Together with soil clays (mainly kaolinite and montmorillonite), humic substances are responsible for much of the chemical activity in soils.

Kaolinite minerals are hydrated aluminosilicates, with a general chemical composition Al_2O_3:SiO_2:H_2O = 1:2:2 per unit cell. Structurally they are 1:1 type phyllosilicates with some isomorphous substitution, and a very small permanent charge per unit cell. Because of the presence of exposed hydroxyl groups, kaolinite has a variable, pH-dependent charge. The cation exchange capacity is very small (in the range of 1–10 mEq/100 g) because of its restricted surface area (approximately 7–30 $m^2\ g^{-1}$) that limits the adsorption capacity for cations. On the other hand, montmorillonite has a symmetrical unit cell structure. It also has OH groups on the crystal edges or on exposed planes, and especially at high pH, the hydrogens of these hydroxyls dissociate slightly at the surface of the clay. Its negative charge arises mainly from isomorphous substitutions and it has a cation exchange capacity of 70 mEq/100 g, due to its large specific surface area (approximately 700–800 $m^2\ g^{-1}$). Analogously to clay components, humic substances are typical constituents of soils. Humic acids are complex aromatic macromolecules with amino acids, amino sugars, peptides and aliphatic compounds involved in linkages between the aromatic groups, which are synthesized during the decomposition of plant and animal residues. The total acidity or exchange capacity of humic acid is attributed to the presence of acidic H in aromatic and aliphatic carboxyl and phenolic hydroxyl groups. In addition, they contain dissociable H^+ ions from amino and thiol groups. However, their acidities (1.5–2.7 mEq/100 g) and their carboxylic contents are low. The charges of humic acids are determined by the dissociation of their functional groups, and are thus pH-dependent [5].

X-ray Absorption Spectroscopy (XAS) techniques are proposed for the direct study of soil samples contaminated with mercury compounds; these techniques can be used to determine the interaction between methyl mercury and soil components with almost no sample pre-treatment (and therefore a minimum of sample modification), and without the poor ability to predict the mobility and bioavailability of methyl mercury that results from using chemical extraction [6, 7]. XAS techniques have been used to determine the speciation and binding of mercury in a variety of compounds, such as coal [8], humic substances [9–11], and Al/Fe-hydroxides [12], but methyl mercury interactions have only been studied in natural organic matter [13–15].

The use of XAS techniques in combination with assays based on living organisms is expected to provide a deeper understanding of the environmental hazards posed by soil-adsorbed Hg compounds, by clarifying their bioavailability and toxicity. In the present study, the bioavailability of Hg compounds was determined using recombinant luminescent sensor bacteria, which report on the presence of mercuric compounds by increasing their bioluminescence [16]. It should be stressed that this increase in bioluminescence is only caused by bioavailable Hg compounds: these compounds have to cross the biological membrane, enter the cell and bind a specific protein, triggering the synthesis of luciferase (light-producing enzyme). The specific luminescent response of the sensors towards mercuric compounds has been measured and quantified previously for very low, sub-toxic amounts of these compounds (limit of determination for CH_3Hg^+ is 0.05 μg kg^{-1} and for Hg^{2+} 2 μg kg^{-1}) [16]. Analogously to XAS, analysis of the samples with bacterial biosensors does not require any pre-treatment.

Experimental

Equipment

The XAS spectra were measured at both the European Synchrotron Radiation Facility (ESRF) in Grenoble (France), at the beamline ID26, and at Hamburger Synchrotronstrahlungslabor (HASYLAB) in Hamburg (Germany), at the beamline A1. The beam set-ups are detailed in Table 1.

A test tube shaker (TTS 2, Wilmington, USA) was used to carry out methyl mercury adsorption on model soil components. Mercury was quantified by means of an Inductively Coupled Plasma-Optical Emission Spectrometer (ICP-OES, Model 3410 equipped with minitorch, from ARL, USA) with a detection limit of 0.5 mg L^{-1}.

Pellets were prepared for synchrotron analysis using a mortar (to mill the sample), a magnetic shaker (A-05, SBS, Spain), and a press (25-ton ring press, RIIC (Research Industrial Instruments Company), London, UK).

In the analysis of bioavailable organic mercury, the spiked soil components were analyzed using *Escherichia coli* MC1061 (pmerBR$_{BS}$luc) sensor bacteria. The bioluminescence was quantified by 1253 luminometer (Thermo Labsystems, Helsinki, Finland).

Sample description and preparation

The montmorillonite K-10, kaolinite and humic acids were supplied by Aldrich (Germany). These synthetic materials represent typical soil components, although these three substrates do not represent the complex "soil" matrix.

The samples were prepared for synchrotron analysis as follows. 0.25 g of each soil material (kaolinite, montmorillonite or humic acid) was mixed with 25 mL

Table 1 Beamline set-ups

Element	ESRF, beamline ID26	HASYLAB, beamline A1
(Insertion) Device	Undulator	Bending magnet
Source energy	6 GeV	4.5 GeV
Maximum current	200 mA	100 mA
Monochromator crystal	Si(1,1,1)	Si(1,1,1)
Resolution ($\Delta E/E$)	$\sim 10^{-4}$	$\sim 10^{-4}$
Photon flow in the sample	$> 10^{13}$ photons s^{-1}	About 10^{8} photons s^{-1}
Spot size in the sample	200×80 μm	2×3 mm
Detectors	Photodiodes for flux monitoringGe (13 elements)	Three ionisation chambersGe (five elements)
Angle bunch-sample	45°	45°
Temperature	Room	Room, liquid N_2

of an aqueous solution of methyl mercury (25 μg mL^{-1}) chloride or hydroxide. The pH of each sample was adjusted (see pH values below) with diluted HNO_3 or NaOH. After 24 h of equilibration (with regular control and adjustment of pH), the samples were centrifuged and the resultant solid was air-dried in a fume hood until constant weight.

Once dried, spiked samples were mixed with polyethylene in a plastic vial by stirring for 10 min in a Vortex apparatus, until the final homogenisation. Then the mixture was pressed into pellets under 5 tons cm^{-2} of pressure for 5 min. The total amount of spiked material in each pellet varied from 50 to 100 mg and polyethylene (as a diluting agent) from 100 to 150 mg.

Additionally, eight samples of pure compounds ($HgCl_2$, $HgSO_4$, HgO_{red}, $Hg(CH_3COO)_2$, CH_3HgCl, HgS_{red}, HgS_{black}, and C_6H_5HgCl) were prepared to serve as standards for XAS. These references were also mixed with polyethylene and pressed to obtain corresponding pellets.

The supernatant from spiking experiments (remaining solution) was filtered, stabilized and analysed by ICP-OES, in order to determine the final concentration for each soil sample as the difference between the initial concentration and this remaining solution.

The analysis of bioavailability followed essentially the same procedure as used for sorption studies, except that much more dilute samples were prepared: 2 g of soil material (kaolinite, montmorillonite and humic acid) was mixed with 25 mL of 0.8 μg L^{-1} aqueous solutions of methyl mercury chloride, and the pH of each sample was adjusted to 7. Dried spiked samples (soil components) were used to prepare suspensions and extracts as described below.

All glassware and plastic containers used for spiking were previously soaked overnight in 25% nitric acid and rinsed.

Safety aspects

Due to the high toxicity of the mercury compounds used in this study, special safety precautions were used. Thus, open samples were only handled under the fume hood, and they were encapsulated in Kapton foils, avoiding direct contact of the mercury pellets with the atmosphere or any material at the beamline. Vermiculita Exfoliada, a universal absorbent of laminated hydrated minerals, mainly aluminium, iron and magnesium silicates (Carl Roth, Spain), was used to absorb Hg compounds in poured solutions.

Precautions and adequate clothing (protective clothing, gloves, goggles and mask) were always used when manipulating Hg solutions. Special disposal of mercury-containing waste was also required. A specialist company managed the final waste.

XAS measurements

The photon absorption of the target element (Hg) was recorded at the edge energy for its L_{III} line at 12284 eV, while the monitored fluorescence lines were the $L_{\alpha 1}$ (9988.8 eV) and $L_{\alpha 2}$ (9897.6 eV). The selection of the detection mode depends upon the sample concentration and the matrix background [17]. Therefore, pure reference compounds were analysed in transmittance mode (photo-diodes (ESRF) and three ionisation chambers (HASYLAB) as a detectors), while the fluorescence detection mode was used when analysing spiked samples (Ge detector with 13 (ESRF) and five (HASYLAB) elements). Fluorescence-yield measurements are more sensitive and therefore enable the detection of low concentrations of elements of interest, due to the higher signal-to-noise obtained with this mode for a given sample. In addition, fluorescence analysis of high concentration samples leads to problematic self-absorption effects. The detection limits for the transmittance and fluorescence detection modes were found to be 300 (± 20) and 100 (± 20) ppm, respectively, although these are strongly dependent on several parameters such as source energy, insertion device (if present), experimental set-up, as well as presence of (spectral and non-spectral) interferences.

The XANES technique was selected as the most adequate tool for Hg characterization due to the important fingerprint information obtained after the edge jump [18]. The Si (1,1,1) monochromator was chosen for both beamlines, taking into account the scan step width shown in Table 2.

Table 2 Energy and scan step width of the Si (1,1,1) monochromator

ESRF, beamline ID26		HASYLAB, beamline A1	
Energy (eV)	Measurement intervals (eV)	Energy (eV)	Measurement intervals (eV)
12000–12250	5	12150–12240	2
12250–12270	1	12240–12270	1
12270–12295	0.5	12270–12350	0.5
12295–12600	5	12350–12450	1
		12450–12550	5

After the experiments at the synchrotron facility, data treatment was carried out using WinXAS, a commercial program developed by Ressler [19]. To correct any energy displacement, a thin $HgCl_2$ pellet was equally measured as reference for all samples, and the energy was corrected by using the zero value from the second derivative, located at the inflexion point of the edge jump. Although the energy variation is usually small, the correction is especially important when comparing spectra obtained at different analysis times or at different synchrotron facilities. Then a pre- and post-edge region of the spectrum was corrected, to allow the different spectra to be standardised and directly compared. Our choice was to use a second- and a third-degree polynomial, respectively. Finally, the edge jump was normalised due to its direct dependency on the concentration of the mercury in the sample. The absorbance (or fluorescence) of the sample at an energy approximately 300 eV above the edge jump was used to normalise the spectra.

In terms of qualitative data, XAS is able to obtain information on the bonding type of the target analyte [20]. This information is obtained from the energy difference between the two edge steps observed in the plot of the first derivative of the original XANES spectra (see Fig. 1). The energy gap observed is related to the interaction between Hg and its neighbouring atoms (see "XAS studies" in the "Results and discussion" section).

Bioavailability measurements using sensor bacteria

The bioavailable methyl mercury chloride in the spiked samples was determined by recombinant *E. coli* MC1061 (pmerBR$_{BS}$luc) sensor bacteria [16]. The spiked air-dried samples were mixed with water (1:9 w/v solid-to-water ratio), the suspension was rotated for 24 h at room temperature, and it was analysed as described in [21]. Briefly, the suspensions and the respective particle-free extracts (centrifuged at 10,000×*g*) were incubated at 37 °C with sensor bacteria at pH = 7 for 2 h. During that time, the bioavailable fraction of methyl mercury enters the sensor bacteria and induces the synthesis of luciferase (a reporter protein). The luminescence is measured after 2 h of exposure (Fig. 2).

The analysis of particle-free water extracts with the bacterial sensors provides information on water-extracted bioavailable metals, whereas the analysis of suspensions (contact exposure) reports on the particle-bound fraction of metals made bioavailable due to direct contact of the test bacteria with solid particles. In order to take into account the interference of the bacterial luminescence from the sample (quenching of the luminescence by solid particles/colour or toxicity of the sample), we used the luminescent control bacteria, *E. coli* MC1061 (pTOO02) [21]. Triplicate measurements were performed for each sample. To calibrate the assay, the methyl mercury chloride standard was included. The quantification of bioavailable methyl mercury chloride in suspensions and extracts was performed as described in [22] by taking into account the standard curve and correcting the bioluminescence values obtained by the sensor with those obtained with control bacteria. The bioavailable methyl mercury in contact exposure was determined by subtracting the value obtained for particle-free extracts from that obtained for the suspension.

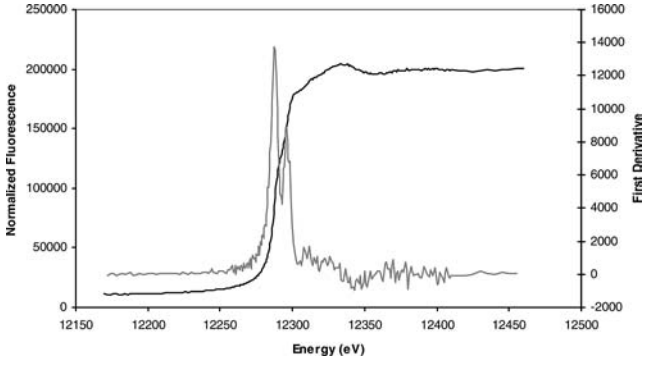

Fig. 1 X-ray absorption spectra of $HgCH_3Cl$ (*black line*), and the corresponding first derivative spectrum (*grey line*)

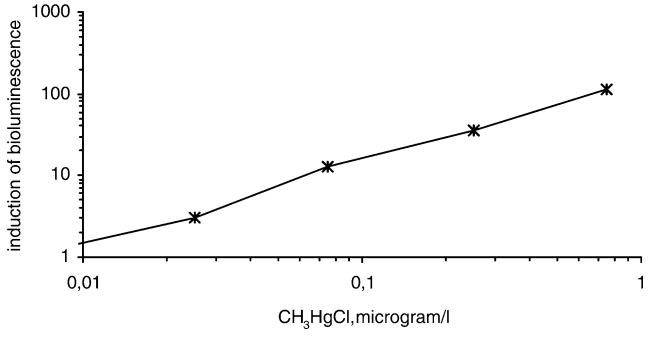

Fig. 2 Response (expressed as increase in bioluminescence compared with that produced in water) of sensor *E. coli* MC1061 (pmerRB$_{BS}$luc) bacteria to different sub-toxic concentrations of methyl mercury

Results and discussion

Sorption experiments

Figure 3 shows adsorption trends for methyl mercury chloride and hydroxide on different soil components, within the pH range 3–9.

Looking at the adsorption by the different soil components assayed, similar behaviour can be observed between the two-methyl mercury salts for all soil components. However, the adsorption was higher for the CH_3HgOH, probably due to its hydroxide group, which is more reactive with soil components than the corresponding chloride.

Clay minerals (montmorillonite and kaolinite) appear to have higher adsorption capacities than the humic acid material, probably due to the higher cation exchange capacity of clays. On the other hand, the higher adsorption of methyl mercury on montmorillonite compared to kaolinite is due to the restricted surface area of the latter, which limits the adsorption of cations. The tendencies seen in the experiments for clays are consistent with literature data on mercury affinity: montmorillonite > vermiculite > kaolinite [23].

Although the variation is small, the adsorption of methyl mercury on humic acid is seen to be slightly higher at acidic pH (Fig. 3). For pH >9, adsorption is expected to decrease due to the competition of OH^- anions with surface functional groups for CH_3Hg^+ complexation. This fact can be appreciated in Fig. 4, where the distribution diagram of the species formed in the system CH_3Hg^+/H_2O is plotted versus the pH. On the other hand, below the studied pH, the extent of adsorption decreases due to the competition of CH_3Hg^+ with H^+ for the active sites of the functional groups [24].

Furthermore, according to the titration curves, at pH 6.0–7.0 the carboxyl group of humic acids is unprotonated, whereas the alcohol, amino and thiol groups are protonated; this is probably the reason for the fall in CH_3HgOH adsorption in this pH range [5].

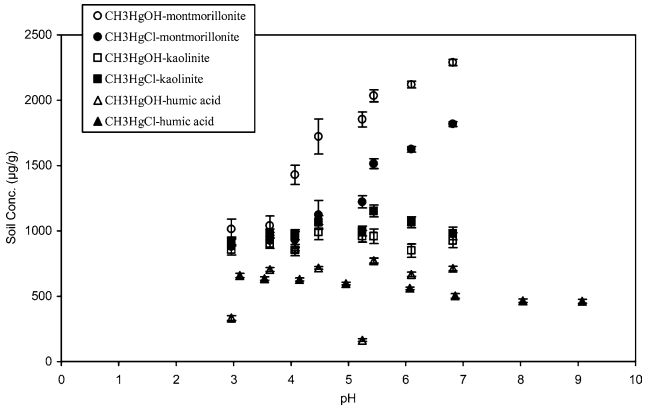

Fig. 3 Adsorption of CH_3HgCl and CH_3HgOH on three different soil components: montmorillonite, kaolinite and humic acids (results correspond to the average of three replicates)

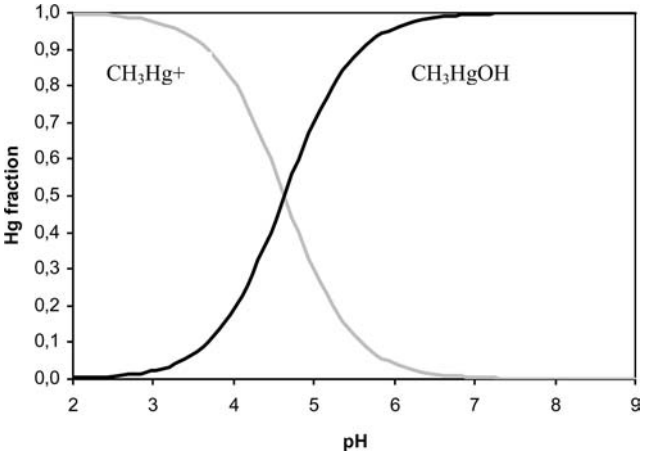

Fig. 4 Distribution diagram of dissolved CH_3Hg^+ species as a function of pH. Calculations performed with MEDUSA program [25]

XAS studies

In order to obtain information on the bonding character of the mercury atom, spiked samples were studied by XANES. Table 3 shows the behaviour of the reference compounds in these measurements.

The first inflexion point provides insight into the electronic environment around the absorbing atom. This is mainly a transition to the 6s orbital of Hg, and its position varies within the interval 12284.1 ± 1 eV. This fact proves the presence of Hg(II), since the existence of additional Hg(0) would increase the electron density around the absorbing mercury atom, consequently decrease the energy required to excite a core electron, and lower the energy of the first inflection point [20].

The distance between the two absorption maxima in the XAS spectra is linked to the covalent or ionic character of the Hg-ligand bonding. In general, the higher the distance, the lower the covalent character, as demonstrated by the series: $HgCl_2$ > CH_3HgCl > C_6H_5HgCl (Table 3).

HgO and HgS cannot be included in this series because they are double-bonded compounds, showing sp-hybridised σ and π bonds. The spacing between transitions is quite wide for HgO (12.5) and relatively narrow for HgS (7.5). ΔE is particularly large for HgO, since transitions to empty π orbitals are forbidden in this compound for the Hg L_{III} edge. The lower ΔE values for the Hg–S compounds reflect the greater orbital overlapping, and therefore greater covalent character, of the complexes formed from the softer sulphur anions with the soft cation mercury(II). Nevertheless, the two polymorphic species of HgS (red and black) have similar but not identical ΔE values, since their different lattice parameters produce slightly different degrees of orbital overlapping.

Additionally, Fig. 5 shows ΔE values corresponding to experiments with montmorillonite and humic acid samples analysed by the synchrotron facilities (kaolinite analysis was not performed due to the excess of photons

Table 3 ΔE (energy difference between the two maxima peaks of the first derivative of the XANES spectra) for pure Hg compounds

Reference compound	First peak E (eV)	Second peak E (eV)	ΔE (eV)
HgS_{red}	12284.3	12291.8	7.5
HgS_{black}	12284.6	12291.8	7.2
HgO	12283.7	12296.2	12.5
$HgCl_2$	12284.1	12292.6	8.5
$HgSO_4$	12283.2	12292.5	9.3
C_6H_5HgCl	12285.1	12292.7	7.6
CH_3HgCl	12284.6	12292.4	7.8
$Hg(CH_3COO)_2$	12284.5	12295.7	11.2

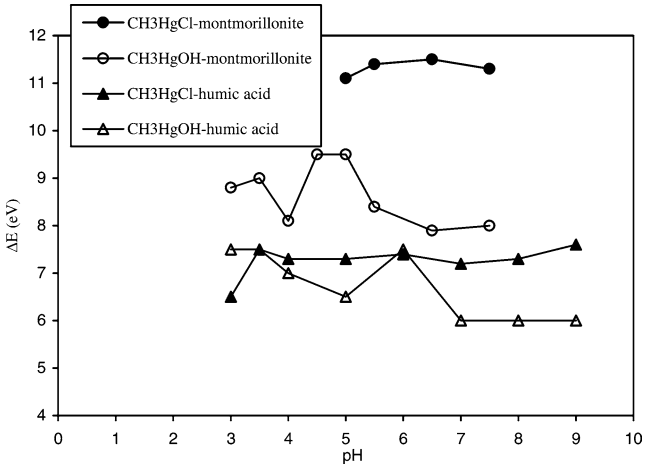

Fig. 5 ΔE (energy difference between the two peaks of the first derivative of the XANES spectra) for montmorillonite and humic acid spiked with CH_3HgCl and CH_3HgOH

released by strong non-spectral interferences, mainly Fe, which resulted in detector saturation in fluorescence mode).

Although all of the soil components studied showed different adsorption capacities depending on the pH (Fig. 3), the bonding character at different pH values appears to be similar (Fig. 5). However, when comparing the different soil components, different ΔE values are observed (Fig. 5), indicating a higher covalent bond character between methyl mercury and humic acids than between methyl mercury and clay mineral montmorillonite. This fact is probably due to the presence of thiol groups in humic acids, which are "soft" Lewis bases that can form strong covalent bonds with the highly polarizable mercury atom (a "soft" Lewis acid).

Upon comparing CH_3HgCl and CH_3HgOH, the latter exhibits more covalent bond character in bonds with the different soil components. This is probably due to the stabilization provided by the OH group, which can establish hydrogen bonds with functional surface groups of soil compounds and form condensed chemical bonds with surface OH^- groups by eliminating water.

Bioavailability studies

Results on the bioavailability of methyl mercury to recombinant luminescent *E. coli* MC1061 (pmerRB_{BS}luc) sensor bacteria for spiked humic acid are presented in Fig. 6, and data for all three spiked soil components are summarized in Table 4.

Due to the low spiking concentration of CH_3HgCl used, 10 μg kg^{-1}, it was assumed that all of the spiked methyl mercury was adsorbed onto the soil components. As seen from Table 4, the bioavailability of methyl mercury chloride for sensor bacteria in the suspension assay (bacteria exposed to solid clay or humic acid particles loaded with methyl mercury) was different for different soil components. Thus, the biosensor showed the highest hazard in the sample where organic mercury was added to montmorillonite: about 50% of the spiked methyl mercury was available to the bacteria in the contact assay. For kaolinite and humic acids, the bioavailable amounts were about five times lower than for montmorillonite (Table 4). The high bioavailability for CH_3Hg^+–montmorillonite correlates with results from XANES analysis data, which revealed that the ionic bonding character (related to mobility) of this system was higher than that of the spiked humic acids system.

Thus, the different bioavailabilities of methyl mercury in the different soil components can be attributed to the

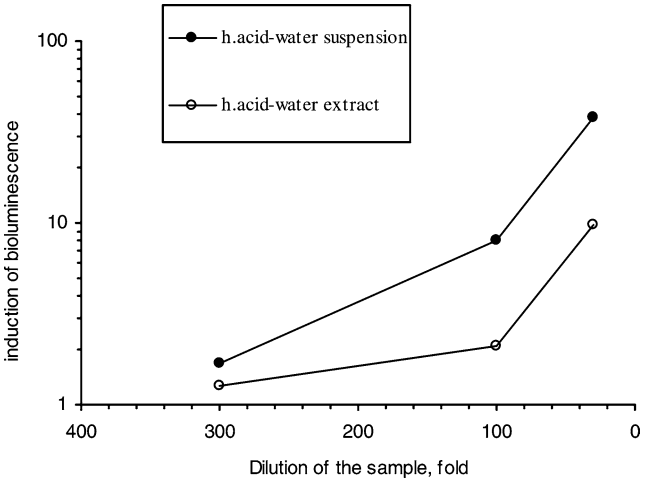

Fig. 6 Response of the sensor *E. coli* MC1061 (pmerRB_{BS}luc) bacteria to different dilutions of humic acid samples spiked with 10 μg of methyl mercury chloride/kg. For details, see the "Experimental" section. (Vertical axis shows the luminescence of the sensor bacteria in the sample divided by the luminescence exhibited by the bacteria in water)

Table 4 Bioavailability of methyl-HgCl in contact exposure of sensor *E. coli* MC1061 (pmerRB_{BS}luc) bacteria in spiked soil model components (suspension assay)

Soil component spiked with CH_3HgCl (pH7; 10 μg kg^{-1})[a]	Bioavailable CH_3HgCl in contact exposure [b] (% of total ± SD)
Montmorillonite	55.9 ± 14.7
Kaolinite	8.9 ± 1.7
Humic acid	13.4 ± 2.6

[a] Soil components were spiked and analysed as described in "Experimental" section

[b] Bioavailable CH_3HgCl in contact exposure = bioavailable CH_3HgCl in suspension assay − bioavailable CH_3HgCl in particle-free extract, as % of the spiked CH_3HgCl

different ionic bond characters exhibited by the systems formed during adsorption.

Conclusions

In this study of various typical soil compounds spiked with methyl mercury, the XANES technique has provided valuable information on the interaction established between the different methyl mercury compounds and some key soil components. This information can be used to evaluate the potential desorption of methyl mercury and therefore the environmental hazard of this compound, because the toxicity, leachability, and volatility of mercury in soils are all dependent on the bonding characteristics of the solid phase.

Results for methyl mercury adsorption by the different soil components showed that adsorption of CH_3HgCl differed only slightly from that of CH_3HgOH in terms of the dependence upon pH, although the adsorption efficiency was higher for the CH_3HgOH.

Compared with the kaolinite and humic acids, montmorillonite exhibited a higher sorption capacity towards the organic mercury compounds studied, and its adsorption capacity increased with pH.

Differences observed between the target clays (kaolinite and montmorillonite) can be explained by the large differences in terms of surface area, which has a direct influence on the cation-exchange capacity of the clay. On the other hand, the adsorption capacity of humic acid has a smaller pH dependence than the adsorption capacities of the clays, due to it being more weakly acidic.

In terms of the type of methyl mercury bonding established with the different soils components assayed, the interaction is shown to be dependent upon the nature of the component. On the other hand, this interaction is shown to be almost independent of pH for all of the soil components evaluated.

Montmorillonite showed a more ionic interaction with methyl mercury than humic acid did. This can be explained if we take into account the presence of thiol groups in humic acids, since the sulphide is able to establish more strongly covalent bonds with methyl mercury. On the other hand, the interaction is more covalent for CH_3HgOH than CH_3HgCl due to the higher reactivity of the hydroxyl groups.

The luminescent *E. coli* MC1061 (pmerRB_{BS}luc) bacterial sensor permitted the measurement of sub-ppb concentrations of bioavailable organic mercury. In addition, if used in soil suspension assays, the sensor bacteria detect the truly bioavailable (desorbed) fraction of a given pollutant. Our data showed that the fraction of CH_3HgCl bioavailable to sensor bacteria was about fivefold higher for spiked montmorillonite (indicating a higher hazard to soil biota via contact exposure) than for spiked humic acids. Comparison of XAS data on the character of the bond between sorbed methyl mercury and the sorption substrate (montmorillonite and humic acids) and bioavailability data showed that the higher bioavailability of montmorillonite-sorbed methyl mercury as compared to humic acid-sorbed methyl mercury could be due to the fact that this clay component forms bonds with more ionic character with methyl mercury than with humic acids.

Therefore, the bacterial sensors have been shown to be appropriate tools, that complement the XAS results, for characterizing methyl mercury adsorption in polluted sites. Moreover, these XAS tools appear to promise answers to a crucial question in environmental toxicology: what are the mechanisms associated with the bioavailability of metals in different environmental matrices?

Acknowledgements We acknowledge the ESRF for provision of the synchrotron radiation facilities, and we would like to thank Laurent Álvarez for assistance in using beamline ID26. Synchrotron experiments at HASYLAB were supported by the IHP-Contract HPRI-CT-1999-00040 of the European Commission. Edmund Welter is gratefully acknowledged for his technical support during the synchrotron experiments. Financial contribution from the EU project: EVK1-CT-1999-00002 and the Spanish grant PPQ2002-04267-C03-01 are also acknowledged. Experiments with biosensors were financed by the SENSPOL Thematic Network (Contract No. EVK1-CT1999-20001, EC Environment and Sustainable Development Programme, DG Research, Key Action "Management and Quality of Water"), and the Estonian Science Foundation Grant No. 5551. We thank Anu Leedjärv for assisting in measurements. Anna Bernaus thanks the Spanish "Ministerio de Educación, Cultura y Deporte" for a PhD scholarship (2002–2004).

References

1. Förstner U (1998) Integrated pollution control. Springer, Berlin Heidelberg New York
2. Davis JM (1987) Nature 329:297–300
3. Odin M, Feurtet-Mazel A, Ribeyre F, Boudou A (1994) Environ Toxicol Chem 13(8):1291–1302
4. Maury-Brachet R, Ribeyre F, Boudou A (1990) Ecotox Environ Safe 20(2):141–155
5. Tan HK (1998) Principles of soil chemistry, 3rd edn. Marcel Dekker, Basel
6. Rodriguez I, Carro A (2002) Anal Bioanal Chem 372:74–90
7. Kim CS, Bloom NS, Rytuba JJ, Brown GE Jr (2003) Environ Sci Technol 37(22):5102–5108
8. Huffman CP (1997) Symp Div Fuel Chem 42:1118–1122
9. Xia K, Skyllberg UL, Blean WF, Bloom PR, Nater EA, Helmke PA (1999) Environ Sci Technol 33:257–261

10. Korshin GV, Frenkel AL, Stern EA (1998) Environ Sci Technol 32:2699–2705
11. Haitzer M, Aiken GR, Ryan JN (2003) Environ Sci Technol 37(11):2436–2441
12. Kim CS, Rytuba JJ, Brown GE Jr (2004) J Colloid Interf Sci 271:1–15
13. Khwaja AR, Bloom P, Brezonik P, Lin CM (2003) Prepr Ext Abstr ACS National Meet 43(1):628–631
14. Khwaja AR, Brezonik P, Bloom P, Lin CM (2004) RMZ-Mater Geoenviron 51(2):1115–1118
15. Karlsson T, Skyllberg U (2003) Environ Sci Technol 37(21):4912–4918
16. Ivask A, Hakkila K, Virta M (2001) Anal Chem 73(21):5168–5171
17. Koningsberger DC, Prins R (1988) X-ray absorption. Wiley, New York
18. Morin G (1999) Am Miner 84:420–434
19. Ressler T (1992–2001) WinXAS Version 2
20. Riddle G, Sarah, Tran H, Huy, Dewitt G, Jane, Andrews G (2002) Environ Sci Technol 36:1965–1970
21. Ivask A, Francois M, Kahru A, Dubourguier HC, Virta M, Douay F (2004) Chemosphere 22:14
22. Hakkila K, Green T, Leskinen P, Ivask A, Marks R, Virta M (2004) J Appl Toxicol 24:333–342
23. Obukhovskaya TD (1982) Pochvovedenie 6:53–8
24. Zvonarev BA (1982) Pochvovedenie 4:43–8
25. Puigdomenech I (2004) Chemical Equilibrium Software (updated 18 February 2004)

Annex 3

PAPER

Characterisation of Almadén mercury mine environment by XAS techniques

Anna Bernaus, Xavier Gaona and Manuel Valiente*

Centre GTS, Unitat de Química Analítica, Departament de Química, Universitat Autónoma de Barcelona, Facultat de Ciències, Edifici CN, 08193, Bellaterra, Barcelona, Spain. E-mail: Manuel.Valiente@.uab.es; Fax: +34 935812379; Tel: +34 935812903

Received 8th February 2005, Accepted 25th May 2005
First published as an Advance Article on the web 16th June 2005

This manuscript describes the analysis and evaluation of mercury species present in three different types of samples (ore, slag and soil) belonging to the abandoned mining area of Almadén (Spain), by means of X-ray Absorption Spectroscopy (XAS) techniques. The applied methodology includes the analysis of possible interfering compounds by ICP-OES and the characterisation of solid samples by identification of heterogeneities using SEM-EDS technique prior to measurements at the synchrotron facilities (ESRF in Grenoble, France and HASYLAB in Hamburg, Germany) and subsequent analysis of data. Results show that cinnabar is the main species both in ore and soil samples, its concentration ranging from 41 to 77% of the total mercury content. On the other hand, metacinnabar (a polymorph of cinnabar) is shown to be the main species in slag samples (42–88%). Other mercury forms have been found in minor proportions (<30%), such as slightly soluble mercury salts ($HgCl_2$ and $HgSO_4$) and HgO. This is the first time that Almadén-type mercury ores have been characterised by a synchrotron-based spectroscopic technique for a direct determination of mercury species. The conclusions presented in this report show the important similarities between Almadén and hot-spring type mercury mineral deposits, despite its different geological origin.

Introduction

During the 1950s and 60s, the catastrophic poisoning incidents with mercury in Japan led to worldwide public attention and sensitivity to environmental contamination and prompted a number of studies on the disposition of this metal in the environment. Two associated hazards became quite obvious: on the one hand, heavy metal contamination, in contrast to organic contamination, is not degraded by natural processes in soil and water. On the other hand, Hg is easily absorbed, concentrated and stored over long periods of time through various mechanisms in mineral and organic matter. Through the food chain, Hg eventually enters humans and can cause chronic or acute damage.[1]

Since Hg toxicity is strongly affected by its chemical form, the reliability of determining such species becomes of paramount importance. Conventional speciation procedures normally deal with a solvent extraction step, followed by chromatographic separation and selective detection. However, there are some drawbacks related to these techniques, such as the risk of species modification by the extraction process, the poor capacity for the determination of inorganic species, as well as the poor prediction reliability regarding mobility and availability.[2–4]

In this sense, XAS techniques have become a very useful tool for environmental studies. These techniques take advantage of the highly brilliant X-ray radiation generated in synchrotron facilities for the study of the atomic environment, showing a high speciation capacity while having almost no sample pre-treatment (and as a result a minimum of sample modification).[5–8] Nevertheless, XAS techniques also have some related drawbacks, such as their relatively poor detection limits, the complex data treatment, and the limited number of synchrotron facilities available worldwide.

μ-XANES (micro-X-ray Absorption Near Edge Structure) is used (among other applications) as a tool for improving the poor detection limits of XAS techniques. This technique is based on the identification and focusing of individual (mercury-rich) particles, as a previous step to the speciation analysis. Hence, higher signal-to-noise ratios are obtained, which is highly demanded in the characterisation of heterogeneous samples.[9]

Natural mercury deposits are globally distributed in three types of minerals belts: silica-carbonate, hot-spring, and Almadén type, which are co-genetic and reflect similar tectonic and volcanic processes that contributed to the concentration of mercury.[10] The most important of these types is the Almadén mercury mineral deposit in central Spain, where over one-third of the world's mercury has been produced. The mining operation dates from the Carthaginian age, while the total Hg extracted from the mine amounts to about 7.5 million Hg flasks (approximately 270 000 tons of Hg).[11] The deposit essentially contains Hg as massive cinnabar (HgS) and appreciable amounts of native Hg.[12] Hg ores were crushed and roasted in large furnaces at temperatures approaching 600 °C. This process volatilized most of the Hg into elemental form, which was subsequently passed through condenser columns and collected as liquid Hg in flasks. The roasted mine wastes, or slag, were typically transported a short distance from the furnace and dumped in loose, unconsolidated piles. Due to the extensive mining of the Hg activity, Hg concentrations in the neighbouring areas have been found to be very high. The high summer temperatures achieved in the region also increase rock and soil degassing rates; in addition, mercury cycling in the area may be altered by the biota.

In spite of the importance of this area, only a few studies based on conventional extraction techniques have been conducted to evaluate mercury pollution and its environmental impact.[13–16] Thus, the present work is focused on the speciation of mercury in the Almadén ore, soil and slag samples by using XAS techniques. We provide direct information about chemical speciation within the studied system that has to be considered in the assessment of mercury mobility and the consequent potential hazards for the environment.

DOI: 10.1039/b502060n

Experimental

Reagents

Prior to synchrotron experiments, samples were characterized by digestion and ICP-OES analysis. Within these analyses, ultrapure water (Milli-Q), high-purity nitric acid, hydrochloric acid and hydrofluoric acid were used (see below). All reagents were of analytical-reagent grade supplied by Baker (Phillipsburg, USA). A 2% (w/v) H_3BO_3 solution was prepared as a neutralising reagent for HF.

Baker Instra Analysed Hg, As, Zn, Cu, Ni, Pb, Fe and Mn Inductively Coupled Plasma standards of 1000 mg l^{-1}, were used to prepare the standards solutions by dilution with 0.5 mol l^{-1} HNO_3. A gold atomic absorption standard solution 1000 mg l^{-1}, supplied by Aldrich Chemical Company (Germany) was used for the stabilisation of Hg in the standards solution.

The standard reference material SRM 2710 was used to assess the reliability of the digestion process. The above mentioned SRM, was obtained from the National Institute of Standards and Technology (NIST, USA), and corresponds to a soil fraction collected from the upper 10 cm of pasture along Silver Bow Creek in Butte, Montana.[17]

Concerning XAS experiments, solid compounds selected as reference compounds were $HgCl_2$, Hg_2Cl_2, $HgSO_4$, HgO_{red}, $Hg(CH_3COO)_2$, CH_3HgCl, HgS_{red} (cinnabar) and HgS_{black} (metacinnabar). All of these chemicals, p.a. grade, were purchased from Aldrich. Polyethylene powder (Merck UVASOL, Germany) was utilised as a diluting agent for the preparation of the pellets.

Safety precautions (*i.e.*, adequate clothing) were absolutely necessary when manipulating Hg solutions. In addition, Vermiculita Exfoliada, an absorbent of laminated hydrated minerals, mainly aluminium, iron and magnesium silicates (CARL ROTH, Spain), was used to absorb poured Hg compounds.

Sample description and preparation

Ore samples were collected at the entrance of the oven, before their roasting. Slag was sampled at the exit of the oven, after 1 hour 45 min of ore treatment through the conveyor belt. Soil samples were collected within the mine surroundings. After sampling, ores, soils and slag were dried, milled with a pestle in an automatic agate mortar, and then homogenized and sieved under 100 μm.

Total metal content was determined by ICP-OES analysis, prior to sample digestion. Digestions were performed in perfluoroalcoxy (PFA) vessels in an Analytical Microwave system (MARS-5 model from CEM Corporation, USA). Mercury (as well as some possible interfering elements, *i.e.* As, Zn, Cu, Ni, Pb, Fe, Mn) was quantified by means of ICP-OES analysis (ICP-OES model 3410 equipped with minitorch from ARL, USA). All glassware and plastic containers were previously soaked overnight in 25% nitric acid and rinsed, in order to avoid any interference by metal adsorption.

Digestions were undertaken by two different methodologies. Firstly, the modified EPA method 3051 was utilised, by digesting 0.5 g of sample with 9 ml of *aqua regia* (6 ml HCl, 2 ml HNO_3, 1 ml H_2O). The digestion program starts with a power of 100 W and an increasing pressure over 18 min up to 120 psi, which was then held for 15 minutes.

After digestion, vessels were cooled down to room temperature and the remaining solution filtered through 0.22 μm cellulose paper. Then, a few μl of $AuCl_3$ solution (1000 mg L^{-1}) were added in order to stabilize the Hg in solution, and the mixture was diluted with Milli-Q water to a final volume of 50 ml. The final solution was then analysed by means of ICP-OES.

A second digestion method, where samples were submitted to a stronger media, was applied to ensure the total digestion.[18] Thus, total metal content was determined by the digestion of the soil (0.25 g) with a mixture of 10 ml *aqua regia*, 10 ml water and 4 ml hydrofluoric acid in a microwave. In this case, the microwave program consisted of a first step where samples were placed under 50 W of power and an increasing pressure over 30 minutes to reach 50 psi, which was held for 10 minutes. This condition was followed by two steps of 100 W of power to reach a pressure of 120 psi over 60 minutes that was then held for 30 minutes.

Likewise, the resulting solution was cooled down, filtered, and diluted with H_3BO_3 to neutralize the HF. The final treatment with H_3BO_3 produced the chemical degradation of the remaining HF, in order to prevent damage of the glass apparatus.

This second method of sample digestion was also assayed using the certified reference material SRM 2710.

Special attention was paid to the analysis of As, Zn or Pb, since these elements might represent an important spectral interference for Hg analysis by XAS in fluorescence mode. On the other hand, the analysis of major species such as Fe was considered as a must within the experiments, since strong non-spectral interferences can be observed (again in fluorescence mode) due to the excess of photons released by highly concentrated elements, easily leading to detector saturation.

In order to condition samples for XAS analysis, corresponding aliquots, as well as reference compounds, were mixed with polyethylene. Homogenisation was undertaken in a Vortex apparatus, and the final mixture was pressed as a pellet under 5 tons cm^{-2} for 5 minutes.

The total amount of sample in each pellet varied from 50 to 100 mg and polyethylene from 100 to 150 mg.

SEM-EDS analysis

Those pellets prepared for μ-XANES experiments were also analysed by SEM-EDS, in order to evaluate the elemental background of the samples, while acquiring qualitative information about the chemical speciation of those Hg-rich particles. The apparatus utilised was an electron microscope JEOL JSM 6300 (Jeol LTD, Tokio, Japan), equipped with an energy X-ray dispersive spectrometer Link ISIS-200 (Oxford Instruments, England).

Five ore samples and four reference compounds (HgS_{red}, HgS_{black}, HgO and $HgCl_2$) were pressed as pellets (similarly to the XAS experiments) and coated with a carbon spray in order to improve sample conductivity. After that, they were scanned in an electronic microscope, and analysed with a coupled energy dispersive X-ray spectroscopy unit (EDS), with resolution of 138 eV. The aim of the analysis was to describe the bulk characteristics of each sample and to investigate the association of Hg with specific matrix phases.

Samples were scanned in back scattering mode. Mercury is an electron dense atom and an effective electron backscatterer. Consequently, it becomes visibly bright in a matrix consisting of low Z elements. The elemental composition of those Hg-rich particles identified was studied by using the X-ray spectrometer coupled to the electron microscope.

SEM-EDS analysis was also used for a qualitative evaluation of the chemical speciation of Hg-rich particles in ore samples, by following the Hg and S fluorescent lines. Since the S-K_α line (2.31 KeV) and Hg-M_α (2.28 KeV) fluorescence lines overlap, the Hg-L_α line (9.98 KeV) was used to perform a line ratio analysis (LIR),[19] defined as the intensity ratio of the netto area between the Hg-M_α or S-K_α lines (as a %) and the netto area of the Hg-L_α line. Therefore, when dealing with mercury-rich particles (relative to sulfur) lower line ratios were found, whereas sulfur-rich (relative to mercury) particles showed higher line ratios.

Table 1 Beamline set-up

Element	ESRF, beamline ID26	HASYLAB, beamline A1	HASYLAB, beamline L
(Insertion) device	Undulator	Bending magnet	Bending magnet
Source energy	6 GeV	4.5 GeV	4.5 GeV
Maximum current	200 mA	100 mA	100 mA
Monochromator crystals	Si (1,1,1) (Si (2,2,0) also available)	Si (1,1,1) (Si (3,1,1) also available)	Si (1,1,1)
Resolution ($\Delta E/E$)	$\sim 10^{-4}$	$\sim 10^{-4}$	$\sim 10^{-4}$
Photon flow at the sample	$>10^{13}$ γ s^{-1}	About 10^{8} γ s^{-1}	About 10^{8} γ s^{-1}
Spot size at the sample	200 μm × 80 μm	2 mm × 3 mm	10 μm × 10 μm
Detectors	Three ionisation chambers	Three ionisation chambers	Two ionisation chambers
	Photo-diodes for flux monitoring	Ge (5 elements)	Ge (1 element)
	Si (13 elements)		
Angle bunch-sample	45°	45°	45°
Temperature	Room	Room, liquid N_2 (liquid He also available)	Room

XAS measurements

XAS spectra were obtained at both ESRF (Beamline ID26) in Grenoble (France), and HASYLAB (Beamlines A1 and L) in Hamburg (Germany), synchrotron facilities. Details about beamline set-up are given in Table 1.

The photon absorption of the target element (Hg) was recorded at the edge energy for its L_{III} line at 12 284 eV, while the monitored fluorescent lines were the $L_{\alpha 1}$ (9988.8 eV) and $L_{\alpha 2}$ (9897.6 eV). The selection of the detection mode depended on sample concentration and matrix background.[20] Therefore, pure reference compounds were analysed in transmittance mode (three ionisation chambers in beamlines ID26 and A1, and two ionisation chambers in beamline L, as detectors) in the ESRF and HASYLAB facilities, while fluorescence detection mode was used for the analysis of diluted samples (detector of Si in ESRF and of Ge in HASYLAB). Arsenic and aluminium filters were used to attenuate elastic scattering and fluorescence from iron, respectively.

Data from minerals were collected at beamline ID26 at ESRF (Si (1,1,1) monochromator utilised), while data from polluted soils samples and slag were collected at beamline A1 and L at HASYLAB, using Si (1,1,1) monochromator crystals. In each case, spectra of each reference compound were collected for the later data fitting.

XAFS data treatment was undertaken with WinXAS, a commercial program developed by Thorsten Ressler (Version 2.χ).[21] A linear least-squares fitting procedure was employed to fit the model spectra from the compound database to sample spectra within an energy range of 12 200–12 600 eV. Chemical speciation present in the sample is revealed by the linear combination of reference spectra better fitting to the sample spectra. The quality of the process is given by the residual value (R), representing the proportion of the spectrum that remains unfitted. R is calculated by the equation listed below where N is the number of data points, and y_{exp} and y_{theo} experimental and theoretical data points, respectively.

$$R = \frac{\sum_{i=1}^{N} \left| y_{exp}(i) - y_{theo}(i) \right|}{\sum_{i=1}^{N} \left| y_{exp}(i) \right|}$$

A significant residual value may result from noisy data, low total Hg concentrations, as well as the presence of additional unknown components not included in the model compound database.[16] Ostergren *et al.*[6] reported a quantitative accuracy of the method of 25%, while other authors have achieved quantitative values as low as 1%.[22–25] In the present work, the limiting proportion for a given component has been fixed at 3% of the total mercury composition. Nevertheless, values under 25% must only be taken as indicative.

Results and discussion

The obtained results are described by first including the analysis by ICP-OES followed by the observations from SEM-EDS and finally the study by XAS.

In sample treatment for ICP-OES it was found that *aqua regia* was unable to completely digest ore samples, while total digestion was achieved using HF (see Table 2). This second methodology was also demonstrated to be effective when dealing with the certified reference material, since obtained results were found within the certified range provided, and, therefore, it was selected as the standard methodology for the whole set of samples.

Results of total metal content in Almadén samples are shown in Table 3. Very high mercury concentrations were found in ore samples, ranging from 30 to 40 g kg^{-1}. On the other hand, the concentration in soils and slag presents a high variation ranging from 200 to almost 2000 mg kg^{-1}.

Quantification of those elements likely to produce spectral interferences in fluorescence detection mode (namely As, Pb and Zn) revealed relatively low metal concentrations. On the other hand, higher nickel concentrations were found within some of the studied samples. Nevertheless, this Ni background should not be problematic taking into account Ni fluorescence lines (K_α 7460–7480 eV, K_β 8264 eV).

The high iron content of all samples was found to be an unbearable problem for fluorescence analysis undertaken at the ESRF synchrotron facility, where a very high photon rate (compared to HASYLAB) is provided by the source. Under these conditions, the high iron content (see Table 3) was responsible for the easy saturation of the fluorescence detector. Consequently, only highly concentrated ore samples were analysed at ESRF in transmittance mode, while more diluted samples (soils and slag) were analysed at HASYLAB (2nd generation source, lesser photon flow) in fluorescence mode. This paradox is a common problem concerning XAS analysis of environmental samples, and is the principal culprit of the difficulties encountered in trying to improve the detection limits of the technique.

Table 2 Hg concentration by ICP-OES after MW digestion (average of three replicates in mg kg^{-1})

	Hg concentration	
	Aqua regia digestion	HF digestion
Ore 1	18 000 ± 2000	39 000 ± 1000
Ore 2	14 800 ± 100	33 000 ± 3000
Ore 3	19 000 ± 2000	41 000 ± 3000
Ore 4	14 300 ± 600	28 900 ± 800
Ore 5	15 000 ± 300	38 600 ± 300

Table 3 Total metal concentration quantified in Almadén samples by MW digestion + ICP-OES analysis (mg kg^{-1})

	Hg	As	Zn	Cu	Ni	Pb	Fe[a]	Mn
Ore 1	39 000 ± 1000	430 ± 40	185 ± 6	<1	1700 ± 300	260 ± 40	52.4 ± 0.4	600 ± 10
Ore 2	33 000 ± 3000	470 ± 9	<1	<1	1400 ± 100	290 ± 20	50 ± 2	540 ± 10
Ore 3	41 000 ± 3000	490 ± 10	<1	<1	1580 ± 50	278 ± 5	53 ± 4	639 ± 7
Ore 4	28 900 ± 800	500 ± 8	280 ± 10	<1	1580 ± 80	295 ± 2	51.6 ± 0.8	553 ± 2
Ore 5	38 600 ± 300	450 ± 70	<1	<1	1500 ± 100	260 ± 40	49.9 ± 0.2	632 ± 3
Soil 1	630 ± 30	290 ± 50	<1	<1	670 ± 10	<1	43 ± 1	<1
Soil 2	1080 ± 30	320 ± 30	<1	<1	950 ± 90	260 ± 20	51.0 ± 0.5	460 ± 10
Soil 3	1090 ± 30	340 ± 10	<1	<1	960 ± 60	229 ± 7	44 ± 3	510 ± 10
Soil 4	1200 ± 100	340 ± 20	<1	<1	1000 ± 200	208 ± 6	51 ± 2	420 ± 20
Soil 5	1450 ± 30	310 ± 6	<1	<1	860 ± 30	<1	44 ± 1	<1
Soil 6	400 ± 10	320 ± 20	<1	<1	1008 ± 6	<1	37.1 ± 0.2	330 ± 10
Soil 7	840 ± 20	310 ± 30	<1	<1	1160 ± 20	220 ± 30	40.9 ± 0.2	632 ± 6
Soil 8	1820 ± 10	340 ± 40	<1	<1	1100 ± 200	210 ± 20	41.9 ± 0.7	301 ± 6
Soil 9	1360 ± 50	310 ± 20	<1	<1	1100 ± 100	<1	40.2 ± 0.4	640 ± 10
Soil 10	1720 ± 10	320 ± 5	310 ± 30	<1	1260 ± 90	287 ± 8	47.5 ± 0.3	390 ± 10
Slag 1	460 ± 30	320 ± 20	<1	<1	1410 ± 40	<1	61.7 ± 0.5	<1
Slag 2	380 ± 6	300 ± 10	390 ± 10	65 ± 1	1290 ± 80	<1	78.96 ± 0.04	<1
Slag 3	240 ± 3	340 ± 40	<1	73 ± 1	1400 ± 200	206 ± 7	86.4 ± 0.8	<1

[a] (g kg^{-1}). Each value is the average of three replicates. Standard deviations within the 95% confidence interval.

Samples were analysed by SEM-EDS in order to obtain raw information on Hg speciation, as well as on major components. Fig. 1 shows a typical EDS spectrum from a full-field area of ore sample number one, where the spectrum is dominated by a clayey composition (aluminium, silicon, potassium and iron). Likewise, the study of samples with anomalous Hg content showed that Hg is related closely to the epigenetic minerals: clays (mostly kaolinite and dickite), bitumens, Fe sulfides (pyrite and marcasite), and carbonates (calcite and dolomite).[26]

Moreover, the microscope images and EDS mapping of the isolated Hg rich particles suggest the presence of cinnabar (particles where Hg and sulfide were spatially related, see Fig. 2).

This fact was semi-quantitatively evaluated by means of SEM-EDS measurements. Considering the close energy of Hg-M_α and S-K_α fluorescence lines, the study was undertaken taking into account LIR analysis. Consequently, LIR values are obtained by the ratio between the netto area (the background noise is removed from the brutto area) of the Hg-M_α and S-K_α lines (as a %) and the netto area of the Hg-L_α line.

Table 4 shows the results of Hg rich particles from the first five ore samples. The table also includes the LIR analysis of four mercury reference compounds, the two polymorphs of HgS (cinnabar and metacinnabar), HgO and $HgCl_2$.

The collected information in Table 4 allows for a direct comparison between LIR values of Hg standards and the samples, showing a clear predominance of HgS_{red} among the particles evaluated. However, approximately 20% of the studied particles have shown dissimilar LIR ratios. This fact might be related both to the uncertainties of the technique (associated error ~2–5% depending on the type of sample, present elements, concentration of the target element, *etc.*), and the possible presence of other mercury compounds with different Hg–S ratios (*e.g.* corderoite mineral ($Hg_3S_2Cl_2$)).

Treatment of raw XAS data led to the spectra shown in Fig. 3. Once corrected and normalized, sample and reference compound spectra were available for the fitting process. As stated before, WinXAS was utilised for the determination of the linear combination of reference compounds to create the best fit to the sample spectra. Fig. 4 (a, b, c) shows the results obtained for samples ore_1, soil_1 and slag_1, while Table 5 reports the speciation results determined for each of the samples analysed. Table 5 also indicates the synchrotron facility and beamline where each sample was analysed, as well as the detection method utilised (transmittance/fluorescence).

Table 5 reveals cinnabar (HgS_{red}) as the main mercury compound present in all samples other than slag. In mercury ores, cinnabar is the thermodynamically stable form at low temperature and reducing conditions. Hg had been predominately converted to mercuric sulfide as a consequence of sulfate reduction in the soils.[27] Moreover, HgS is kinetically resistant to oxidation, and once formed, HgS may remain in soils even under oxidizing conditions.

It is interesting to note how metacinnabar (HgS_{black}), a less stable polymorph form of cinnabar, appears to be the main component in slag samples. As stated in Kim *et al.*,[28] this fact can be attributed to the high working temperatures (around 600 °C) of the mineral processing for Hg extraction. These high

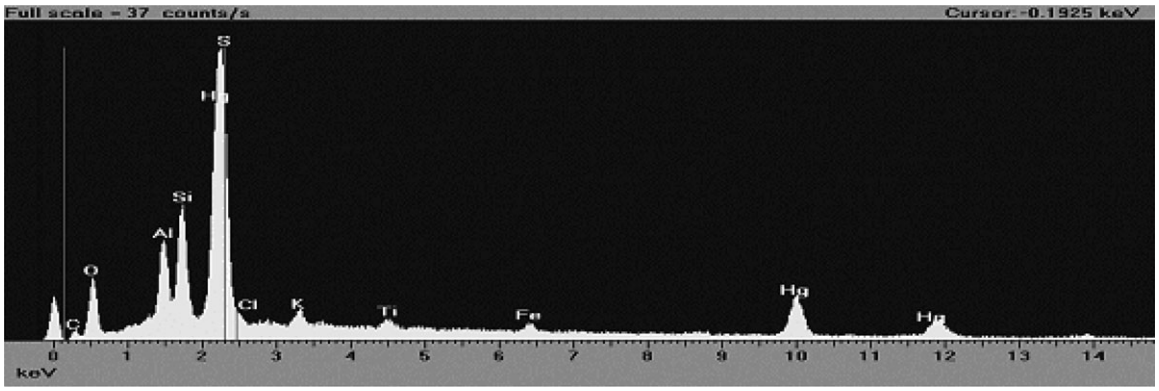

Fig. 1 EDS spectrum from a full-field area of the first Almadén's ore.

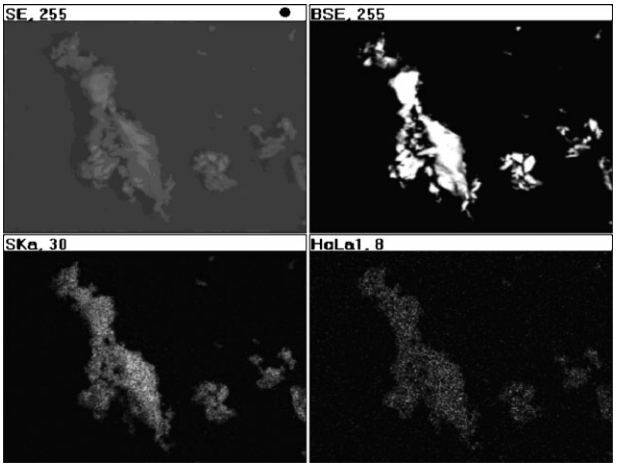

Fig. 2 Mapping of a HgS grain from sample ore 1, where the two images above are one particle, using contrast (right) and without contrast (left). The two images below correspond to the Hg-M_α + S-K_α (left) and Hg-L_α (right) fluorescent lines.

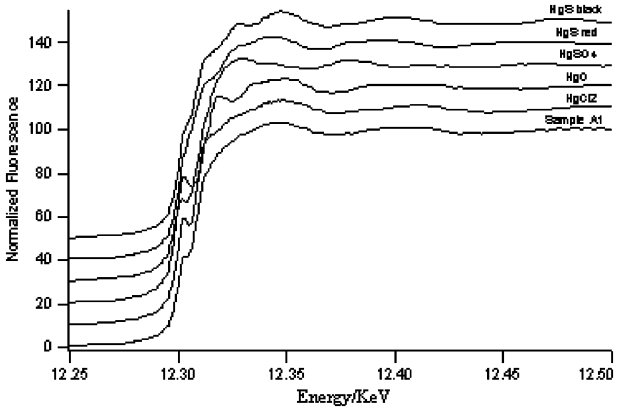

Fig. 3 Comparison of raw XANES reference spectra of: $HgCl_2$, HgO, $HgSO_4$, red and black HgS, with the first ore sample from Almadén (note deliberate offset of spectra to show differences).

temperatures enhance the structural conversion of HgS, which, in addition, is stabilised by the presence of some inorganic impurities, especially zinc, iron and selenium, that hinders the conversion of metacinnabar to cinnabar by decreasing the inversion temperature and by retarding the kinetics of conversion.[29]

Nevertheless, metacinnabar is also found in raw mineral samples. This presence can be justified by the geological origin of the mine and its environment. Hence, the deposits are associated spatially with mafic submarine vent complexes that consist of mafic dikes and sills, and oval craters typically with dimensions of 300 × 150 metres. Juvenile magma clasts within the craters are typically alkali basalts.[30] Consequently and because of the high temperatures reached during the formation

Table 4 LIR averages of Hg-rich particles from the five ore samples and from three pure compounds, by using SEM-EDS technique

Sample		Brutto area Hg-M_α + S-K_α	Brutto area Hg-L_α	Netto area Hg-M_α + S-K_α	Netto area Hg-L_α	% Hg-M_α + S-K_α	% Hg-L_α	LIR	$LIR_{average}$
Ore 1	Part 1	55 991	6672	44 441	4412	91	9	10.1	
	Part 2	50 704	5924	35 637	3634	90.7	9.3	9.8	
	Part 3	10 340	1068	8408	528	94.1	5.9	15.9	
	Part 4	9363	1079	7568	499	93.8	6.2	15.1	
	Part 5	38 891	5989	30 008	3589	89.3	10.7	8.3	11.8 ± 3.8
Ore 2	Part 1	317 129	34 394	255 515	21 204	92.3	7.7	12	
	Part 2	458 987	40 476	373 874	25 166	93.7	6.3	14.9	
	Part 3	437 150	33 123	350 966	20 513	94.5	5.5	17.2	
	Part 4	363 751	26 576	292 866	16 286	94.7	5.3	17.9	
	Part 5	7201	1317	6004	927	86.6	13.4	6.5	13.7 ± 5.2
Ore 3	Part 1	301 637	31 952	250 156	19 262	92.9	7.1	13.1	
	Part 2	383 152	34 768	314 083	20 718	93.8	6.2	15.1	
	Part 3	19 442	2294	11 525	1294	89.9	10.1	8.9	
	Part 4	278 437	33 062	228 562	20 122	91.9	8.1	11.3	
	Part 5	4930	1083	4006	643	86.2	13.8	6.2	10.9 ± 3.9
Ore 4	Part 1	45 122	4542	34 181	2322	93.6	6.4	14.6	
	Part 2	311 990	31 463	252 245	19 553	92.8	7.2	12.9	
	Part 3	382 097	29 998	305 248	18 578	94.3	5.7	16.5	
	Part 4	399 314	35 629	325 142	21 869	93.7	6.3	14.9	
	Part 5	336 009	53 020	278 427	33 520	89.3	10.7	8.3	13.4 ± 3.5
Ore 5	Part 1	429 271	35 229	348 694	22 139	94	6	15.7	
	Part 2	435 867	33 010	352 235	19 680	94.7	5.3	17.9	
	Part 3	434 258	35 020	351 245	22 200	94.1	5.9	15.9	
	Part 4	228 613	23 456	181 710	15 236	92.3	7.7	11.9	
	Part 5	311 095	35 044	259 173	21 754	92.3	7.7	11.9	14.7 ± 3.0
HgS_{red}	Part 1	335 140	44 286	274 860	27 766	90.8	9.2	9.9	
	Part 2	14 494	1386	11 491	716	94.1	5.9	15.9	
	Part 3	7567	828	6234	518	92.3	7.7	12	12.6 ± 4.8
HgS_{black}	Part 1	14 246	1782	11 653	1182	90.8	9.2	9.9	
	Part 2	9652	1408	8140	868	90.4	9.6	9.4	
	Part 3	10 918	1365	8965	895	90.9	9.1	10	9.8 ± 0.5
HgO	Part 1	7947	1345	6477	905	87.7	12.3	7.1	
	Part 2	7492	1254	6075	834	87.9	12.1	7.3	
	Part 3	5532	1070	4598	640	87.8	12.2	7.2	7.2 ± 0.1
$HgCl_2$	Part 1	3227	482	2293	342	87	13	6.7	
	Part 2	648	113	390	53	88	12	7.3	
	Part 3	2630	402	1969	272	87.9	12.1	7.3	7.1 ± 0.5

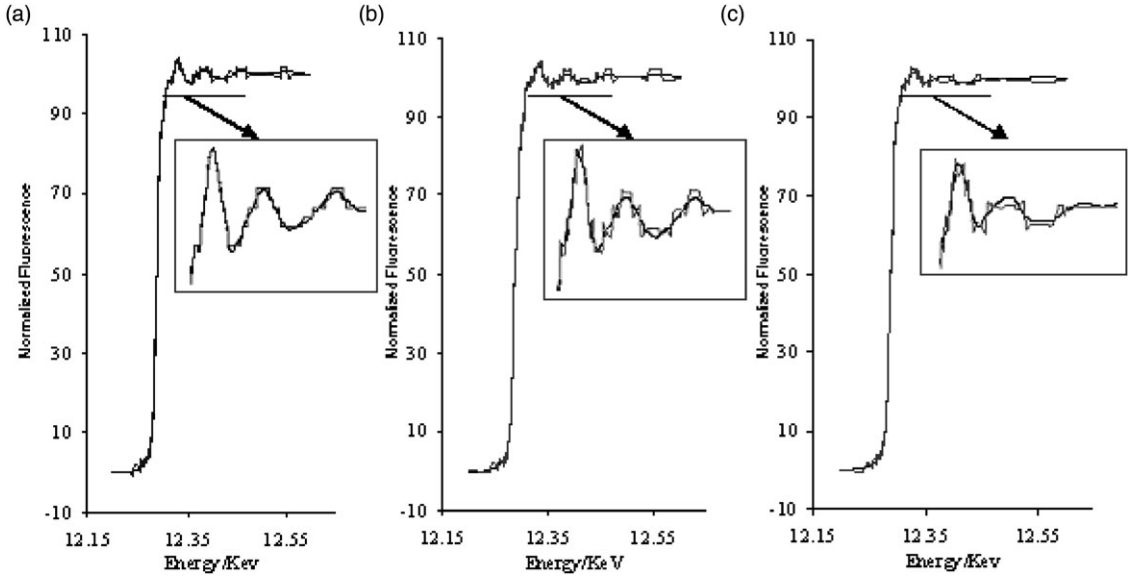

Fig. 4 Comparison of sample spectra (grey line) with best fit spectra (black line) achieved for three different Almadén samples: (a) ore 1, (b) soil 1 and (c) slag 1. The inset figure shown in each plot corresponds to a magnification of the region slightly above the edge.

Table 5 Chemical speciation of ore, soil and slag samples from Almadén's mercury mine. Concentration values expressed in % over total mercury content in each sample

Sample	Beamline	Det. mode	HgS_{red}	HgS_{black}	$HgSO_4$	$HgCl_2$	HgO	Residual
Ore 1	ID26	Transmit.	77	12	6	6	<3	0.025
Ore 2	ID26	Transmit.	54	19	14	6	5	0.059
Ore 3	ID26	Transmit.	51	9	6	29	4	0.047
Ore 4	ID26	Transmit.	63	10	8	14	4	0.054
Ore 5	ID26	Transmit.	68	7	6	14	5	0.035
Soil 1	A1	Fluoresc.	66	<3	14	<3	17	0.218
Soil 2	A1	Fluoresc.	56	<3	22	22	<3	0.186
Soil 3	A1	Fluoresc.	41	<3	24	19	16	0.282
Soil 4	A1	Fluoresc.	74	<3	14	<3	10	0.178
Soil 5	A1	Fluoresc.	66	<3	17	18	<3	0.149
Soil 6	L	Fluoresc.	34	<3	5	47	14	0.111
Soil 7	A1	Fluoresc.	64	<3	18	18	<3	0.191
Soil 8	A1	Fluoresc.	62	<3	20	19	<3	0.155
Soil 9	A1	Fluoresc.	54	<3	21	25	<3	0.160
Soil 10	A1	Fluoresc.	76	<3	24	<3	<3	0.195
Slag 1	L	Fluoresc.	<3	88	12	<3	<3	0.126
Slag 2	L	Fluoresc.	10	65	18	<3	7	0.172
Slag 3	L	Fluoresc.	29	42	16	12	<3	0.122

of the mine, metacinnabar (as well as volcanic materials with quartz inclusions) is found within the Almadén Hg belt area.

It is also important to highlight the presence of slightly soluble solid mercury compounds as $HgSO_4$ or $HgCl_2$, with a content normally ranging from 5 to 47% of the total mercury concentration. Although products other than HgS are unlikely to occur naturally, the physical fractionation of soil organic matter (dissolved *vs*. adsorbed) that determines the behaviour and distribution of Hg in soils, makes these types of species possible to a large extent.[31] This fact reveals an evident risk of mercury mobilisation, as can be observed in Fig. 5, where solubility of different mercury solid phases has been plotted against the pH.

Hg speciation has been found to be influenced by the type of geological environment in which the Hg ore is formed.[28] Thus, silica-carbonate type deposits are associated with serpentinite that has been altered to an assemblage of silica and carbonate minerals, while many of the hot-spring Hg deposits are associated with volcanic rocks that have been silicified and altered to a clay alteration assemblage, as well as Almadén mercury deposits, despite their different geological origin.[10] Both were found to contain soluble Hg-chloride and sulfate phases, which were largely absent in samples from silica-carbonate Hg depos-

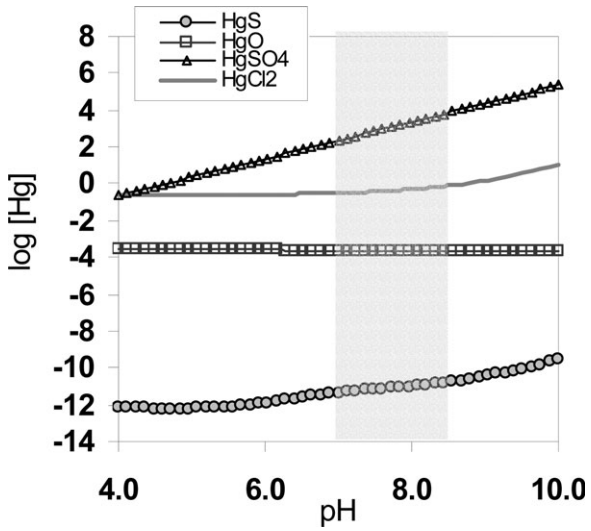

Fig. 5 Solubility limits of some solid mercury phases evaluated in the study: cinnabar, HgO, $HgCl_2$ and $HgSO_4$. Calculations undertaken by HYDRA.[32] The vertical guideline shows the pH range found in the Almadén aquatic environment.

its. Such phases could become available during roasting processes, due to the decomposition of the abundant hydrothermal alteration products, particularly clays, which are bathed in saline fluids or by the vaporization of remnant water.[33,34] Moreover, mercury ores and slag are exposed to repeated wetting and drying cycles and weathering processes, that can induce dissolution and reprecipitation of soluble Hg species with time.[28]

The higher solubility of many of these phases compared to the almost insoluble Hg-sulfides indicates that, although representing a smaller percentage of the total Hg in the sample, these species may largely contribute to the ionic Hg in the surrounding environment, which can be methylated by sulfate-reducing bacteria.

Acknowledgements

We acknowledge the European Synchrotron Radiation Facility for provision of synchrotron radiation facilities and thank Laurent Álvarez for his valuable assistance in using beamline ID26 at ESRF. Synchrotron experiments at HASYLAB were supported by the IHP-Contract HPRI-CT-1999-00040 of the European Commission. Edmund Welter and Gerald Falkenberg are gratefully acknowledged for their technical support during synchrotron experiments. Financial contribution from both the EU project: EVK1-CT-1999-00002 and the Spanish grant PPQ2002-04267-C03-01 is also acknowledged. Special gratitude for Ricardo Lacámara from "Mina de Almadén y Arrayanes", for his invaluable assistance providing samples, and priceless advice. Anna Bernaus thanks the "Ministerio de Educación, Cultura y Deporte" for a PhD scholarship (2002–2004).

References

1 U. Förstner, in *Integrated Pollution Control*, ed. A. Weissbach and H. Boeddicker, Springer-Verlag, Berlin, 1998, pp. 81–130.
2 I. Rodriguez and A. Carro, *Anal. Bioanal. Chem.*, 2002, **372**, 74.
3 C. S. Kim, N. S. Bloom, J. J. Rytuba and G. E. Brown Jr., *Environ. Sci. Technol.*, 2003, **37**(22), 5102.
4 M. O. Barnett, L. A. Harris, R. R. Turner, T. J. Henson, R. E. Melton and R. J. Stevenson, *Water, Air, Soil Pollut.*, 1995, **80**, 1105.
5 G. Morin, J. D. Ostergren, F. Juillot, P. Ildefonse, G. Calas and G. E. Brown Jr., *Am. Mineral.*, 1999, **84**(3), 420.
6 J. D. Ostergren, G. E. Brown Jr., G. A. Parks and T. N. Tingle, *Environ. Sci. Technol.*, 1999, **33**(10), 1627.
7 A. L. Foster, G. E. Brown Jr., T. Tingle and G. A. Parks, *Am. Mineral.*, 1998, **83**(5–6), 553.
8 D. Hesterberg, D. E. Savers, W. Zhou, G. M. Plummer and W. P. Robarg, *Environ. Sci. Technol.*, 1997, **31**, 2840.
9 L. Vincze, F. Wei, K. Proost, B. Vekemans, K. Janssens, Y. He, Y. Yan and G. Falkenberg, *J. Anal. At. Spectrom.*, 2002, **17**, 177.
10 J. J. Rytuba, *Environ. Geol.*, 2003, **43**, 326.
11 E. Ortega and A. Hernández, *Chron. Rech. Min.*, 1992, **506**, 3.
12 J. J. Rytuba, R. O. Rye, A. M. Hernandez, J. A. Deen and A. Ambas, *Int. Geol. Congr.*, 1988, 2–741, (Abstracts with Program).
13 S. E. Lindberg, D. R. Jackson, J. W. Huchabee, S. A. Janzen, M. J. Levin and J. R. Lund, *J. Environ. Qual.*, 1979, **8**, 572.
14 J. W. Huckabee, F. Sanz-Diaz, S. A. Janzen and J. Solomon, *Environ. Pollut., Ser. A*, 1983, **30**, 211.
15 R. Ferrara, B. E. Maserti, M. Andersson, H. Edner, P. Ragnarson, S. Svanberg and A. Hernandez, *Atmos. Environ.*, 1998, **32**, 3897.
16 C. S. Kim, J. J. Rytuba and G. E. Brown Jr., *Sci. Total Environ.*, 2000, **261**, 157.
17 Certificate of analysis standard reference material 2710 Montana soil (highly elevated trace element concentrations), National Institute of Standards & Technology, Gaithersburg, MD, 28 October 1997.
18 R. Fernández-Martínez and M. I. Rucandio, *Anal. Bioanal. Chem.*, 2003, **375**, 1089.
19 M. O. Barnett, L. A. Harris, R. R. Turner, R. J. Stevenson, T. J. Henson, R. C. Melton and D. P. Hoffman, *Environ. Sci. Technol.*, 1997, **31**(11), 3037.
20 G. A. Waychunas and G. E. Brown Jr., *Adv. X-Ray Anal.*, 1994, **37**, 607.
21 T. Ressler, *J. Synchrotron Radiat.*, 1998, **5**(2), 118.
22 G. Falkenberg, S. Mangold and E. Welter, μ-*XAFS investigations of Pb-contaminated soil samples*, Hasylab Annual Report, 2002. [on line], http://www-hasylab.desy.de/science/annual_reports/2002_report/main.htm, ed. U. Krell, J. R. Schneider and M. von Zimmermann, December 23, 2002.
23 A. Prange, B. Birzele, J. Kraemer, H. Modrow, R. Chauvistre, J. Hormes and P. Koehler, *J. Agric. Food Chem.*, 2003, **51**(25), 7431.
24 G. Sarret, T. Mongenot, J. Connan, S. Derenne, M. Kasrai, M. G. Bancroft and C. Largeau, *Org. Geochem.*, 2002, **33**(8), 877.
25 G. P. Huffman, N. Shah, F. E. Huggins, L. M. Stock, K. Chatterjee, J. J. Kilbane, M. M. Chou and D. H. Buchanan, *Fuel*, 1995, **74**(4), 549.
26 K. G. Sushchuk and I. I. Sakhatskii, *Geol. Geofiz.*, 1972, **34**(3), 222.
27 N. W. Revis, T. R. Osborne, G. Holdsworth and C. Hadden, *Water, Air, Soil Pollut.*, 2001, **45**, 105.
28 C. S. Kim, J. J. Rytuba and G. E. Brown Jr., *Appl. Geochem.*, 2004, **19**(3), 379.
29 F. W. Dickson and G. Tunell, *Am. Mineral.*, 1959, **44**, 471.
30 J. J. Rytuba, *Mercury Geoenvironmental Models*, in *Progress on geoenvironmental models for selected mineral deposit types*, ed. R. R. Seal and N. K. Foley, 2002. [on line], http://pubs.usgs.gov/of/2002/of02-195/, [25 February 2004].
31 E. Schuster, *Water, Air, Soil Pollut.*, 1991, **56**, 667.
32 I. Puigdomenech, Chemical Equilibrium Software MEDUSA and Data Base HYDRA, 2002, http://www.kemi.kth.se/utbildning/gk/kemiskjmv/, Updated 18 February 2004.
33 F. W. Dickson and G. Tunell, in *Mercury and antimony deposits associated with active hot springs in the western United States*, ed. J. D. Ridge, New York, 1968, pp. 1673–1701.
34 D. E. White and C. E. Roberson, in *Sulfur Bank, California: a major hot-spring quicksilver deposit*, ed. A. E. J. Engel, H. L. James and B. F. Leonard, Geological Society of America, New York, 1962, pp. 397–428.

Annex 4

Available online at www.sciencedirect.com
SCIENCE DIRECT
Analytica Chimica Acta 565 (2006) 73–80
ANALYTICA CHIMICA ACTA
www.elsevier.com/locate/aca

Determination of mercury in polluted soils surrounding a chlor-alkali plant Direct speciation by X-ray absorption spectroscopy techniques and preliminary geochemical characterisation of the area

Anna Bernaus [a], Xavier Gaona [a], Derk van Ree [b], Manuel Valiente [a,*]

[a] *Grup de Tècniques de Separació en Química (GTS), Departament de Química, Universitat Autònoma de Barcelona, 08193 Bellaterra, Spain*
[b] *GeoDelft-National Institute for Geo-Engineering, Stieltjesweg 2, P.O. Box 69, 2600 AB Delft, The Netherlands*

Received 22 November 2005; received in revised form 8 February 2006; accepted 8 February 2006
Available online 6 March 2006

Abstract

Soil samples collected in the surroundings of a chlor-alkali plant in the Netherlands were characterised by synchrotron-based techniques and conventional analytical procedures, in order to evaluate the environmental impact of Hg emissions and other heavy metals present in these locations. Analysis of total metal content by inductively coupled plasma-optical spectroscopy (ICP-OES) revealed a heterogeneous contamination of Hg, with concentrations ranging from 4.3 to 1150 $\mu g\, g^{-1}$. In addition, significant concentrations of Cu, Ni, Pb, Zn, Mn and principally Fe were also identified within the studied samples. Direct determination of mercury species by X-ray absorption near edge spectroscopy (XANES) showed inorganic Hg compounds to prevail in all soils, being Cinnabar (HgS_{red}) and Corderoite ($Hg_3S_2Cl_2$) the main species. Nevertheless, more soluble mercury compounds, such as HgO and $HgSO_4$, have been also identified in significant proportion (from 6 to 20% of total mercury content), indicating a potential risk of mercury mobilisation. On the other hand, the application of sequential extraction schemes (SES) revealed large portions of weakly available Hg extracted in the residual fraction, while Hg associated to the exchangeable phase amounts as much as 19% of total Hg, thus, supporting the results obtained by XANES.

Finally, synchrotron-based micro X-ray fluorescence (μ-XRF) was applied to identify qualitative trends on elemental associations in sample particles through a systematic mapping of its surface. In this concern, results show a well-defined correlation between Hg and Cu/Ni in the analysed particles. On the other hand, an absence of correlation between Hg and several other elements (Fe, Ti, Ca, Zn, Mn and S) was also observed. These effects have been attributed to chemical and physical interactions of mercury species on both enriched particles and sample matrices.

Keywords: Soil mercury speciation; Chlor-alkali plant; Mercury mobility; X-ray absorption near edge spectroscopy (XANES); Micro X-ray fluorescence (μ-XRF); Sequential extraction schemes

1. Introduction

The chlor-alkali industry, which produces caustic soda, hydrogen and chlorine by the mercury process, has been one of the biggest Hg users and emitters, responsible for 90% of Hg utilisation prior to 1980 [1]. Mercury input from the chlor-alkali industry has been decreasing due to process improvement [2], and conversion to the membrane process not involving Hg, and is nowadays about two orders of magnitude lower than in 1980s [3]. Nonetheless, the effects can be observed long after the plants had closed down [4,5], since mercury is found into nearby waters and accumulated in soils, plants and across the aquatic food web [6,7].

The main sources of Hg, primarily found as Hg^0 (gas) and Hg^{2+}, are ventilation air outlets from cell rooms, as well as the release from waste water and solid wastes removed from the settling tanks dumped in the nearby field [8]. The sum of such sources reported Hg concentrations up to 75 times the background in soils surrounding chlor-alkali plants [9] (considering $100\ \mu g\, kg^{-1}$ as threshold level [10]).

Once released to the environment, Hg can be exposed to several processes, including chemical, biological and photochemical reactions [11]. Many mercury compounds, both organic and inorganic, decompose to yield elemental Hg, which may volatilise, convert to HgS (depending on redox conditions of the environment) or complex with inorganic ligands. In this sense,

* Corresponding author. Tel.: +34 935812903; fax: +34 935812379.
E-mail address: Manuel.Valiente@uab.es (M. Valiente).

0003-2670/$ – see front matter © 2006 Elsevier B.V. All rights reserved.
doi:10.1016/j.aca.2006.02.020

the chemical form in which Hg is found largely determines the mobility of this element, affecting parameters such as solubility, sorption or bioavailability [12]. On the other hand, the behaviour of Hg in soil profiles is strongly influenced by the presence of certain soil materials: organic matter (OM), clays, as well as oxyhydroxides of Fe and Mn play also an important role on the retention of mercury. In acidic soils, the role of OM may predominate but in alkaline and calcareous soils, clay mineralogy and the presence of iron oxides become key parameters for the evaluation of Hg behaviour.

Many efforts have been previously devoted to the study of Hg contamination around chlor-alkali industries [13–15], but limited reliable data on Hg speciation have been described. In this concern, only analytical procedures, such as thermal desorption [16] which may substantially alter the speciation of Hg from its initial state [17], have been applied. Moreover, little has been reported about the binding and mobility of Hg derived from such emissions [18].

In this context, the aim of the present work is to evaluate the environmental impact of Hg in the neighbouring area of a chlor-alkali industry, by determining the chemical speciation as well as the geochemical factors that contribute to the mercury fate within the affected area. For this purpose, synchrotron-based X-ray absorption spectroscopy (XAS) techniques have been selected for the study of molecular-level environments, showing species-specific detection capacities while needing almost no sample pre-treatment (with a consequent minimal species modification) [19–22]. The study takes also advantage of μ-XRF measurements, which have been utilised aiming to identify possible geochemical linkages between elements contained within the sample [23]. Additional characterisation methods, such as total digestion, elemental analysis by ICP-OES and sequential extraction schemes, have been applied to evaluate the overall chemical composition of the samples as well as the possible behaviour of Hg in the soil environment.

2. Experimental methods

2.1. Sampling and storage of soil samples

Five Hg-contaminated surface soil samples (M1, M2, M3, M4 and M5) were collected from January 14 to 16, 2004, around a chlor-alkali plant in the Netherlands. The site is located next to a river in an alluvial plain, and consists of fine sand with clayey lenses. An overview of the samples and site conditions is shown in Table 1.

M1, M2, M3 and M4 were collected in the vicinity of the mercury cell and the mercury recycling unit (distillation) in the northern part of the site, whereas M5 was collected in the settling basins located at the southern end of the site.

Shallow depth sampling of the soil materials was done by means of a hand-auger, and samples were kept in glass jars sealed by a rubber ring. These samples were later split into several aliquots and sent in a polystyrene box in dry ice pellets to the analysis laboratory.

Before the beginning of the analysis, samples were de-frozen, and air-dried until constant weight. Then, each aliquot was milled to a grain size <100 μm, sieved and stirred for 10 min in a Vortex apparatus until the final homogenisation. During the whole process, samples were protected against light in order to avoid possible transformation of the species.

2.2. Total metal and methyl mercury content analyses

Sample digestion was undertaken in order to quantify total metal concentration. In addition to Hg, the elemental analysis included: As, Cu, Fe, Mn, Ni, Pb and Zn. Total metal content was achieved by digestion with an Analytical Microwave system (MARS-5 model from CEM Corporation, USA). As described elsewhere [24], digestion was undertaken in hydrofluoric acid media, in order to ensure the total digestion of the soil sample. Elemental analysis over the aqueous phase was undertaken by means of an ICP-OES equipment (Thermo Elemental, model Iris Intrepid II XSP, USA). A detailed description of the power program utilised for microwave digestion can be found in Bernaus et al. [23].

Additionally, to counteract poor detection limits of XAS techniques, methyl mercury concentration was determined by a first extraction process (following the modified Westöo process), combined with the separation and quantification of the species by a high performance capillary electrophoresis (HPCE) system. Exact details of the methyl mercury extraction and speciation procedures can be found elsewhere [25].

2.3. Sequential extraction procedure

A novel sequential extraction scheme (SES) developed by Neculita et al. has been used to determine the distribution of Hg and other metals present, bound or associated in several groups

Table 1
Physico-chemical characterisation of samples and site conditions

	Depth (m-bgl)	Water content (%)	pH	C total (%)	S total (%)	Cl^- (mg kg^{-1})
M1	0–0.15	8.38				
M2	0–0.15	13.01				
M3	0.15–0.30	10.66				
M4	0–0.10	10.67				
M5	0–0.20	41.35				
Site condition			7.92 ± 0.04	2.15	0.051	5

Data from GeoDelft-National Institute for Geo-Engineering, The Netherlands.

of different leachability [26–29]. This SES procedure is reported to have been tested in soils from chlor-alkali plants and validated using a certified reference material (CRM) and pure Hg compounds [18].

The procedure consists of four steps, permitting the identification of four different fractions defined as: F1, water-soluble, in which Hg is easily released; F2, exchangeable under alkaline conditions (pH 8.4) in the presence of a complexing agent (0.5 mol l^{-1} NH_4-EDTA); F3, bound to organic matter or available under successive extraction with 0.2 mol l^{-1} NaOH and CH_3COOH 4% (v/v); and F4, residual Hg, quantified in our study by subtracting the total amount of metals extracted in previous steps from the total amount obtained by digestion with HF.

Following the Neculita's protocol, the extraction was performed by weighing 2 g of soil sample mixed with 20 ml of solvent in a 50-ml centrifuge tube. In all steps, the mixture was agitated for 2 h at room temperature in a test tube shaker (*TTS 2*, Wilmington, USA). The extract from the solid residue was separated by centrifugation (Digicen CE 007, Barcelona, Spain) at 4700 rpm for 25 min and filtrated through a 0.22 μm filter. In all extractions, the extract was immediately analysed by means of an ICP-OES. Finally, the residue was washed by adding 10 ml of milli-Q water, agitated for 15 min and centrifuged for 15 min at 4700 rpm. The supernatant was decanted and discarded, and the solid residue was used in the next extraction step.

2.4. XANES analyses

XANES spectra were obtained at the Beamline A1 of the Hamburger Synchrotronstrahlungslaborin (HASYLAB) synchrotron facility in Hamburg (Germany). Details about beamline set-up are given in Table 2.

Hg species present and their relative abundance were obtained by comparing the spectra of unknown samples with a set of spectra of reference Hg minerals and pure compounds collected at the same beamline conditions. The reference compounds included: $HgCl_2$, Hg_2Cl_2, $HgSO_4$, HgO_{red}, $Hg(CH_3COO)_2$, CH_3HgCl, HgS_{red} (Cinnabar), HgS_{black} (Metacinnabar), $Hg_2NCl_{0.5}(SO_4)_{0.3}(MoO_4)_{0.1}(CO_3)_{0.1}\cdot H_2O$ (Mosesite) and $Hg_3S_2Cl_2$ (Corderoite).

Prior to synchrotron analysis, soil samples and reference compounds were powdered and diluted with polyethylene, homogenised in a Vortex apparatus, and pressed as a pellet under 5 tonnes cm^{-2} for 5 min. The total amount of sample in each pellet varied from 50 to 100 mg, while polyethylene amount was kept between 100 and 150 mg.

Reference compounds were analysed in transmittance mode (detection with two ionisation chambers) following the Hg absorption L_{III} line at 12,284 eV, while spectra of unknown samples were obtained in fluorescence mode (solid state detector), by following Hg $L_{\alpha1}$ (9988.8 eV) and $L_{\alpha2}$ (9897.6 eV) fluorescent lines. Selection of the detection mode was based on sample concentration and matrix background [30]. In both cases, a double crystal Si(1 1 1) monochromator was used.

Raw XANES data were evaluated by using SixPACK software package [31]. Spectra processing included energy correction, signal normalisation and background correction. Subsequently, a principal component analysis (PCA) was applied to derive the number and the type of reference compounds from the database required to reconstruct the spectrum of the unknown sample [32–34]. Finally, a linear least-square fitting procedure was used to fit the model spectra from the compound database to sample spectra. The energy range considered for the fitting process was 12,200–12,600 eV. Quality of the analysis can be evaluated by the reduced chi-square value (χ^2), which represents the goodness of the fit by the linear combination procedure [35]. In the present work, the limiting proportion for a given component has been fixed at 5% of total mercury composition. Nevertheless, values below 10% must be mainly taken as indicative.

2.5. Microprobe analyses

μ-XRF and μ-XANES analyses were performed at the Beamline L of HASYLAB synchrotron facility (see beamline set-up

Table 2
Beamline set-up

Beamline	Source	Source energy (GeV)	Maximum current (mA)	Monochromator crystals	Resolution ($\Delta E/E$)	Photon flow at the sample (phot s^{-1})	Spot size at the sample	Detectors	Angle bunch-sample (°)	Temperature
A1	Bending magnet	4.5	150	Si(1 1 1) (Si(3 1 1) also available)	$\sim10^{-4}$	About 10^9	2 mm × 3 mm	-Three ionisation chambers -Si(Li) (7 pixel)	45	Room, liquid N_2 (liquid He also available)
L	Bending magnet	4.5	150	Si(1 1 1)	$\sim10^{-4}$	About 10^9	15 μm × 15 μm	-Two ionisation chambers -Si(Li) and silicon drift detector	45	Room

Table 3
Total metal concentration in samples M1, M2, M3, M4 and M5 from a chlor-alkali industry, by MW digestion + ICP-OES analysis (mg kg^{-1}), and determination of methyl mercury (mg kg^{-1}) by HPCE-UV

Sample	Hg_{total}	CH_3Hg	As	Cu	Fe	Mn	Ni	Pb	Zn
M1	4.3 ± 0.2	<5	6.0 ± 0.2	11.7 ± 0.1	14900 ± 155	656 ± 4	7.1 ± 0.1	25.6 ± 0.4	62 ± 1
M2	1150 ± 8	<5	17.2 ± 0.8	26.7 ± 0.2	31090 ± 54	667 ± 8	51 ± 2	165 ± 7	183 ± 6
M3	70.9 ± 0.8	<5	7.7 ± 0.5	227 ± 1	16300 ± 130	419 ± 3	5.2 ± 0.2	113 ± 2	194 ± 3
M4	36.1 ± 0.2	<5	8.9 ± 0.2	20.51 ± 0.06	16600 ± 239	582 ± 6	23.7 ± 0.9	55 ± 1	73 ± 2
M5	130 ± 0.9	<5	1.8 ± 0.9	106 ± 1	5325 ± 93	30 ± 0.5	8200 ± 345	60 ± 2	290 ± 12

The S.D. value given corresponds to the standard deviation of three replicates within the 95% confidence interval.

in Table 2). The application of these techniques intended to resolve phase associations and establish elemental relationships between Hg and other elements present including, As, Cl, Ca, Fe, Cu, Ni, Pb, Ti, Zn, Mn and S. Moreover, this tool has been applied to M1 speciation for improving the poor detection limits of XANES [36].

The methodology applied took advantage of the identification and focusing of individual (mercury-rich) particles by μ-XRF, as a previous step to μ-XANES analysis. In this sense, to gain precision and time during beam time at HASYLAB, particles were previously identified in the laboratory by using an electron microscope JEOL JSM 6300 (Jeol Ltd., Tokyo, Japan), equipped with an energy X-ray dispersive spectrometer Link ISIS-200 (Oxford Instruments, England). Samples were scanned in a back scattering mode, and Hg-rich particles were identified taking into account their position referred to two platinum filaments inserted into the corresponding sampler.

Within synchrotron measurements, samples were monitored by a long distance zoom microscope with a magnification of 300×, and a CCD-camera with a resolution of 3 μm, and Hg-rich particles were identified by XRF and focused with a highly collimated beam ($\phi \sim 2$ μm), reached with a capillary optic device.

The μ-XRF mapping was performed by using a step-scan mode over squares of 100 μm^2, with a step width of 10 μm. Consequently, each mapping figure was composed by 100 different pixels. During the whole mapping analysis, the energy of the incident radiation was monochromatised at 13 keV with a Si(1 1 1) crystal. The time of signal accumulation was selected as a function of total count-rate, varying between 1 and 10 s per step. μ-XANES data from two Hg-rich particles identified in M1 were collected following the Hg L_{III} line at 9988.8 eV, and the fluorescence signal was recorded using the abovementioned fluorescent detector.

3. Results and discussion

3.1. Chemical characterisation

Table 3 summarises the total metal content present in samples M1–M5, after MW digestions and analysis by ICP-OES. The analyses intended to broaden information of the geochemistry of the sampling sites while improving the knowledge about the presence of possible interferences for synchrotron analyses.

Mercury content was found to be highly variable, ranging from concentrations higher than 1 g kg^{-1} in sample M2 (∼1150 mg kg^{-1}) to the slightly contaminated sample M1 with 4 mg kg^{-1}. These results demonstrate the significant spatial variability occurring in this type of sites, which, in this case, shows differences in mercury concentration of about 250-fold. The impacted area is not only related to the proximity of the mercury source in the industrial installations, but the distribution of mercury is also strongly influenced by the transport mechanism, type of substrate and particle size [37], and redistribution by human activities on site (building, resurfacing, redistribution of materials from basins, etcetera).

Quantification of other heavy metals revealed a strong variation in their distribution. Thus, a very high amount of Fe and Mn has been found in all samples while As is present only in very small amounts. On the other hand, a significant presence of Cu, Ni, Pb and Zn was identified. The high content of Fe is important when performing XAS analysis in fluorescence mode, since iron excitation can lead to an easier saturation of the detector with the consequent increasing of the related detection limits. Taking into account naturally occurring substrates and the pH of the site (Table 1), Fe- and Al-oxyhydroxides are abundant in this type of areas, being effective sorbents of Hg(II). In addition, Pb and Zn are sensible to produce spectral interferences in XAS analysis of Hg (fluorescence detection mode).

Table 4
Mercury fractionation (mg kg^{-1} and %) in samples M1, M2, M3, M4 and M5, by the specific three-step sequential extraction procedure proposed by Neculita et al., and final residue (total amount extracted by digestion − total amount extracted by the six-step SEP)

Sample	Total Hg (mg kg^{-1})	Fraction 1 (mg kg^{-1})	% (approx.)	Fraction 2 (mg kg^{-1})	% (approx.)	Fraction 3 (mg kg^{-1})	% (approx.)	Fraction 4 (mg kg^{-1})	% (approx.)
M1	4.3 ± 0.2	0	0.0	0.7 ± 0.1	16.3	0.44 ± 0.08	10.2	∼3.2	74.4
M2	1150 ± 8	2.7 ± 0.2	0.2	107 ± 4	9.3	35 ± 2	3.0	∼1005.6	87.4
M3	70.9 ± 0.8	0.6 ± 0.1	0.8	12.2 ± 0.2	17.2	8.5 ± 0.5	12.0	∼49.6	70.0
M4	36.1 ± 0.2	0	0.0	6.78 ± 0.05	18.8	16.3 ± 0.3	45.3	∼13.0	36.0
M5	130 ± 0.9	0.09 ± 0.02	0.1	7.53 ± 0.07	5.8	0.4 ± 0.1	3.4	∼117.9	90.7

Methyl mercury in soil samples was not detectable below 5 mg kg^{-1} (detection limit, see Table 3).

3.2. Sequential extraction schemes in soils

Sequential extractions of five samples (see Table 4) indicate that mercury distribution among the different fractions in all samples is similar, except for M4.

Mercury extracted from samples M1, M2, M3 and M5 was mainly attached to the residual fraction (F4), with average composition ranging from 70.0 to 90.7%. Therefore, mercury is expected to be found under the form of non-volatile and weakly available Hg, most likely HgS (sulphide minerals have been reported to be excellent scavengers for heavy metals [38,39]).

The second main group of mercury species was extracted within the 'exchangeable phase', which can be correlated with soluble species of Hg in the oxic layer of the soil (16.3% M1, 9.3% M2, 17.2% M3, 18.8% M4 and 5.8% M5).

On the other hand, mercury present in sample M4 was mainly found in the organic fraction (F3) (45.3%). In addition, the lower residual fraction of this soil and the highest percentages of mobile Hg (F1 + F2) indicate a higher risk of Hg mobilisation, due to the presence of mercury soluble compounds and organic complexes [15]. These results corroborate the anthropogenic source of the Hg presence, given the lack of correlation between Hg content and organic matter in soils. This correlation has been demonstrated by different authors in natural soils [40–42], confirming that Hg(II) is preferment bounded to OM [43,44].

All samples resulted in low mercury concentrations in the water-soluble fraction (F1), indicating a poor Hg availability due to weathering processes. However, when talking in terms of concentration, the environmental impact of mercury content in sample M2 must be taken into consideration, given the relatively high mercury concentration in the F1 fraction (2.7 mg kg^{-1}).

Moreover, mercury can be released to the porewaters if iron and manganese oxyhydroxides undergo a reductive dissolution as a consequence of microbial degradation of organic matter [45].

3.3. Mercury speciation by XANES and μ-XANES

Refined XANES spectra obtained at Beamline A1 are given in Fig. 1 for samples M2, M3, M4 and M5. The analysis of sample M1 did not result in valuable data, given the presence of lower mercury concentrations. Therefore, μ-XANES analysis was undertaken for this sample over two Hg-rich particles, previously identified by means of μ-XRF. Results correspond to the average of five replicates for each XANES and μ-XANES spectrum.

Results of principal component analysis of samples M1 (Hg-rich particles), M2, M3, M4 and M5 and the model compounds listed above indicate a main contribution of four inorganic species: Cinnabar, HgO_{red}, $HgSO_4$ and Corderoite. On the basis of the PCA concept, these four reference compounds are needed to reconstruct each of the sample spectra above the 95% of confidence level.

Fig. 1 shows the corrected XANES spectra for samples M2, M3, M4 and M5 as well as the adjusted spectra from the linear combination of reference compounds obtained according to the PCA results. The relative proportions of each reference compound found for each XANES analysis undertaken, as well as the sum of components in each sample and the reduced chi-square value (χ^2) are given in Table 5.

The bulk of the samples contained Cinnabar and Corderoite as the main Hg phases, each compound representing about one-third of the total mercury content. Readily soluble inorganic mercury compounds ($HgSO_4$ and HgO) have been also identified in significant proportions (between 6 and 20%), posing a significant source for mercury mobilisation. Concerning sample M1, μ-XANES analyses undertaken on mercury rich particles have led to the identification of important heterogeneities among the sample core, being HgO and $HgSO_4$ the main mercury compounds identified.

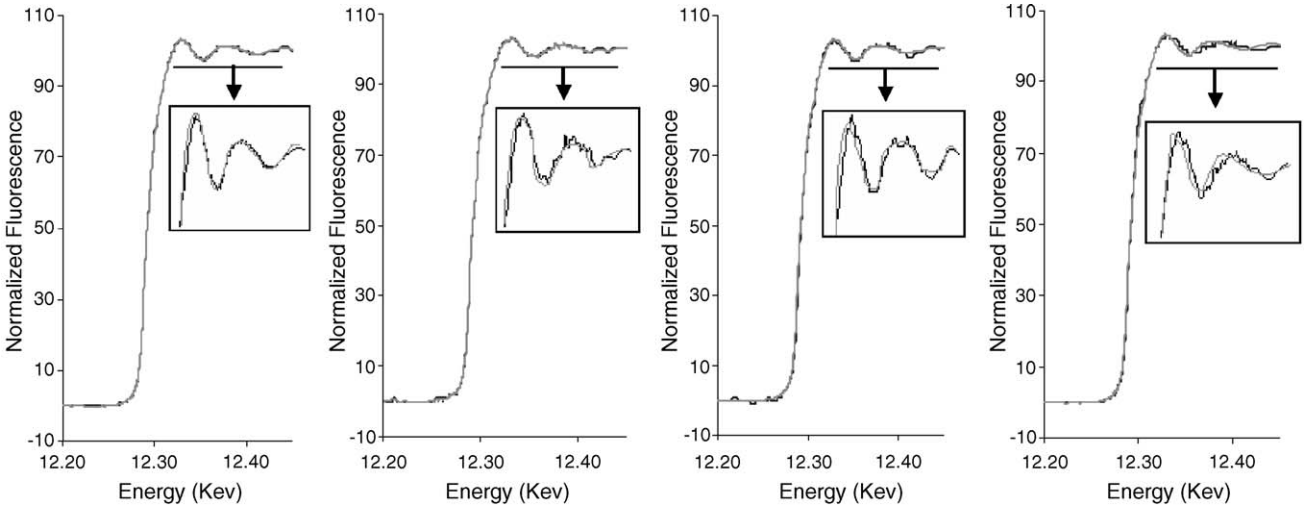

Fig. 1. Comparison of normalised XANES spectra (black line) of M2, M3, M4 and M5 (showed in this order), with the best fit spectra (grey line). The inset figure shown in each plot corresponds to a magnification of the region slightly above the edge.

Table 5
Chemical speciation of Hg rich particles in M1, and samples M2, M3, M4 and M5

Sample	HgS_{red}	HgO	$HgSO_4$	Corderoite	Component sum.	Reduced χ^2
M1 part. 1		86.4	16.85		103.25	0.028
M1 part. 2	26.28		79.95		106.23	0.030
M2	32.85	10.31	19.82	33.47	96.45	0.00028
M3	32.96	10.19	19.79	33.58	96.52	0.00030
M4	33.18	9.91	19.85	33.82	96.76	0.00045
M5	36.78	6.12	18.05	37.28	98.23	0.00020

Concentration values expressed in percent over total mercury content in each sample determined by ICP-OES analysis.

The chemical speciation ascertained by means of XAS measurements can be explained in terms of the specific environmental conditions found in the site. Hence, the presence of high concentrations of S in soils (see Table 1) can involve the formation of complexes with trace metals, such as Hg, showing high stability constant for sulphide compounds (i.e., $\log K_{HgS} = 42.0$) [16].

On the other hand, the presence of chloride ions (see Table 1) can induce the formation and release of mercury chlorocomplexes, such as Corderoite. The presence of this solid phase might be explained as the result of secondary processes, with $HgCl_2$ and HgS being the reactants [46], through the prolonged weathering of the site. The chloride ions originate from the raw material, NaCl, of the electrolytic process.

Mercury association to sulphides can be, however, remobilised by oxidation. It is known that transport of dissolved oxygen by burrowing organisms can cause the local oxidation of reduced inorganic compounds [47], with the consequent formation of HgO. Moreover, the partial or full oxidation of oxygen-reactive metastable sulphides (e.g., iron sulphides) to $S_xO_y^{-z}$, can form soluble mercury complexes, such as $HgSO_4$, and be released to the porewaters [48].

3.4. Geochemical characterisation of elemental composition by μ-XRF

μ-XRF elemental maps undertaken on a 100 μm^2 section from sample M5 (showing the vicinity of a Hg-rich particle) are given in Fig. 2. The XRF elemental analysis included Hg, As, Cl, Ca, Fe, Cu, Ni, Pb, Ti, Zn, Mn and S. In spite of the poor uniformity of Hg distribution in the soils, similar qualitative information was obtained for each particle analysed by μ-XRF. Nevertheless, it must be pointed out that this information might not be representative for the bulk of the samples, since μ-XRF mappings were only undertaken in surface areas with the presence of a relatively large Hg particle (30 μm × 30 μm).

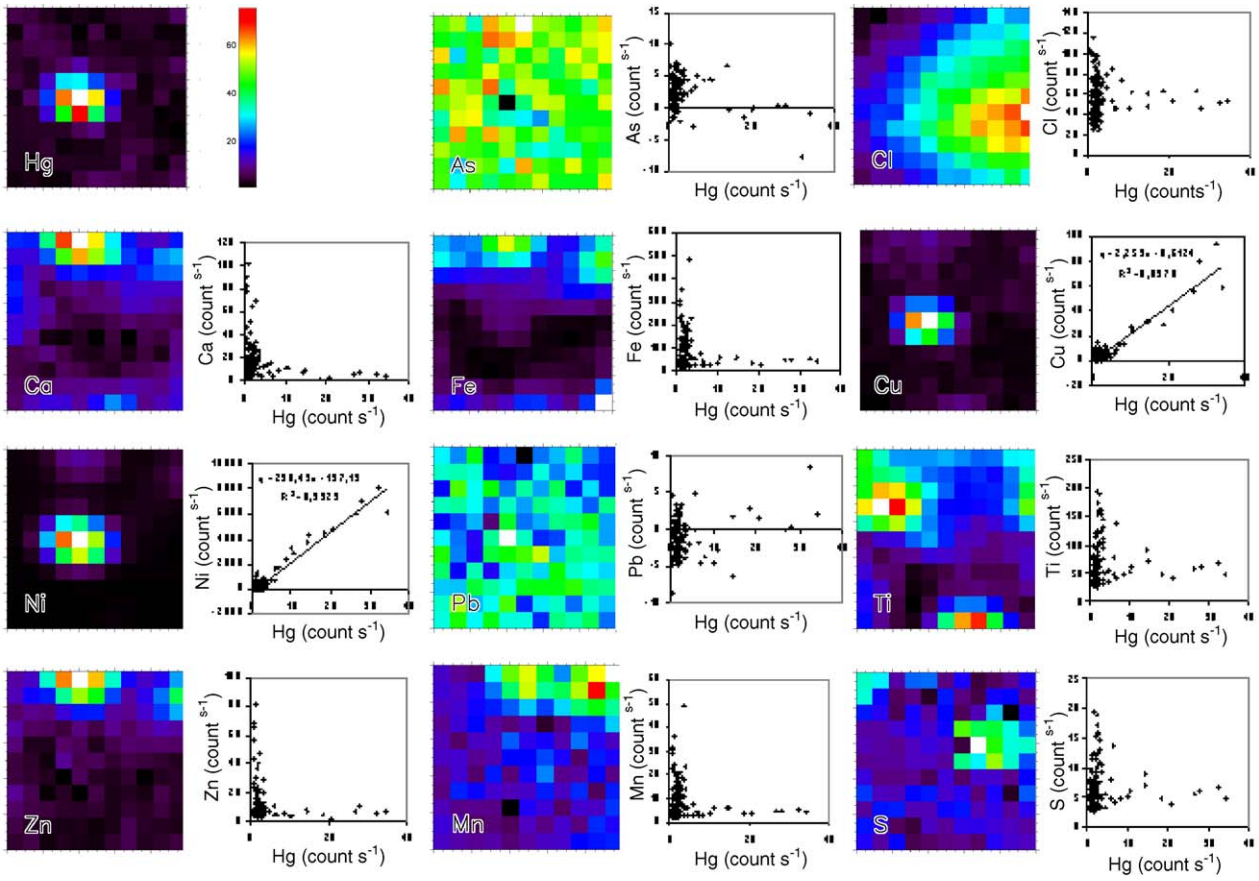

Fig. 2. μ-XRF elemental maps for Hg, As, Cl, Ca, Fe, Cu, Ni, Pb, Ti, Zn, Mn and S on a 100 μm^2 area in a Hg-rich particle found in M5, and pair correlation diagrams of each element relative to Hg, as normalised fluorescence intensity (counts/s). White colour shows the greatest point of counts found, at the fluorescence energy of each element, without normalising.

Likewise, Fig. 2 shows pair correlation diagrams of different elements related to Hg, taking into account data about total count-rate extracted from each pixel in each mapping analysis.

Different trends have been identified within this evaluation:

- A linear correlation of Cu and Ni with Hg. This result might suggest the possible formation of solid solutions of these elements within the same crystalline structure. Nevertheless, this hypothesis cannot be totally confirmed by means of μ-XRF analysis. The absence of correlation between these elements and S would indicate that, when concerning big crystals, the spatial coincidence of Cu, Ni and Hg has nothing to do with their known affinity toward sulphide.
- An observed correlation between the presence of Fe and Mn (as well as Ti, Ca and Zn) and the absence of Hg, and vice versa. This fact would indicate that signal from Hg-rich particles do not correspond neither to Hg compounds adsorbed onto Fe- or Mn-oxyhydroxides nor to Hg metal amalgam.
- Random relationship between Hg and As, Cl and Pb. The relatively low presence of these elements together with their weak excitation at the irradiated energy (13 keV, i.e., Cl ($K_\alpha = 2622$ eV)) may explain this lack of correlation.

Finally, a linear correlation between Zn and Fe was also identified, and attributed to the possible sorption of Zn onto Fe oxyhydroxides.

4. Conclusions

Mercury concentration in surface soils around a chlor-alkali plant increases by a factor of $\sim 10^4$-fold when compared to the pre-industrial level. Consequently, mercury contamination is a major concern in which speciation, accumulation in the aquatic food web and entering into the food chain is a potential risk to humans. For a number of samples mercury speciation, leachability based on sequential extraction techniques and the correlation with other compounds has been studied. Although the concentrations in soil varied by a factor of more than 250, with 1150 mg kg^{-1} as the highest value, low mercury concentrations were found in the water-soluble fraction. No methyl mercury was found, however the detection limit was too high to conclude on the environmental implications.

Information on the chemical speciation obtained by XANES and SES procedures indicate a main contribution of inorganic species of Hg weakly available, despite the existence of significant concentrations (up to 20% of total Hg content) of more soluble inorganic compounds ($HgSO_4$ and HgO). Nevertheless, SES results have shown a preferred bounding of Hg to the organic fraction in one of the evaluated samples (M4). This fact that was not identified by means of XANES speciation (probably due to specific parameters not measured in this study, i.e., the accurate size distribution of soil particles and the specific organic content of this sample which is probably the highest of the target samples because it was taken in the only place of the sampled area having growing grass) reveals the appropriateness of the proposed coupling scheme of applying different analytical techniques. Hence, this approach should be considered as a useful tool for a more extensive risk assessment when evaluating contaminant reduction strategies for a specific site.

Acknowledgements

Synchrotron experiments at HASYLAB were financially supported by the European Community-Research Infrastructure Action under the FP6 “Structuring the European Research Area” Programme (through the Integrated Infrastructure Initiative “Integrating Activity on Synchrotron and Free Electron Laser Science”). Edmund Welter and Gerald Falkenberg are gratefully acknowledged for their technical support during synchrotron experiments. Anna Bernaus thanks the Ministry of Science and Education for a Ph.D. scholarship (2003–2005), and the financial contribution from the Spanish MEC grants: PPQ2002-04267-C03-01 and CTQ2005-09430-C05-01 is also acknowledged. Sample collection was a contribution of SENSPOL EU project (EVK1-CT-1999-20001).

References

[1] L.D. Lacerda, W. Salomons, Mercury from Gold and Silver Mining: A Chemical Time Bomb? Springer-Verlag, Berlin, 1998, p. 146.
[2] Chlorine Ondine, Information Resource, revised November 2005, http://www.eurochlor.org/.
[3] E.G. Pacyna, J.M. Pacyna, N. Pirrone, Atmos. Environ. 35 (2001) 2987.
[4] R.R. Turner, S.E. Lindberg, Environ. Sci. Technol. 12 (8) (1978) 918.
[5] J.W. Parks, J.A. Sutton, J.D. Hollinger, Mercury pollution in the Wabigoon-English River system of north-western Ontario, and possible remedial measures, Technical Report, Minister of Supply and Services, Canada, 1984.
[6] H. Gonzalez, Water Air Soil Pollut. 56 (1991) 83.
[7] B.P. Shaw, A. Sahu, A.K. Panigrahy, Bull. Environ. Contam. Toxicol. 36 (1986) 299.
[8] B.E. Maserti, R. Ferrara, Water Air Soil Pollut. 56 (1991) 15.
[9] U.S. EPA, Office of Air Quality Planning & Standards and Office of Research and Development, EPA, Mercury Study: Report to Congress, vol. III, Fate and Transport of Mercury in the Environment, EPA-452/R-97-005, 1997.
[10] D.C. Adriano, Trace Elements in Terrestrial Environments, second ed., Springer-Verlag, Berlin, 2001 (Chapter 11).
[11] G. Kaiser, G. Tölg, in: O. Hutzinger (Ed.), Handbook of Environmental Chemistry, Part A, vol. 3, Springer-Verlag, New York, 1980.
[12] T.J. Hogg, J.W.B. Steward, J.R. Bettany, J. Environ. Qual. 7 (1978) 440.
[13] S. Suckcharoen, Bull. Environ. Contam. Toxicol. 24 (1980) 463.
[14] M. Lodenius, E. Tulisalo, Bull. Environ. Contam. Toxicol. 32 (1984) 439.
[15] H. Biester, G. Müller, H.F. Schöler, Sci. Total Environ. 284 (2002) 177.
[16] C. Gagnon, É. Pelletier, A. Mucci, Mar. Chem. 59 (1997) 159.
[17] M.O. Barnett, L.A. Harris, R.R. Turner, T.J. Henson, R.E. Melton, R.J. Stevenson, Water Air Soil Pollut. 80 (1995) 1105.
[18] C.M. Neculita, G.J. Zagury, L. Deschênes, J. Environ. Qual. 34 (2005) 255.
[19] G. Morin, F. Juillot, J.D. Ostergren, P. Ildefonse, G. Calas, G.E. Brown Jr., Am. Mineral. 84 (1999) 420.
[20] J.D. Ostergren, G.E. Brown Jr., G.A. Parks, T.N. Tingle, Environ. Sci. Technol. 33 (10) (1999) 1627.
[21] A.L. Foster, G.E. Brown Jr., T.N. Tingle, G.A. Parks, Am. Mineral. 83 (5–6) (1998) 553.
[22] D. Hesterberg, D.E. Savers, W. Zhou, G.M. Plummer, W.P. Robarg, Environ. Sci. Technol. 31 (1997) 2840.
[23] A. Bernaus, X. Gaona, M. Valiente, J. Environ. Monit. 7 (2005) 771.
[24] R. Fernández-Martínez, M.I. Rucandio, Anal. Bional. Chem. 375 (2003) 1089.

[25] X. Gaona, M. Valiente, Anal. Chim. Acta 480 (2003) 219.
[26] P. Quevauviller, Operationally defined extraction procedures for soil and sediments analysis. I. Standardization TrAC Trends Anal. Chem. 17 (1998) 89.
[27] C.M.M. Davidson, A.L. Duncan, D. Littlejohn, A.M. Ure, L.M. Garden, Anal. Chim. Acta 363 (1998) 45.
[28] M. Pueyo, G. Rauret, D. Luck, M. Yli-Halla, P. Quevauviller, J.F. Lopez-Sanchez, J. Environ. Monit. 3 (2001) 243.
[29] P.S. Fedotov, A.G. Zavarzina, B.Y. Spivakov, R. Wennrich, J. Mattusch, K.P. de Cunhal-Titze, V.V. Demin, J. Environ. Monit. 4 (2002) 318.
[30] G.A. Waychunas, G.E. Brown Jr., Adv. X-Ray Anal. 37 (1994) 607.
[31] SIXPack (Sam's Interface for XAS analysis Package), Powered by IFEFFIT 1.2.6, Copyright ©Matt Newville, University of Chicago, 2004.
[32] E.R. Malinowski, Factor Analysis in Chemistry, second ed., Wiley & Sons, New York, 1991, p. 350.
[33] T. Ressler, J. Wong, J. Roosa, I.L. Smith, Environ. Sci. Technol. 34 (6) (2000) 950.
[34] S.R. Wasserman, P.G. Allen, D.K. Shuh, J.J. Bucher, N.M. Edelstein, Synchrotron Rad. 6 (1999) 284.
[35] A.J. Slowey, S.B. Johnson, J.J. Rytuba, G.E. Brown Jr., Environ. Sci. Technol. 39 (20) (2005) 7869.
[36] L. Vincze, F. Wei, K. Proost, B. Vekemans, K. Janssens, Y. He, Y. Yan, G. Falkenberg, J. Anal. At. Spectrom. 17 (2002) 177.
[37] C. Marvin, S. Painter, R. Rossmann, Environ. Res. 95 (2004) 351.
[38] M.M. Hyland, G.E. Jean, G.M. Bancroft, Geochim. Cosmochim. Acta 54 (1990) 1957.
[39] G.E. Jean, G.M. Bancroft, Geochim. Cosmochim. Acta 50 (1986) 1455.
[40] S.R. Aston, J.E. Rae, Environ. Int. 7 (1982) 331.
[41] D.H. Loring, R.T.T. Rantala, J.N. Smith, Response time of Saguenay Fjord sediments to metal contamination, Environmental Biogeochemistry, Ecol. Bull. 35 (1983) 59.
[42] E. Pelletier, G. Canuel, Mar. Pollut. Bull. 19 (1988) 336.
[43] K. Xia, U.L. Skyllberg, W.F. Bleam, P.R. Bloom, E.A. Nater, P.A. Helmke, Environ. Sci. Technol. 33 (2) (1999) 257.
[44] Y. Yin, H.E. Alen, C.P. Huang, Environ. Sci. Technol. 4b31 (1997) 496.
[45] C. Gobeil, D. Cossa, Can. J. Fish. Aquat. Sci. 50 (1993) 1794.
[46] E.E. Carlson, J. Cryst. Growth 1 (1967) 271.
[47] O. Oenema, R. Steneker, J. Reynders, Hydrobiol. Bull. 22 (1988) 21.
[48] J.W. Morse, Mar. Chem. 46 (1994) 1.

Annex 5

Environ. Sci. Technol. **2006**, *40,* 4090−4095

Microprobe Techniques for Speciation Analysis and Geochemical Characterization of Mine Environments: The Mercury District of Almadén in Spain

ANNA BERNAUS,[†] XAVIER GAONA,[†] JOSÉ MARIA ESBRÍ,[‡] PABLO HIGUERAS,[‡] GERALD FALKENBERG,[§] AND MANUEL VALIENTE*,[†]

Grup de Tècniques de Separació en Química (GTS), Departament de Química, Universitat Autònoma de Barcelona, 08193 Bellaterra, Barcelona, Spain, Departamento de Ingeniería Geológica y Minera, Escuela Universitaria Politécnica de Almadén, Universidad de Castilla-La Mancha, 13400 Almadén, Ciudad Real, Spain, and Hamburger Synchrotronstrahlungslabor at Deutsches Elektronen-Synchrotron DESY, Notkestrasse 85, D-22603 Hamburg, Germany

Metallurgic calcines with very high mercury and methylmercury content from the Almadén mining district were analyzed by synchrotron-based microprobe techniques. Information about mercury speciation was obtained by μ-EXAFS (microscopic extended X-ray absorption fine structure) spectroscopy, whereas elemental associations were evaluated by μ-XRF (microscopic X-ray fluorescence analysis) mapping. Complementary characterization methodologies, including X-ray diffraction (XRD), inductively coupled plasma-optical spectroscopy (ICP-OES), as well as a sequential extraction scheme (SES), were used to predict the potential availability of mercury. Analysis of total metal content revealed extremely high concentrations of mercury and iron (between 7 and 35 and 65−70 g kg^{-1}, respectively) and high zinc concentrations (2.2−2.5 g kg^{-1}), whereas other metals such as copper, nickel, and lead were found at low concentration levels (30−300 mg kg^{-1}). μ-EXAFS results indicate that cinnabar (HgS_{red}) is one of the main species within the studied mercury-rich particles (5−89% of total mercury content), together with more soluble mercury compounds such as $Hg_3(SO_4)O_2$ (schuetteite) and HgO (5−55% of total mercury content). Additionally, element-specific μ-XRF maps of selected mercury-rich particles in the studied samples revealed an evident correlation among Hg−Pb−Ni (and S), indicating a possible geochemical linkage of these elements. Correlations were also found among Fe−Mn and Hg, which have been attributed to sorption of mercury onto oxyhydroxides of Fe and Mn. This finding was supported by results from a sequential extraction scheme, where a significant amount of Hg was extracted with the fraction soluble in 6 M HCl.

Introduction

Natural mercury deposits are globally distributed in three types of mineral belts: silica−carbonate, hot-spring, and Almadén type, which are cogenetic and reflect similar tectonic and volcanic processes that contribute to the concentration of mercury (*1*). The most important of these is the Almadén mercury mineral belt in central Spain, where over one-third of the world's mercury has been produced. The mining activity dates from the Roman age, while the Hg extracted from the mine amounts to about 8.3 million Hg flasks (approximately 285 000 metric tons of Hg) (*2*). The deposit is primarily composed of cinnabar (HgS_{red}, hexagonal) and appreciable amounts of native Hg (*3*).

During metallurgical beneficiation, mercury was extracted from the mineral by volatilization, involving the crushing and roasting of the ores in large furnaces at temperatures higher than 600 °C. The process decomposes most of the Hg minerals producing Hg vapor, which is subsequently passed through condenser columns and collected as metallic (liquid) Hg in flasks. The roasted mine wastes (calcines) were typically transported short distances from the furnace and dumped in loose, unconsolidated piles, containing high Hg concentrations, typically ranging from 160 to 34 000 g kg^{-1} (*4*).

Although Hg mining activity in the Almadén district ceased in May 2002, abandoned and untreated mine wastes continue releasing Hg to the nearby streams (*5*) and the atmosphere (*6*, *7*) given the associated weathering, transport, and biological processes controlling the Hg cycle in these mine-impacted environments (*8*). Only a few studies have been conducted to evaluate the environmental impact of mercury contamination in this area (*9*−*13*). These studies show an important gap concerning the identification and quantification of inorganic mercury compounds, which are known to be the dominant components of mercury chemistry. This gap has a significant importance, because molecular-level speciation is one of the main parameters governing mercury mobility, toxicity, and bioavailability (*14*).

Recent studies have shown the applicability of synchrotron-based X-ray absorption spectroscopy (XAS) techniques to the characterization of both crystalline and noncrystalline Hg compounds in mine environments (*15*−*17*). This technique is becoming widely used for the study of molecular-level environments, showing species-specific detection capacities, while needing almost no sample pretreatment (and consequently with a minimum species modification) (*18*).

During the past decade, synchrotron-based microprobe techniques, with X-ray beams of 1−20 μm in diameter, have become increasingly utilized to map elemental distributions in environmental samples. The mapping process allows one to establish correlations among elements, while also identifying particles enriched in the target element (Hg in this study case). Both XANES (X-ray absorption near-edge structure) and EXAFS spectroscopy measurements can be performed at each spot of the incident microbeam.

The present study takes advantage of μ-XRF and μ-EXAFS microprobe techniques for the determination of mercury species in old furnace calcine samples. Complementary techniques, such as XRD, total digestion and elemental analysis by ICP-OES, or SES schemes, have been also applied to obtain an adequate knowledge of the bulk mineralogy of the sample matrixes, as well as to identify and understand

* Corresponding author phone: +34-935812903; fax: +34-935811985; e-mail: Manuel.Valiente@uab.es.
[†] Universitat Autònoma de Barcelona.
[‡] Escuela Universitaria Politécnica de Almadén.
[§] Deutsches Elektronen-Synchrotron DESY.

10.1021/es052392l CCC: $33.50

Published on Web 06/06/2006

trends within Hg association to specific matrix phases (*19*−*21*). The overall aim of this study is to utilize information on mercury speciation to predict mercury mobility and availability, as well as to relate this information to the anthropogenic and geochemical processes taking place in the Almadén environment.

Experimental Section

Sample Collection and Storage. Samples were collected at the Almadenejos decommissioned metallurgical plant, which is located some 10 km southeast of Almadén (see the Supporting Information). The plant was active during the period of the 17th to 19th century, until its closure in 1860. Two calcine samples were taken from the top of two of the old furnaces, where Gray and co-workers (*4*) quantified the highest methylmercury contents yet found in this type of samples worldwide. The two calcine samples, identified as AJ-701 and AJ-702, were collected at 10−20 cm depth using an Eijkelkamp 04.15.SA undisturbed soil sampler device, on an anthrosol (soil taxonomy, 1975) (*22*) situated on the top of the ruins of the furnace building. During sample collection, weather conditions were dry, with temperatures between 30 and 35 °C.

After collection, samples were dried and sieved to a particle size smaller than 1 cm. Then, the sieved part was milled and sieved again to <53 μm (the most suitable size for XRD and XRF analysis). Finally, and before further analyses, samples were homogenized and air-dried for 24 h. This process was considered to not modify the actual speciation of Hg in the treated samples but be most representative of the grain heterogeneity of the soil analyzed.

Mineralogical and Chemical Characterization. X-ray diffraction was used to identify the bulk mineralogy and primary matrix components of the calcines. The XRD analyses were carried out at the I. R. I. C. A. (University of Castilla-La Mancha), using a Philips diffractometer (model 1700, with Cu Kα radiation, automatic divergence aperture, and curved graphite monochromator). The reception and dispersion aperture were 0.1 mm and 1°, respectively. A Xe-filled gas was used, and the scan range was 3−75° 2Θ with a scan speed of 0.1° 2Θ s^{-1}.

Digestion of samples AJ-701 and AJ-702 was performed to quantify total metal concentration. In addition to Hg, the elemental analysis included As, Cu, Fe, Ni, Pb, Mn, and Zn. Sample digestion was carried out with an analytical microwave system (MARS-5 model from CEM Corporation, U.S.A.) and a hydrofluoric acid media, to ensure the total digestion of the sample (*23*). The electrical power steps used in the digestion process can be found elsewhere (*24*). The concentration of target elements in the aqueous solution was determined by an ICP-OES equipment (Thermo Elemental, model Iris Intrepid II XSP, U.S.A.).

Sequential Extractions. A specific SES procedure developed by the CIEMAT Research Centre (*25*) has been applied to study the distribution of Hg, As, Cu, Fe, Ni, Pb, and Mn in the calcine samples. This scheme includes six different extraction steps (*26*), which permit an accurate characterization of the heavy metal distribution among the different soil phases. The sequential extraction steps permit the identification of water-soluble compounds, exchangeable cations, carbonates fraction, easily reducible fraction, compounds soluble in 6 M HCl, and oxidizable phases. The residual metal concentration was estimated by the difference between total concentration (from HF digestion) and the sum of metal concentration within the complete extraction procedure. Detailed information on the SES experimental procedure is given as Supporting Information (see also refs *25* and *26*).

Microprobe Analyses. Microprobe analyses were performed at the synchrotron facility Hamburger Synchrotronstrahlungslabor (HASYLAB) at Deutsches Elektronen-Synchrotron DESY in Hamburg (Germany), at the bending magnet beamline L (*24*). All experiments were carried out at room temperature.

First, μ-XRF mapping was performed on samples AJ-701 and AJ-702, which provided an overview of the elemental distribution within the sample and permitted the identification of Hg-rich particles. Moreover, this mapping aims to determine spatial correlations among mercury and other elements, such as Fe and Mn, as well as other toxic elements including As, Zn, Ni, and Pb. Beamline L allows the detection of elements with atomic numbers between 13 and 92, reaching detection limits below 0.1 mg kg^{-1}, depending on the element and sample matrix. The beam was monochromatized at 13 000 eV with a Si(111) monochromator and collimated to a size of ∼15 μm diameter fwhm by using a polycapillary half-lens. The sample area around the beam position was monitored by a long-distance zoom microscope with a magnification of 300× and a CCD camera with a resolution of 3 μm. The fluorescence signal was detected with a GRESHAM Si (Li) detector and a RADIANT VORTEX silicon drift detector (50 mm^2 active area), respectively. The μ-XRF maps contained 11 × 11 points with a step size of 10 μm vertically and horizontally. The time of fluorescence signal accumulation was selected as a function of maximum total count rate of the sample and varied between 1 and 10 s per step. Elements included within the μ-XRF analysis were Hg, Fe, Mn, Ca, Cu, Ni, Pb, Ti, Zn, and S.

μ-EXAFS analyses were carried out on Hg-rich particles identified in the previous μ-XRF evaluation. For this purpose, Hg L_{III}-edge EXAFS spectra were collected from three Hg-rich particles (five replicates undertaken for each particle) identified in each calcine sample. Pure reference compounds were analyzed in transmittance mode (detection with two ionization chambers) following the Hg absorption L_{III} line at 12 284 eV. On the other hand, fluorescence detection mode was used for the analysis of unknown samples, by measuring Hg Lα1 (9988 eV) and Lα2 (9897 eV) fluorescent line intensities. Selection of the detection mode was based on sample concentration and matrix background (*27*).

Speciation data (Hg phases present and relative abundances) were obtained by comparing the spectra from the unknown samples with spectra from reference Hg minerals and pure compounds, including $HgCl_2$, Hg_2Cl_2, $HgSO_4$, HgO_{red}, $Hg(CH_3COO)_2$, CH_3HgCl, HgS_{red} (cinnabar), HgS_{black} (metacinnabar), $Hg_2NCl_{0.5}(SO_4)_{0.3}(MoO_4)_{0.1}(CO_3)_{0.1}\cdot(H_2O)$ (mosesite), $Hg_3S_2Cl_2$ (corderoite), and $Hg_3(SO_4)O_2$ (schuetteite). Reference compounds were powdered and diluted with polyethylene. Homogenization was undertaken in a vortex apparatus, and the final mixture was pressed as a pellet under 5 tons cm^{-2} for 5 min. The total amount of sample in each pellet varied from 50 to 100 mg, whereas the amount of polyethylene was kept between 100 and 150 mg.

μ-EXAFS spectra were processed by using the SixPACK data analysis software package (*28*). Spectra processing included background correction, signal normalization, and data transformation from energy to *k*-space (range considered, 1−9 $Å^{-1}$). Then, principal component analysis, PCA (*29*−*31*), was applied to derive the number and type of reference compounds from the database required to reconstruct the spectrum of an unknown sample. Finally, a linear least-squares fitting procedure was utilized to fit the spectra from the unknown samples with the spectra selected in the previous PCA analysis. The determination of the relative proportion of each reference compound contribution allows quantification of the phases present in the unknown sample. The quality of the analysis can be evaluated by the reduced chi-square value (χ^2), which represents the goodness of the model fit to the spectra data using the linear combination procedure (*32*).

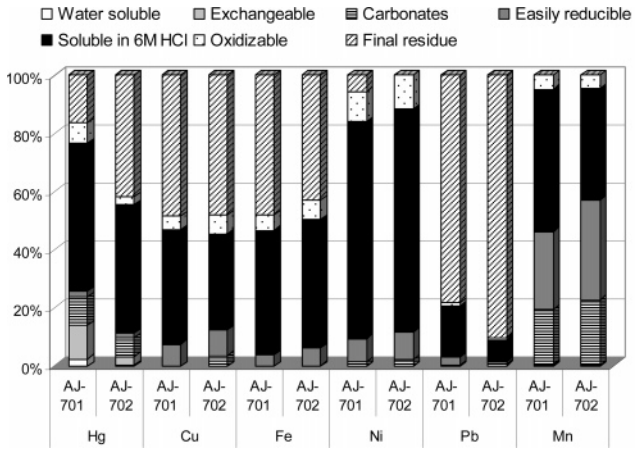

	Total content (mg kg^{-1}) AJ-701	AJ-702
Hg	35000 ± 6000	6700 ± 500
As	< 1	< 1
Cu	33 ± 7	33 ± 2
Fe	70000 ± 16000	65000 ± 2000
Ni	36 ± 6	41 ± 2
Pb	91 ± 13	276 ± 190
Mn	280 ± 60	798 ± 8
Zn	2200 ± 400	2500 ± 200

FIGURE 1. Results from the SES procedure applied to samples AJ-701 and AJ-702, and total metal content determined by HF digestion.

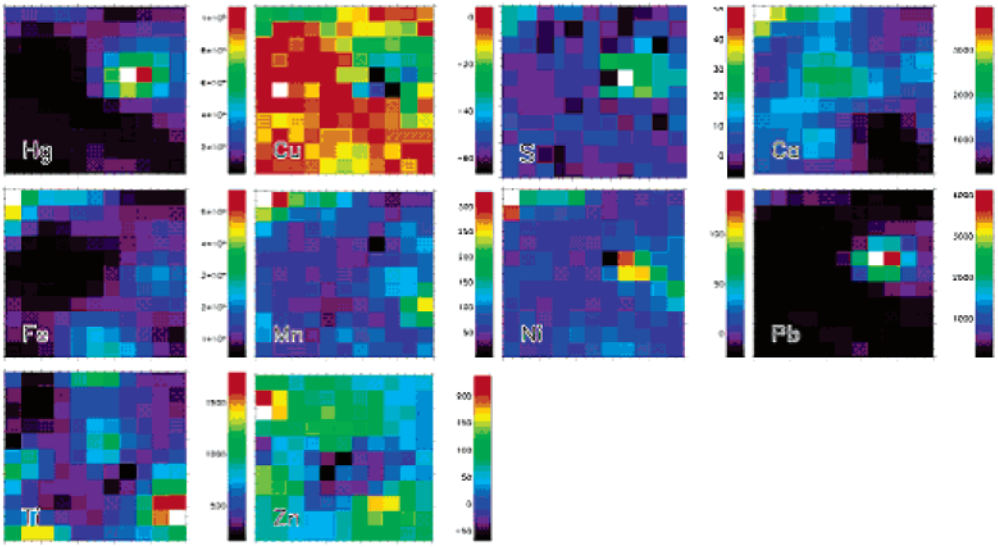

FIGURE 2. μ-XRF elemental maps for Hg, Cu, S, Ca, Fe, Mn, Ni, Pb, Ti, and Zn on a thin section (100 × 100 μm^2 area) close to particle 1 found in soil AJ-701. The color index scales indicate the measured counts s^{-1} for each element.

Results and Discussion

Mineralogical and Chemical Characterization. Results from XRD analysis highlight the predominance of phyllosilicates (mica and kaolinite, with SiO_4^{4-} partially substituted by Al^{3+} or Fe^{3+}) in both samples. This mineralogy is consistent with the geological origin of the Almadén mercury belt, because these deposits are primarily localized in Silurian quartzite adjacent to mafic craters (*1*, *2*). Plagioclase ($Na_{0.5}Ca_{0.5}Si_3AlO_8$) and calcite ($CaCO_3$) were found as typical igneous and hydrothermal minerals from the surroundings. In addition, gypsum ($CaSO_4{\cdot}2H_2O$) was detected in one of the samples (AJ-701), presumably as a product of weathering or as a building material from the furnace ruins. No Hg crystalline phases were detected by XRD, indicating their presence in relatively low proportions (below 2%).

Results of total digestion of calcine samples collected at the furnace facility of the Almadenejos mine are given in Figure 1. High mercury concentrations (compared to those of other mine facilities) have been found in these mine wastes, indicating an inefficient and incomplete Hg roasting process. This fact might also indicate the presence of unconverted cinnabar and other Hg compounds usually formed during the processing of the ore (*1*, *33*, *34*).

These results are consistent with those achieved by Gray and co-workers (*4*), where similar samples have shown mercury concentrations between 200 and 34 000 mg kg^{-1}. It is also important to note the extremely high methylmercury concentrations (between 0.2 and 3100 μg kg^{-1}) found by these authors, indicating the high methylation rates under the conditions present in this mine waste. In this sense, speciation experiments performed in our study may provide some insights about possible inorganic mercury species that underwent methylation.

Quantification of those elements that could produce spectral interferences in the XAS analysis of Hg (in fluorescence detection mode) revealed the absence of As (Kα = 10 508 eV) and relatively low concentrations of Zn (Kβ = 9572 eV) and Pb (Lα = 10 449 eV). Nevertheless, Fe (an important nonspectral interference, Kβ = 7058 eV) was found in very high concentrations, leading to a possible saturation of the fluorescence detector and consequent reduction of the detection limit of the XAS technique.

Geochemical Characterization by μ-XRF and Sequential Extraction Schemes. Figure 2 shows a set of μ-XRF elemental maps, corresponding to particle 1 from sample AJ-701. Similar results were obtained for each particle analyzed from both calcine samples. To evaluate possible correlations among elements in the samples, line intensities of all elements evaluated were extracted from each pixel in each mapping analysis. Three different correlations have been identified (see Figures 2 and 3): (i) linear Pb−Hg, Ni−Hg, and (possible) S−Hg correlations within mercury-rich areas; (ii) linear correlations among Hg and the background of Fe and Mn; (iii) no correlation among Hg and Ca, Ti, Zn, or Cu.

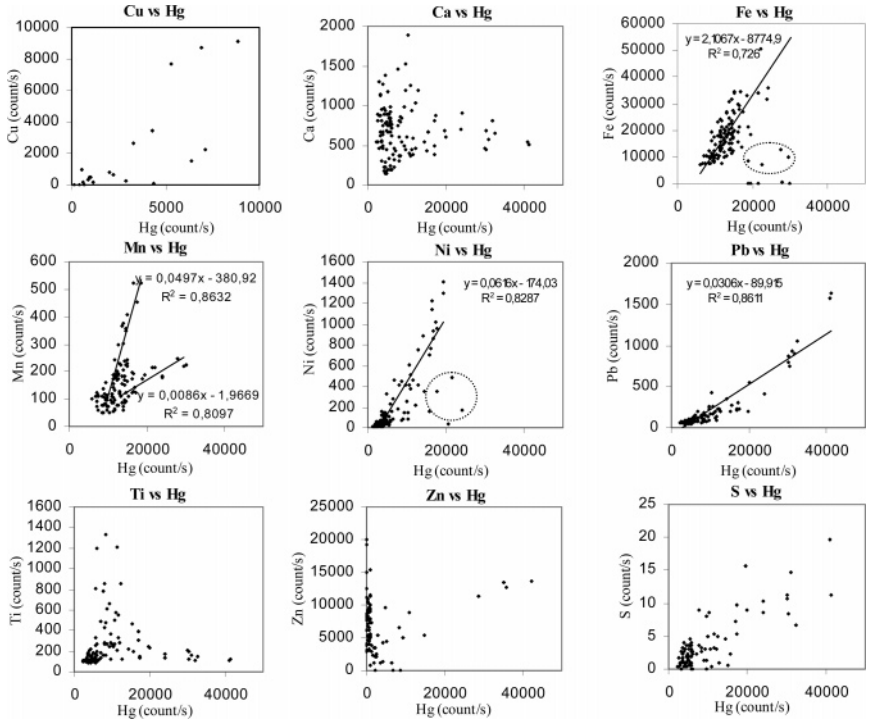

FIGURE 3. Pair correlation diagrams obtained from the μ-XRF maps of samples AJ-701 and AJ-702 (average of six regions belonging to the mercury-rich particles), as fluorescence line intensity (counts s^{-1}). Outliers of Fe and Ni (dashed circles) are not considered for linear regressions.

The observed association trend among Hg−Pb−Ni might be explained by the well-known tendency of these three elements to form very stable compounds with sulfide. In this sense, Figure 3 might also corroborate the affinity of Hg toward S, taking into account that sulfur is a "soft" Lewis base that can form strong covalent bonds with the highly polarizable mercury atom ("soft" Lewis acid). However, the correlation Hg−S must be taken with care, given the low count rate shown by S. Further interpretations of the Hg−Pb−Ni−S correlation are driven by SES analyses (see below).

Figure 3 points out significant Fe−Hg and Mn−Hg correlations. In both cases, the main correlation is found within the sample background, instead of the mercury-rich particles. The correlation Fe−Hg might be explained by two hypotheses: (i) there may be phase association between cinnabar and pyrite. Nevertheless, this option has been disregarded given the low presence of pyrite in the area. (ii) There may be sorption of mercury onto Fe oxyhydroxides. According to Kim and co-workers (*16*), Hg(II) sorbs strongly to fine-grained powders of goethite (α-FeOOH) with a sorption density of 0.39−0.42 μmol m^{-2}. Iron oxyhydroxides are also known as effective substrates for Hg sorption in natural aquatic systems, where Hg(II) forms bidentate inner-sphere complexes with the substrate surface (*16*, *35*).

Hg(II) is also known to form inner-sphere complexes with manganese oxides (*1*). Although Mn is found in lower concentration than Fe in the Almadén mine wastes (see Table 1), this fact might explain the linear correlation observed between Hg and Mn. In this sense, Figure 3 shows two different tendencies concerning the Hg−Mn linear correlation, which may indicate the occurrence of two different sorption processes.

To corroborate the presence of Hg sorbed onto oxyhydroxides of Fe and Mn, the SES procedure developed by CIEMAT was applied to samples AJ-701 and AJ-702. This procedure also provides useful information on the potential mobilization of mercury (*25*, *36*).

Results of the SES procedure applied to samples AJ-701 and AJ-702 (Figure 1) indicate that the mercury distribution in both samples is relatively similar. Mercury extracted with 6 M HCl (51% AJ-701, 44% AJ-702) has been found to be exceptionally high compared with other steps, which can be explained by the strong binding of Hg(II) to crystalline Fe−Mn oxyhydroxides or sulfides. On the other hand, the easily reducible fraction releases little mercury (4% in both samples), suggesting the lack of Hg associated with amorphous Fe−Mn oxyhydroxides or to organic matter. Concerning the average Hg concentrations found in the final residue (16% AJ-701, 42% AJ-702), these would correspond to HgS (either cinnabar or metacinnabar). Finally, the significant mercury concentrations found in the water-soluble, exchangeable, and carbonate fractions are related to the presence of more soluble mercury compounds, therefore posing an evident risk of mercury mobilization. This fact has been also ascertained by the following μ-EXAFS analyses.

TABLE 1. Chemical Speciation of Hg-Rich Particles from Calcine Samples of the Almadenejos Mercury Mine[a]

sample	cinnabar	HgO	schuetteite	χ^2
AJ-701; particle 1	< 5	47	49	0.17
AJ-701; particle 2	34	41	24	0.74
AJ-701; particle 3	9	55	36	0.26
AJ-702; particle 1	89	5	6	0.23
AJ-702; particle 2	26	47	27	1.68
AJ-702; particle 3	14	38	47	1.32

[a] Concentration values expressed in percent relative to the total mercury content in each sample.

Concerning other metal components, nickel is principally found in the fifth extraction step, therefore being associated to crystalline Fe−Mn oxyhydroxides. On the other hand, lead is not extracted but mainly remains in the final residue (see Figure 1), thus providing similar behavior as Hg that is expected to be found as a sulfide compound. This information helps to understand the Hg−Pb and Hg−Ni correlations found by μ-XRF. Thus, mixed Hg−Pb−S compounds are expected to be present in the samples analyzed, while Hg

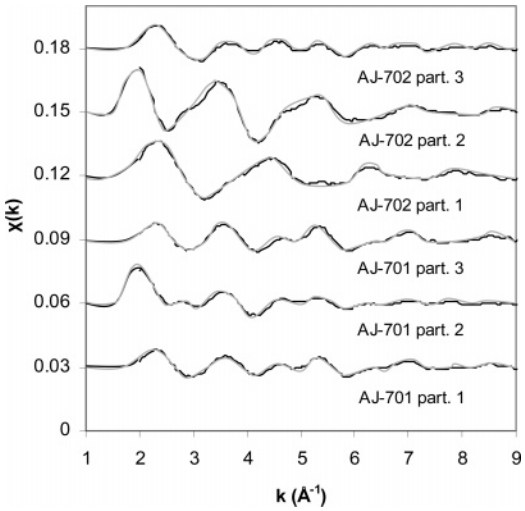

FIGURE 4. Linear combination fits of the samples (black line = raw data, gray line = fit). (Note the deliberate offset of spectra to show differences.) Each spectrum is the mean value of five replicates.

and Ni correlations might be explained by the related sorption of these metals on crystalline Fe−Mn oxyhydroxides.

Speciation Analysis by μ-EXAFS. Results of PCA using the L_{III}-edge EXAFS spectra from Hg-rich particles found in the calcine samples indicate that a minimum of four components (cinnabar, HgO, schuetteite, and $HgCl_2$) are required to reconstruct each of the experimental spectra above the 95% confidence level. As stated in the Experimental Section, the original set of reference compounds included 11 mercury phases.

On the basis of the previous PCA analysis, Figure 4 shows the corrected EXAFS spectra for all the particles evaluated from samples AJ-701 and AJ-702, as well as the spectra obtained by linear combination of the four reference compounds, determined by the fitting procedure. The relative proportions of each reference compound identified in each μ-EXAFS analysis, as well as the reduced chi-square value (χ^2) associated with the related fit, are given in Table 1.

A diversity of speciation results from mercury-rich particles has been obtained in both samples, indicating the significant heterogeneity of the samples. Cinnabar is present in most of the particles (5−89% of the total mercury content), although schuetteite and HgO (both more soluble than cinnabar) have also been identified in high proportions (5−55% of the total mercury content). This fact results in a significant source of relatively mobile mercury. Indications of the possible presence of $HgCl_2$ have been observed within the fitting procedure, although in nonsignificant proportions.

These speciation results are not consistent with those previously published (*17*, *24*) dealing with Almadén calcine samples, where significant concentrations of metacinnabar were identified by EXAFS. The presence of this metastable polymorph of cinnabar is consistent with the high temperatures applied to the mineral during the extraction process.

The historical investigation of the Almadenejos mine and its furnace facilities brought to light the high Hg losses through the oven ashtrays, piping, and chimneys, as well as the very low efficiency of the roasting procedure applied at this facility (*37*). As a result of the lower ore roasting temperatures, lower mercury recovery was achieved (see the extremely high mercury concentrations, Figure 1). This finding helps to explain the lower conversion of cinnabar to metacinnabar found in our studies of the site.

The presence of schuetteite (and probably of $HgCl_2$) is related to supergene alteration of cinnabar, as shown by the common presence of schuetteite in many mine dumps, especially on sunlight-exposed rocks (*11*).

As stated before, previous studies undertaken by Gray and co-workers (*4*) showed the extremely high methylmercury concentrations present within the analyzed calcine samples, compared with those of similar samples from other mine and metallurgic facilities worldwide. Therefore, the identification of the inorganic source species for the biomethylation processes becomes of a significant importance for the overall definition of the mercury cycle. In this context, this study shall be considered as a first approach to understand the insights of this process.

Summarizing, the proposed coupling of techniques have demonstrated the existence of relatively soluble Hg phases in the analyzed calcine samples, which might be mobilized through different weathering processes. This fact poses an evident risk both to the biota and to human beings, given the well-known mercury toxicity. Nevertheless, it must be highlighted that these conclusions are driven in the frame of a reduced number of samples, and therefore, the analysis of additional samples could contribute positively to the robustness of such indication.

The presented coupling of techniques may be considered as a good alternative to the more traditional solid-phase speciation based on chemical information and, therefore, a useful tool to consider when assessing the risk associated to mobility and potential bioavailability of Hg.

Acknowledgments

Synchrotron experiments at HASYLAB were financially supported by the European Community−Research Infrastructure Action under the FP6 "Structuring the European Research Area" Program (through the Integrated Infrastructure Initiative "Integrating Activity on Synchrotron and Free Electron Laser Science"). Anna Bernaus thanks the Ministry of Science and Education for a Ph.D. scholarship (2003−2005). The Spanish Project PPQ2002-04267-C03-01 provided financial support for the present study. Projects PPQ2003-01902 and PCC-05-004-3 also contributed to related expenses. Gordon Brown (Stanford University) is thanked for helpful comments on the manuscript after it was submitted to ES&T for review.

Supporting Information Available

Figure detailing the location of the mines, metallurgical plants, and the sampling area and a table outlining the sequential extraction procedure. This material is available free of charge via the Internet at http://pubs.acs.org.

Literature Cited

(1) Rytuba, J. J. Mercury from mineral deposits and potential environmental impacts. *Environ. Geol.* **2003**, *43*, 326−338.
(2) Hernández, A.; Jébrak, M.; Higueras, P.; Oyarzun, R.; Morata, D.; Munhá, J. The Almadén mercury mining district, Spain. *Mineralium Deposita* **1999**, *34*, 539−548.
(3) Rytuba, J. J.; Rye, R. O.; Hernandez, A. M.; Dean, J. A.; Arribas, A. Characterisation of Almadén mercury mine environment by XAS techniques. *Int. Geol. Congr. Abstr. Prog.* **1988**, 2−741.
(4) Gray, J. E.; Hines, M. E.; Higueras, P. L.; Adatto, I.; Lasorsa, B. K. Mercury speciation and microbial transformations in mine wastes, stream sediments, and surface waters at the Almadén Mining District, Spain. *Environ. Sci. Technol.* **2004**, *38*, 4285−4292.
(5) Ganguli, P. M.; Mason, R. P.; Abu-Saba, K. E.; Anderson, R. S.; Flegal, A. R. Fishing for identity: mercury contamination and fish consumption among indigenous groups in the United States. *Sci., Technol. Soc.* **2000**, *34* (22), 4773−4779.
(6) Gustin, M. S.; Coolbaugh, M.; Engle, M.; Fitzgerald, B.; Keislar, R.; Lindberg, S. E.; Nacht, D.; Quashnick, J.; Rytuba, J.; Sladek, C.; Zhang, H.; Zehner, R. Atmospheric mercury emissions from mine wastes and surrounding geologically enriched terrains. *Environ. Geol.* **2003**, *43*, 339−351.
(7) Gustin, M. S.; Lindberg, S. E.; Austin, K.; Coolbaugh, M.; Vette, A.; Zhang, H. Assessing the contribution of natural sources to

regional atmospheric mercury budgets. *Sci. Total Environ.* **2000**, *259* (1−3), 61−71.
(8) Wershaw, R. L. Sources and behaviour of mercury in surface waters; Mercury in the Environment. *U.S. Geol. Surv Prof. Pap.* **1970**, *713*, 29−34.
(9) Berzas Nevado, J. J.; García Bermejo, L. F.; Rodríguez Martín-Doimeadios, R. C. Distribution of mercury in the aquatic environment at Almadén, Spain. *Environ. Pollut.* **2003**, *122*, 261−271.
(10) Ferrara, R.; Maserti, B. E.; Andersson, M.; Edner, H.; Ragnarson, P.; Svanberg, S.; Hernandez, A. Atmospheric mercury concentrations and fluxes in the Almadén district (Spain). *Atmos. Environ.* **1998**, *32*, 3897−3904.
(11) Higueras, P.; Oyarzun, R.; Biester, H.; Lillo, J.; Lorenzo, S. J. A first insight into mercury distribution and speciation in soils from the Almadén mining district, Spain. *Geochem. Explor.* **2003**, *80*, 95−104.
(12) Higueras, P.; Oyarzun, R.; Lillo, J.; Sánchez Hernández, J. C.; Molina, J. A.; Esbrí, J. M.; Lorenzo, S. The Almadén district (Spain): anatomy of one of the world's largest Hg-contaminated sites. *Sci. Total Environ.* **2005**, *356*, 112−124.
(13) Moreno, T.; Higueras, P.; Jones, T.; McDonald, I.; Gibbons, W. Size fractionation in mercury-bearing airborne particles (HgPM10) at Almadén, Spain: implications for inhalation hazards around old mines. *Atmos. Environ.* **2005**, *39*, 6409−6419.
(14) Brown, G. E., Jr.; Foster, A. L.; Ostergren, J. D. Mineral surfaces and bioavailability of heavy metals: a molecular-scale perspective. *Proc. Natl. Acad. Sci. U.S.A.* **1999**, *96*, 3388−3395.
(15) Kim, C. S.; Rytuba, J. J.; Brown, G. E., Jr. Geological and anthropogenic factors influencing mercury speciation in mine wastes: an EXAFS spectroscopy study. *Appl. Geochem.* **2004**, *19* (3), 379−393.
(16) Kim, C. S.; Rytuba, J. J.; Brown, G. E., Jr. EXAFS study of Hg(II) sorption to Fe- and Al-(hydr)oxide surfaces: I. Effects of pH. *J. Colloid Interface Sci.* **2004**, *271* (1), 1−15.
(17) Kim, C. S.; Brown, G. E., Jr.; Rytuba, J. J. Characterization and speciation of mercury-bearing mine wastes using X-ray absorption spectroscopy (XAS). *Sci. Total Environ.* **2000**, *261* (1−3), 157−168.
(18) Morin, G.; Juillot, F.; Ostergren, J. D.; Ildefonse, P.; Calas, G.; Brown, G. E., Jr. XAFS determination of the chemical form of lead in smelter-contaminated soils and mine tailings: importance of adsorption processes. *Am. Mineral.* **1999**, *84*, 420−434.
(19) Quevauviller, P. Operationally defined extraction procedures for soil and sediments analysis I. Standardization. *TrAC, Trends Anal. Chem.* **1998**, *17*, 89−298.
(20) Davidson, C. M. M.; Duncan, A. L.; Littlejohn, D.; Ure, A. M.; Garden, L. M. A critical evaluation of the three-stage BCR sequential extraction procedure to assess the potential mobility and toxicity of heavy metals in industrially contaminated land. *Anal. Chim. Acta* **1998**, *363*, 45−55.
(21) Fedotov, P. S.; Zavarzina, A. G.; Spivakov, B. Y.; Wennrich, R.; Mattusch, J.; de Cunhal-Titze, K. P.; Demin, V. V. Accelerated fractionation of heavy metals in contaminated soils and sediments using rotating coiled columns. *J. Environ. Monit.* **2002**, *4*, 318−324.
(22) Soil Survey Staff. *Soil Taxonomy: A Basic System of Soil Classification for Making and Interpreting Soil Surveys*; U.S. Department of Agriculture Handbook No. 436; U.S. Department Agriculture: Washington, DC, 1975.
(23) Fernández-Martínez, R.; Rucandio, M. I. Study of extraction conditions for the quantitative determination of Hg bound to sulfide in soils from Almadén (Spain). *Anal. Bioanal. Chem.* **2003**, *375*, 1089−1096.
(24) Bernaus, A.; Gaona, X.; Valiente, M. Characterisation of Almadén mercury mine environment by XAS techniques. *J. Environ. Monit.* **2005**, *7*, 771−777.
(25) Pérez del Villar, L.; Quejido, A. J.; Crespo, M. T.; Sánchez, M.; Cózar, J. S.; Galán, M. P.; Fernández-Díaz, M. Sequential leaching methods: review, previous experiences and proposed method for Fe(III)−U(VI)-rich fracture filling materials. *Trends Geochem.* **2002**, *2*, 19−42.
(26) Sánchez, D. M.; Quejido, A. J.; Fernández, M.; Hernández, C.; Schmid, T.; Millán, R.; González, M.; Aldea, M.; Martín, R.; Morante, R. Mercury and trace element fractionation in Almadén soils by application of different sequential extraction procedures. *Anal. Bioanal. Chem.* **2005**, *381*, 1507−1513.
(27) Waychunas, G. A.; Brown, G. E., Jr. Fluorescence yield XANES and EXAFS experiments: application to highly dilute and surface samples. *Adv. X-Ray Anal.* **1994**, *37*, 607−617.
(28) Webb, S. M. SIXPack: a graphical user interface for XAS analysis using IFEFFIT. *Phys. Scr.* **2005**, *T115*, 1011−1014.
(29) Malinowski, E. R. *Factor Analysis in Chemistry*, 2nd ed.; Wiley & Sons: New York, 1991; p 350.
(30) Ressler, T.; Wong, J.; Roos, J.; Smith, I. L. Quantitative speciation of Mn-bearing particulates emitted from autos burning (methylcyclopentadienyl)manganese tricarbonyl-added gasolines using XANES spectroscopy. *Environ. Sci. Technol.* **2000**, *34* (6), 950−958.
(31) Wasserman, S. R.; Allen, P. G.; Shuh, D. K.; Bucher, J. J.; Edelstein, N. M. EXAFS and principal component analysis: a new shell game. *J. Synchrotron Radiat.* **1999**, *6*, 284−286.
(32) Slowey, A. J.; Johnson, S. B.; Rytuba, J. J.; Brown, G. E., Jr. Role of organic acids in promoting colloidal transport of mercury from mine tailings. *Environ. Sci. Technol.* **2005**, *39* (20), 7869−7874.
(33) Kim, C. S.; Rytuba, J. J.; Bloom, N. S.; Brown, G. E., Jr. Mercury speciation by X-ray absorption fine structure (XAFS) spectroscopy and sequential chemical extractions: a comparison study. *Environ. Sci. Technol.* **2003**, *37*, 5102−5108.
(34) Biester, H.; Gosar, M.; Müller, G. Mercury speciation in tailings of the Idrija mercury mine. *J. Geochem. Explor.* **1999**, *65*, 195−204.
(35) Collins, C. R.; Sherman, D. M.; Ragnarsdottir, K. V. Surface complexation of Hg^{2+} on goethite: mechanism from EXAFS spectroscopy and density functional calculations. *J. Colloid Interface Sci.* **1999**, *219*, 345−350.
(36) Davidson, C. M.; Thomas, R. P.; McVey, S. E.; Perala, R.; Littlejohn, D.; Ure, A. U. Evaluation of sequential extraction procedure for speciation of heavy metals in sediments. *Anal. Chim. Acta* **1994**, *291*, 277−286.
(37) Sumozas, R. Arquitectura Industrial en Almadén: Antecedentes, Génesis y Extensión de un Modelo, Ph.D. Thesis, University of Castilla−La Mancha, 2005; pp 171−202.

Received for review November 29, 2005. Revised manuscript received April 20, 2006. Accepted May 4, 2006.

ES052392L

Supporting Information

Microprobe techniques for speciation analysis and geochemical characterization of mine environments: the mercury district of Almadén in Spain

Anna Bernaus, Xavier Gaona, José Maria Esbrí, Pablo Higueras, Gerald Falkenberg and Manuel Valiente

Contents

3 pages (including this cover page)

1 Figure

1 Table

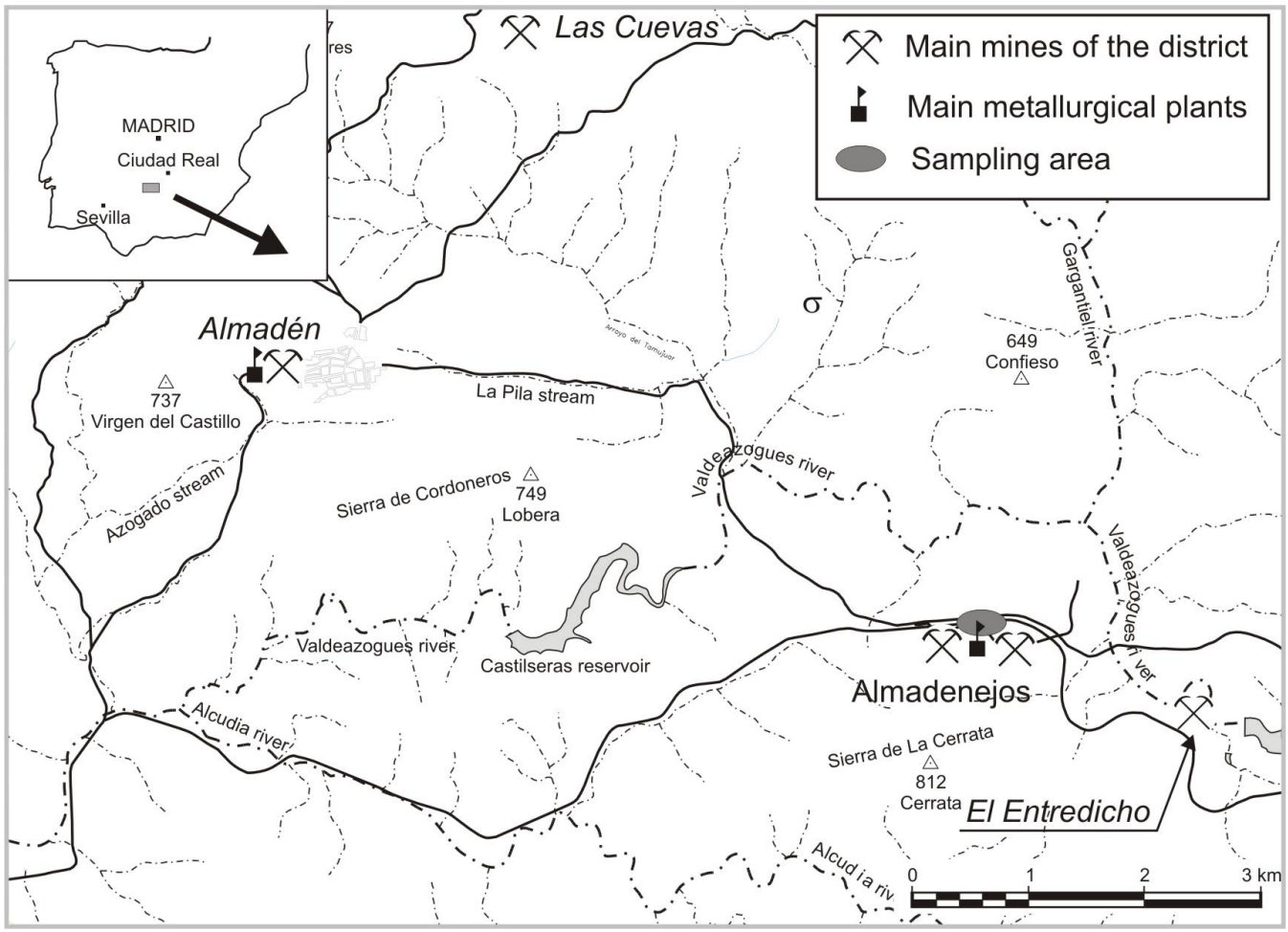

Figure SI-1. Location of Almadén in Spain, main mines and metallurgical plants of the district, and sampling area of calcines collected for this study.

Table SI-1 . Sequence of operationally defined fractions and extracting agents in the specific six-step CIEMAT sequential extraction procedure

Step	Fraction	Reagents	Contact time (hours)
1	**Water soluble**	0.5 g sample + 25 mL H_2O milli-Q	1
2	**Exchangeable cations**	Residue + 8 mL 1M NH_4Cl at pH 7 (Morgan's solution)	1
3	**Carbonates**	Residue + 20 mL 1M CH_3COONH_4 at pH 4.5 (HNO_3)	4
4	**Easily reducible**	Residue + 20 mL 10.9 g L^{-1} $C_2H_2O_4.2H_2O$/ 16.1 g L^{-1} CH_3COONH_4 at pH 2.85 (Tamm's solution)	4
5	**Soluble in 6M HCl**	Residue + 30 mL 6M HCl	2
6	**Oxidizable**	Residue + 5 mL 8.8M H_2O_2 at pH 2 (HNO_3) + 25 mL 1M CH_3COONH_4 at pH 2	2 + 16

Complementary Documentation

Annex 1

SENSPOL: European Network on Sensors for Monitoring Water Pollution

Newsletter No. 11 March 2004

Project Co-ordinator: Dr Susan Alcock.
Cranfield University, Silsoe, Bedfordshire, MK45 4DT, UK.
Fax: +44 1525 863540. Email: s.alcock@cranfield.ac.uk
http://www.cranfield.ac.uk/biotech/senspol.htm

The aim of the SENSPOL Thematic Network is to enhance the development of sensors for practical applications in the abatement of water pollution from contaminated land, landfills and sediment.

CONTENTS **Page no.**

Editorial

SENSPOL has now concluded and this is the final Newsletter.

The activities undertaken by SENSPOL have undoubtedly accelerated the development of sensor systems for practical applications in the abatement of water pollution from contaminated land, landfills and sediment. The usefulness of new environmental monitoring devices that can be used on site has been demonstrated and many of the instruments are ready for commercial demonstration. Most of the targeted analytes are heavy metals, chloroorganics, BTEX and. PAHs. Novel sensing technologies exist that are capable of measuring new parameters relevant to the environment, including general toxicity, genotoxicity and endocrine-disrupting substances.

The Final Report submitted to the European Commission provides information about the overall scientific achievements and deliverables. An executive summary of the overall achievements including the strategic aspects e.g. contribution to EU policies will be added to the SENSPOL website, to inform all possible interested parties about the outcome of the project. It may also be published by the Commission on CORDIS. The full report with more detailed information on the final scientific achievements may be used by the Commission to disseminate in an Energy, Environment and Sustainable Development Programme publication series and/or to be downloaded from CORDIS.

I would like to thank the members of the SENSPOL Steering Group, the workshop co-organisers (Prof E Dominguez, Dr P. Corbisier, Dr R Abuknesha, Prof M Valiente, Prof P Koscielniak, Dr P Heininger, Dr D van Ree and others), Dr. J Büsing, (European Commission Scientific Officer), staff at Cranfield University, all the individuals who have been involved in SENSPOL's activities, and the European Commission and other sponsors very much for their contributions to the steady progress that has been achieved by this network. I wish all developers and supporters of sensor technologies every success in future efforts that will contribute to the abatement of water pollution.

SENSPOL Steering Group:
Dr S Alcock, Cranfield University, Bedfordshire, UK
Prof E Dominguez, University of Alcalá, Spain
Prof L Fiksdal, Norwegian University of Science and Technology, Trondheim, Norway
Prof M Mascini, University of Florence, Italy
Dr T Krantz-Rülcker/Prof I. Lundström, Linköping University (S-SENCE), Sweden
Dr V Shulz-Berendt, Umweltshutz Nord, Ganderkesee, Germany *(2001-3)*
Prof M Valiente, Autonomous University of Barcelona, Spain
Prof A P F Turner, Cranfield University, Bedfordshire, UK
Drs Derek van Ree, Geodelft, The Netherlands (NICOLE representative)

Susan Alcock
SENSPOL Project Co-ordinator

Assessment of adsorption and bioavailability of mercury compounds in soils and sediments by using conventional separation methodologies, XAFS techniques and whole-cell luminescent sensors

*Report on visits of **Angela Ivask** (from National Institute of Chemical Physics and Biophysics, NICPB, Akadeemia tee 23, 12618, Tallinn, Estonia) to Autonomous University of Barcelona (UAB), 08193 Bellaterra, Barcelona, Spain (January 12-17, 2004) and **Anna Bernaus** (from UAB) to NICPB (January 17-23, 2004).*

***Keywords**: Soil, methylmercury, bioavailablility, XAFS, sensor*

Introduction

The aim of these meetings was to deepen collaboration between Autonomous University of Barcelona (UAB) and National Institute of Chemical Physics and Biophysics (NICPB) in the field of bioavailability studies of soil/sediment-adsorbed heavy metals. The collaboration will be more focused on Hg compounds as the adsorption of Hg to the sediments as well as the speciation of Hg compounds (by using conventional separation techniques or XAFS (X-ray Absoption Fine Structure Spectroscopy) has been studied in the group of Prof. Manuel Valiente in UAB already for several years [1]. On the other side, the group in NICPB, in collaboration with Dr. M. Virta from University of Turku, Finland, has constructed Hg and organomercury sensitive bacterial cells [2] and used them for the analysis of bioavailable Hg from different sample matrices. The combination of these techniques, the speciation of different Hg compounds e.g., by XAFS or conventional separation techniques and determination of bioavailability by using bacterial biosensors will provide an understanding on the environmental hazard of different Hg compounds (both organic and inorganic) considering their bioavailability and toxicity. Furthermore, the results will show the applicability of the currently existing bacterial sensors to the assessment of the biological hazard of complex matrices such as contaminated soils or sediments.
During these visits 6 MeHgCl-spiked samples were prepared and analysed for bioavailability by bacterial sensors.

Methods

The conventional speciation of Hg is a modification of the Westöö method [3], including an acid leaching and solvent extraction of the organomercury species from the soil sample, followed by stripping with an aqueous solution containing cysteine as a selective reagent for mercury extraction. Determination of the different chemical species of mercury (three species, $HgCH_3^+$, $HgC_6H_5^+$, and Hg^{2+} can be distinguished) is accomplished by capillary electrophoresis (HPCE-UV) of the corresponding stripping solution.

A considerably higher speciation capacity can be achieved by XAFS techniques. Unlike conventional separation techniques, the analysis with XAFS requires hardly any pre-treatment of the sample (minimized sample modifications). The XAFS technique is based on the interaction of highly brilliant X-radiation from a special X-ray source (synchrotron) with a sample containing the target elements. The spectra are taken over a given energy range close to the region of an electronic excitation level of the target element. The absorbance of the X-radiation by the sample is observed. In the region of the absorption edge some

interferences appear due to the interaction of X-rays with the neighbouring atoms of the target element, which provide information about the chemical surrounding of Hg, and thus the related Hg species. However, there are also some drawbacks in XAFS techniques: high detection limits, the complex data evaluation and only few synchrotron facilities around the world.

The bacterial sensor cells have been successfully used for the assessment of bioavailable heavy metals including Hg from environmental matrices. These bacteria give a specific luminescent response to sub-toxic amounts of metals and manifest that the metal had entered the bacterial cell. Analogously to XAFS the analysis of the samples with bacterial biosensors does not need much pre-treatment. However, the detection limits of the bacterial sensors are considerably lower compared to the XAFS, reaching 0.02 ppb for $HgCH_3^+$ and 2 ppb for Hg^{2+}. Moreover, the bacterial biosensors are capable of distinguishing the biologically available fraction of Hg from the non-bioavailable one. However, the drawback of the use of bacterial sensor cells in mercury speciation is the relatively low speciation capacity – only organic species of Hg (mainly $HgCH_3^+$) and inorganic Hg can be reliably differentiated.

The samples analysed during the visits were prepared as following: 2g of soil material (kaolin, montmorillonite and humic acid) was mixed with 25 ml of 0.8 and 5 ppb aqueous solutions of methylmercury chloride ($HgCH_3Cl$). This should result theoretically 10 and 63 µg of $HgCH_3Cl$ per kg dry weight of the samples. Each sample was fixed at pH 7 with HNO_3 or NaOH. After 24 hours of equilibration, samples were air dried in a fume hood until constant weight. The final concentration of $HgCH_3Cl$ for each soil sample was determined by ICP-MS, after spin-drying, filtering and stabilisation of the remaining aqueous sample.

The bioavailable amount of $HgCH_3^+$ in the samples was determined by mixing the sample with water (1:9 soil-water suspension), rotating it for 24 hours and incubating for 2 h at 30 °C together with the bacterial organomercury sensors [*Escherichia coli* strain MC1061(pmerRBluxCDABE)]. In parallel, soil-water suspensions were centrifuged at 10000 g and the particle-free extracts were analysed with the sensors. As shown in our previous studies [4] the analysis of particle-free soil-water extracts by the bacterial sensors provides us with information about the water-extracted bioavailable metals whereas the analysis of soil-water suspensions reports also on the particle-bound, i.e., adsorbed but still bioavailable fraction of metals. In order to take into account the interferences of the samples with the bacterial luminescence (quenching of the light by solid particles/colour or toxicity of the sample) special luminescent control bacteria were used [4].

The quantification of the bioavailable methylmercury was performed as described in [5]. Briefly, the bioluminescence value of the sensor in the sample is divided to the bioluminescence value of the sensor in blank water. The obtained value is multiplied with a correction factor (obtained by dividing the bioluminescence of the control bacteria in blank water with the bioluminescence of the control bacteria in the respective sample) and the resulting value is referred to as normalized luminescence (NL) of the sensor bacteria. The bioavailable $HgCH_3Cl$ in the sample was calculated according to the NL of the sensor bacteria in the sample and the standard calibration curve (see Figure 1).

Results

The 6 samples analyzed during these visits are presented in Table 2. The concentrations of $HgCH_3Cl$ added to montmorillonite, kaolin and humic acid were 10 and 63 µg/kg of dry weight as maximum. Prior to analysis of the samples with the organomercury sensor

Escherichia coli strain MC1061(pmerRBluxCDABE) the standard calibration curve of the sensor was prepared (Figure 1). The limit of determination for the sensors in this study was 0.04 μg/l of $HgCH_3Cl$.

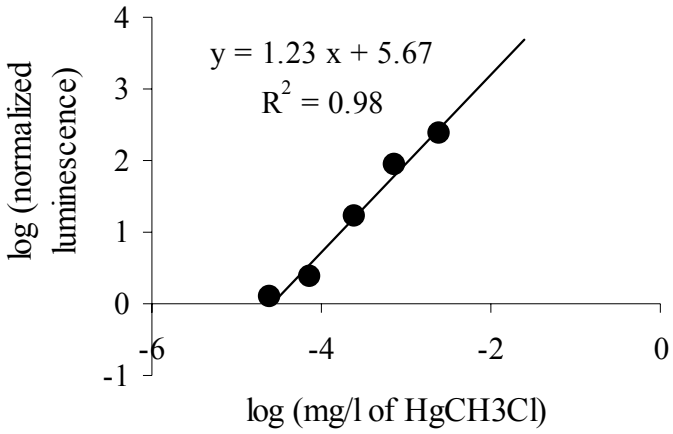

Figure 1 *Induction of luminescence (expressed as log of the normalized luminescence) of the organomercury sensor MC1061(pmerRBluxCDABE) in response to the $HgCH_3Cl$.*

The parallel analysis of the soil-water suspensions and particle-free extracts with the sensor bacteria showed that a different amount of $HgCH_3Cl$ was adsorbed (determined according to the bioavailable methylmercury) in montmorillonite, kaolin and humic acid samples (typical building constituents of soils). In general, relatively higher adsorbed amounts of $HgCH_3Cl$ were detected in montmorillonite compared to kaolin and humic acid samples. These data are in agreement with the results found in the bibliography [6, 7]: the greatest adsorption of $HgCH_3Cl$ was observed in the case of montmorillonite, whereas the adsorption to kaolin and humic acid was somewhat lower (Table 1). The higher adsorption of methylmercury to clay minerals compared to humic acid is probably due to the higher cation exchange capacity of montmorillonite and kaolin while the higher adsorption of $HgCH_3Cl$ to montmorillonite compared to kaolin is due the different tightnesses of the structural bonds in these materials. Moreover, the restricted surface area of kaolin limits the adsorption of cations [8].

Table 1 *Adsorption of $HgCH_3Cl$ at pH7 to different materials (data from ICP-OES [6]).*

Sample type	% of $HgCH_3Cl$ adsorbed of that added to the soil
Montmorrilonite	68
Kaolin	36
Humic acid	20

The adsorbed bioavailable amounts (bioavailable in soil-water suspension – bioavailable in particle-free extract) of $HgCH_3Cl$ in montmorillonite, kaolin and humic acid samples determined by the organomercury sensors are presented in Table 2. As mentioned above the

adsorbed bioavailable fractions of methylmercury were higher in montmorillonite (55 % of the added $HgCH_3Cl$) compared to kaolin (15-33 % of the added $HgCH_3Cl$) and humic acid samples (14-22 % of the added $HgCH_3Cl$). The somewhat lower adsorbed bioavailable fraction seen in the kaolin and humic acid samples with 10 ppb of added $HgCH_3Cl$ could not be appropriately explained by the current data. It is interesting to note that the data from bacterial sensors are coherent with the data obtained by Gaona *et al.* and by XAFS analysis [6]. The data from XAFS techniques showed that the bonds between methylmercury and montmorillonite have more ionic character whereas the methylmercury-humic acid bond is more covalent. Thus, the differences in the bioavailabilitiy of methylmercury (Table 2) in different samples are probably due to different strengths of the bonds formed during adsorption.

Table 2 *Bioavailable fraction of $HgCH_3Cl$ in the samples according to the organomercury sensor MC1061(pmerRBluxCDABE).*

Sample type	$HgCH_3Cl$ added to the sample, µg/l[a]	bioavailable of that adsorbed to the sample µg/kg dwt[b]	bioavailable of that adsorbed to the sample, % of added[c]
Montmorrilonite	0.8	6.8	54.9
	5	43.9	55.3
Kaolin	0.8	3.6	14.5
	5	22.7	33.6
Humic acid	0.8	2.0	14.0
	5	12.6	22.7

[a] 25 ml of the $HgCH_3Cl$ solution with the specified concentration was added to 2 g of the sample. Thus, the theoretical final concentrations for dry weight of the soil were 10 and 63 ppb (for 0.8 and 5), respectively.

[b] bioavailable $HgCH_3Cl$ in soil-water suspension-bioavailable $HgCH_3Cl$ in particle-free soil-water suspension

[c] bioavailable $HgCH_3Cl$ in soil-water suspension-bioavailable $HgCH_3Cl$ in particle-free soil-water suspension as the percentage of the added $HgCH_3Cl$.

Conclusions

The luminescent bacterial organomercury sensors used in this study proved applicable for the analysis of bioavailable methylmercury from contaminated soils/sediments. The sample-adsorbed methylmercury was determined by the parallel analysis of soil-water suspensions (contact assay – assessment of water-extracted and particle-bound bioavailable methylmercury) and particle-free soil-water extracts (assessment of water-extracted bioavailable methylmercury). According to the results the adsorbed bioavailable fraction of $HgCH_3Cl$ decreased in the order montmorillonite>kaolin>humic acid, showing a strong correlation with the total adsorbed methylmercury (ICP-OES and XAFS data). Moving from spiked samples (as used in this study) to real environmental samples, the speciation of metals in parallel to adsorption and bioavailability studies would provide us with unique information about the behaviour (bioavailability, toxicity) of different metal species in complex natural samples.

References

[1] Gaona, X., Mangold, S., Calmano, W., Valiente, M. Manuscript submitted to Analytical and Bioanalytical Chemistry.
[2] Ivask, A., Hakkila, K., Virta, M. 2001. Analytical Chemistry, 73(21), p. 5168-5171
[3] Westöö, G., 1968. Acta Chem Scand 22, p. 2277-2280
[4] Ivask, A., Francois, M., Kahru, A., Dubourguier, H. C., Virta, M., Douay, F. Corrected Proof in Chemosphere available online
[5] Hakkila, K., Green, T., Leskinen, P., Ivask, A., Marks, R., Virta, M. Accepted for publication to Journal of Applied Toxicology
[6] Gaona, X., 2004. SENSPOL Newsletter no. 10, January, p. 10-14
[7] Obukhovskaya, T. D. 1982. Pochvovedenie, (6), 53-8.
[8] Tan H. Kim. 1998. Principles of soil chemistry. 3rd ed.

Annex 6

Assessment of Hg behaviour in human teeth restored with dental amalgam by synchrotron microprobe techniques

[The present manuscript is to be completed with additional new EXAFS data]

Anna Bernaus[1], Xavier Gaona[1], David Singer[2], Gordon Brown Jr.[2], Carlos Muñoz[3], Isabel Martinez[4] and Manuel Valiente[1].

[1] Grup de Tècniques de Separació en Química (GTS), Departament de Química, Universitat Autònoma de Barcelona, 08193 Bellaterra (Barcelona), Spain.

[2] Department of Geological and Environmental Sciences, Stanford University, Stanford, CA 94305-2115, USA.

[3] Department of Restorative Dentistry, School of Dental Medicine, Squire Hall Rm. 215, 3435 Main St., Buffalo, NY 14214-3008.

[4] Facultat d'Odontologia, Universitat de Barcelona, Campus de Bellvitge - Pavelló de Govern, Feixa Llarga, s/n, 08907 L'Hospitalet de Llobregat (Barcelona), Spain.

ABSTRACT

Synchrotron X-ray microprobe techniques have been proposed for the direct observation of mercury and other heavy metals present in human teeth restored with mercury amalgams. The study has focussed on the possible diffusion of Hg and other heavy metals forming the amalgams (including the partial substitution of Ca) throughout different tooth regions (enamel, dentine, pulp and root structures), whilst assessing the molecular environment of mercury in these regions and its possible impact on Hg release to saliva.

μ-XRF analysis has shown the poor diffusion of Hg from the amalgam to other tooth regions, therefore limiting its possible release to the blood stream. On the other hand, a significant diffusion of Cu and Zn from the amalgam to the dentine region has been

identified. The increase of the concentration of both elements in the dentine seems to be correlated with the slight depletion on Ca concentration in this region, therefore suggesting the possible exchange of Ca^{2+} by Cu^{2+}/Zn^{2+} in hydroxiapatite crystals ($Ca_{10}(PO_4)_6(OH)_2$), the dominating mineral compound in the dentine region. Nevertheless, these phenomena would entail the partial oxidation of some metallic elements and alloys in the amalgam, a point which has been already described elsewhere[1,2,3,4]. Lead has been shown not to diffuse into the dentine region, therefore reinforcing its stability in the metallic phase forming the amalgam.

μ-EXAFS analysis has indicated the same Hg coordination environment both in the amalgam and in the interfaces amalgam/dentine and amalgam/enamel. Data evaluation considering the first coordination shell in the amalgam region has revealed the presence of Ag and Hg as neighbouring atoms of mercury, as well as the absence of oxygen. This result corroborates, within the sensitivity limits of the μ-EXAFS technique, the poor (or null) interaction of mercury with the dental environment and the stability of the amalgam with time.

INTRODUCTION

Metallic amalgam has been used since 150 years to fill carved cavities of carious teeth. This amalgam is produced by mixing liquid mercury (40%-50 % by weight) with solid particles of an alloy of silver, tin, copper, and sometimes zinc, palladium, indium, and selenium. During the amalgamation process, mercury diffuses into the Ag_3Sn phase of the alloy particles and reacts with silver and tin fractions. This process lead to the formation of various compounds, predominantly silver-mercury (Ag_2Hg_3) and tin-mercury ($Sn_{7-8}Hg$) phases. The final distribution depends on the exact composition

of the alloy, and usually contains impurities of Sn and Cu that dissolve in small amounts in the Ag_2Hg_3 phase[1].

Mercury amalgam has had a bright clinical success, principally caused by its excellent mechanical properties, easy handling and reduced costs. On the other hand, the main drawback refers to the toxicity, mobility and bioavailability of mercury, as metallic mercury is released in small quantities in all clinical procedures as well as during mastication and drinking of hot beverages[1]. In the body, inhaled Hg^0 is oxidized by catalase to Hg^{2+}, which reacts with tissue functional groups and may cause neurotoxic and nephrotoxic effects[5]. Moreover, mercury entering natural water bodies from amalgam wastes can be transformed (by bacteria) into methylmercury, which persists in the environment, bioaccumulates in living tissues and organs, whilst being extremely toxic[6].

A number of alternatives to mercury amalgam have been largely utilised for teeth filling, mainly with concern of esthetical parameters. Nowadays, the use of resin composite restorative materials is growing in developed countries and has already become more popular than metallic amalgams.

The release of mercury from amalgam restorations and its uptake by human body has been widely studied by the dental scientific community[5,7-9]. In this concern, some studies have suggested that dental amalgams are associated with multiple sclerosis[10] and neurodegenerative disorders such as Alzheimer[11]. Similarly, an association between the number of amalgam fillings and the concentration of inorganic Hg in blood and total Hg in urine has been proposed by Vater and co-workers[5]. Nevertheless, the majority of these studies have not been able to identify unambiguous scientific evidence regarding amalgam restorations effect on human health[12-16].

If occurring, blood uptake and toxicity of mercury from dental amalgam would be expected to vary according to mercury speciation and spatial distribution in teeth. Consequently, the use of analytical methodologies able to determine mercury speciation in this environment would be of key significance to the study of Hg behaviour and the potential risk posed for human health. To the best of our knowledge, only a few publications have been devoted to clarify this point, without significant success.

In this sense, some publications have used microanalytical techniques to study elemental distribution in dental tissues[17,18], whereas laser ablation coupled to ICP-MS was used for *in- situ* trace-mercury profiling of individual teeth[19,20]. On the other hand, recent studies have shown that the use of synchrotron-based X-ray Absorption Spectroscopy (XAS) techniques[21,22], can be successfully applied to study the local coordination environment of mercury. However, scarce information still exists regarding interaction of mercury with tooth bulk and other heavy metals, as well as its diffusion pattern throughout the different tooth regions.

This work aims to face this problematic by taking advantage of microprobe techniques capacities. In order to achieve this objective, a representative set of sixteen teeth samples restored with mercury amalgam has been studied. A qualitative study of tooth bulk has been first undertaken by means of SEM-EDS and μ-XRF techniques. This first observation intended to assess elemental distribution in depth and along different tooth regions. Then, μ-EXAFS scans of the Hg L_{III}-edge were taken to evaluate the local environment of mercury in the amalgam, enamel-amalgam and dentine-amalgam interfaces. Similar studies have been attempted elsewhere to predict diffusion mechanisms of Ca[23,24], Zn[25,26], Fe[27] and Ni[28] ions in dental tissues, although none has been focussed on Hg yet.

MATERIALS & METHODS

Sample preparation

Sixteen human molar teeth restored with mercury amalgam of similar composition were collected from dental school donors. After extraction, each tooth was rinsed, disinfected and air-dried. The dry tooth was transferred to a cylindrical plastic mould, where a mixture of 15:2 epoxy resin (Epofix Resin, Struers, Spain): hardener (Epofix Hardener, Struers, Spain) was poured and allowed to set in a vacuum chamber. Once teeth were secured in the hardened resin block, they were removed from the plastic mould and longitudinally sectioned with a diamond blade (Petro-Thin, Buehler, USA). Teeth surface was polished with a silicon carbide grit (320-1200 particle size), whilst ultra pure water was used as lubricant and to minimize contamination of the tooth surface. Smooth and flat surfaces of teeth samples were thus obtained. The sectioned teeth were dried and embedded in epoxy resin (epoxy mounting media resin, Microtec section Lok, USA) and several slices between 50 and 600 μm thickness were cut from each specimen with the diamond blade. Finally, slices were protected with a cover-slip and polyester-Grieβharz casting-resin (GTS, Vosschemie, Spain).

In this work only one slice of each tooth was analysed, taking into account the sample thickness optimisation of one selected tooth. For each tooth, a similar scan pattern was adopted to enable comparison between the different specimens studied and the different regions of the teeth, including amalgam, enamel, dentine, pulp and root structures.

SEM-EDS analysis

Before measuring at the synchrotron facility, samples were analysed by Scanning Electron Microscopy (SEM) with a coupled energy dispersive X-ray spectroscopy (EDS) unit. The aim of this analysis was to describe the bulk metal content of each

sample by obtaining a first qualitative overview of the elemental composition within the different regions of teeth samples (enamel, dentine and root region).

The apparatus utilized was an electron microscope JEOL JSM 6300 (Jeol LTD, Tokio, Japan), equipped with an energy X-ray dispersive spectrometer Link ISIS-200 (Oxford Instruments, England). The energy resolution of the EDS unit was ~ 140 eV.

Microprobe analyses

Microprobe analyses were performed at the synchrotron facility Hamburger Synchrotronstrahlungslabor (HASYLAB) at Deutsches Elektronen-Synchrotron DESY in Hamburg (Germany), at the bending magnet beamline L[29].

For μ-XRF analysis, beamline set-up provided a monochromatic beam with an energy of 17 keV from a Si(111) double crystal monochromator[30], collimated to a size of ~ 15 μm diameter FWHM by a polycapillary halflens. The sample was also monitored by a long distance zoom microscope (magnification up to 300x) and a CCD-camera (3 μm spatial resolution). The fluorescence signal was detected with a GRESHAM Si (Li) detector and a RADIANT VORTEX silicon drift detector (50 mm^2 active area). The angles beam – sample and sample – detector, were kept at 45º in order to reduce the scattered radiation reaching the fluorescence detector. Each μ-XRF map held 11 × 11 points with a 10 μm step size, both along x and y axes. The time of fluorescence signal accumulation was selected according to the maximum count-rate in each scan, and varied between 1 and 5 seconds per step.

Elements included within the μ-XRF analysis were: Ca, Hg, Fe, Mn, Cu, Pb, Zn and Br. Silver and tin signals were not monitored given the high ionization energy of their K_{1s} electrons (25514 and 29200 eV respectively). On the other hand, L lines of these elements were neither considered due to their weak excitation at the irradiated energy (3806 and 4465 eV respectively, for their L_{2s} electrons).

When analysing the amalgam region, an aluminium filter was placed in front of the fluorescence detector to attenuate the high count-rate of the amalgam.

In order to obtain information about the local Hg coordination environment in the amalgam and interface regions, Hg L_{III}-edge μ-EXAFS data were collected from the amalgam, enamel-amalgam and dentine-amalgam interfaces. EXAFS spectra were collected at room temperature in fluorescence detection mode, and corrected by pre-edge subtraction and spline fitting using SixPack[31]. The Fourier Transform (FT) was performed over a k-range of 3 to 9.5 $Å^{-1}$.

Hg L_{III}-edge EXAFS spectra of relevant model compounds in dental amalgam, γ-Ag_2Hg_3 and $Hg_{0.1}Sn_{0.9}$ as well a HgO, were evaluated by FEFF7.0 calculations using, as reference, known crystallographic data for these Hg-bearing compounds and reasonable values for the Debye-Waller factor (σ^2= 0.001) with amplitude reduction function (S_0^2= 0.9).

RESULTS AND DISCUSSION

SEM-EDS

A first qualitative bulk analysis of major element composition was performed by SEM-EDS. Figure 1.a shows a contrast microscope image at the interface enamel-amalgam-dentine, and the elemental mapping of this interface from a representative sample. Similar results were obtained for each sample analysed. As expected, SEM-EDS measurements suggest a main contribution of Ca, P and O at the enamel region and the presence of Hg, Ag, Sn and Cu at the amalgam region. Zinc, Ca, Na and O appeared to be the main elements in the dentine region (see Figure 1.b).

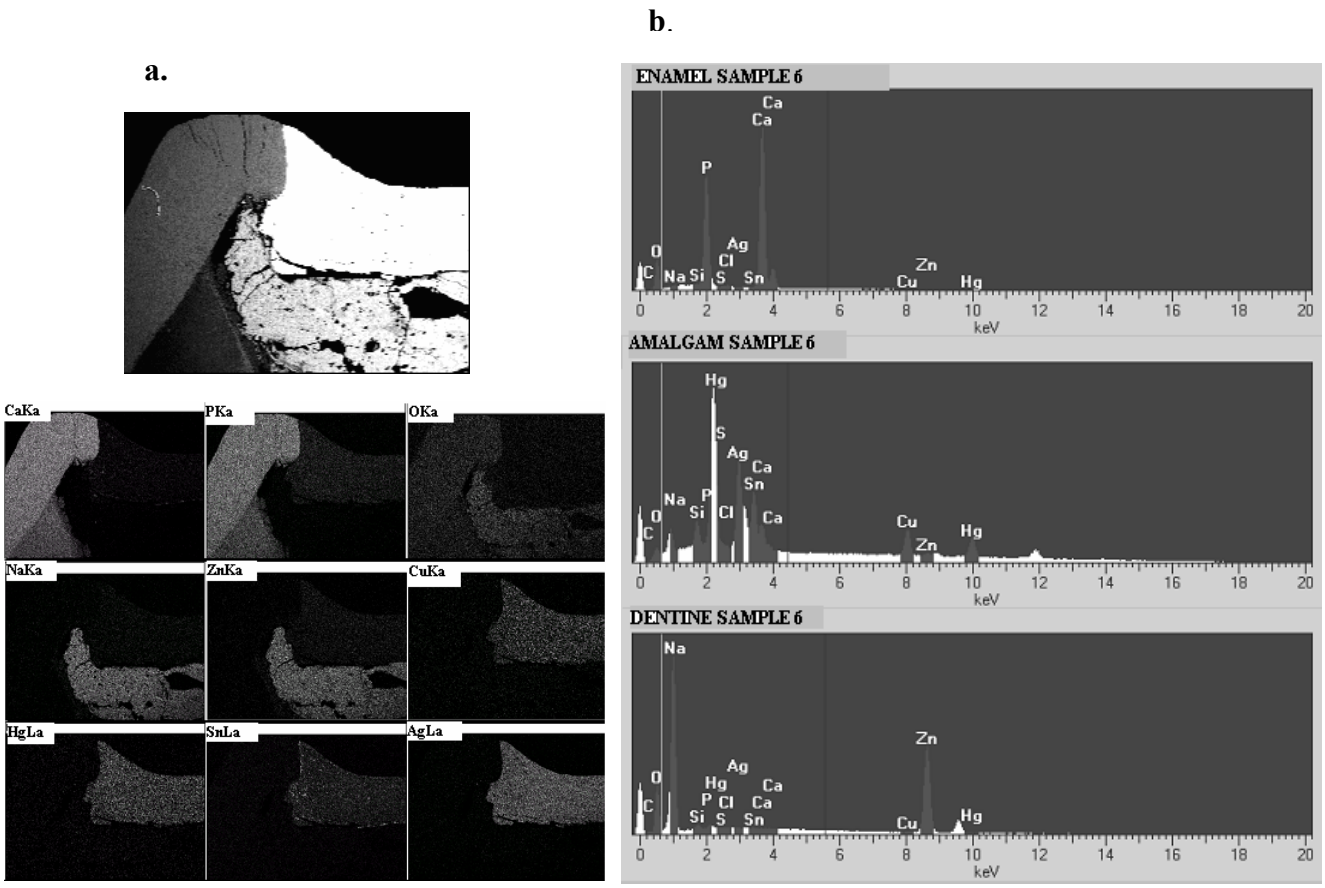

Figure 1. a. Contrast microscope image and elemental mapping of the interface enamel-amalgam-dentine from a representative sample tooth; **b.** EDS spectra from a full-field area of the enamel, amalgam and dentine regions from the same sample.

μ–X-ray fluorescence analysis

The first step consisted of the optimisation of sample thickness and depth for signal acquisition. Individual μ-XRF mapping analyses at different depths (from 10 to 210 μm) were performed at the amalgam, enamel and dentine regions. Figure 2 shows the correspondent elemental profile from a representative sample. Given the heterogeneous elemental distribution, a compromise analysis depth of 100 μm was selected. Therefore, and being aware that thinner samples are expected to yield better spatial resolution in

the X-ray fluorescence images[32], 100 μm thick samples were considered for microprobe analyses.

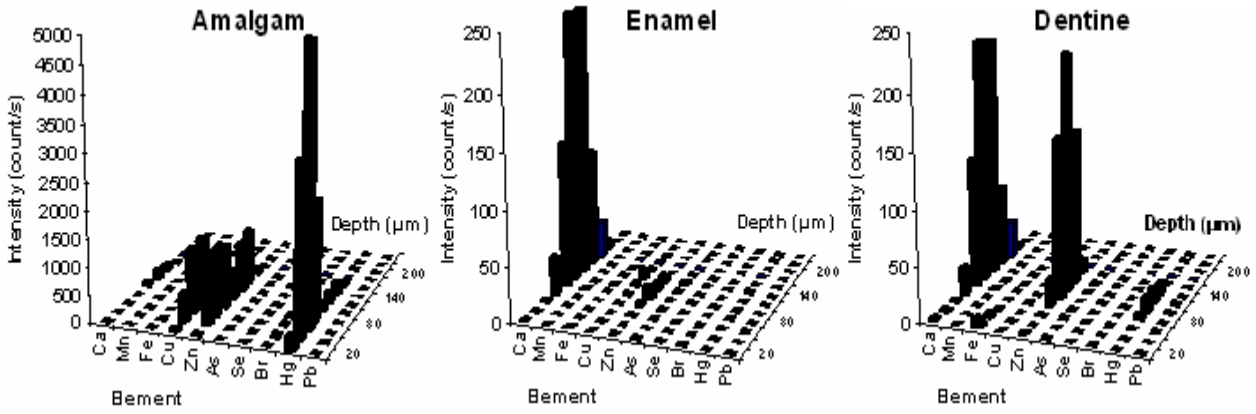

Figure 2. Fluorescence signal variations in selected points into the tooth (amalgam, enamel and dentine regions) as function of depth, of the studied metals in the first studied tooth sample.

Figure 3 shows the distribution profiles for Hg, Cu, Zn, Ca, Mn, Fe, Pb and Br along the different tooth regions considered (amalgam, dentine, pulp cavity and root). Elemental profiles were obtained by means of μ-XRF elemental maps, and correspond to the average of measurements collected for the sixteen restored teeth.

As expected, Hg is mainly located in the amalgam region of the tooth. Although high mercury concentrations are still found within the border amalgam-dentine, fluorescence signal decreases very rapidly along the dentine. This fact suggests that diffusion of mercury throughout the dentine region is very limited, below the detection limit of the technique (~0.1 ppm).

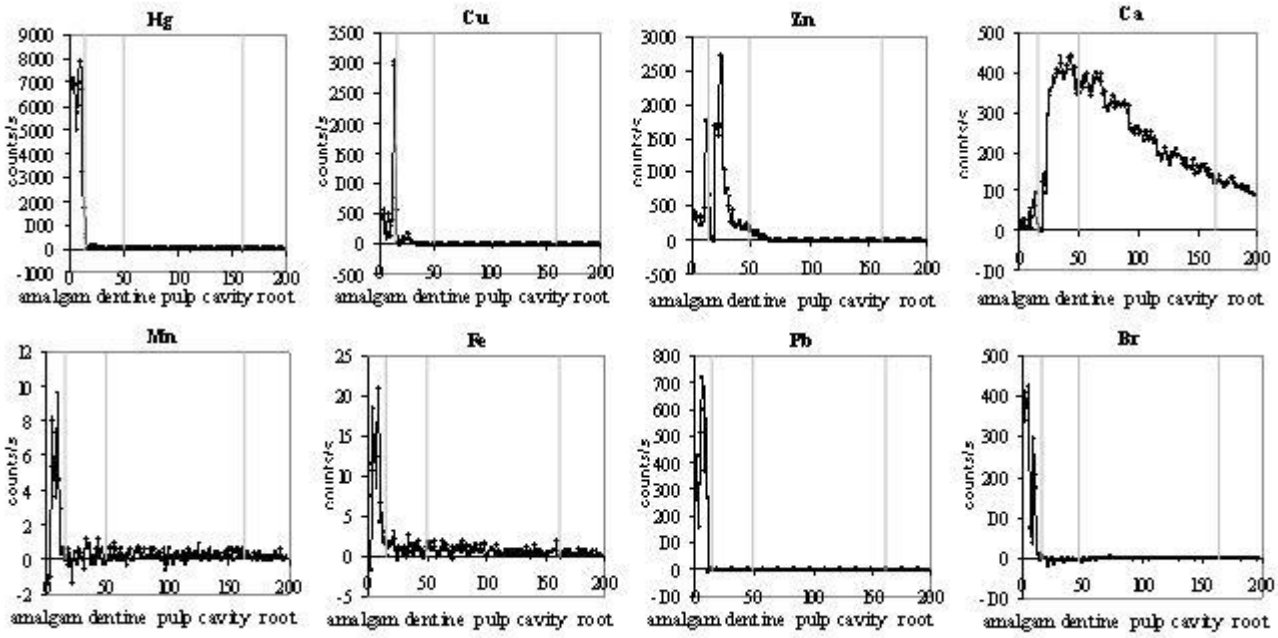

Figure 3. Spatial distribution of Hg, Cu, Zn, Ca, Mn, Fe, Pb and Br throughout the tooth structure (amalgam, dentine, pulp cavity and root) determined by μ–XRF. Each plot corresponds to the measurements average of the sixteen target samples. Grey lines indicate interfaces between tooth regions.

Cu can be incorporated to teeth through the diet, although the relatively high concentrations measured within the metallic amalgam seem to indicate that this is the main (and probably only) source of Cu within the studied samples. On the other hand, Zn naturally occurs in bulk dental enamel in small quantities (100 – 300 ppm)[22,33,34,35], while being found in higher concentrations (400 to 2000 ppm)[34,35] at the enamel surface. Additionally, Zn is one of the minor components of the amalgam, and therefore this must be also considered as an important source of Zn within the studied teeth. As observed in Figure 3, both Cu and Zn show a similar pattern, which differs significantly from that observed for Hg. The higher concentrations of these elements observed in the dentine region show a higher tendency to diffuse, which might be related to a partial exchange with Ca ions present in the dentine. This hypothesis is reinforced by the

observations made for hard tissues regarding the Zn^{2+} and Cu^{2+} isovalent replacement of Ca^{2+} in hydroxyapatite[19,22,25,26,36-41].

Although feasible, this trend seems to indicate a relative ionic character of these elements within the studied teeth. In this sense, Sutow and co-workers[3] observed in vitro corrosion products resulting from crevice corrosion of low- and high-copper dental amalgams. Also in that study, several Sn and Cu oxy(hydroxides) were identified ($Sn_4(OH)_6Cl_2$, SnO, Cu_2O and CuCl), which could be considered as a potential source of ionic Cu. On the other hand, Zn metal is added to the amalgam to prevent Cu oxidation by atmospheric oxygen. Therefore, Zn(II) is formed in the alloy melting process as the oxidation product. Although the main fraction of Zn(II) is released within a short period (from several hours to a few weeks) after completion of the dental application[4], a smaller fraction of oxidised Zn may remain at the amalgam, being therefore a potential source of ionic Zn.

Although lead content in teeth has been normally associated to environmental pollution or diet, the whole lead in evaluated teeth samples comes from the metallic amalgam. As for Cu and Zn, Pb has been reported to substitute Ca in the hydroxyapatite lattice[38,41,42]. Nevertheless, this observation has not been noticed in the studied samples, therefore suggesting that Pb is found in a less available form than Cu and Zn.

Fluorescence signal from Mn and Fe appears to be very low, probably due to the high incident energy considered (17000eV), far from their respective ionisation energies ($Fe(K_{1s})$ = 7116eV and $Mn(K_{1s})$ = 6539eV). Given the poor sensitivity for these elements, Mn and Fe have been only identified within the metallic amalgam.

Calcium is one of the main elements found at the enamel, basically present as calcium hydroxyapatite ($Ca_{10}(PO_4)_6(OH)_2$) crystals. On the other hand, dentine composition consists of approximately 75% inorganic calcium hydroxyapatite and up to 25% organic

material (mainly collagen). This point is consistent with observations made in Figure 3, where the amount of Ca decreases when approaching to the pulp region.

It is also important to highlight the apparent Ca depletion observed in the nearby of the amalgam. Although further experiments would be advisable, this fact might be related with the proposed ion exchange mechanism with Cu and Zn.

No heavy metals have been observed in the pulp cavity and root regions, above the detection limits of the technique (0.1 ppm). Both regions consist of a soft connective tissue, richly supplied with blood vessels and nerve endings[43]. Consequently, our observations suggest that a minimum diffusion of metals to the blood occurs.

Figure 4 shows the element correlation plots obtained from the μ-XRF mapping exercise. Figure 4a details a well-defined linear correlation between Hg and Cu. This correlation can be explained by the formation of mixed Hg – Cu compounds during the amalgamation process. Figure 4a also suggests the almost null Hg diffusion taking place in the studied samples, given the observed incompatibility between Hg and Ca.

Figure 4b supports the hypothesis of a substitution reaction taking place between Cu/Zn and Ca, as for a given region, the depletion on Ca is linearly related with the increase of Cu and Zn signal (see dotted circles). On the other hand, no Ca – Pb correlations is given, therefore suggesting the presence of this element in a less mobile form.

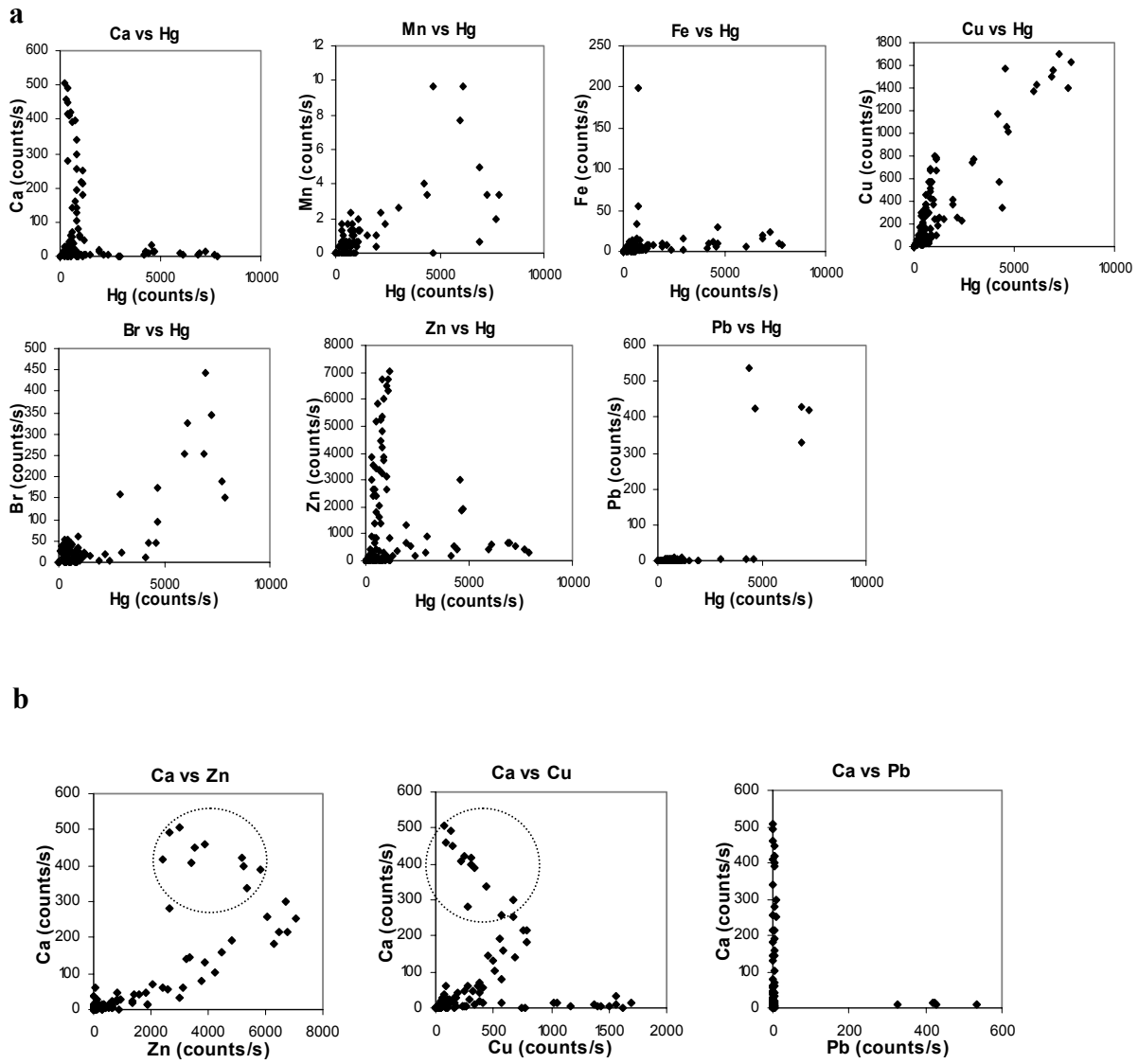

Figure 4. Pair correlation diagrams from the μ-XRF maps of the sixteen studied samples, as fluorescence line intensity (counts s^{-1}); **a.** Hg with Ca, Mn, Fe, Cu, Br, Zn and Pb; **b.** Ca with Zn, Cu and Pb.

μ–EXAFS analysis

The Hg L_{III}-line μ–EXAFS spectra of the amalgam, amalgam/dentine interface and amalgam/enamel interface are nearly identical (Figure 5). This observation indicates that Hg coordination environment is very similar within the considered regions. This

could be due to either (1) no diffusion of Hg out of the amalgam resulting in a new Hg-bearing phase, or (2) to diffusion taking place by small molecular-scale clusters that are similar to the amalgam with respect to the local Hg coordination environment. As μ-XRF mapping detected no Hg beyond the amalgam interface, we conclude that no diffusion of Hg occurs beyond this region above the detection limit of the technique.

EXAFS spectrum at the amalgam region was then compared with the simulated EXAFS spectra of the model compounds (γ-Ag_2Hg_3, $Hg_{0.1}Sn_{0.9}$, and HgO). The most remarkable difference between the simulated model compound spectra and that of the amalgam region is the lack of strong backscattering at higher k values in the amalgam spectra (see Figure 6 left), which would be expected from Hg-Hg neighbours. Due to this low signal-to-noise ratio above k=6 $Å^{-1}$, only the initial coordination environment of Hg has been constrained.

Fits of the two first shells of the Fourier transform, show a first shell of three Ag atoms to about 2.89 Å, and a second shell of four Hg atoms at around 2.97 Å (see Table 1). This observation suggests the presence of the γ-Ag_2Hg_3 phase, which in fact forms during the amalgamation process. Nevertheless, it is important to highlight the large fit values for the Debye-Waller factors, which may be related to a poor data quality at intermediate to higher k values.

The Fourier transform feature at ~ 1.7 Å has not been attributed to any element but to the poor background subtraction, as it is too short to be a real Hg-M distance. In the system Hg-O, the shortest predicted distance derived from the addition of the Shannon radius for $^{II}Hg^{2+}$ (0.69 Å) and $^{III}O^{2-}$ (1.36 Å) is 2.05 Å[44]. Therefore, the absence of oxygen corroborates the poor (or null) interaction of mercury with the environment and the improbable transformation of this element with time.

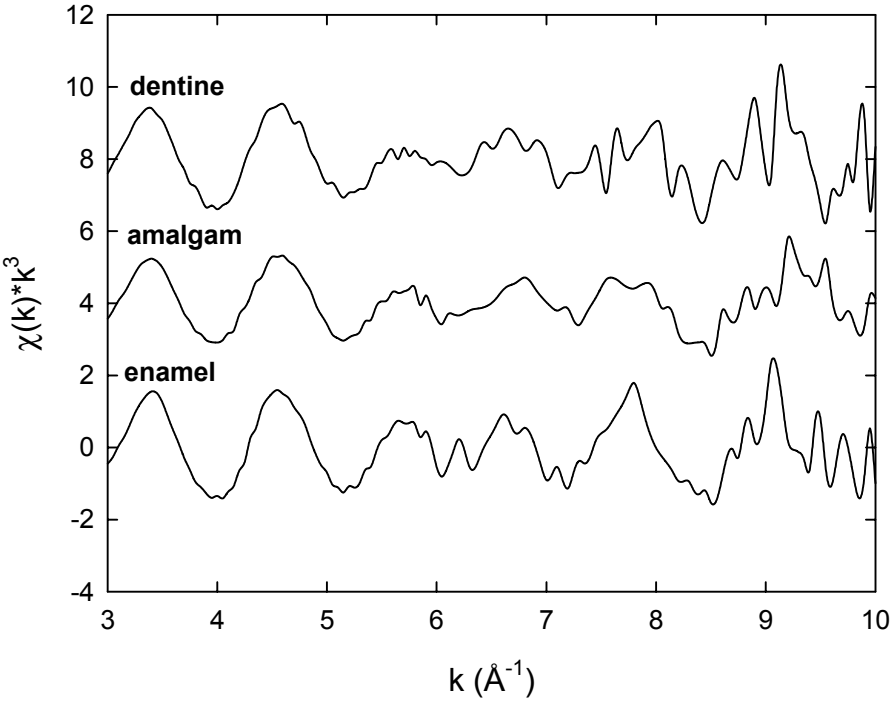

Figure 5. k^3-weighted Hg L_{III}-edge μ–EXAFS at three locations; **1.** the middle of the amalgam ("amalgam"); **2.** at the amalgam/dentine interface ("dentine");and **3.** at the amalgam/enamel interface ("enamel").

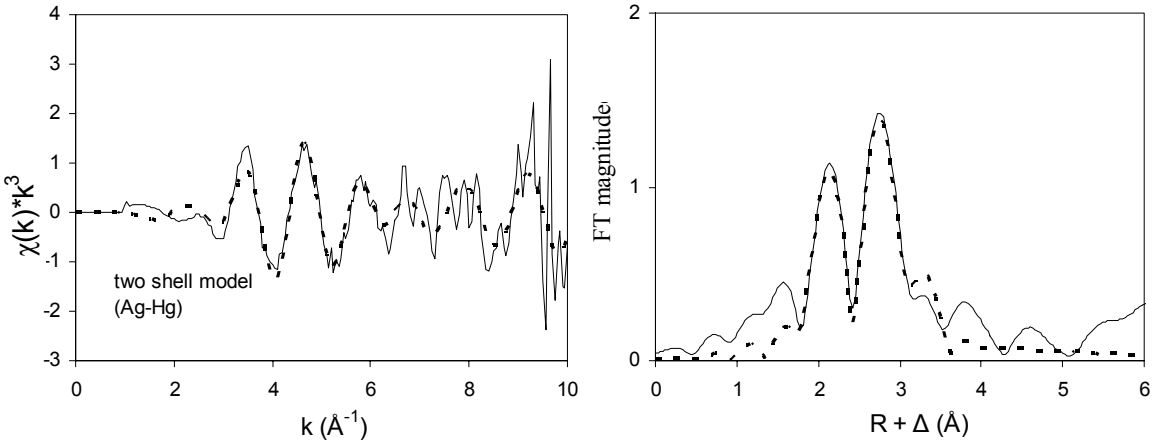

Figure 6. EXAFS data (left) and Fourier transform (right) in the amalgam region. Data are represented by the solid black line, and fits are shown as dashed lines.

Table 1. Fit results of the two first shells of the Fourier transform, in the amalgam region.

Z	CN	R (Å)	σ^2(Å^2)	ΔE^o	red χ^2	S_o^2
Ag	3	2.89	0.02	-1	2.6	0.9
Hg	4	2.97	0.02			

CONCLUSIONS

Experiments have demonstrated the ability of μ-XRF and μ-EXAFS techniques to provide unique information in micro spatial areas of dental hard tissues. Also, the trend for the elemental composition and distribution throughout the teeth provides interesting information for research in dentistry.

Microprobe analyses have showed a minimum diffusion of Hg throughout the tooth, with the identification of a linear correlation between Hg and Cu. However, smaller but significant amounts of Hg may have diffused from the amalgam into other parts of the tooth, taking into account the high detection limit of the technique (~0.1 ppm). In this sense, additional evidence using more sensitive analytical methods should be required to observe if lower levels of Hg can diffuse into the enamel or dentine. On the other hand, a significant diffusion of Cu and Zn from the amalgam to the dentine region has been identified, which is correlated with the slight depletion on Ca concentration in this region. This fact suggested the possible exchange of Ca^{2+} by Cu^{2+}/Zn^{2+} in hydroxiapatite crystals ($Ca_{10}(PO_4)_6(OH)_2$), and the release of such ions to the saliva.

μ-EXAFS analyses have determined that the initial molecular environment of Hg in the amalgam region is limited to the γ-Ag_2Hg_3 phase formed during the amalgamation process. The absence of oxygen in this region reveals a low (or null) interaction of

mercury with the environment and its transformation with time, which corroborate the μ-XRF results. Nevertheless, fits must be taken with caution, due to the high Debye-Waller factors. In order to improve the signal-to-noise spectra over the entire k-range, further experiments should be performed by using more optimal data collection protocols, including cooling the sample or collecting EXAFS data during longer time.

Although clinical implications from the results of this manuscript show no reason to a discontinue use of mercury amalgams, results reported could only be considered as indicative due to the limited number of specimens analysed and the limitations of the technique. Therefore, further studies will be needed with samples of different nature and exposure time, taking into account the species evolution and their distribution with time.

ACKNOWLEDGEMENTS

Synchrotron experiments at HASYLAB were financially supported by the European Community - Research Infrastructure Action under the FP6 "Structuring the European Research Area" Programme (through the Integrated Infrastructure Initiative "Integrating Activity on Synchrotron and Free Electron Laser Science"). Anna Bernaus thanks the Ministry of Science and Education for a PhD scholarship (2003-2006) and for the stay at Stanford University (2005). The financial contribution from the projects: PPQ2002-04267-C03-01 and CTQ2005-09430-C05-01 is also acknowledged.

REFERENCES

[1] Craig RG, Powers JM (2002). Restorative dental materials. 11th edition. United States of America, pp. 288-327.

[2] Ferracane JL, Mafiana P, Cooper C, Okabe T (1987). Time-dependent dissolution of amalgams into saline solution. *J Dent Res* 66(8):1331-1335.

[3] Sutow EJ, Jones DW, Hall GC, Owen CG (1991). Crevice corrosion products of dental amalgam. *J Dent Res* 70(7): 1082-1087.

[4] Sanna G, Pilo MI, Piu PC, Spano N, Tapparo A, Campus GG, Seeber R (2002). Study of the short term release of the ionic fraction of heavy metals from dental amalgam into synthetic saliva, using anodic stripping voltammetry with microelectrodes. *Talanta* 28: 979-985.

[5] Vater M, Akesson A, Lind B, Björs U, Schütz A, Berglund M (2000). Longitudinal study of methylmercury and inorganic mercury in blood and urine of pregnant and lactatinc women, as well as in umbilical cord blood. *Environ Research Section A* 84: 186-194.

[6] Trip L (2001). Canada-wide standards: a pollution prevention program for dental amalgam waste. *J Can Dent Assoc* 67: 270-273.

[7] Barregard L, Sällsten G, Järvholm B (1995). People with high mercury intake from their own dental amalgam fillings. *Occup Environ Med* 52: 124-128.

[8] Vimy MJ, Lorscheider FL (1985). Serial measurements of intraoral air mercury: estimation of daily dose from dental amalgam. *J Dent Res* 64(8): 1072-75.

[9] Weiner JA, Nylander M, Berglund F (1990). Does mercury from amalgam restoration constitute a health hazard?. *Sci. Total Environ* 99: 1-2.

[10] Bates MN, Fawcett J, Garrett N, Cutress T, Kjellstrom T (2004). Health effects of dental amalgam exposure: a retrospective cohort study. *Int J Epidemiol* 33:894-902.

[11] Mutter J, Naumann J, Sadaghiani C, Schneider R, Walach H (2004). Alzheimer disease: mercury as pathogenetic factor and apolipoprotein E as a moderator. *Neuroendocrinol Lett.* 25:331-339.

[12] Bellinger DC, Trachtenberg F, Barregard L, Tavares M, Cernichiari E, Daniel D, *et al* (2006). Neuropsychological and Renal Effects of Dental Amalgam in Children. A Randomized Clinical Trial. *JAMA* 295:1775-1783.

[13] Kingman A, Albers JW, Arezzo JC, Garabrant DH, Michalek JE (2005). Amalgam exposure and neurological function. *Neurotoxicology* 26:241-255.

[14] Factor-Litvak P, Hasselgren G, Jacobs D, Begg M, Kline J, Geier J, Mervish N, Schoenholtz S, Graziano J (2003). Mercury derived from dental amalgams and neuropsychologic function. *Environ Health Perspect* 111: 719-723.

[15] Dalen K, Lygre GB, Klove H, Gjerdet NR, Askevold E (2003). Memory functions in persons with dental amalgam. *J Dent* 31:487-492.

[16] Nitschke I, Muller F, Smith J, Hopfenmuller W (2000). Amalgam fillings and cognitive abilities in a representative sample of the elderly population. *Gerodontology* 17:39-44.

[17] Grunke K, Stärk HJ, Wennrich R, Franck U (1996). Determination of traces of heavy metals (Mn, Cu, Zn, Cd and Pb) in microsamples of teeth material by ETV-ICP-MS. *Fresenius J Anal Chem* 354: 633-635.

[18] Borea G; Borsetti A (1968). Distribution of mercury in silver amalgams restorations. Effects of different techniques and instruments. *Archivio Stomatologico* 9(2): 175-88.

[19] Lochner F, Appleton J, Keenan F, Cooke M (1999). Multi-element profiling of human deciduous teeth by laser ablation-inductively coupled plasma-mass spectroscopy. *Anal Chim Acta* 401: 299-306.

[20] Hoffmann E, Stephanowitz H, Ullrich E, Skole J, Lüdke C, Hoffmann B (2000). Investigation of mercury migration in human teeth using spatially resolved analysis by laser ablation-ICP-MS. *J Anal At Spectrom* 15: 663-667.

[21] Carvalho ML, Pinheiro T, Barreiros MA, Casaca C, Cunha AS, Chevallier P (1998). Amalgam components drift in teeth-toxicity risks: A preliminary approach. *Nucl Instr and Meth B* 136: 913-918.

[22] Carvalho ML, Marques JP, Brito J, Casaca C, Cunha AS (2002). Hg, Bi, Cu and Zn distribution in human teeth treated by dental amalgam measured by synchrotron microprobe. *Nucl Instrum Methods Phys Res Sect B* 196: 148-154.

[23] Elliot JC (1994). Substitucions of calcium ions. In: Fluorapatite and Chlorapatite. Elliot JC., editor. Amsterdam: Elsevier Science, pp. 82-94.

[24] Hasnain, SS (1984). Environment of calcium in biological calcium phosphates. Springer Proceedings in Physics, 2: 145-150.

[25] Barrea RA, Pérez CA, Ramos AY, Sánchez HJ, Grenón M (2003). Distribution and incorporation of zinc in biological calcium phosphates. *X-Ray Spectrom* 32: 387-395.

[26] Tsutomu T, Junko H, Hitoshi M, Tetsuo H (2005). X-ray absorption fine structure analysis of the local environment of zinc in dentine treated with zinc compounds. *Eur J Oral Sci* 113(2): 180-183.

[27] Suzuki Y, Uchida F, Hayakawa K, Suga S (1994). Hard X-ray scanning microscopy and micro X-ray absorption fine-structure spectroscopy studies on iron compounds in the enameloid of fish teeth. *Synchrotron Radiat Biosci* 618-23.

[28] Doebler U, Wenzel L, Arvanitis D, Baberschke K (1986). Surface extended X-ray absorption fine structure study on (2x1) oxygen on nickel (110). *J Physique Colloque* 8 (1): 473-478.

[29] Bernaus A.; Gaona X.; Valiente M (2005). Characterisation of Almadén mercury mine environment by XAS techniques. *J Environ Monit* 7: 771-777.

[30] Falkenberg G, Clauβ O, Swiderski A, Tschentscher Th (2001). Optics for the X-ray fluorescence beamline at HASYLAB. *Nucl Instrum Methods Phys Res Sect A* 467-468: 737-740.

[31] Newville M. SIXPack (Sam's Interface for XAS analysis Package), Powered by IFEFFIT 1.2.6, University of Chicago, 2004.

[32] Martin RR, Naftel SJ, Nelson AJ, Feilen AB, Narvaez A (2004). Synchrotron X-ray fluorescence and trace elements in the cementum rings of human teeth. *J Environ Monit* 6: 783-786.

[33] Kang D, Amarasiriwardena D, Goodman AH (2004). Application of laser ablation-inductively coupled plasma-mass spectrometry (LA-ICP-MS) to investigate trace metal spatial distributions in human tooth enamel and dentine growth layers and pulp. *Anal Bioanal Chem* 378:1608-1615.

[34] Curzon ME, Cutress TW (1983). Trace Elements and Dental Disease. Wright; Boston, MA.

[35] Frank RM, Sargentini-Maier ML, Turlot JC, Leroy MJF (1989). Zinc and strontium analyses by energy dispersive X-ray fluorescence in human permanent teeth. *Arch Oral Biol* 34: 593-597.

[36] Stevens A, Lowe J (1997). Human Histology. Mosby. London.

[37] Bowen HJM (1979). Environmental Chemistry of the Elements. Academic Press., London.

[38] Wakamura M, Kandori K, Ishikawa T (1998). Surface composition of calcium hydroxyapatite modified with metal ions. *Colloids Surf A* 142(1): 107-116.

[39] Rheingold AL, Hues S, Cohen MN (1983). Strontium and zinc content in bones as an indication of diet: an undergraduate project in quantitative analysis with interdisciplinary interest. *J Chem Educ* 60:233-234.

[40] Ingram GS, Horay CP, Stead WJ (1992). Interaction of zinc with dental mineral. *Caries Res* 26:248-253.

[41] Carvalho ML, Casaca C, Pinheiro T, Marques JP, Chevallier P, Cunha AS (2000). Analysis of human teeth and bones from the chalcolithic period by X-ray spectrometry. *Nucl Instrum Methods Phys Res Sect B* 168: 559-565.

[42] Wiechula D, Fischer A, Kwapulinski J, Loska K, Fischer T, Kurpas P (2006). Multivariate Statistical Analysis of Metal Concentrations in Teeth of Residents of Silesian Region, Southern Poland. *Arch Environ Contam Toxicol* 51: 314-320 .

[43] Marques AF, Marques JP, Casaca C, Carvalho ML (2004). X-ray microprobe synchrotron radiation X-ray fluorescence application on human teeth of renal insufficiency patients. *Spectrochim. Acta, Part B* 59:1675-1680.

[44] Shannon RD (1976). Revised effective ionic radii and systematic studies of interatomic distances in halidfes and chalcogenides. *Acta Crystallogr Sect. A* 32:751-767.

Annex 7

Quantitative mercury speciation in Almadén mining district. XANES analysis of ore, calcine, soil and sediment samples

José Maria Esbrí[1], Anna Bernaus[2], Xavier Gaona[2], Carlos Jesús Sánchez-Jimenez[3], Pablo Higueras[1], and Manuel Valiente[2]

[1] Departamento de Ingeniería Geológica y Minera, Escuela Universitaria Politécnica de Almadén, Universidad de Castilla-La Mancha, 13400 Almadén (Ciudad Real), Spain.

[2] Grup de Tècniques de Separació en Química (GTS), Departament de Química, Universitat Autònoma de Barcelona, 08193 Bellaterra (Barcelona), Spain.

[3] Laboratorio de Mineralogía Aplicada, Facultad de Ciencias Químicas de Ciudad Real, Universidad de Castilla-La Mancha. 13071 Ciudad Real, Spain.

ABSTRACT

Mobility and bioavailability of mercury in mining regions is strongly dependent on its chemical speciation and spatial distribution at regional scale. In order to face both key issues, synchrotron-based X-ray absorption near edge spectroscopy (XANES) techniques were applied to samples of untreated mineral, calcines, soils and stream sediments from the Almadén mining district. Results indicate that sulfide phases of mercury are the predominant species in ore dumps and calcines, whereas non-sulfide species are most common in soils and sediments of Valdeazogues River. Cinnabar is predominant in unroasted mineral, while metacinnabar is an important Hg-phase in calcines and soils from decommissioned metallurgical plants of the district. On the other hand, schuetteite is conspicuously present in samples from the San Quintín and Almadenejos area, which is strongly related with the presence of metallic mercury in the ore dump, this species typically appearing at the sunlight exposed side of the rock surface. Finally, as a consequence of predominance of more soluble Hg-phases in

riparian soils and sediments of Valdeazogues river basin, a good correlation with conductivity of these waters was found.

INTRODUCTION

Mercury mines in the Almadén area have been active since Roman times to present days, having produced about one third of total Hg world production. This longterm mine and metallurgical activity has produced a widespread contamination of this heavy metal in the surrounding environment.

The high contents of total mercury in calcines, soils and sediments of Almadén mining district are well documented (Berzas-Nevado et al., 2003; Higueras et al., 2003, 2006; Gray et al., 2004), although only a few studies dealing with mercury speciation are available (Bernaus et al., 2005, 2006). In this sense, it is widely accepted that mercury mobility in dumps, soils and sediments is strongly dependent on its chemical speciation. Therefore, the proper knowledge of mercury speciation in the Almadén area must be considered as a key issue before carrying out further risk assessment exercises and remediation actions.

The main objective of the present work is to evaluate the speciation of Hg in the Almadén district and the geochemical factors that control its transport and deposit throughout the drainage network. For this purpose, XANES techniques have been selected for Hg speciation, whereas mineralogical and chemical characterization of the samples was achieved by X-ray diffraction (XRD), X-ray fluorescence (XRF) spectroscopy and Zeeman atomic absorption spectrometry with high frequency modulated light polarization (ZAAS-HFM).

EXPERIMENTAL METHODS

Sample collection, storage and preparation

The survey of the present work was carried out in the main mines and metallurgical plants of the Almadén district (Fig. 1), as well as in their vicinity. Four sites have been selected for this study:

1. The Almadén area, which hosts the main mine of the Almadén area and has produced about 90% of total Hg output of the district. Samples collected in this site include calcines and soils from the locality so-called "Huerta del Rey" (an old metallurgical plant of the 17th century) (HR), mine tailings from the principal dump of Almadén mine (CH), and riparian soils and stream sediments from the Azogado stream (AZG).

2. The second site was Almadenejos area, an old metallurgical plant with five decommissioned furnaces used for mercury recovery from cinnabar. Most samples (ALM) taken from this area are calcines and soils over and around the roasting furnaces.

3. The Valdeazogues river, downstream from El Entredicho open pit, where a sample of suspended particles (RD-124) was collected.

4. The San Quintín area, where some cinnabar ores were transported from Almadén to perform mercury recovery tests at its flotation plant in 1987, and nowadays remains a spoil heap. Samples from this area (SQ) include mine wastes and soils.

Soils, riparian soils, mine tailings and calcines samples (~1.5 kg) were collected at 10-30 cm depth, stored in polyethylene bags, air-dried in a clean room and sieved with a 0.100 mm sieve in the laboratory. Samples of suspended particles were collected from the water column, sedimented in laboratory and air-dried in a clean room.

Water samples in Azogado stream and Valdeazogues River were taken simultaneously to the solid sampling. The sampling method was based upon the USEPA (1996) criteria for sampling ambient water for trace metals (method 1669). Samples were collected in

100 ml plastic flasks, preserved with 0.5 ml ultrapure HNO_3 and 0.5 ml $KMnO_4$, and finally kept below 4ºC until the analysis (Parker et al., 2004). Samples for soluble mercury analysis were filtered in situ with syringe filters of 0.45 μm (Horowitz et al., 1996). Simultaneously, physico-chemical parameters including pH, Eh, conductivity, dissolved oxygen, turbidity and temperature were measured in each sampling site.

All solid samples were prepared for synchrotron analysis using an aliquot, mixed with polyethylene for IR spectroscopy, homogenized with a vortex and pressed to a pellet with 5 tones cm^{-2} of pressure.

Mineralogical and chemical characterization

X-ray diffraction was used to identify the bulk mineralogy and primary matrix components of the geologic samples. The XRD analyses were carried out at the I.R.I.C.A. (University of Castilla-La Mancha), using a Philips diffractometer (Model 1700, with CuK_α radiation, automatic divergence aperture, and curved graphite monochromator). The reception and dispersion aperture were 0.1 mm and 1º respectively. A Xe-filled gas was used, and the scan range was 3º - 75º 2Θ with a scan speed of 0.1º 2Θ s^{-1}.

The XRF analyses were carried out also at the I.R.I.C.A, over fused glass discs, on a sequential spectrometer Philips, model Magix Pro. This technique used a 4kW light element super sharp RH target end window X-ray tube, and a set of analyzer crystals of LiF220, LiF200, Ge, PE and PX1. Signal detection is composed by a tandem of flow and sealed proportional detectors, plus a scintillation detector in parallel.

Total mercury content of solid and aqueous samples was determined with a Lumex RA-915+ analyzer, an instrument based on Zeeman atomic absorption spectrometry, using high frequency modulation of light polarization (ZAAS-HFM) (Sholupov and Ganeyev, 1995).

Analysis of solid samples was made by using the pyrolysis RP-91C accessory of the RA-915+, at the laboratories of the Almadén School of Mines. In this treatment, total mercury content is converted from a bound state to the atomic state by thermal decomposition in a two-section atomizer. As a first step, samples are vaporized and the mercury compounds partly decomposed. This is followed by heating up samples to 800°C, where mercury compounds become fully decomposed and organic compounds and carbon particles catalytically transform to carbon dioxide and water. Detection limit of the technique for soils and sediments samples is 0.5 μg Hg kg^{-1}

The analysis of water samples was carried out with a Cold Vapour RP-91 unit coupled to the RA-915+ analyzer, and using $SnCl_2$ as reducer agent. Standard solutions to be used for calibration were daily prepared from certified standards. Detection limit of the technique (for this sample-type) is 0.2 ng Hg l^{-1}.

XANES analyses

XANES analyses were performed at the synchrotron facility Hamburger Synchrotronstrahlungslabor (HASYLAB) at Deutsches Elektronen-Synchrotron DESY in Hamburg (Germany), at the bending magnet beamline A1 (see further technical details in Bernaus et al., 2005). All experiments were carried out at room temperature.

The photon absorption of Hg was recorded at the edge energy for its L_{III} line at 12284 eV, while the monitored fluorescent lines were $L_{\alpha 1}$ (9988.8 eV) and $L_{\alpha 2}$ (9897.6 eV). Pure reference compounds were analysed in transmittance mode, whereas fluorescence detection mode was used for the analysis of unknown samples. Minerals and pure compounds considered for the speciation analyses included: $HgCl_2$, $HgSO_4$, HgO, CH_3HgCl, Hg_2Cl_2 (calomel), HgS_{red} (cinnabar), HgS_{black} (metacinnabar), $Hg_2NCl_{0.5}(SO_4)_{0.3}(MoO_4)_{0.1}(CO_3)_{0.1}\bullet(H_2O)$ (mosesite), $Hg_3S_2Cl_2$ (corderoite), $Hg_3(SO_4)O_2$ (schuetteite) and Hg_2ClO (terlinguaite).

A Si(111) monochromator was chosen for Hg analysis, taking into account the energy range and scan step width detailed in Table 1. A thin pellet of $HgCl_2$ was periodically measured during Hg analysis, aiming at the correction of any energy displacement produced during experiments.

XANES spectra were processed by using SixPACK data analysis software package (SIXpack, 2004). Spectra processing included energy correction, signal normalization and background correction. After data correction and normalization, a model based on lineal combination of reference compounds spectra was obtained by applying a principal component analysis (PCA), in order to determine the number and nature of reference compounds from the database required to reconstruct the spectrum of the unknown samples (Malinowski, 1991; Ressler et al., 2000; and Wassermann et al, 1999). Chemical speciation was finally obtained by applying a linear least-square fitting procedure within the energy range shown in Table 1. The quality of the analyses was evaluated through the reduced chi square value (χ^2), which represents the goodness of the fit to the spectra data.

RESULTS AND DISCUSSION

Sample characterization

The mineralogy of the samples (Table 2) is in good agreement with their geological characters: soils and sediments of a region with shales and quartzites as main components of the stratigraphic sequence (García Sansegundo et al., 1987, among others). This mineralogy includes quartz, feldspar, and phyllosilicates (illite with minor proportions of kaolinite and/or phyrophillite) as main constituents, and with occasional traces of cinnabar (Huerta del Rey samples), goethite (at Azogado stream), calcite or dolomite (Almadenejos metallurgical plant).

The geochemistry of the studied samples (Table 3) is also in good agreement with this mineralogy: major elements contents in soil samples from Almadenejos, Almadén-Huerta del Rey and San Quintín areas, as those of riparian soils from Azogado stream are typical of developed soils at areas with shales and quartzites as major substrate, with high SiO_2 and Al_2O_3 contents pointing clay minerals and silica as major components. The presence of variable amounts of CO_2 is indicative of the variable presence of carbonates, and the relatively high Fe content (expressed as Fe_2O_3) is related with the presence of abundant interbeddings of mafic magmatic rocks at the district scale (Higueras et al., 2000; for instance). Calcine samples from Almadenejos show a similar mineralogy, reflecting the siliciclastic composition of the processed ore. Nevertheless, the high SO_3 content (4.5-6.0%) indicates the presence of non-decomposed sulphides, and/or sulphates, both hinting the low performance of the metallurgical processes taking place in the studied furnace facilities. Lower (although still higher than average) SO_3 contents are also present in San Quintín mine soils (1.86%) and dumps (0.86-1.49%). Trace elements reach normal values for this type of samples, but for the generally high Hg contents and for the Pb, Zn and Ba values in San Quintín area soils and mine wastes. Analysis of total mercury content carried out by ZAAS-HFM evidences elevated Hg contents in calcine samples and soils from metallurgical sites (see Table 4). These high mercury concentrations have been attributed to the inefficient metallurgical techniques carried out in the ancient plant of Almadenejos and Huerta del Rey (Sumozas, 2005). As expected in a mining area active since Roman times, high total mercury concentrations have been also found in sediments and riparian soils from Valdeazogues River, but especially from Azogado stream (1800-2816 μg Hg g^{-1}). The latter are only one order of magnitude below calcine samples, and agree with previous studies undertaken at the same sampling site (see Gray et al., 2004).

Chemical speciation by XANES analysis

Mercury sulfides are the most common species found in almost all samples (Table 4), especially in those collected in abandoned metallurgical plants like Almadenejos area and Huerta del Rey, in the Almadén area. Other non sulfide phases like schuetteite ($Hg_3O_2SO_4$), montroydite (HgO), calomel (Hg_2Cl_2) and mercuric chloride ($HgCl_2$) are present in different proportions in samples of soils and sediments.

Mercury phases present in samples from San Quintín area are representative of unroasted waste rocks. This observation agrees with the historical use of this site, as are samples from the Almadén mine were brought to San Quintín to perform a number of flotation tests. Additionally, it must be highlighted the lack of metacinnabar in the composition of these samples, as well as the high proportions of cinnabar (46.8-59.3%) and minor proportions of more soluble species like calomel (23.9-32.7%) or schuetteite (16.6-20.7%), which may be attributed to the weathering processes taking place.

On the other hand, soils from the Almadenejos area show significant proportions of metacinnabar (31.5-38.8%). The transformation of cinnabar to metacinnabar in roasting process occurs at 345º C, and is typical of incomplete roasting in old furnaces like those installed in Almadenejos metallurgical plant. This is corroborated by lower proportions of metacinnabar (~23%) in samples of soils from Huerta del Rey, where the roasting of the ore was carried out with and older but more efficient technique. Other non-sulfide phases like mercuric chloride (37.6-43%) have been also identified and attributed to the process of soil formation.

High proportions of schuetteite have been identified in ore stockpile in San Quintín and Almadenejos area. This is a phase typically linked with the presence of Hg^0 and appears in the sunlight exposed side of the rock surface. Schuetteite has been frequently found near old furnaces or ore dumps in Almadén mining district (Higueras et al., 2003).

High proportions of more soluble phases have been identified in soil and sediment samples from Valdeazogues River (~ 99%) and Azogado stream (54.5 -96.2%). These phases (Hg_2Cl_2, $HgCl_2$ and $Hg_3O_2SO_4$) have been considered as the result of the weathering processes taking place within the drainage network of the mining district. The diagrams of Piper of these waters show a clear preponderance of sulphate (39.7%) and chloride-sulphate (43.0%) phases over the bicarbonate ones (17.1%) (Berzas-Nevado, 2003).

A good correlation of soluble phases in sediments samples and high conductivity values in these rivers was found (Table 5). Hence, very high contents of schuetteite (~94%) were found in samples downstream El Entredicho mine, the point of Valdeazogues river with higher contents of soluble salts (43-818 μSiemens/cm). The same pattern was observed in Azogado stream, where 54.5-96.2% of mercury phases were non-sulphide in a tributary of Valdeazogues river with also high values of conductivity (795-2227 μSiemens/cm). In both cases, mercury content in waters was found to be high to very high, averaging 5.15 μg Hg l^{-1} in Azogado stream and 0.81 μg Hg l^{-1} in Valdeazogues River of total mercury. Dissolved mercury content was 23 and 30% respectively (see Table 5).

The presence of sulphide mercury phases in sediments and riparian soils from Azogado stream (7-45.7%) and the absence of these phases at detectable levels in suspended particles of Valdeazogues River is probably linked with the different mining history of their main mercury sources: Almadén mine and El Entredicho mine respectively. The mining and metallurgic activity in the Almadén mine has been very important since 16th Century to the present days (Sumozas, 2005), therefore posing a long-term source for transport and deposition of waste, calcines and mine tailings throughout the Azogado stream. On the other hand, El Entredicho mine has lower dimensions (less

than 10% reserves that those of Almadén mine), and a shorter mining history. None in situ metallurgic activity took place at El Entredicho, whilst the exploitation technique used minimized the transport of mine products from the open pit to the Valdeazogues river.

CONCLUSIONS

This study represents the first regional approach to mercury speciation within the mining area of Almadén. Five different sampling sites have permitted to identify the predominance of less soluble mercury compounds in dumps and wastes from mines and metallurgical plants, whereas more soluble Hg-phases (Hg_2Cl_2, $HgCl_2$ and $Hg_3O_2SO_4$) were found in soils and sediments of the whole area. This extent must be taken into account in further risk assessment exercises.

A correlation between soluble mercury compounds and conductivity of the water stream has been established for sediments and suspended particles from Valdeazogues and Azogado rivers. This relationship suggests a main transport of these soluble mercury phases linked to the weathering and wash-up processes of ores and mine wastes.

ACKNOWLEDGEMENTS

Synchrotron experiments at HASYLAB were financially supported by the European Community - Research Infrastructure Action under the FP6 "Structuring the European Research Area" Programme (through the Integrated Infrastructure Initiative "Integrating Activity on Synchrotron and Free Electron Laser Science"). The financial contribution from the projects: CTQ2005-09430-C05-01 and PPQ2003-01902 is also acknowledged.

References cited

Berzas Nevado JJ, García Bermejo LF, Rodríguez Martín-Doimeadios RC (2003). Distribution of mercury in the aquatic environment at Almadén, Spain. *Env Poll* 122: 261-271.

Bernaus A, Gaona X, Valiente M (2005) Characterisation of Almadén mercury mine environment by XAS techniques. *J Environ Monit* 7: 771 – 777.

Bernaus A, Gaona X, Esbrí JM, Higueras P, Falkenberg G, Valiente, M (2006). Microprobe techniques for speciation analysis and geochemical characterization of mine environments: the mercury district of Almadén in Spain. *Environ Sci Technol* 40 (13): 4090-4095.

Higueras P, Oyarzun R, Biester, H, Lillo J, Lorenzo S (2003). A first insight into mercury distribution and speciation in soils from the Almadén mining district. *J Geochem Explor* 80: 95–104.

Higueras P, Oyarzun R, Lillo J, Sánchez-Hernández JC, Molina JA, Esbrí JM, Lorenzo S (2006). The Almadén district (Spain): anatomy of one of the world's largest Hg-contaminated sites. *Sci Tot Env* 356: 112-124.

Higueras P, Oyarzun R, Munhá J, Morata D (2000). The Almadén metallogenic cluster (Ciudad Real, Spain): alkaline magmatism leading to mineralization process at an intraplate tectonic setting. Revista de la Sociedad Geológica de España, 13-1: 105-119.

García Sansegundo J, Lorenzo S, Ortega E (1987). Mapa geológico nacional a escala 1:50.000, Hoja 808 (Almadén). Servicio de Publicaciones, Ministerio de Industria y Energía. Madrid. 60 p.

Gray JE, Hines ME, Higueras PL, Adatto I, Lasorsa BK (2004). Mercury speciation and microbial transformations in mine wastes, stream sediments, and surface waters at the Almadén Mining District, Spain. *Environ Sci Technol* 38: 4285-4292.

Horowitz AJ, Lum KR, Garbarino JR, Hall GEM, Lemieux C, Demas CR (1996). Problems associated with using filtration to define dissolved trace element concentrations in natural water samples. *Environ Sci Technol* 30: 954– 63.

Malinowski ER (1991). Factor analysis in chemistry; 2nd edition; Wiley & Sons, Inc.; New York, p 350.

Parker JL, Bloom NS (2004). Preservation and storage techniques for low-level aqueous mercury speciation. *Sci Total Environ* 337: 253– 263.

Ressler T, Wong J, Roos J, Smith IL (2000). Quantitative speciation of Mn-bearing particulates emitted from Autos burning (methylcyclopentadienyl) manganese tricarbonyl-added gasolines using XANES spectroscopy. *Environ Sci Technol* 34 (6): 950-958.

SIXPack (Sam's Interface for XAS analysis Package). 2004 Powered by IFEFFIT 1.2.6. Copyright ©. Matt Newville: University of Chicago.

Sholupov SE, Ganeyev AA (1995). Zeeman absorption spectrometry using high frequency modulated light polarization. *Spectrochim Acta* 50B: 1227-1238.

Sumozas R. (2005). Arquitectura industrial en Almadén: Antecedentes, genesis y extensión del modelo. PhD Thesis, Castilla-La Mancha University.

Slowey AJ, Johnson SB, Rytuba JJ, Brown, GEJr (2005). *Environ Sci Technol* 39(20): 7869-7874

USEPA, 1996. Method 1669. Sampling ambient water for trace metals at EPA water quality criteria levels. http://dnr.wi.gov/org/water/wm/ww/mercury/1669.pdf.

Wasserman SR, Allen, PG, Shuh DK, Bucher JJ, Edelstein NM (1999). EXAFS and principal component analysis: a new shell game. *J Synchrotron Rad* 6: 284-286.

Table 1 Energy and scan step width of the Si(111) monochromator.

Hg	
Energy (eV) (XANES region)	Measurement intervals (eV)
12170-12240	2
12240-12260	1
12260-12300	0.5
12300-12410	1
12410-12460	5

Table 2 Mineralogical composition of the studied samples, after XRD.

Location	**Material**	**Quartz**	**Plagioclase**	**Phylosilicate**	**Goethite**	**Calcite**	**Cinnabar**	**Dolomite**
Almadén area (Huerta del Rey)	Soil	47	Traces	51			Traces	
Valdeazogues river	Suspended particles	14	7	79 (Illite, Kaolinite)				
Azogado stream	Sediment	19	8	79 (Illite, Kaolinite)	<5			
Azogado stream	Riparian soil	31	5	64 (Illite, Kaolinite, Phyrophillite)				
Almadenejos metallurgical plant	Calcines	19	7	72 (Kaolinite)		5		
Almadenejos metallurgical plant	Soil	28	<5	65 (Illite, Kaolinite)				<5
San Quintín area	Mine tailings	9	11	90 (Illite, Kaolinite, Clinotirolite)				

Table 3 Geochemical composition of the studied samples, after XRF.

	ALM-101	ALM-102	ALM-103	ALM-104	CH-126	AZG-105	AZG-106	CH-128	HR-108	HR-109	HR-110	CH-127	RD-153	SQ-111	SQ-112	SQ-113
Locality	**Almadenejos**	**Almadenejos**	**Almadenejos**	**Almadenejos**	**Almadenejos**	**Azogado**	**Azogado**	**Azogado**	**Huerta Rey**	**Huerta Rey**	**Huerta Rey**	**Almadén**	**Valdeazogues**	**San Quintin**	**San Quintin**	**San Quintin**
Sample type	**Soil**	**Soil**	**Calcines**	**Calcines**	**Soil**	**Sedim**	**Rip. Soil**	**Rip. Soil**	**Soil**	**Soil**	**Soil**	**Mine dump**	**Susp. Part.**	**Mine dump**	**Mine dump**	**Soil**
SiO_2	49,403	59,78	40,603	43,296	58,331	59,101	59,769	62,461	58,401	51,042	49,969	60,056	50,889	56,226	56,024	61,017
Al_2O_3	16,341	17,314	11,204	12,88	16,049	17,038	14,11	15,083	18,345	24,48	22,573	18,37	19,567	16,23	18,944	14,624
Fe_2O_3	7,452	9,14	6,067	8,524	7,416	5,228	6,742	5,204	6,023	5,53	7,443	6,397	11,94	8,859	6,595	5,738
Cr_2O_3	0,016	0,042				0,023	0,016		0,024	0,018	0,022	0,017	0,056	0,019	0	0,018
MnO	0,106	0,156	0,062	0,093	0,079	0,057	0,072	0,062	0,047	0,032	0,053	0,057	0,196	0,072	0,066	0,065
MgO	1,082	1,169	0,953	1,217	1,268	0,793	0,817	0,608	0,36	0,474	0,468	0,678	1,353	1,983	1,304	1,834
CaO	4,941	6,653	7,185	6,853	1,034	0,762	1,493	1,005	0,502	0,571	1,031	1,544	0,495	0,554	0,703	0,49
Na_2O	0,47	0,321	0,441	0,44	0,306	0,388	0,447	0,35	0,321	0,313	0,399	0,567	1,451	0,648	0,41	0,501
K_2O	2,253	2,523	1,763	2,088	2,537	2,686	2,266	2,054	2,582	2,153	1,912	2,403	1,318	3,437	3,792	3,29
TiO_2	0,994	1,534	0,685	0,929	0,977	0,991	0,814	0,958	1,025	1,278	1,163	0,87	2,211	0,723	0,878	0,672
P_2O_5	0,544	0,384	0,182	0,24	0,324	1,237	1,217	0,726	0,363	0,376	0,364	0,311	0,269	0,176	0,225	0,18
SO_3	0,358	0,353	6,011	4,543	0,647	0,564	0,796	0,312	0,771	0,192	0,257	0,304	0,08	1,487	0,855	1,862
CO_2	15,59		21,987	15,5	10,05	10,43	10,93	10,93	10,39	13,34	14,13	8,08	9,95	6,47	8,79	6,42
Majors total	**99,55**	**99,369**	**97,143**	**96,603**	**99,018**	**99,298**	**99,489**	**99,753**	**99,154**	**99,799**	**99,784**	**99,654**	**99,775**	**96,884**	**98,586**	**96,711**

	ALM-101	ALM-102	ALM-103	ALM-104	CH-126	AZG-105	AZG-106	CH-128	HR-108	HR-109	HR-110	CH-127	RD-153	SQ-111	SQ-112	SQ-113
Locality	**Almadenejos**	**Almadenejos**	**Almadenejos**	**Almadenejos**	**Almadenejos**	**Azogado**	**Azogado**	**Azogado**	**Huerta Rey**	**Huerta Rey**	**Huerta Rey**	**Almadén**	**Valdeazogues**	**San Quintin**	**San Quintin**	**San Quintin**
Sample type	**Soil**	**Soil**	**Calcines**	**Calcines**	**Soil**	**Sedim**	**Rip. Soil**	**Rip. Soil**	**Soil**	**Soil**	**Soil**	**Mine dump**	**Susp. Part.**	**Mine dump**	**Mine dump**	**Soil**
Ni	31	39	24	31	39	71	24	39	16	39		24	244	24	55	31
Cu	88		80		88	144	120	112	80	72		128		136	200	232
Zn	153	193	56	137	265	233	257	185	96	104	185	112	129	6.877	1.221	7.134
Rb	41	55	55	64	46	46	41	41	46	55	46	41	23	69	69	69
Sr	203	237	194	245	237	186	186	144	194	161	152	144	144	85	169	68
Y	13	25		8	13	13	21	17	13	21	17		13		17	
Zr	222	311	111	207	229	415	304	400	304	222	252	429	163	215	237	170
Nb	7	14			10	10		7	10	14	10	10	17		14	
Ba	923	985	493	672	1.003	627	519	475	555	457	421	27	546	1.012	663	1.254
Hg	**2.204**	**2.945**	**24.644**	**31.600**	**6.705**	**3.964**	**1.926**	**343**	**852**	**343**	**148**	**1.139**		**3.167**	**2.241**	**1.028**
Pb	74	102				139	724	102	214	111	130			15.837	2.154	19.049
Cl		170	550	510		260	330	190	220		150	120	100			
Ce				285							261	244	252			
Br		290				20		10	10						10	10
As			64			23										
Ge		180				76	28		14					62	56	21
Ga							15			15	15		22	15		
Sb																

Table 4 Main mercury phases and their relative proportions (%).

Location	Material	Sample	Hg (µg.g^{-1})	Cinnabar	Metacinnabar	HgO	$HgCl_2$	Hg_2Cl_2	Schuetteite	X^2
Almadén area	Mine tailings	CH-127	989	62.2				36.9		0.064
Almadén area (Huerta del Rey)	Soil	HR-108	976	36.9	23.1			40.2		0.094
Almadén area (Huerta del Rey)	Soil	HR-109	404	33.1	24.3			43		0.13
Almadén area (Huerta del Rey)	Soil	HR-110	200	40.6	22			37.6		0.11
Valdeazogues river	Suspended particles	RD-124	105				6.4		93.8	0.65
Azogado stream	Sediment	AZG-105	1800	7			10		82.8	0.34
Azogado stream	Riparian soils	AZG-106	2816	3.4			19.2		77	0.36
Azogado stream	Riparian soil	CH-128	450	24.1	21.6		18.7	35.8		0.088
Almadenejos metallurgical plant	Soil	ALM-101	2720	38.4	38.8				22.8	0.27
Almadenejos metallurgical plant	Soil	ALM-102	2629	38.5	31.5				29.9	0.58
Almadenejos metallurgical plant	Calcines	ALM-103	21,000	46.9		15.9			37.6	0.4
Almadenejos metallurgical plant	Calcines	ALM-104	27,000	51.6		20.8			27.3	0.41
Almadenejos metallurgical plant	Soil	CH-126	2230	33.4	32.4				21.7	0.03
San Quintín area	Mine tailings	SQ-111	902	54				29.5	16.6	0.065
San Quintín area	Mine tailings	SQ-112	1730	51.4				28	20.7	0.066
San Quintín area	Soil	SQ-113	1935	59.3				23.9	17	0.067
San Quintín area	Soil	SQ-114	390	46.8				32.7	20.4	0.11

Table 5 Mercury contents in suspended particles, sediments, riparian soils and waters of Valdeazogues River and Azogado stream.

Location	Material	Sample	Geological	Water		Conductivity
			Hg (µg g^{-1})	Total Hg (µg l^{-1})	Dissolved Hg (µg l^{-1})	
Valdeazogues river	Suspended particles	RD-124	105	(0.10-2.82) n=26	(0.004-0.31) n=8	(43-818) n= 26
Azogado stream	Sediment	AZG-105	1800	(0.80-20.60) n=19	(0.097-0.529) n=4	(795-2227) n=19
Azogado stream	Riparian soils	AZG-106	2816	(0.80-20.60) n=19	(0.097-0.529) n=4	(795-2227) n=19
Azogado stream	Riparian soil	CH-128	450	(0.80-20.60) n=19	(0.097-0.529) n=4	(795-2227) n=19

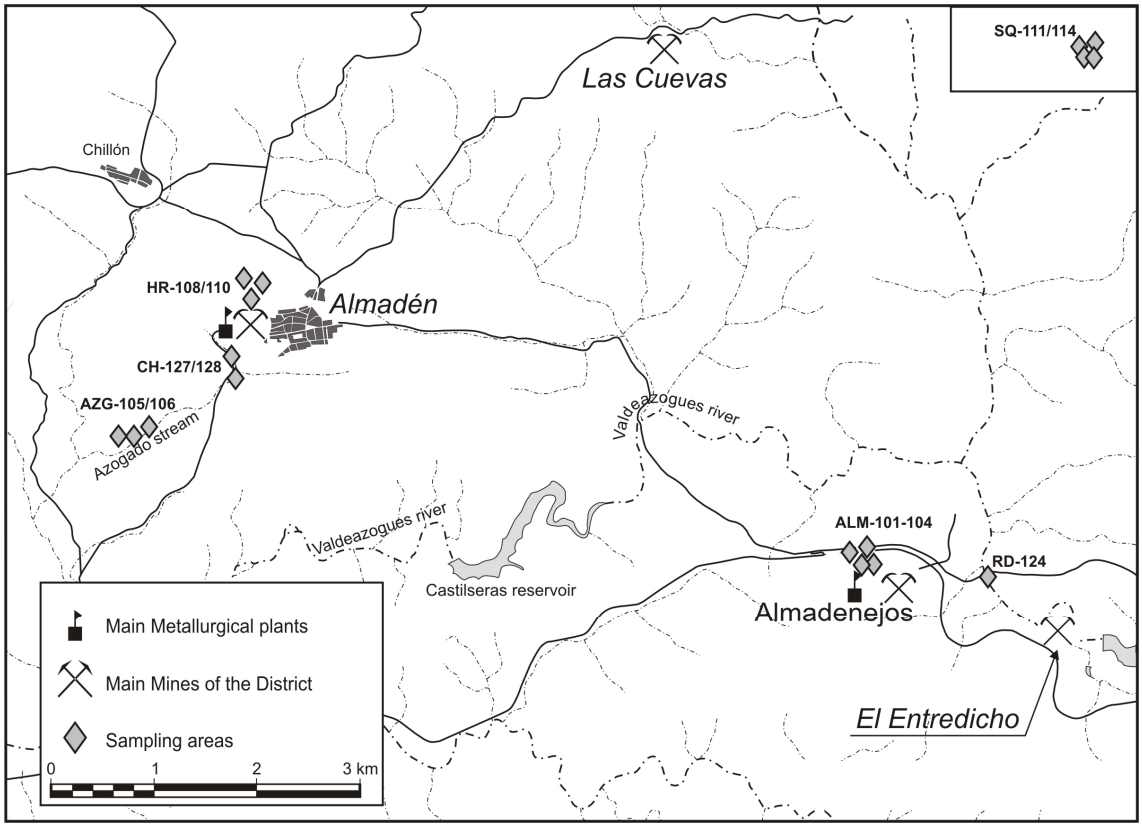

Figure 1 Sampling locations, mines and metallurgical sites of the Almadén district. Abbreviations correspond to the project's internal data management.